MEASUREMENT OF DIJET CROSS SECTIONS IN DEEP INELASTIC EP SCATTERING AT HERA

Dissertation
zur Erlangung des Doktorgrades
des Department Physik
der Universität Hamburg

Vorgelegt von
Thorben Theedt
aus Kiel

Hamburg
2009

Gutachter der Dissertation: Prof. Dr. Robert Klanner
Prof. Dr. Dieter Horns

Gutachter der Disputation: Prof. Dr. Robert Klanner
Dr. Thomas Schörner-Sadenius

Datum der Disputation: 09.11.2009

Vorsitzender des Prüfungsausschusses: Dr. Georg Steinbrück

Vorsitzender des Promotionsausschusses: Prof. Dr. Robert Klanner

Dekan der MIN Fakultät: Prof. Dr. Heinrich Graener

Leiter des Department Physik: Prof. Dr. Jochen Bartels

Abstract

Dijet cross sections have been measured in deep inelastic neutral current electron-proton scattering at HERA. Cross sections have been measured differentially as functions of the photon virtuality, Q^2, the scaling variable, Bjorken x, the mean transverse jet energy, $\overline{E}_T$, the invariant dijet mass, M_{jj}, the difference in jet pseudorapidity, $\eta' = |\eta^{\text{jet1}} - \eta^{\text{jet2}}|$ and the momentum fraction, ξ. Cross sections as function of ξ have also been measured in different regions of the photon virtuality. The analysed data were recorded at a centre-of-mass energy of 318 GeV with the ZEUS detector in the years 1998, 1999, and 2000 and correspond to an integrated luminosity of 81.74 pb^{-1}. The phase space of the analysis is defined by $125 < Q^2 < 5000$ GeV^2 and $|\cos\gamma_h| < 0.65$, where γ_h is the polar angle of the hadronic final state. Jets are reconstructed with the inclusive k_T cluster algorithm in the Breit reference frame. Dijet events are selected by applying an asymmetric cut on the transverse jet energy according to $E_{T,Breit}^{\text{jet1(2)}} > 12(8)$ GeV, where the indices correspond to the two highest energetic jets in the pseudorapidity range $-2 < \eta_{Breit} < 1.5$. The measured cross sections are compared to QCD calculations in next-to-leading order (NLO) as implemented in the DISENT program. For the comparison the data and the theoretical predictions are corrected to hadron level. The applied correction procedures are based on Monte Carlo models. The data are (for all measured variables) in good agreement with the theoretical predictions. Dijet cross sections allow, as compared to inclusive-jet measurements, the reconstruction of additional kinematic observables like the invartiant dijet mass, M_{jj}, or the momentum fraction, ξ. The presented dijet analysis thus represents a very detailed test of perturbative QCD. Moreover, the cross sections measured in different regions of Q^2 are shown to be sensitive to the gluon density of the proton. They might thus be well suited to provide additional constraints on the gluon PDF when included in (NLO) QCD fits.

In the years 2000 and 2001 HERA was upgraded from HERA I to HERA II. The shutdown allowed an upgrade of the detector in order to adapt it to the high-luminosity environment and the physics program of HERA II. The detector upgrade comprised a new luminosity (monitoring) system which was designed to cope with the increased luminosity and the high rate of synchrotron radiation. The new luminosity system comprised an electromagnetic calorimeter located at about 6m from the interaction point in the rear region of the ZEUS detector. For the 6m (electron) tagger a trigger was designed and tested, a calibration procedure was established and the radiation damage of the scintillating fibres was monitored via a series of Cobalt scans. In 2007 a detailed study of multiplicities and energy flows based on NC low-Q^2 DIS jet data showed that the energy flow in the upgraded ZEUS detector was not described by the HERA II Monte Carlo predictions. The results triggered the so called *single pion study*, in which single pion events were used to investigate the response of the simulated detector. The study helped to improve the HERA II detector simulation and revealed imperfections of a (at ZEUS commonly used) reconstruction algorithm.

Kurzfassung

Es wurden differentielle Zweijet-Wirkungsquerschnitte in tiefunelastischer Elektron-Proton-Streuung als Funktion der Photon-Virtualität, Q^2, des Impulsbruchteils, Bjorken-x, der mittleren transversalen Jet-Energie , $\overline{E}_T$, der invarianten Zweijet-Masse, M_{jj}, der Differenz in den Jet-Pseudorapiditäten, $\eta' = |\eta^{\text{jet1}} - \eta^{\text{jet2}}|$ und des Impulsbruchteils, ξ, bei HERA gemessen. Die analysierten Daten wurden in den Jahren 1998, 1999 und 2000 bei einer Schwerpunktsenergie von 318 GeV mit dem ZEUS-Detektor aufgenommen und entsprechen einer integrierten Luminosität von 81.74 pb^{-1}. Der Phasenraum ist durch $125 < Q^2 < 5000$ GeV^2 und $|\cos\gamma_h| < 0.65$ gegeben, wobei γ_h der Polarwinkel des hadronischen Endzustandes ist. Jets werden mit Hilfe des inklusiven k_T-Cluster-Algorithmus im Breit-Bezugssystem rekonstruiert. Zweijet-Ereignisse werden durch einen asymmetrischen Schnitt auf die transversale Jet-Energie gemäß $E_{T,Breit}^{\text{jet1(2)}} > 12(8)$ GeV selektiert. Die Indizes beziehen sich hierbei auf die beiden höchstenergetischen Jets im Pseudorapiditätsbereich $-2 < \eta_{Breit} < 1.5$. Die gemessenen Zweijet-Wirkungsquerschnitte werden mit QCD-Rechnungen der nächstführenden Ordnung (NLO) verglichen, wie sie im Programm DISENT implementiert sind. Vor dem Vergleich werden sowohl die Daten als auch die theoretischen Vorhersagen auf Hadronlevel korrigiert. Die Korrektur basiert auf Monte Carlo Modellen. Die Daten werden (für alle gemessenen Variablen) gut durch die QCD-Vorhersagen beschrieben. Zweijet-Ereignisse erlauben, im Vergleich zu inklusiven Jet-Ereignissen, die Rekonstruktion zusätzlicher kinematischer Variablen wie der invarianten Zweijet-Masse, M_{jj} und dem Impulsbruchteil, ξ. Die hier präsentierte Zweijet-Analyse stellt daher einen sehr detaillierten Test der QCD dar. Desweiteren wurde gezeigt, dass die Wirkungsquerschnitte als Funktion von ξ, gemessen in verschiedenen Q^2-Bereichen, sensitiv auf die Gluondichte im Proton sind. Verwendet in (NLO) QCD-Fits können diese Wirkungsquerschnitte daher zu einer Verringerung der Unsicherheit auf die Gluon-PDFs beitragen.

In den Jahren 2000 und 2001 wurde HERA von HERA I zu HERA II aufgerüstet. Der Shutdown ermöglichte eine Umrüstung des ZEUS Detektors, der an die höhere Luminosität und das HERA II Physik-Programm angepasst wurde. Die Umrüstung des Detektors beinhaltete ein neues Luminositäts-System. Eine Komponente des neuen Systems war ein elektromagnetisches Kalorimeter im Rückwärtigen Bereich des ZEUS Detektors. Für diesen 6m-(Elektron-)Tagger wurde ein spezieller Trigger entwickelt und getestet, eine Kalibrationsroutine etabliert, und eine Reihe von Cobalt-Scans durchgeführt, um Strahlenschäden an den Scintillatorfasern zu untersuchen. 2007 zeigte eine detaillierte Untersuchung von Multiplizitäten und Energieflüssen basierend auf Jet-Daten bei niedrigen Photon-Virtualitäten, dass der Energiefluss im umgerüsteten Detektor nicht richtig durch das HERA II Monte Carlo vorhergesagt wurde. Die Ergebnisse triggerten die so genannte *Single-Pionen-Studie*, bei der Ereignisse mit einzelnen Pionen verwendet wurden, um das Ansprechverhalten des simulierten Detektors zu untersuchen. Die Studie half, die HERA II Detektorsimulation zu verbessern und deckte Schwächen eines (bei ZEUS häufig verwendeten) Rekonstruktions-Algorithmus auf.

"Er wurde geboren mit einem sonnigen Gemüt und der Gewissheit, dass die Welt verrückt ist."

Aus "Garp und wie er die Welt sah " von John Irving

Für meine Eltern

Contents

List of Figures

List of Tables

Introduction

According to our present understanding all visible matter consists of point-like elementary particles, quarks and leptons. These spin 1/2 particles (also referred to as fermions) come in three generations, each generation comprising one lepton duplet and one quark duplet (see figure 1). Interactions between these elementary particles are based on four fundamental forces: gravity, the electromagnetic, the weak and the strong interaction. The properties of gravity are described by the general theory of relativity whereas the electromagnetic, the weak and the strong force are described in the framework of the Standard Model of elementary particle physics (SM). In this model, the interactions are described by the exchange of (spin 1) gauge bosons and the electromagnetic and the weak force are combined into the electroweak force.

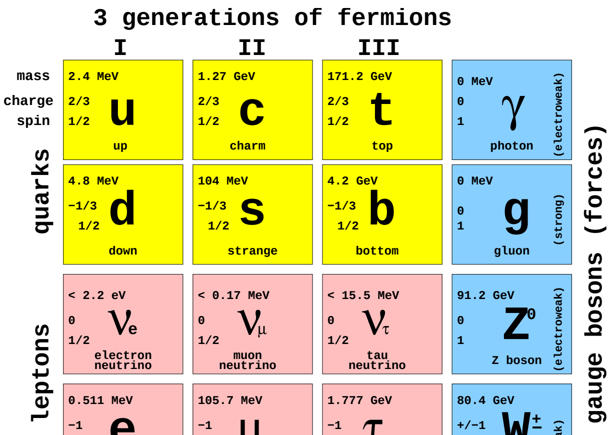

Figure 1: Constituents of the Standard Model (SM) and their basic properties. According to the SM all visible matter consists of point-like particles, quarks and leptons. These spin 1/2 fermions come in three generations, each generation comprising one lepton and one quark duplet. In contrast to leptons, which participate in the electroweak interaction only, quarks, carrying colour charge are also interaction via the strong interaction. Interactions between the fermions are mediated by the exchange of (spin 1) gauge bosons.

Mathematically the SM is based on gauge field theories. The interaction between quarks and gluons (gluons being the gauge bosons of the strong force) is described by the non-Abelian $\mathrm{SU}(3)_\mathrm{C}$ gauge theory, Quantum Chromodynamics (QCD). QCD is by now accepted as the fundamental theory of the strong interaction. Among the successes of QCD are the excellent understanding of the running of the strong coupling constant, α_s, and the agreement of data and theoretical predictions for many final states including strongly interacting particles.

Deep inelastic scattering experiments have played an important role in establishing QCD as the theory of the strong interaction and, in the case of lepton-hadron and hadron-hadron scattering, in investigating the inner structure of hadrons in terms of parton density functions (PDFs). Due to the confinement of colour charge, quarks and gluons can not be observed directly. Instead they are revealed through the appearance of collimated flows of colourless hadrons, referred to as jets. Since the hadrons approximately emerge along the direction of the final state partons, jets provide access to the kinematics and dynamics of the fundamental hard scattering process. In the last decades a large variety of jet cross sections (inclusive jet, dijet, multi-jet, jet-substructures) has been measured, many of them at HERA, where high-energetic electrons were used as a probe to investigate the inner structure of the proton and to study the properties of the strong interaction. The comparison of data with QCD predictions allows to test basic properties of the theory like the perturbative approach, the factorisation Ansatz, the dynamics of the strong interaction and the universality of the PDFs. The corresponding measurements demonstrate the high predictive power of (perturbative) QCD and its character as a precision theory [1]. In addition jet cross sections are used to extract basic constants of the theory like the strong coupling constant, α_s, and the proton PDFs. An exact knowledge of the proton structure is of vital importance for the physics at the Tevatron and the LHC since at hadron-hadron colliders both signal and background for new physics phenomena directly depend on the PDFs of the initial hadron.

In a recent ZEUS analysis [2] cross section data on inclusive jet production in DIS and on dijet events in photoproduction have been used in addition to inclusive cross section data to simultaniously fit α_s and the PDFs of the proton. As a result the uncertainty on the measured gluon density could (in some regions of the phase space) be reduced by up to 35 %, compared to the PDFs not including jet data (see figure 2).

In this thesis a measurement of dijet cross sections in deep inelastic electron-proton scattering at high Q^2 at HERA is presented. The results of this analysis have been published in [3]. The data for the analysis has been recorded with the ZEUS detector (one of two multi-purpose detectors at HERA) and correspond to an integrated luminosity of 81.74 pb^{-1}. The measured cross sections are compared to the predictions of a fixed order QCD calculation of order $\mathcal{O}(\alpha_s^2)$, which for the observed dijet process is the next-to-leading order (NLO). The data and the theoretical predictions are corrected for limited acceptance of the detector and non-perturbative hadronisation processes, respectively. The applied correction procedures are based on the predictions of leading order Monte Carlo generators.

Dijet cross sections allow, as compared to inclusive-jet measurements, the re-

---

[1] It should be noted that the precision of QCD measurements is still far from that of electroweak measurements. As an example the uncertainty on the strong coupling constant, α_s, is in the order of $1 - 2$ % at the scale corresponding to the mass of the Z^0 boson whereas the mass of the electroweak Z^0 boson itself is known to a precision of about 0.002 % [1].

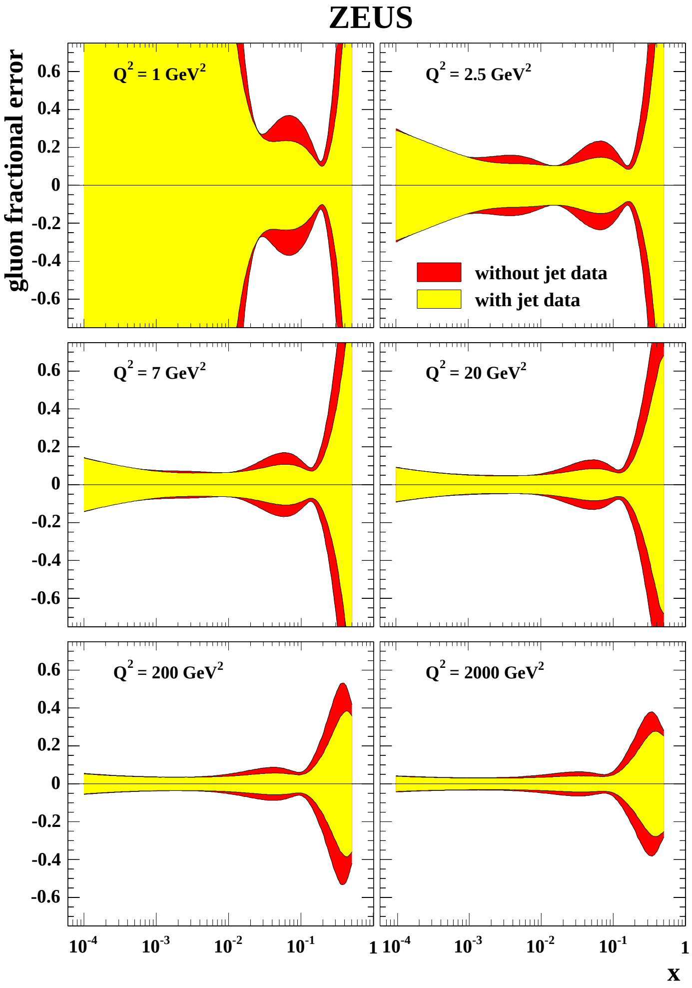

Figure 2: Effect of the use of HERA jet data in ZEUS global PDF fits. The figure shows the relative errors on the gluon PDFs in different regions of the photon virtuality, Q^2. The errors are shown as a function of x, where x is the fraction of the proton momentum carried by the struck parton. The outer darker band indicates the uncertainty when no jet data is included. The inner, lighter band indicates the relative uncertainty when including additional jet data. In some regions there is a reduction of the uncertainty of up to 35 %. Figure taken from [2]

construction of additional kinematic observables like the invariant dijet mass or the momentum fraction ξ. This analysis thus represents a very detailed test of perturbative QCD and QCD dynamics. Moreover dijet cross sections are (via the boson gluon fusion process) directly sensitive to the gluon density of the incoming proton. The presented cross sections thus might be well suited to provide additional constraints on the gluon PDF when included in (NLO) QCD fits.

This thesis is organised as follows

The first part of this document is dedicated to the before-mentioned measurement of dijet cross sections at HERA I.

In chapter 1 the theoretical concepts, necessary to understand the presented analysis, are described. This chapter comprises the introduction of the kinematic variables, a description of the quark parton model as well as a brief introduction into the basic concepts of QCD and jet physics.

The Monte Carlo generators used to obtain acceptance, QED and hadronisation corrections and the utilised fixed order QCD calculations are presented in chapter 2.

Chapter 3 gives an overview of the experimental setup, the HERA storage ring and the components of the ZEUS detector most relevant to this analysis.

The event reconstruction, including the reconstruction of the scattered electron, the hadronic final state and the kinematic variables, is described in chapter 4.

The used data set and the cuts applied to select the inclusive DIS sample are presented in chapter 5. This chapter closes with a comparison of the selected DIS sample to the predictions of the leading-order Monte Carlo generators.

The selection of the final dijet sample is described in chapter 6. This chapter comprises a description of the jet reconstruction and the applied MC-based jet-energy correction. It closes with a comparison of the selected data to the Monte Carlo predictions.

In chapter 7 a detailed description of the cross-section determination (including the applied acceptance and QED corrections) and the determination of the experimental uncertainties is given.

The obtained single- and double-differential dijet cross sections are presented in chapter 8. In this chapter the measured cross sections are compared to the predictions of the fixed order QCD calculation.

The second part of this document is dedicated to the ZEUS experiment at HERA II.

Chapter 10 gives an overview of the HERA luminosity upgrade, comprising a brief description of the upgraded interaction region, the upgraded ZEUS detector and its new luminosity system.

A detailed description of the 6m tagger, a small electromagnetic calorimeter designed and built as part of the upgraded ZEUS luminosity system, is given in chapter 11[2]. This chapter includes a description of the 6m-tagger trigger and its efficiency, a description of the position and energy reconstruction and the calibration of the tagger as well as a detailed description of the so called Cobalt scans which were used to monitor the radiation damage of the tagger.

Chapter 12 presents the results of the so called 'single pion study'. In this study the response of the (simulated) detector to single pions was investigated. The study helped to improve the detector simulation and to identify imperfections of a reconstruction algorithm.

---

[2] The author of this thesis was (on-call) expert for the 6m-tagger and worked on the design and performance of the 6m-tagger trigger, the energy calibration, the online-monitoring and the investigation of of radiation damage of the scintillating fibers.

Part I

Dijet Cross Sections in NC DIS at HERA I

Chapter 1

Theory

In this chapter the theoretical concepts necessary to understand the presented dijet analysis are described. The first part (section 1.1) is dedicated to deep inelastic electron-proton scattering (DIS). In this part the variables commonly used to describe the scattering process are introduced and the DIS cross section is presented. The second and the third part (sections 1.2 and 1.3) are dedicated to the composition of the proton as seen in the quark-parton model and in the framework of Quantum Chromodynamics (QCD), respectively. The third part also contains a brief introduction into QCD and its basic properties. The fourth part (section 1.4) is dedicated to the subject of jet physics. In this section the QCD-Compton (QCDC) and the boson-gluon fusion (BGF) processes (both contributing to the measured dijet cross sections) are presented, an overview of commonly used jet algorithms is given and the Breit reference frame, in which the jet reconstruction is performed in this analysis, is described.

1.1 Deep inelastic scattering

In the framework of the Standard Model (SM) the interaction between elementary particles is described by the exchange of bosons. In the case of electron-proton scattering the exchanged boson can either be a photon (γ) or Z^0 or a $W^{\pm}$ boson. The interactions mediated by the exchange of an electrically neutral γ or Z^0 are called neutral current (NC), those mediated by an electrically charged W^+ or W^- are called charged current (CC) processes. For virtualities greater than about 1 GeV^2 ($Q^2 > 1$ GeV^2) the wavelength of the exchanged boson is smaller than the dimension of the proton[1] ($\mathcal{O}(10^{-15}m)$). In this kinematic region the exchanged boson is able to probe the internal structure of the proton. If in addition the invariant mass of the hadronic final state is much larger than the invariant mass of the proton ($W^2 \gg M_p^2$), the process is called deep inelastic scattering (DIS).

---

[1] The virtuality, Q^2, is defined as the negative of the squared four-momentum transfer. Virtuality and wavelength, λ, of the exchanged boson are related to each other according to $\lambda \propto 1/\sqrt{Q^2}$.

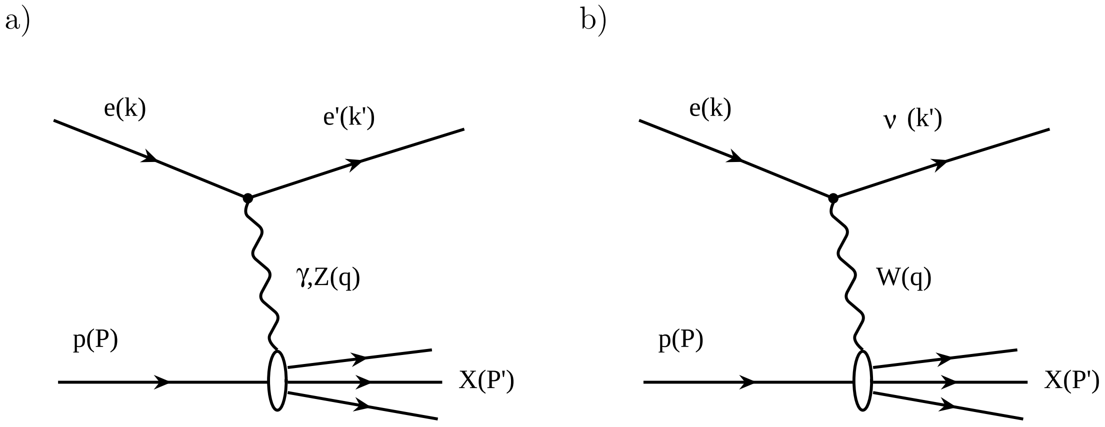

Figure 1.1: Schematic diagram of a) neutral current (NC) and b) charged current (CC) deep inelastic electron-proton scattering. Four-momenta are given in parentheses. The main signature of NC events is the occurrence of the scattered electron in the final state. In CC events the electron transforms into an electron neutrino, leading to missing transverse momentum.

Figure 1.1 shows schematic diagrams for neutral and charged current electron-proton scattering. As can be seen the two processes do not only differ by the exchanged boson but also by the final state lepton which is either an electron (NC event) or an electron neutrino (CC event). According to this the main signature of NC events is the occurrence of the scattered electron in the final state whereas for CC events, where the electron transforms into an electron neutrino which can not be detected, it is the occurrence of missing transverse momentum.

1.1.1 Kinematic variables

The inclusive deep inelastic scattering process $e(k)+p(P) \rightarrow l'(k')+X(P')$ is (for unpolarised electrons and protons) typically described in terms of the following Lorentz-invariant variables:

- centre-of-mass energy squared, s,

  $$s = (k + P)^2. \tag{1.1}$$

  Neglecting the masses of the electron and the proton, the centre-of-mass energy is related to the initial electron and proton energies according to $\sqrt{s} \approx \sqrt{4E_e E_p}$;

- virtuality of the exchanged boson, Q^2,

  $$Q^2 = -q^2 = -(k - k')^2; \tag{1.2}$$

- Bjorken scaling variable, x_{Bj},

$$x_{Bj} = \frac{-q^2}{2P \cdot q}. \tag{1.3}$$

  In the quark-parton model described in section 1.2 the scaling variable x_{Bj} is equal to the fraction of the proton momentum carried by the struck quark;

- inelasticity, y,

$$y = \frac{P \cdot q}{P \cdot k}. \tag{1.4}$$

  In the proton rest frame the inelasticity is related to the energies of the initial and the final lepton according to $y = \frac{E_e - E'}{E_e}$. The inelasticity can thus be interpreted as the energy transfer from the electron into the hard scattering;

- invariant mass of the hadronic system, W,

$$W = \sqrt{(q + P)^2}. \tag{1.5}$$

Neglecting the masses of the electron and the proton, the following relations hold:

$$Q^2 = x_{Bj} y s; \tag{1.6}$$

$$W^2 = Q^2 \left(\frac{1}{x_{Bj}} - 1 \right) = (1 - x_{Bj}) y s. \tag{1.7}$$

At a given centre of mass energy, $\sqrt{s}$, the inclusive process is completely described by a set of two of the Lorenz invariant variables defined in Eqs. 1.2-1.5.

Figure 1.2 shows the kinematic range in the variables Q^2 and x_{Bj} covered by the H1 and ZEUS experiments which are located at HERA. The figure also shows the kinematic range covered by other colliding-beam experiments and different fixed-target experiments probing the structure of the proton. Besides the centre-of-mass energy the kinematic range of an experiment is determined by the acceptance of the detector. As can be seen HERA has significantly extended the kinematic range accessible for DIS experiments and has spanned a bridge between the fixed-target experiments and the colliding-beam experiments, DO and CDF, located at the Tevatron[2].

1.1.2 QED radiation

In the above derivations higher order QED effects like the additional emission of real photons from the initial or scattered electron or quark, referred to as initial

---

[2] The Tevatron is a $p\bar{p}$ collider with a centre-of-mass energy of 1.96 TeV located at the Fermi National Accelerator Laboratory (Fermilab) near Chicago.

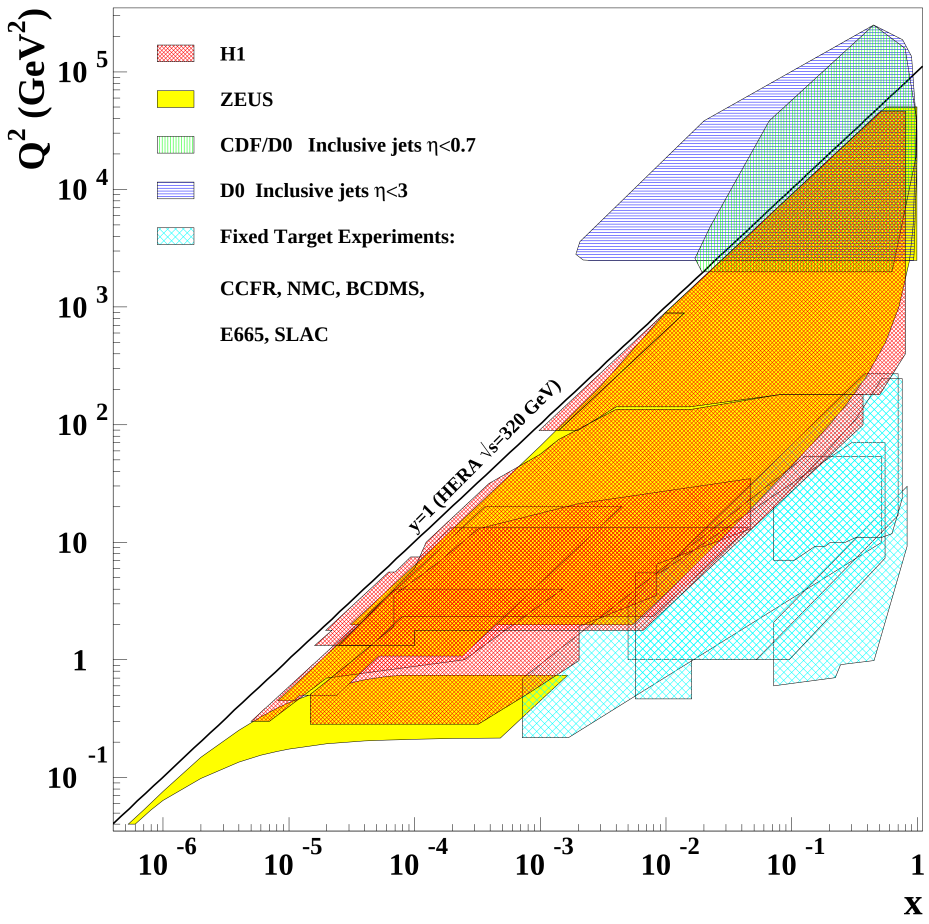

Figure 1.2: Kinematic range in terms of Q^2 and x_{Bj} for the H1 and ZEUS experiments located at HERA. The figure also shows the kinematic range covered by other colliding-beam experiments and different fixed-target experiments probing the structure of the proton. HERA has significantly extended the x_{Bj} and Q^2 range accessible for DIS experiments and spanned a bridge between the fixed-target experiments and the colliding-beam experiments,DO and CDF, located at the Tevatron.

(ISR) and final state radiation (FSR), and virtual loops have not been taken into account. These higher order QED effects may, however, have an impact on the kinematic variables and are, of course, included in any measured cross section. As an example the emission of a photon by the incident electron will lead to a reduction of the effective electron beam energy and will thus have an impact on the kinematic variables. In the case of final state radiation the emission of a real photon after the hard scattering process will lead to both, a reduction of the electron energy and a change of the electron scattering angle. This will have an impact on kinematic variables determined from the scattered electron.

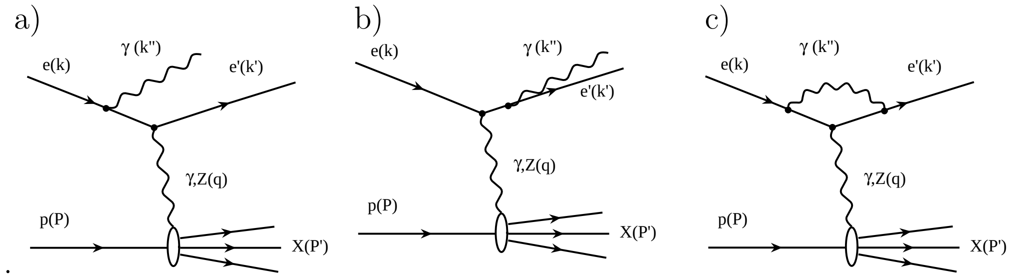

Figure 1.3: Schematic diagram of neutral current electron-proton scattering including higher order QED corrections: a) Initial state radiation of the electron, b) final state radiation of the electron. These processes are of order $\mathcal{O}(\alpha^3)$. c) Virtual correction of order $\mathcal{O}(\alpha^4)$: The photon emitted by the incoming electron is absorbed by the scattered electron.

Figures 1.3a and 1.3b show the schematic diagrams for NC electron-proton scattering including initial and final state radiation of the electron. The shown processes are of order $\mathcal{O}(\alpha^3)$. In figure 1.3c the photon emitted by the incoming electron is absorbed by the scattered electron. This process is of order $\mathcal{O}(\alpha^4)$.

In this analysis the data has been corrected for the described QED effects, including initial and final state radiation of the electron and the proton, vertex loop and self energy corrections using the bin-by-bin method. This method utilises two Monte Carlo samples including and not including higher order QED effects. The correction procedure is described in section 7.1.2.

1.1.3 Inclusive DIS cross section

The cross section for inclusive deep inelastic ep scattering can, in a single boson exchange approximation, be factorised into a leptonic and a hadronic tensor,

$$\sigma \sim L_{\alpha\beta} W^{\alpha\beta}, \tag{1.8}$$

where the leptonic tensor $L_{\alpha\beta}$ describes the vector boson coupling to the electron and the hadronic tensor $W^{\alpha\beta}$ describes its interaction with the proton. Neglecting the mass of the lepton, the leptonic tensor for NC DIS is given according to

$$L_{\alpha\beta} = k_\alpha k'_\beta + k'_\alpha k_\beta - g_{\alpha\beta} k \cdot k' + i\epsilon_{\alpha\beta\gamma\delta} k^\gamma k'^\delta, \tag{1.9}$$

where k and k' are the four-momenta of the incoming and the scattered electron, $\epsilon_{\alpha\beta\gamma\delta}$ is the completely anti-symmetric tensor and $g_{\alpha\beta}$ is the metric tensor given according to

$$g_{\alpha\beta} = \begin{pmatrix} 1 & 0 & 0 & 0 \\ 0 & -1 & 0 & 0 \\ 0 & 0 & -1 & 0 \\ 0 & 0 & 0 & -1 \end{pmatrix}. \tag{1.10}$$

In contrast to the leptonic tensor, the hadronic tensor can not be calculated from first principles. For electron scattering on an unpolarised target the most general form of the hadronic tensor is given according to

$$W^{\alpha\beta} = -g^{\alpha\beta}W_1 + \frac{P^\alpha P^\beta}{M^2}W_2 - \frac{i\epsilon^{\alpha\beta\gamma\delta}P_\gamma q_\delta}{2M^2}W_3, \tag{1.11}$$

where q and P are the four-momenta of the exchanged boson and the proton, M is the proton mass and W_1, W_2 and W_3 are scalar functions of two independent kinematic variables such as (x_{Bj}, Q^2) or (x_{Bj}, y) describing the structure of the proton. Introducing the dimensionless structure functions

$$\begin{aligned} F_1(x_{Bj}, Q^2) &= MW_1(\nu, Q^2), && (1.12)\\ F_2(x_{Bj}, Q^2) &= \nu W_2(\nu, Q^2), && (1.13)\\ F_3(x_{Bj}, Q^2) &= \nu W_3(\nu, Q^2), && (1.14) \end{aligned}$$

where ν is defined according to $\nu = (P \cdot q)/M$, the the double-differential cross section for neutral current ep scattering can be written as

$$\frac{d^2\sigma_{\mathrm{NC}}^{e^\pm p}}{dxdQ^2} = \frac{2\pi\alpha^2}{xQ^4}\left[Y_+F_2^{\mathrm{NC}}(x,Q^2) \mp Y_- xF_3^{\mathrm{NC}}(x,Q^2) - y^2F_L^{\mathrm{NC}}(x,Q^2)\right]. \tag{1.15}$$

Here, α is the electromagnetic coupling constant, $Y_\pm$ is defined in terms of the inelasticity, y, according to $Y_\pm = 1 \pm (1-y)^2$ and $F_L = F_2 - 2xF_1$ is the so called longitudinal structure function, which is related to the cross section for longitudinally polarised virtual photon scattering. The NC structure functions are the same for e^-p and e^+p scattering. The difference in the cross section resulting from interference Z^0/γ exchange is taken into account in the $Y_- xF_3$ contribution which changes sign with the charge of the lepton.

Similarly, the cross section for charged current deep inelastic ep scattering is given according to

$$\begin{aligned} \frac{d^2\sigma_{\mathrm{CC}}^{e^\pm p}}{dxdQ^2} &= \frac{G_F^2}{4\pi x}\left(\frac{M_W^2}{M_W^2+Q^2}\right)^2 \times \qquad (1.16)\\ &\left[Y_+F_2^{\mathrm{CC,W^\pm}}(x,Q^2) \mp Y_- xF_3^{\mathrm{CC,W^\pm}}(x,Q^2) - y^2F_L^{\mathrm{CC,W^\pm}}(x,Q^2)\right], \end{aligned}$$

where G_F is the Fermi constant and M_W is the mass of the $W^\pm$ boson. The superscript $W^\pm$ indicates the sign of the W boson being absorbed by the proton. In general $F_i^{W^+} \neq F_i^{W^-}$, reflecting the different u- and d-quark content of the proton (more details are given in the following paragraph).

Figure 1.4 shows the differential cross section $d\sigma/dQ^2$ for NC and CC deep inelastic e^-p and e^+p scattering as measured by the H1 and ZEUS experiments and the

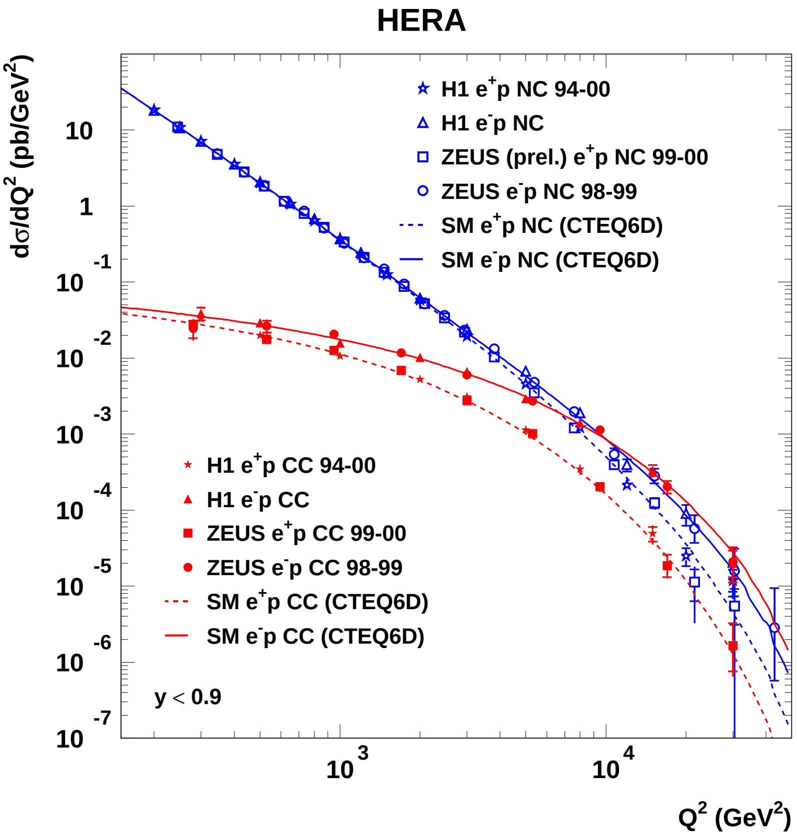

Figure 1.4: Differential cross section $d\sigma/dQ^2$ as a function of Q^2 for inclusive NC and CC e^-p and e^+p scattering as measured by the H1 and ZEUS experiments and the Standard Model predictions. The measurements are based on the HERA I data. For the calculated cross sections the CTEQ6D parametrisation of the proton PDF has been used.

predictions of the Standard Model. The figure demonstrates the unification of the electromagnetic and the weak interaction at large values of Q^2. While for $Q^2 \ll M_W^2$ the CC process is, due to the large mass of the W boson ($M_W \approx 80$ GeV), suppressed with respect to the NC process, the cross sections become comparable for $Q^2 \gtrsim M_W^2$. In the kinematic region where the NC process is mainly mediated by the exchange of the massless photon ($Q^2 \ll M_{Z^0}^2 \approx (91\text{ GeV})^2$) the cross sections are the same for e^-p and e^+p scattering. At higher values of Q^2, where the exchange of the Z^0 boson becomes sizable, differences occur reflecting a specific property of the weak force according to which only left-handed (right-handed) particles (antiparticles) participate in the weak interaction. For charged current differences between the e^-p and e^+p cross sections are observed over the whole Q^2 range. The ratio between the e^-p and e^+p CC cross section increases with Q^2 and is about 1.25 for $Q^2 = 200\text{ GeV}^2$

and about one order of magnitude at $Q^2 = 10000$ GeV^2. There are two reasons for the observed behaviour. First the density of the u quark in the proton is in general larger than the density of the d quark. As the u quark (d quark) only interacts with the virtual W^- (W^+) emitted by the electron (positron) this leads to a larger cross section for e^-p compared to e^+p scattering. The second reason is again the nature of the weak interaction which suppresses the quark (antiquark) contribution to the CC cross section for e^+p (e^-p) scattering.

The analysis presented in this thesis is based on NC DIS events. Since the kinematic region of the analysis is restricted to virtualities smaller than 5000 GeV^2 $< M_Z^2$ and thus the exchange of the Z^0 boson is suppressed, the parity-violating term $Y_- xF_3^{\mathrm{NC}}(x, Q^2)$ in equation 1.15 can be neglected[3]. The double-differential cross section for deep inelastic ep scattering relevant for this analysis is thus given according to

$$\boxed{\frac{d^2\sigma_{NC}^{e^\pm p}}{dx dQ^2} = \frac{2\pi\alpha^2}{xQ^4}\left[Y_+ F_2^\gamma(x, Q^2) - y^2 F_L^\gamma(x, Q^2)\right]. \qquad (1.17)}$$

While the magnitude of F_L is proportional to the absorption cross section of longitudinal polarised photons by the proton ($F_L \propto \sigma_L$), F_2 also includes the absorption cross section for transversely polarised virtual photons ($F_L \propto \sigma_L + \sigma_T$). In the kinematic range given according to $20 < Q^2 < 130$ GeV^2 and $5 \times 10^{-4} < x < 0.007$ the ratio $F_L/(F_2 - F_L)$ was measured to be smaller than 0.3 [4].

1.2 Quark-parton model

According to the parton model invented by Richard P. Feynman [5] in 1969, the proton consists of point-like constituents with spin 1/2, called partons. The partons were later identified with the quarks introduced by Gell-Mann [6] and Zweig [7], thus leading to the name *quark-parton model*[4]. According to the quark-parton model inside the proton the partons, each carrying a fraction x of the proton momentum, act as free particles which do not interact with each other. This assumption is only valid in the so called *infinite momentum frame* where the proton momentum is infinite and thus the transverse momenta of the quarks can be neglected. The HERA laboratory frame provides a good approximation for the infinite momentum frame. In this frame time dilation slows down the rate at which partons interact with each other so that, during the short time that the virtual boson interacts with the parton, the parton is essentially free. According to this considerations in the quark-parton model the cross section for DIS ep scattering can be written as the incoherent sum of the calculable

---

[3] In the following considerations, the exchange of Z^0 bosons is not taken into account unless stated differently.

[4] Gell-Mann and Zweig had introduced the quarks to explain the variety of hadrons discovered in collision experiments in the 1950s and 1960s.

individual lepton-parton cross sections for two point-like spin 1/2 particles. Using the differential cross section for elastic electron scattering on a quark carrying a fraction x' of the proton momentum,

$$\frac{d\sigma}{dy} = \frac{2\pi\alpha^2}{Q^4}[1+(1-y)^2]x'se_i^2, \tag{1.18}$$

where e_i is the charge of the quark in terms of the electron charge, and introducing the distribution function $q_i(x)$, which gives the probability density to find a quark carrying a fraction x of the protons momentum inside the proton, the double-differential *ep* cross section can be written as

$$\frac{d^2\sigma^{ep}}{dxdy} = \frac{2\pi\alpha^2}{Q^4}[1+(1-y)^2]s\sum_i e_i^2 xq_i(x) \tag{1.19}$$

or, equivalently,

$$\frac{d^2\sigma^{ep}}{dxdQ^2} = \frac{2\pi\alpha^2}{xQ^4}[1+(1-y)^2]\sum_i e_i^2 xq_i(x). \tag{1.20}$$

It is useful to define the momentum distribution $xq(x)$ (also called the momentum density), which is also referred to as the *parton distribution function* (PDF). Comparing the results obtained for the quark-parton model (Eqn. 1.20) with the general form of the inclusive NC DIS cross section for ep scattering (Eqn. 1.17) implies that according to the QPM the structure function F_2 is given according to

$$F_2(x,Q^2) = F_2(x) = \sum_i e_i^2 xq_i(x). \tag{1.21}$$

As can be seen, in the framework of the quark-parton model, the structure function F_2 is a function of x only. The fact that F_2 does not depend on the virtuality of the exchanged boson, Q^2, is also referred to as scaling. The scaling behaviour had been predicted by Bjorken [8] and was observed in the early SLAC[5] data [9]. Later experiments showed that scaling is only given in a restricted x range ($x \approx 0.25$). The later observed scaling violations can be explained in the framework of Quantum Chromodynamics (QCD). Besides scaling the quark-parton model also predicts

$$F_L(x,Q^2) = 0, \tag{1.22}$$

also known as the Callan-Gross relation ($F_2 = 2xF_1$), which is a direct consequence of the spin-1/2 nature of the point-like quarks.

It should be noted that in the quark-parton model the Bjorken scaling variable x_{Bj} is identical to the fraction of the proton momentum carried by the initial quark. This can be seen by a simple calculation. If x is defined as the fraction of the proton momentum carried by the initial quark and q and P are the four momenta

---

[5] SLAC stands for **Stanford Linear Accelerator Center**

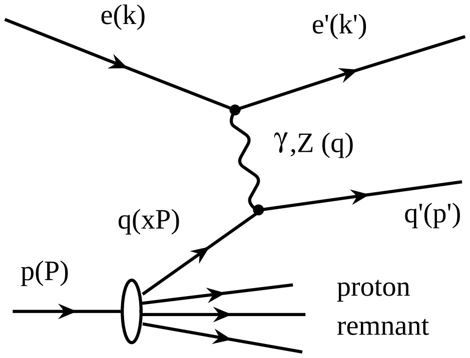

Figure 1.5: Feynman diagram of the QPM process which is identical to the lowest order NC ep scattering process. The QPM process is a purely electroweak process in which no strong interaction takes place.

of the exchanged boson and the proton, the invariant mass of the scattered quark is given according to

$$(q + xP)^2 = p^{'2} \quad = \quad m_q^2 \approx 0 \tag{1.23}$$

$$q^2 + 2q \cdot xP + (xP)^2 \quad \approx \quad 0 \tag{1.24}$$

where $p^{'}$ is the four momentum of the scattered quark and m_q its (negligible) mass. Since $(xP)^2 \ll Q^2$ the term $(xP)^2$ can be neglected and x can therefore be determined according to

$$x = \frac{-q^2}{2q \cdot P} = \frac{Q^2}{2q \cdot P} \tag{1.25}$$

which is identical to the definition of x-Bjorken (see equation (1.3)).

Figure 1.5 shows the Feynman diagram of the so called QPM process which is identical to the lowest order NC ep scattering process. It should be noted that the QPM process is a purely electroweak process in which no strong interaction takes place. The QPM process can therefore not give access to the strong coupling constant α_s.

1.3 Quantum Chromodynamics

Quantum Chromodynamics is a locally gauge-invariant non-Abelian field theory based on $SU(3)_C$ symmetry. In the framework of QCD, the strong interaction between quarks is described by the exchange of the massless field quanta of the theory, called gluons. The QCD Lagrangian is given by

$$L_{QCD} = \sum_f \bar{\psi}_f^i (i\gamma_\mu D^\mu - m_f)_{ij} \psi_f^j - \frac{1}{4} F_a^{\mu\nu} F_{\mu\nu}^a, \tag{1.26}$$

where $D^{\mu}_{ij} = \delta_{ij}\partial^{\mu} + ig_s(t^a)_{ij}A^{\mu}_a$ is the covariant derivative, ψ and A are the quark and gluon fields, g_s is the QCD gauge coupling , $(t^a)_{ij}$ are the $SU(3)_C$ group generators in the fundamental representation, m_f is the quark mass and $F^{\mu\nu}_a$ is the gluon field strength tensor which is given according to

$$F^{\mu\nu}_a = \partial^{\mu}A^{\nu}_a - \partial_{\nu}A^{\mu}_a + g_s f^{abc}A^{\nu}_b A^{\nu}_c \tag{1.27}$$

where f^{abc} are the $SU(3)_C$ structure constants. The Lagrangian of the QCD is in many aspects similar to the one of the quantum electrodynamic (QED), which describes the electromagnetic interaction between fermions via the exchange of massless photons. The main difference between the two is the non-Abelian term $gf^{abc}A^{\nu}_b A^{\nu}_c$ in the definition of the QCD field strength tensor. This term, which is non-existing in QED, describes the interaction of gluons among themselves, which is related to the fact that gluons, in contrast to the electrically neutral photons, carry colour charge. It should be noted that it is the same coupling constant g_s which couples the gluon fields to themselves and to the quark fields.

A summary of the essential properties of the theory of Quantum Chromodynamics is given in the following (enumeration follows [10]):

- in addition to the electric charge quarks do also carry colour charge. Colour charge comes in three flavours which are normally referred to as red (R), green (G) and blue (B). Antiquarks carry anticolour ($\bar{R}, \bar{G}$, or $\bar{B}$);

- the strong interaction between quarks is mediated by the exchange of gluons. Gluons are massless spin-1 particles. In contrast to the electrically neutral photon, gluons carry colour charge, or more precisely colour and anticolour. According to this there are eight bicoloured gluons[6];

- the Abelian diagrams of the QCD, describing the quark-gluon interactions, can be calculated using the rules of QED with the substitution $\sqrt{\alpha} \rightarrow \sqrt{\alpha}_s$ at every vertex and the introduction of calculable colour factors, taking into account all possible colour charges of the initial and final state particles. The non-Abelian part of the QCD, describing the interaction of gluons among themselves, leads to the occurrence of three-and four-gluon vertices nonexistent in QED;

- the strength of the strong coupling constant α_s, which is related to the gauge coupling g_s according to $\alpha_s = g_s^2/4\pi$, strongly depends on the energy scale of the interaction, increasing towards small energies. However at high energy scales, corresponding to short distances, α_s becomes sufficiently small which allows to use the perturbative techniques familiar from QED. The scale dependency of α_s leads to the effects of *confinement* and *asymptotic freedom*;

---

[6] A theoretically possible ninth combination, the totally symmetric colour gluon singlet, would be colourless and unconfined and does not exist.

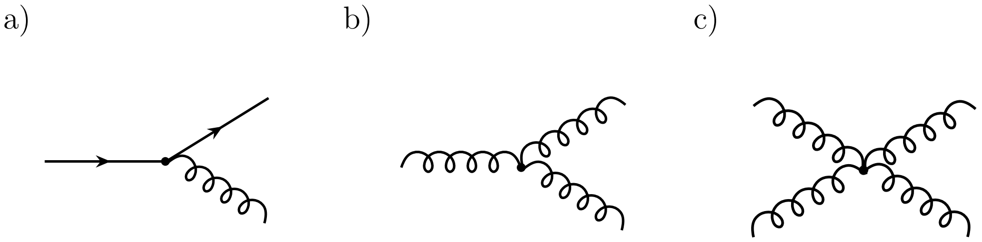

Figure 1.6: The fundamental vertices of QCD. Quarks are represented by solid lines and gluons by helices. While the quark-gluon vertex displayed in a) finds its pendant in QED (the fermion-photon vertex) the three-and four-gluon vertices displayed in b) and c) are unique for QCD. The quark-gluon and the three-gluon (four-gluon) vertex contribute a term proportional to α_s (α_s^2) to the cross section.

- confinement: The coloured quarks and gluons can not be observed as free particle as they only exist in colourless bound states called hadrons;
- asymptotic freedom: At large scales, corresponding to very small distances (smaller than the size of hadrons), the strong force gets so weak that the quarks behave as essentially free, noninteracting particles.

1.3.1 Renormalisation of the strong coupling constant α_s

Under the basic assumption that the strong coupling constant α_s is sufficiently small ($\alpha_s \ll 1$), predictions for scattering processes can, just like in QED, be obtained by perturbative methods using the Feynman rules, which can be derived from the QCD Lagrangian. Any cross section can then be written as a power series in α_s,

$$\sigma(n) = c_0\alpha_s^0 + c_1\alpha_s^1 + c_2\alpha_s^2 + \ldots + c_n\alpha_s^n = \sum_{i=0}^{n} c_i\alpha_s^i, \tag{1.28}$$

where the coefficients c_i are related to the appropriate Feynman diagrams and n is the order of the calculation. It should be noted that in order to obtain physically meaningful results not only α_s has to be sufficient small but also the coefficients c_i have to be finite. At leading order (i.e. the lowest order in α_s which contributes to the process of interest) only tree-level diagrams contribute to the cross section. The corresponding diagrams are compositions of the fundamental vertices of QCD displayed in figure 1.6. However at higher orders also virtual loops (see figure 1.7) have to be taken into account, which lead to divergences due to the integration over infinite (internal) loop momenta. These so called ultraviolet (UV) divergences can be made temporarily finite by applying a *regularisation procedure*, e.g. by the introduction of an ultraviolet momentum cut-off or by dimensional regularisation.[7] The regularised

---

[7] The essential idea of the dimensional regularisation introduced by t'Hooft and Veltman is to evaluate the integrals in an n-dimensional space ($n \neq 4$) in which they converge.

divergences are then removed by absorbing them into the strong coupling constant α_s. This is done according to a specific (but arbitrary) prescription called *renormalisation scheme*. There are different schemes available. The one most commonly used is the modified minimal subtraction ($\overline{\mathrm{MS}}$) scheme [11]. By applying the renormalisation scheme an additional parameter μ_R is introduced and α_s is not longer a constant but depends on the *renormalisation scale* ($\alpha_s = \alpha_s(\mu_R)$). Since μ_R is an arbitrary and unphysical parameter any physical observable, $\mathcal{R}$, has to be independent of μ_R[8]. This physical requirement is expressed by the renormalisation group equation

$$\mu_R^2 \frac{d\mathcal{R}}{d\mu_R^2} = \left[\mu_R^2 \frac{\partial}{\partial \mu_R^2} + \mu_R^2 \frac{\partial \alpha_s}{\partial \mu_R^2} \frac{\partial}{\partial \alpha_s}\right] \mathcal{R} = 0 \tag{1.29}$$

It shows that, in order to keep $\mathcal{R}$ independent of the choice of the renormalisation scale, a change in μ_R has to be compensated by a change in the renormalised effective strong coupling constant $\alpha_s(\mu_R)$. The renormalisation scale dependence of α_s is controlled by the β function of QCD which can be expanded as a power series in α_s. Defining $a(\mu_R) = \alpha_s(\mu_R)/(4\pi)$ this can be written according to

$$\frac{\partial a}{\partial \ln \mu_R^2} = \beta(a) = -\beta_0 a^2 - \beta_1 a^3 - \beta_2 a^4 - \beta_3 a^5 + \mathcal{O}(a^6), \tag{1.30}$$

with

$$\begin{aligned}
\beta_0 &= 11 - \frac{2}{3} n_f, \\
\beta_1 &= 102 - \frac{38}{3} n_f, \\
\beta_2 &= \frac{2857}{2} - \frac{5033}{18} n_f + \frac{325}{54} n_f^2, \\
\beta_3 &= \left(\frac{149753}{6} + 3564\zeta_3\right) - \left(\frac{1078361}{162} + \frac{6508}{27}\zeta_3\right) n_f \\
&\quad + \left(\frac{50065}{162} + \frac{6472}{81}\zeta_3\right) n_f^2 + \frac{1093}{729} n_f^3,
\end{aligned}$$

where ζ is the Riemann zeta function ($\zeta_3 = 1.202056903...$) and n_f is the number of quark flavours with mass lower than the energy scale μ_R. The first two coefficients β_0 and β_1 are universal whereas the further depend on the chosen scheme. β_2 and β_3 are given for the $\overline{MS}$ scheme. The coefficients β_i are related to the appropriate loop diagrams. Figure 1.7 shows the lowest order ($\mathcal{O}(\alpha_s^2)$) loop diagrams related to β_0. There are two kinds of contributions, one from fermion (quark) loops and one from gluon loops. While the fermion loops have their pendants in QED the gluon loops are unique for QCD. It should be noted that the contributions from quark and gluon

---

[8] The requirement that any physical observable $\mathcal{R}$ has to be independent of μ_R is only fulfilled if $\mathcal{R}$ is calculated to all orders in α_s. Since the observables are typically calculated up to LO, NLO, or NNLO only, they become scale-dependent. The theoretical error, related to the truncation of higher orders, is typically estimated by a variation of the renormalisation scale.

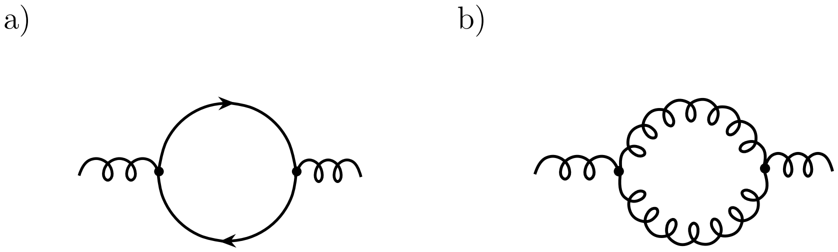

Figure 1.7: Loop corrections to the gluon propagator. While the quark-loop displayed in a) has its pendant in QED the gluon-loop displayed in b) is unique for QCD. The displayed loops contribute with a factor α_s^2 to the cross section.

loops to the scattering amplitude and thus to the coefficients of the β function are of opposite sign, which is related to the fact that quarks are spin 1/2 and gluons are spin 1 particles. As we will see it is the gluon loop contribution that finally leads to the effect of asymptotic freedom. The integration of equation 1.30 according to

$$\ln\left(\frac{\mu_R}{\Lambda}\right)^2 = \int \frac{da}{\beta(a)} \tag{1.31}$$

introduces a constant Λ which is referred to as the asymptotic scale parameter, which determines the value of the renormalisation scale μ_R at which α_s diverges. Using the solution of equation 1.31, the value of α_s can be determined at any scale if either the scale parameter Λ (for which experimentally a value of 200-300 MeV is found) or the value of α_s at a given scale is known. Nowadays it has become conventional to quote α_s in the $\overline{MS}$ scheme at the precisely measured mass of the Z^0 boson ($\mu_R = M_Z = 91.1876 \pm 0.0021$ GeV [12]). The scale parameter Λ can be eliminated from equation 1.31 by subtracting equation 1.31 at $\mu_R = M_Z$ from equation 1.31 at an arbitrary scale, μ. Only taking into account the first coefficient β_0 of the β function, this leads to

$$\boxed{a(\mu_R) = \frac{a(M_Z)}{1 + \beta_0 \ln(\mu_R^2/M_Z^2)a(M_Z)} \tag{1.32}}$$

This one-loop accuracy solution already exhibits the property of asymptotic freedom. For $\beta_0 = 11 - \frac{2}{3}n_f > 0$, which is true for six quark flavours as given in the standard model, the renormalised effective strong coupling constant slowly approaches zero as the renormalisation scale gets large ($\lim \mu_R \to \infty \; \alpha_s = 0$). For small distances, corresponding to high values of μ_R, the partons are quasi-free. It is only in this region that the basic assumption ($\alpha_s \ll 1$) introduced at the beginning of this section holds and perturbative methods can be applied. It should be noted that the scale dependence of α_s is (for $n_f < 17$) dominated by the positive contribution from the gluon loops. As mentioned before it is thus the gluon loop contribution that finally leads to the effect of asymptotic freedom.

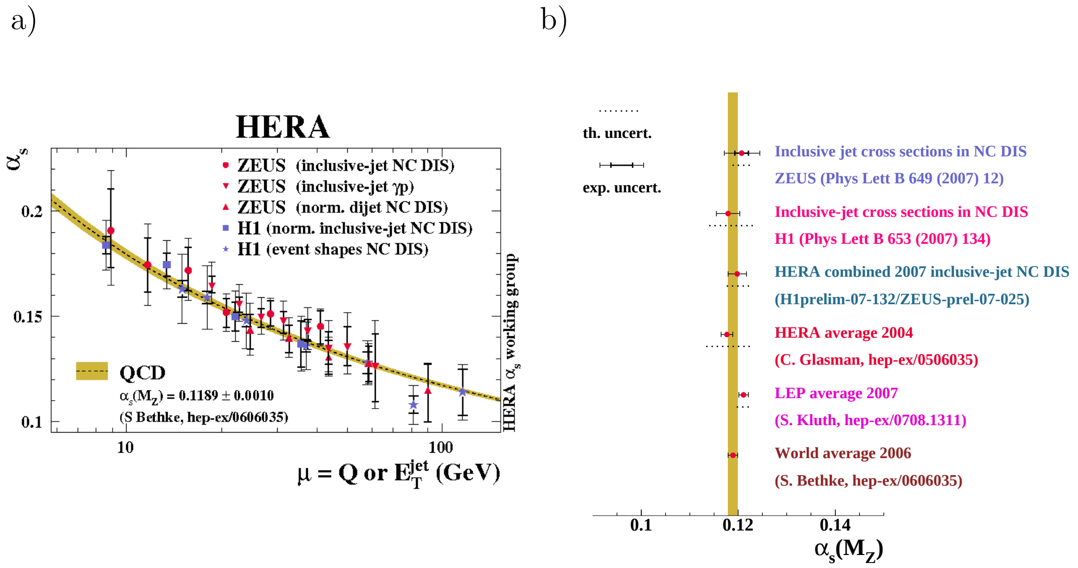

Figure 1.8: a) Running of the strong coupling constant α_s as measured by H1 and ZEUS and the predictions of the QCD theory. b) Values of α_s quoted at $\mu_R = M_Z$ as determined from inclusive jet data by H1 and ZEUS as well as the HERA 2004 average, the HERA combined 2007 value, the LEP average 2007 and the world average 2006. Figures taken from [13].

The scale dependence of α_s, which is also referred to as the running of the strong coupling constant, has been confirmed by many experimental measurements. Figure 1.8a shows the running as measured by the H1 and ZEUS experiments together with the QCD predictions. Figure 1.8b shows values of α_s quoted at $\mu_R = M_Z$ as determined from inclusive jet data by H1 and ZEUS as well as the HERA 2004 average [14], the HERA combined 2007 value [13], the LEP average 2007 [15] and the world average 2006 [16]. Numbers are given below. The determined values are, within the errors, in agreement with each other and with the world average.

$$\begin{aligned}
\alpha_s(M_Z) &= 0.1186 \pm 0.0011\ (\text{exp}) \pm 0.0050\ (\text{theo}) \quad (\text{HERA 2004 average})\\
\alpha_s(M_Z) &= 0.1198 \pm 0.0019\ (\text{exp}) \pm 0.0026\ (\text{theo}) \quad (\text{HERA combined 2007})\\
\alpha_s(M_Z) &= 0.1211 \pm 0.0010\ (\text{exp}) \pm 0.0018\ (\text{theo}) \quad (\text{LEP average 2007})\\
\alpha_s(M_Z) &= 0.1189 \pm 0.0010 \quad (\text{world average 2006})
\end{aligned}$$

1.3.2 Factorisation and parton density functions

According to the quark-parton model described in section 1.2, the proton is a very simple object which consists of three quarks (two up quarks and one down quark) which are, inside the proton, not interacting with each other. However, if

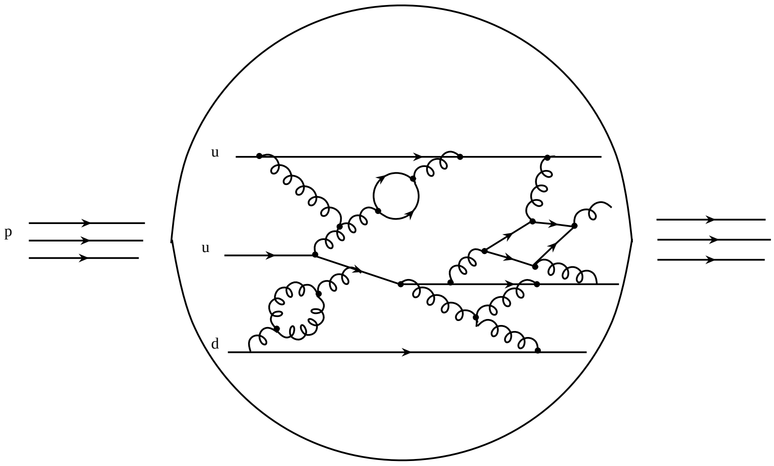

Figure 1.9: Schematic diagram of the proton as seen in the QCD-improved parton model. In contrast to the simple static object in the quark-parton model, in the QCD-improved parton model the proton becomes a complex and also dynamic object, whose internal structure shows a continuous development.

we 'switch on' QCD, the quarks start to interact by emitting and absorbing gluons. As a consequence, the quarks gain transverse momentum which finally leads to a non-vanishing longitudinal structure function F_L. The emitted gluons can split into quark-antiquark pairs, which may emit additional gluons, which may emit gluons themselves and so on, and so on. In the framework of QCD the proton thus becomes a complex and also dynamic object, whose internal structure shows a continuous development. According to the QCD-improved parton model, the proton now consists of the three valence quarks (u,u,d), gluons and a 'sea' of quark-antiquark pairs, also referred to as *sea-quarks*. Figure 1.9 shows a schematic diagram of the proton as seen in the QCD-improved parton model.

Reconsidering electron-proton scattering, in QCD the quark (which may now either be a valence or a sea-quark) may have emitted a number of gluons before absorbing the virtual boson. Figure 1.10 shows the diagrams for the scattering of a virtual photon γ^* on a quark as seen in the quark-parton model (1.10a) and in the QCD-improved parton model (1.10b). Referring to section 1.2, the lowest order cross section for the electron-proton scattering, which is identical to the ep scattering cross section in the quark parton model, can be written as a convolution of the lepton-parton cross section $\tilde{\sigma}$ with a parton density function $\tilde{f}(x)$, which gives the probability to find a parton with a fraction x of the longitudinal proton momentum inside the proton. Taking into account higher orders, diagrams with additional gluon emission (like displayed in figure 1.10b) have to be taken into account. To obtain the related cross section, the contributions from the appropriate diagrams have to be integrated over all possible transverse gluon momenta, $k_\perp$, leading to divergences for collinear gluon emission ($k_\perp \rightarrow 0$). These divergences can not be cured by renormalisation. However it is possible to extract the collinear divergences as universal factors from all coefficients of all orders in perturbative theory and to absorb them into redefined parton density functions. The redefinition is done according to a given prescription, called *factorisation scheme*. By applying the factorisation procedure a new scale, μ_f, referred to as *factorisation scale*, is introduced. This scale can be interpreted as the upper limit of the transverse momentum, $k_\perp$, below which parton emissions are included into the redefined parton density functions. The factorisation scale thus separates the short distance hard scattering process, calculable in perturbative theory, from the long distance soft interactions inside the proton. As a consequence of the factorisation procedure the parton density functions become scale-dependent ($\tilde{f}(x) \rightarrow f(x, \mu_f)$). Furthermore they do depend on the choice of the factorisation scheme. The one most commonly applied is the $\overline{MS}$ scheme which is also used within this thesis. According to their definition the re-defined parton density functions can not be calculated perturbatevely but have to be extracted from experiment. However, once determined at a given scale, μ_f^{meas}, and for all momentum fractions, x ($0 \leq x \leq 1$),the parton density functions can be evolved to an arbitrary higher scale, $\mu_f (\mu_f > \mu_f^{meas})$, using the DGLAP (Dokshitzer-Gribov-Lipatov-Altarelli-Parisi) equation system,

$$\mu_f \frac{\partial}{\partial \mu_f} \begin{pmatrix} q_i(x, \mu_f) \\ g(x, \mu_f) \end{pmatrix} = \frac{\alpha_s}{2\pi} \sum_{q_j, \bar{q}_j} \int_x^1 \frac{d\xi}{\xi} \begin{pmatrix} P_{q_i,q_j}\left(\frac{x}{\xi}, \alpha_s\right) & P_{q_i,g}\left(\frac{x}{\xi}, \alpha_s\right) \\ P_{g_i,q_j}\left(\frac{x}{\xi}, \alpha_s\right) & P_{g,g}\left(\frac{x}{\xi}, \alpha_s\right) \end{pmatrix} \begin{pmatrix} q_i(\xi, \mu_f) \\ g(\xi, \mu_f) \end{pmatrix}, \tag{1.33}$$

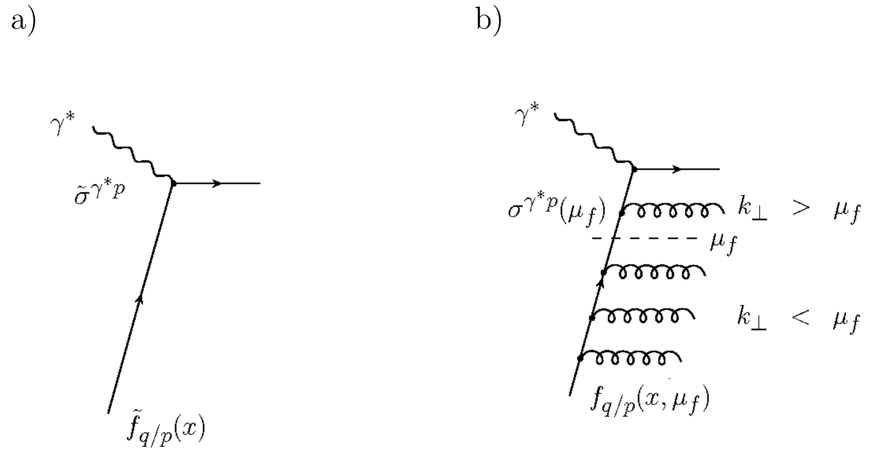

Figure 1.10: Feynman diagram for (virtual) photon-quark scattering at a) lowest order b) higher order. Gluons emitted with a transverse momentum, k_T, smaller than the factorisation scale, μ_f (introduced through the factorisation procedure), are absorbed into the redefined quark density functions, $f(x, \mu_f)$, which thus become scale-dependent.

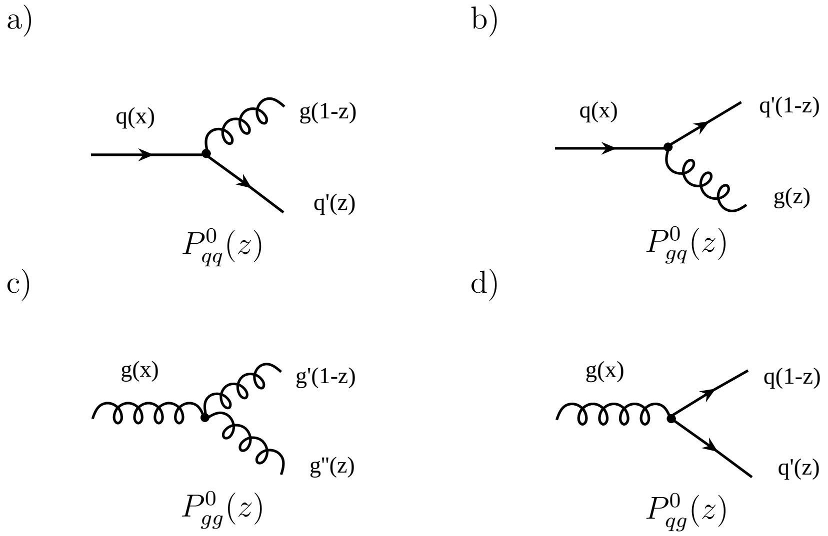

Figure 1.11: Feynman diagrams related to the leading-order DGLAP splitting functions, P^0_{ab}, which can be interpreted as the probability densities of finding a parton a with a longitudinal momentum fraction z of the parent parton and a transverse momentum less than μ_f in parton b.

where q_i are the quark densities for a flavour i and g is the gluon density. P_{ab} are the so called DGLAP splitting functions, also referred to as 'evolution kernels', which can be written as a power series in α_s

$$\begin{aligned}
P_{q_iq_j}(z,\alpha_s) &= \delta_{ij}P^0_{q_iq_j}(z) + \frac{\alpha_s}{2\pi}P^1_{q_iq_j}(z) + \dots \quad , \\
P_{gq}(z,\alpha_s) &= P^0_{gq}(z) + \frac{\alpha_s}{2\pi}P^1_{gq}(z) + \dots \quad , \\
P_{gg}(z,\alpha_s) &= P^0_{gg}(z) + \frac{\alpha_s}{2\pi}P^1_{gg}(z) + \dots \quad , \\
P_{qg}(z,\alpha_s) &= P^0_{qg}(z) + \frac{\alpha_s}{2\pi}P^1_{qg}(z) + \dots \quad .
\end{aligned} \tag{1.34}$$

The diagrams related to the lowest order contributions, P^0_{ab}, are displayed in figure 1.11. The leading order contributions can be interpreted as the probability densities of finding a parton a with a longitudinal momentum fraction z of the parent parton and a transverse momentum less than μ_f in parton b. The perturbative expansion of the splitting functions has been calculated to next-to-leading (NLO) ($\mathcal{O}(\alpha_s)$) and next-to-next-to leading order (NNLO) ($\mathcal{O}(\alpha_s^2)$). It should be noted that, since the evolution of a single parton density function involves mixing with other parton flavours, the full knowledge of *all* parton distributions is necessary.

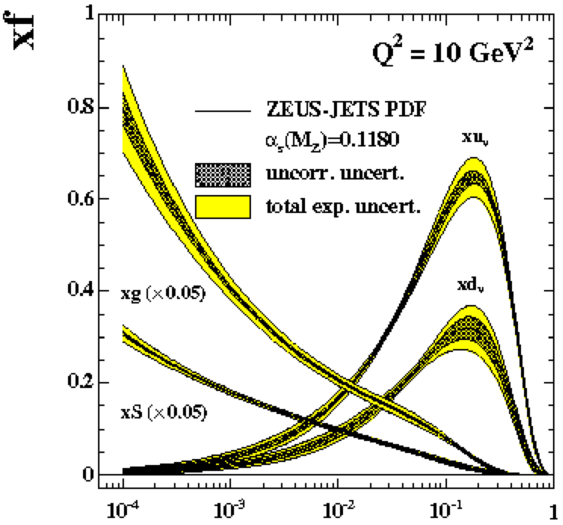

Figure 1.12: Valence quark, sea quark, and gluon PDFs as measured by the ZEUS experiment including jet data [21].

The parton density functions of the proton

As stated above the parton distribution functions can at present not be calculated from first principles but have to be determined from experiment. The best knowledge of the proton parton density functions is obtained by applying global fits to a large number of different data sets, which are in different ways sensitive to the different parton flavours. In these fits the x dependence, which is not predicted by perturbative QCD, is parametrised by polynomial forms. As the DGLAP equations only describe the evolution towards higher scales, the fits are typically performed at a starting scale, Q_0, which is in the order of a just a few GeV. Once determined at the starting scale, the PDFs can be evolved towards higher scales. The obtained results might then be used to calculate perturbative cross sections for processes not included in the fits to test the universality of the distribution functions.

The most recent proton PDFs have been obtained by the CTEQ collaboration [17], the MRST group [18] and by the H1 [19] and ZEUS collaborations [20, 21], which also attempt to combine their PDF analyses [22]. Figure 1.12 shows the valence quark, sea quark, and gluon distributions as measured by the ZEUS experiment including jet data [21]. Figure 1.13 shows the evolution of the gluon and sea quark distributions towards higher scales. As can be seen the gluon and sea quark contributions increase towards higher scales ($\mu_f^2 = Q^2$).

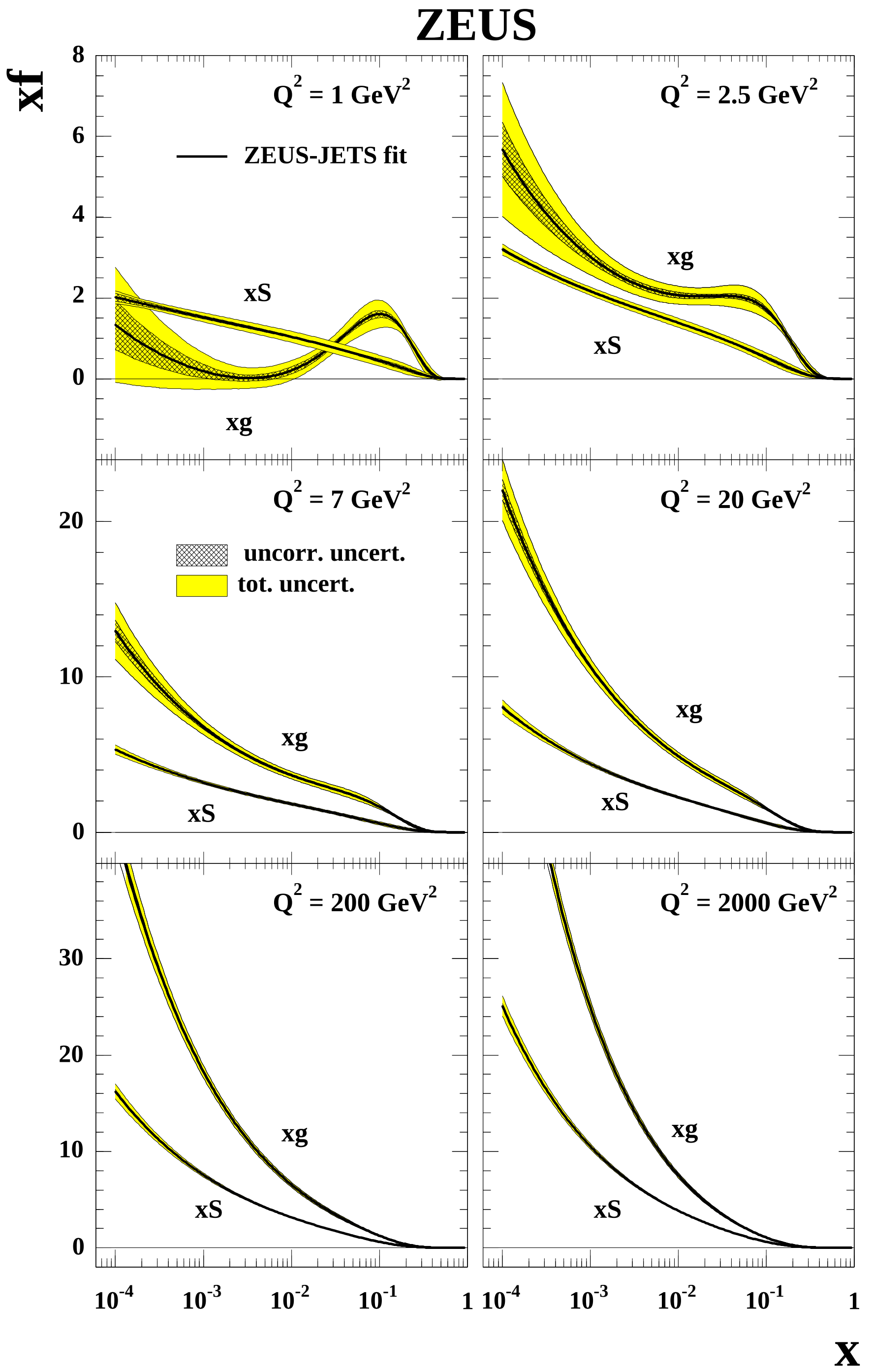

Figure 1.13: Scale dependence of the gluon and sea quark PDFs as measured by the ZEUS collaboration [21].

1.4 Jet physics

The aim of the analysis presented in this thesis is to measure dijet cross sections in neutral current deep inelastic ep scattering and to compare the results to theoretical predictions obtained from fixed order QCD calculations (see section 2.2). Up to leading order in the strong coupling constant ($\mathcal{O}(\alpha_s)$) the processes contributing to jet production at HERA are the purely electroweak quark-parton model (QPM) process (see section 1.2), and the QCD-Compton (QCDC) and the boson-gluon fusion (BGF) processes, which are of order $\mathcal{O}(\alpha_s)$. The final state of the later processes consists, besides the proton remnant and the scattered electron, of two partons. Due to colour confinement, the final state partons can not be observed directly. They evolve via emission of soft gluons and quarks which finally form colourless hadrons[9]. The resulting collimated flow of hadrons is referred to as (hadronic) *jet*. Both processes thus contribute to the dijet cross sections. The typical signature of a jet in the detector is a collimated area of energy deposit in the (hadronic) calorimeter. In order to be able to compare theoretical predictions on parton level to the measurements on hadron level, it is necessary to define observables which are insensitive to the emission of low energetic and collinear partons and also to the hadronisation process. It should be noted that any jet cross section will depend on the exact jet definition which is fixed by the applied jet algorithm.

The QCD-Compton and the BGF processes and the variables used to describe this processes are presented in section 1.4.1. An overview about the commonly used classes of jet algorithms and their basic properties and a detailed description of the k_T cluster algorithm (utilised in this analysis) is given in section 1.4.2. The Breit reference frame in which the jet reconstruction is performed is discussed in section 1.4.3. The motivation for an asymmetric cut on the transverse jet energy is given in section 1.4.4.

1.4.1 BGF and the QCDC process

The lowest order QCD processes ($\mathcal{O}(\alpha_s^1)$) in deep inelastic ep collision are the QCD-Compton process, induced by a quark, and the gluon-induced boson-gluon fusion process. In both processes the final state consists, besides the proton remnant and the scattered electron, of two partons which evolve into two hadronic jets. In figure 1.14 Feynman diagrams are shown for the QCDC and for the BGF process. There are various sets of variables to characterise these events. The ones used in this analysis are defined according to

---

[9] These long distance processes can not be calculated in perturbative QCD but are described by phenomenological models (see section 2.1).

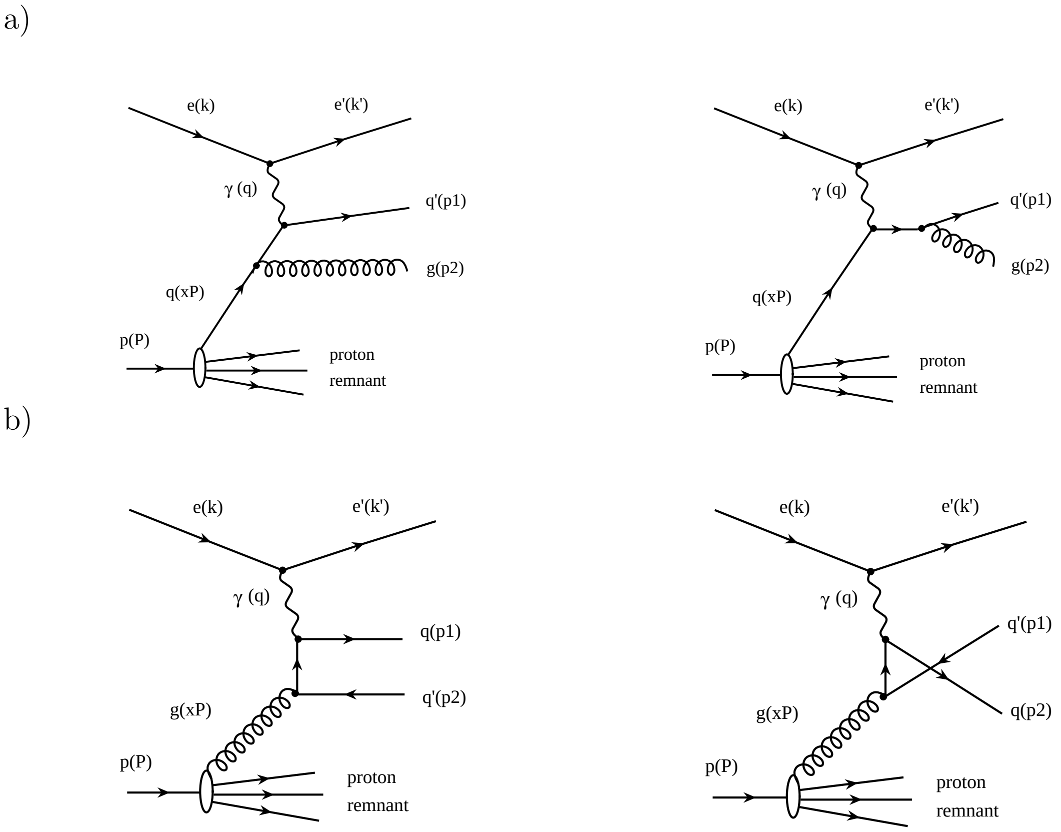

Figure 1.14: Feynman diagrams of the QCDC (a) and the BGF process (b). Both processes are of order $\mathcal{O}(\alpha_s)$. In both processes two partons (jets) are found in the final state.

$$\boxed{\begin{aligned} \overline{E}_T &= \frac{1}{2}\left(E_T^1 + E_T^2\right) \quad , \quad M_{jj} = \sqrt{\left(p^1 + p^2\right)^2}, \\ \xi &= x_{Bj}\left(1 + \frac{M_{jj}^2}{Q^2}\right) \quad , \quad \eta^{'} = \frac{1}{2}|\eta^1 - \eta^2|, \end{aligned} \qquad (1.35)}$$

where $E_T^{1,2}$ are the transverse energies, $p^{1,2}$ are the four momenta and $\eta^{1,2}$ are the pseudorapidities of the two final state jets. The pseudorapidity η is related to the polar angle θ according to $\eta = -\ln\tan(\theta/2)$. For massless particles, differences in pseudorapidities like $\eta' = \frac{1}{2}|\eta_1 - \eta_2|$ are invariant under longitudinal boosts (boosts along the z-axis). $\overline{E}_T$ is the mean transverse energy of the two final state jets and M_{jj} the invariant dijet mass. In leading order ($\mathcal{O}(\alpha_s)$) M_{jj} is identical to the centre-of-mass energy of the parton-boson system and ξ can thus be interpreted as the fraction of the proton momentum carried by the initial parton. This can be easily seen. If x is defined as the fraction of the proton momentum carried by the initial quark (gluon) the invariant dijet mass is given according to

$$
\begin{aligned}
(q + xP)^2 = (p^1 + p^2)^2 &= M_{jj}^2 && (1.36)\\
q^2 + 2q \cdot xP + (xP)^2 &= M_{jj}^2 && (1.37)
\end{aligned}
$$

Since $(xP)^2 \ll Q^2$, the term $(xP)^2$ can be neglected and x can therefore be determined according to

$$
x = \frac{M_{jj}^2}{2q \cdot P} + \frac{Q^2}{2q \cdot P} = x_{Bj}(1 + \frac{M_{jj}^2}{Q^2}), \tag{1.38}
$$

which is identical to the definition of ξ. In the QPM process (see section 1.2) the fraction of the proton momentum carried by the initial parton was given by x_{Bj}. The additional term M_{jj}^2/Q^2 in the definition of ξ can be interpreted as the additional energy (leading to a larger four momentum) that is needed to produce two partons (jets) in the final state.

1.4.2 Jet algorithms

Though there is no unique definition and a large variety of jet algorithms exists, a well designed jet algorithm must (according to the previous considerations) have some basic properties:

- **infrared safety:** The algorithm has to be insensitive to the emission of low energetic particles. Results have to be the same for a n-parton configuration as for the corresponding (n+1)-parton configuration which is obtained by adding an additional parton with $E \rightarrow 0$ to the final state;

- **collinear safety:** The algorithm has to be insensitive to collinear radiation of particles. Results must not change when a pair of collinear particles is replaced by a single particle carrying the same momentum;

- **little sensitivity to hadronisation corrections:** This requirement entails a close correspondence between the measurements from final state hadrons and the parton dynamics;

- **applicability to data, MC, and QCD calculations:** The algorithm has to be designed in such a way that it can be applied to both detector objects and hadrons (partons) originating from Monte Carlo generators or QCD calculations.

It should be noted that these requirements also reduce the sensitivity to experimental limitations such as finite angular resolution and energy trigger thresholds of calorimeter cells. Jet algorithms used in hadron collisions must, in addition to the general requirements listed above, fulfil the following conditions:

- **insensitivity to the hadron remnant:** The algorithm has to be insensible to contaminations from the hadron remnant;
- **factorisability:** The algorithm has to facilitate the factorisation of initial state collinear singularities into universal parton distributions.

For inclusive cross sections the factorisability of initial state collinear singularities into the universal parton distributions is guaranteed by the factorisation theorem of QCD [23]. However, for jet production in deep inelastic scattering factorisability is only given in a special category of reference frames. One of them is the Breit reference frame described in section 1.4.3.

The commonly used jet algorithms can be classified into two different categories:

- **cluster algorithms:** In cluster algorithms a distance between particles is defined according to a given prescription and the closest pair of particles is (again according to a given prescription) combined into a new particle [10]. This procedure is iteratively repeated until some abort criterion is reached;
- **cone algorithms:** In cone algorithms a jet is defined as the sum of objects in an angular cone around some direction of dominant energy flow. To define this direction cone algorithms usually take some of the final state particles as 'seeds' and define angular cones (so called trial cones) around the direction of the seed particles. The four-momenta of particles inside a given cone are summed up and the direction of the resulting particle is used to define a new trial cone. The procedure is repeated iteratively until a stable cone direction is obtained. The use of seeds make cone algorithms sensitive to soft radiation. It has been reported that perturbative QCD calculations based on cone algorithms may be affected by problems related to infrared singularities [24, 25]. Recently there are efforts to overcome this problem by developing seedless infrared safe cone algorithms [26].

In addition to the classifications listed above jet algorithms can be categorised into *exclusive* and *inclusive* algorithms. In exclusive algorithms every final state particle is assigned to one of the hard jets. The final state then solely consists of a number of jets and nothing else. This kind of algorithms is predestined for e^+e^- annihilation where the entire final state emerges from the hard process. In contrast to this in hadron collisions the final state contains energy flow related to the hadron remnant. For this kind of processes it is convenient to use inclusive jet algorithms which only cluster a fraction of the final state particles into jets. The final state thus consists of a number of hard jets with specified properties plus a number of objects not included in jets. Exclusive jet definitions can be extended to processes involving initial state

---

[10] In this context the term particle refers either to a parton, a hadron, a detector object like an energy deposition in a calorimeter cell or a energy flow object, or to a recombined object.

hadrons by introducing beam-remnant jets to which particles related to the beam remnant can be clustered [27].

In this analysis the k_T cluster algorithm [28] in the longitudinally-invariant inclusive mode [29] is used for the jet reconstruction. A detailed description of the algorithm is given in the following.

The k_T cluster algorithm

In the longitudinally-invariant mode the k_T cluster algorithm makes use of differences in pseudorapidities, $\Delta\eta$, differences in azimuthal angles, $\Delta\phi$, and of transverse energies, E_T, of detector objects or simulated hadrons and partons. Under the assumption of massless objects (detector objects, hadrons, partons) these quantities are invariant under longitudinal Lorentz boosts. The algorithm proceeds according to the following steps [29]:

1. for every object, i, as well as for each pair of objects, (i, j), distances, d_i and d_{ij}, are determined according to

   $$d_i = E_{T,i}^2 \cdot R_0^2 \quad \text{and} \quad d_{ij} = min(E_{T,i}^2, E_{T,j}^2) \cdot [(\eta_i - \eta_j)^2 + (\phi_i - \phi_j)^2]. \qquad (1.39)$$

   R_0 is a parameter of the algorithm. In this analysis R_0 is set to $R_0 = 1$ (as recommended in [29]);
2. the smallest distances $d_{min} \in \{d_i, d_{ij}\}$ is determined;
3. if $d_{min} \in \{d_{ij}\}$ the two objects i and j are merged into a new object according to the recombination scheme described below. i and j are removed from the list of objects and the merged object is put into this list. If $d_{min} \in \{d_i\}$ the object is considered as a *protojet*. Protojets are no longer considered for clustering;
4. this procedure is repeated until all objects are assigned to protojets. Due to the design of the algorithm the number of iterations is always equal to the number of original objects;
5. the final jets are selected from the sample of protojets by imposing a cut on the transverse energy E_T of the protojet. This cut suppresses jets originating from soft processes.

The recombination scheme is not fixed by the algorithm. In this analysis the jet quantities are defined according to the Snowmass convention [30]

$$E_{T,jet} = \sum_i E_{T,i} \quad , \quad \eta_{jet} = \sum_i \frac{E_{T,i} \cdot \eta_i}{E_{T,jet}} \quad , \quad \phi_{jet} = \sum_i \frac{E_{T,i} \cdot \phi_i}{E_{T,jet}}. \qquad (1.40)$$

The jet definition of the k_T cluster algorithm implies that all objects i and j with a distance $R = \sqrt{(\eta_i - \eta_j)^2 + (\phi_i - \phi_j)^2}$ smaller than R_0 are merged into a protojet. The distance between resulting jets is at least equal to R_0. The distance between two objects belonging to the same jet can be larger than R_0. Objects with a distance $R < R_0$ with respect to the jet axis do not have to belong to the respective jet.

1.4.3 Breit reference frame

As mentioned above, for jet production in deep inelastic scattering factorisability is only given in a special category of reference frames, one of them being the Breit frame. The Breit reference frame is defined as the frame where the proton and the exchanged boson collide head-on and no energy is transfered from the lepton to the parton. As indicated in figure 1.15 the Breit frame is related to the centre-of-mass system of the initial parton and the exchanged boson by a longitudinal boost along the z-axis. Transverse energies and differences in pseudorapidities are invariant under this transformation. The general expression to define the Breit reference frame in a mathematically form is given according to

$$2x_{Bj}\vec{P} + \vec{q} = 0 \tag{1.41}$$

where $\vec{P}$ is the momentum of the incoming proton and $\vec{q}$ is the boson momentum. In this analysis the z-axis of the Breit frame is defined by the direction of the incoming parton whereas the x-axis is chosen in a way that the scattered lepton points in the positive x-direction. If we define $Q := +\sqrt{Q^2}$, the four momentum of the boson in the Breit frame is given by

$$q = (0, 0, 0, -Q). \tag{1.42}$$

For the purely electroweak QPM process the four momenta of the incoming and the scattered quark in the Breit frame are therefore given according to

$$p_q = (Q/2, 0, 0, Q/2) \quad \text{and} \quad \mathrm{p_{p'}} = (\mathrm{Q}/2, 0, 0, -\mathrm{Q}/2). \tag{1.43}$$

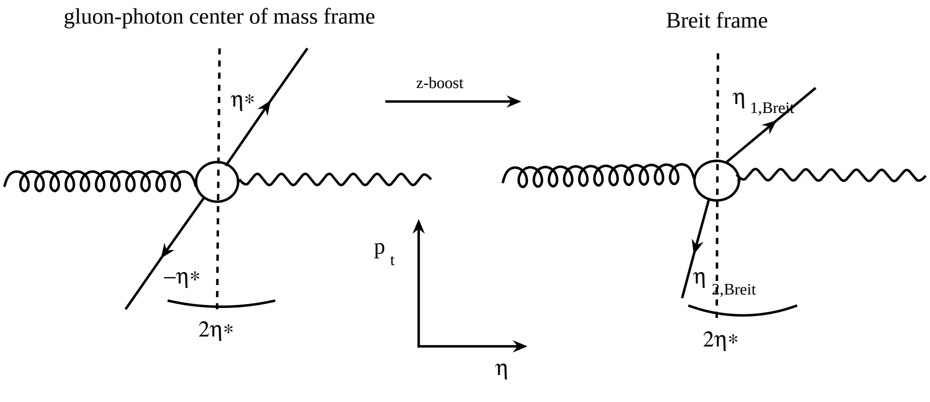

Figure 1.15: Boson-gluon fusion process in deep inelastic scattering in the boson-gluon centre-of-mass frame (left) and in the Breit frame (right). The frames are related to each other by a longitudinal boost along the z-axis.

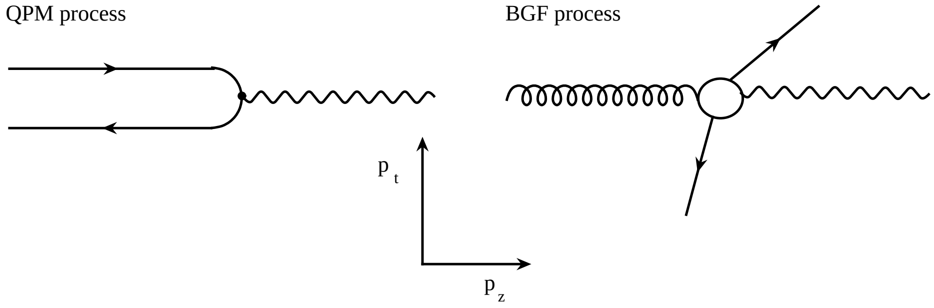

Figure 1.16: The QPM process (left) and the the BGF process (right) as seen in the Breit reference frame. In contrast to the leading order QCD BGF process ($\mathcal{O}(\alpha_s^1)$) in the purely electroweak QPM process ($\mathcal{O}(\alpha_s^0)$) no transverse energy component occurs.

Since no transverse energy occurs in the initial state and only one parton is found in the final state, the quark is scattered back in the negative z-direction. No transverse energy occurs in the final state. As indicated in figure 1.16 the situation is different for higher-order QCD processes where two or more partons are found in the final state. Though again no transverse energy component is provided by the initial state the generation of two (ore more particles) facilitates the occurrence of transverse energies (balancing each other) in the final state. In the Breit reference frame the transverse energy E_T of the final state partons is an indicator for the 'hardness' of the QCD process. A minimum cut on the transverse energy can thus suppress events where no perturbatively calculable strong interaction takes place.

1.4.4 Asymmetric cut on the transverse jet energy

The aim of this analysis is to measure dijet cross sections and to compare them to the predictions of a fixed order QCD calculation ($\mathcal{O}(\alpha_s^2)$). The results of this next to leading order calculation are unphysical if symmetric cuts are applied to the transverse jet energies in the Breit frame. The unphysical behaviour results from a reduction of phase space available for three-parton final states. The NLO calculation incorporates contributions from leading order ($\mathcal{O}(\alpha_s)$) and next to leading order ($\mathcal{O}(\alpha_s^2)$) dijet production including real and virtual corrections. In order to obtain physical meaningful results the negative contributions from the virtual corrections have to be cancelled by the positive contributions from the real corrections. At leading order conservation of energy and momentum requires that the two final state partons (and thus the resulting jets) have the same transverse energies ($E_{T,\mathrm{Breit}}^{\mathrm{jet1}} = E_{T,\mathrm{Breit}}^{\mathrm{jet2}}$). At next to leading order one of the final state partons can emit a real gluon and thus loose a fraction of its energy. If a symmetric cut is applied to the transverse jet energy a fraction of these events will be rejected. In this case the negative contributions from virtual processes will not be completely cancelled by the remaining positive contributions from real corrections. This will lead to unphysical results. One way to avoid this problem is to apply an asymmetric energy cut.

Chapter 2

Theoretical predictions

Physics subsists from the interplay between theory and experiment. In theoretical physics models are developed which describe observable processes in terms of fundamental principles. A theory is, aside its potential aesthetic beauty, only meaningful if it makes predictions which can be verified by experiment. Experimental results can then be used to confirm or falsify the theory, to give input for its modification or to extract its fundamental parameters.

In the field of Quantum Chromodynamics there are mainly two approaches to obtain theoretical predictions:

- so-called **Monte Carlo (MC) generators**, implementing leading-order (LO) matrix elements and phenomenological models for the simulation of higher orders via parton cascades and for the non-perturbative hadronisation processes. Small-angle soft phenomena are supposed to be well described by these event generators;
- **fixed-order QCD calculations** which implement all (real and virtual) corrections up to a given order. A good description of large-angle hard phenomena is expected for these calculations.

The aim of the presented analysis is to measure dijet cross sections and to compare the results with the predictions of a fixed-order QCD calculation in order to test the fundamental principles of perturbative QCD like factorisation, renormalisation and the universality of the parton density functions. The QCD calculations performed with DISENT [11] are of order $\mathcal{O}(\alpha_s^2)$, which for the observed dijet processes is the next-to-leading order (NLO). The predictions of the NLO calculation are available on parton level only, not including any hadronisation processes, whereas the data contain the full physical process (including hadronisation) as 'seen' through the detector. In order to be able to compare the parton level NLO predictions with the measured detector level cross sections both the data and the NLO predictions are corrected to hadron level (sections 2.2.1 and 7.1) by applying correction factors obtained from event samples generated with leading-order Monte Carlo generators. The correction of the predictions from the NLO QCD calculation with factors obtained from LO Monte Carlo models is somehow inconsistent and unsatisfactory. In the last few years NLO Monte Carlo generators such as *MC@NLO* [31] have been developed. Unfortunately at present no such NLO Monte Carlo generator exists for deep inelastic electron-proton scattering.

2.1 Monte Carlo models

In this analysis the leading-order Monte Carlo generators LEPTO 6.5 [32] and ARIADNE 4.08 [33, 34] are used. Both generators utilise the matrix element of the hard scattering process at leading order (section 2.1.1). Higher orders are simulated via the generation of parton cascades based on phenomenological models (section 2.1.2). The fragmentation of the generated partons into hadrons, the so-called hadronisation, is also described by phenomenological models (section 2.1.3). The final state particles of each event are passed through a full simulation of the ZEUS detector (section 2.1.4) including a simulation of the trigger system. The output of the detector simulation is then processed by the same reconstruction and offline programs as the data. After that the event information is available on parton, hadron[1] and detector level. The detector level information is given in the same format as the actual ZEUS data.

2.1.1 Calculation of the leading order matrix element

The hard matrix element is calculated with LEPTO which uses exact first-order matrix elements (ME) to generate the quark parton model, the QCD-Compton and the boson-gluon fusion processes. The photon flux which enters into the calculation of the matrix elements is calculated with DJANGOH 1.1 [35]. Higher order QED processes like initial and final state radiation, loop corrections and two-boson exchanges are simulated using the HERACLES 4.6.1 [36] program, which is implemented in the DJANGOH program. The *ep* cross section is obtained by convoluting the cross section of the hard scattering process with the the CTEQ5D [37] proton PDFs, implemented in the program PDFLIB [38].

2.1.2 Simulation of higher orders: the parton cascades

As mentioned above in LO MC generators higher orders are simulated via the generation of parton cascades based on phenomenological models. In LEPTO the generation of parton cascades is based on the parton shower model whereas ARIADNE uses the colour-dipole model (CDM) [39–42].

---

[1] The hadron level is defined in terms of hadrons with lifetimes $\tau \geq 10$ ps.

The parton shower model: The parton shower model is based on the DGLAP approach by Dokshitzer, Gribov, Lipatov, Altarelli and Parisi. It utilises the parton splitting functions from the DGLAP evolution equation (section 1.3.2) to obtain the branching ratios between the following processes: gluon radiation ($q \rightarrow qg$), gluon splitting ($q \rightarrow gg$), and pair production ($g \rightarrow q\bar{q}$). In the parton shower model a parton from the hard scattering process emits additional quarks and gluons according to the calculated branching ratios until it reaches a minimum virtuality of $Q^2_{min} \approx 1$ GeV^2.

The colour-dipole model: In the colour-dipole model (CDM) the partons participating in the hard scattering process are used to span colour-dipoles which can radiate gluons. The initial dipoles are spanned between the initial partons emerging from the hard scattering process and the proton remnant. The emitted gluon(s) and the primary parton(s) do again form dipoles which can emit additional gluons, and so on. The CDM was originally designed for e^+e^- scattering. For DIS the model had to be modified to take into account the finite size of the proton remnant. ARIADNE utilises the CDM to generate DIS events in the following way [43]: For all QPM processes the colour dipole is spanned between the struck quark and the proton remnant. If the matrix element is of the form of $\gamma q \rightarrow qg$ (QCDC), the gluon is removed and the event is treated as QPM process. This is necessary as the CDM also describes the emission of hard gluons correctly. The rate of QCDC events is thus correctly modelled by adding QPM and QCDC events and having the gluon momentum spectrum governed by the CDM. The BGF process is included by modifying the initial radiation to produce an antiquark instead of a gluon. The ratio between antiquark and gluon emission is fixed by the ratio between the BGF and the $\mathcal{O}(\alpha_s^1)$ matrix element [44].

Figure 2.1 shows a schematic representation of the colour dipole model simulating the parton cascade in an electron-proton event.

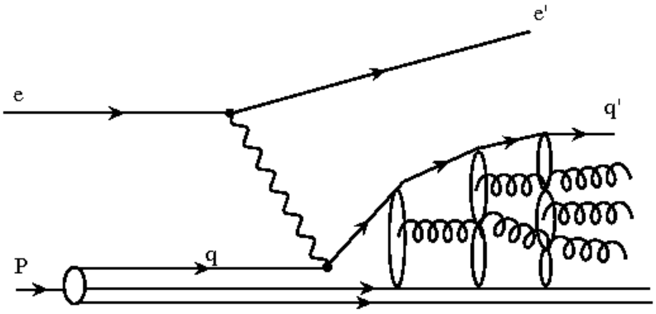

Figure 2.1: Schematic representation of the colour-dipole model simulating the parton cascade in an electron-proton event.

2.1.3 Hadronisation

In both Monte Carlo generators the hadronisation (the transformation from partons into colourless hadrons) is simulated with JETSET 7.4 [45–47], which implements the Lund string model [48]. In this model the colour field between quark pairs is represented by a relativistic string. The energy density and the spatial extension of the string are in the order of 1 GeV/fm and 1 fm, respectively. The field is described by a modified Coulomb potential according to $V(r) \propto a/r + br$. For larger distances, r, the potential linearly increases with the distance. Once the energy of the string exceeds the mass of a $q\bar{q}$ pair, the string splits and a new $q\bar{q}$ pair is created. The process is repeated until all available energy has been used to create new quark-antiquark pairs. The resulting colourless strings form the hadrons of the final state. Figure 2.2 indicates the functional principle of the Lund string model.

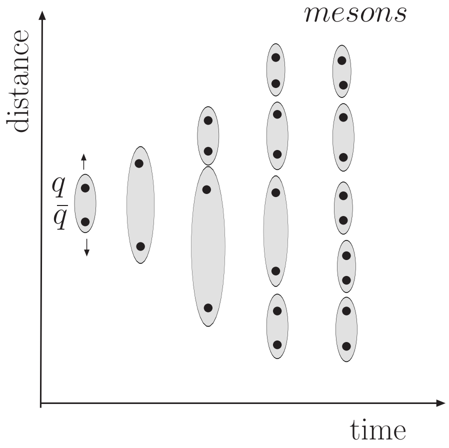

Figure 2.2: Schematic representation of the Lund string model. In this model the colour field between quark pairs is represented by a relativistic string. The energy density and the spatial extension of the string are in the order of 1 GeV/fm and 1 fm, respectively. For larger distances the string potential linearly increases with the distance. Once the energy of the string exceeds the mass of a $q\bar{q}$ pair, the string splits and a new $q\bar{q}$ pair is created. The process is repeated until all available energy has been used to create new quark-antiquark pairs.

2.1.4 Detector simulation

The simulation of the ZEUS detector is based on the GEANT 3.13 [49] Monte Carlo packages. GEANT allows to define volumes of certain shapes and materials at given positions and in this way to create a detailed virtual model of the complete detector. GEANT simulates the transport of particles (generated by another Monte Carlo generator) through the defined detector volumes and their interaction with the detector

material and the magnetic field. Furthermore it simulates the response of the sensitive detector components to the deposited energy.
The simulation of nuclear interactions and hadronic showers is based on GHEISHA7 [50]. In order to save computing time a fast 'porridge' representation of the ZEUS uranium calorimeter is implemented in the ZEUS detector simulation. The simulation based on the CAL porridge is about 4 times faster than that based on a detailed sandwich representation [51]. In order to further reduce the computing time two types of ZEUS specific shower terminators are implemented [52]. The terminators parametrise the low energy components of electromagnetic and hadronic showers. Their implementation avoids the time consuming tracking of the numerous low energetic shower particles and further reduces the execution time by a factor of about 15.

2.2 Fixed-order QCD calculation

In this analysis the FORTRAN-based program DISENT [11] is used to calculate dijet cross sections including the QCD-Compton and the boson-gluon fusion process with QCD corrections up to the order of $\mathcal{O}(\alpha_s^2)$, which for the mentioned processes is the next-to-leading order. The calculations are performed in the $\overline{\mathrm{MS}}$ renormalisation and factorisation schemes using a generalised version [11] of the subtraction method [53]. The renormalisation scale can be set to a linear combination of the photon virtuality, Q^2, and the square of the transverse jet energy, E_T^2: $\mu_R^2 = a \cdot Q^2 + b \cdot E_T^2 + c$, where a, b and c are parameters, that can be fixed by the user. In this analysis μ_R is set to $\mu_R^2 = \overline{E}_T^2 + Q^2$, where $\overline{E}_T$ is the mean transverse energy of the two highest energetic jets. Cross checks are performed using $\mu_R^2 = \overline{E}_T^2$ and $\mu_R^2 = Q^2$. The factorisation scale which can be varied in terms of the photon virtuality according to $\mu_f^2 = a \cdot Q^2 + b$ is in this analysis set to $\mu_f^2 = Q^2$. The calculations are performed using the CTEQ6.1 [54,55] parametrisation of the proton PDFs. The strong coupling constant is calculated at two loop accuracy with $\alpha_s(M_Z) = 0.118$. The number of quark flavours is set to five. Predictions for dijet cross sections are obtained by applying the k_T cluster algorithm (see section 1.4.2) to the generated partons. Since the hadronisation process is a soft phenomenon which can not be calculated within the framework of perturbative QCD the results of the fixed-order calculations are available on parton level only.

2.2.1 Hadronisation correction

Before the calculated parton level dijet cross sections can be compared to the data they have to be corrected for hadronisation effects. In this analysis the bin-by-bin method, based on event samples generated with LO Monte Carlo models, is utilised for this hadronisation correction. This correction procedure can be applied only if the shapes of the calculated NLO cross sections are reasonably well described by the parton level LO Monte Carlo predictions.

Figure 2.3 shows the NLO differential dijet cross sections $d\sigma/dQ^2$, $d\sigma/dx_{Bj}$ $d\sigma/d\bar{E}_T$, $d\sigma/dM_{jj}$, $d\sigma/d\eta'$, and $d\sigma/d\log_{10}\,\xi$ as obtained from DISENT. The shown cross sections have been calculated for a jet phase space given according to $125 < Q^2 < 5000$ GeV^2, $|\cos\gamma_h| < 0.65$, $E^{\rm jet1(2)}_{T,\rm Breit} > 12(8)$ GeV, and $-2 < \eta^{\rm jet}_{\rm Breit} < 1.5$, where $E^{\rm jet1(2)}_{T,\rm Breit}$ and $\eta^{\rm jet}_{\rm Breit}$ are the transverse energies of the two highest energetic jets and the jet pseudorapidities as measured in the Breit reference frame (see section 1.4.3). The NLO cross sections are compared to the parton level predictions as obtained from the LO Monte Carlo generators LEPTO and ARIADNE. For the comparison, the MC prediction, that is the number of dijet events in a certain bin, i, is divided by the width of the respective bin. The obtained distributions are scaled such, that the integral over the distribution is equal to the total NLO cross section. As can be seen in figure 2.3, the NLO cross sections are reasonably described by the scaled parton level predictions of both Monte Carlo generators. The deviations are typically below 10 % (below 20% for the highest $\bar{E}_T$ and M_{jj} bins). Exceptions are the last two Q^2 bins and the last x_{Bj} bin where the description is poor and LEPTO (ARIADNE) lies above (below) the NLO predictions by up to 60 % (40 %).

Figure 2.4 shows the NLO predictions of DISENT and the scaled predictions of the LO Monte Carlo generators for the cross section $d\sigma/d\log_{10}\,\xi$ in different regions of Q^2. The NLO cross sections are again well described by the parton level predictions of both MC models. The deviations are in the order of 5-10 %.

In order to obtain the hadronisation correction factors for every bin, i, a coefficient, $C^{\rm had}_{\rm mc,i}$, is determined for both Monte Carlo samples according to

$$C^{\rm had}_{\rm mc,i} = \frac{MC^{\rm had}_{\rm mc,i}}{MC^{\rm par}_{\rm mc,i}} \quad \text{with} \quad \text{mc} \in \{\text{LEPTO}, \text{ARIADNE}\} \tag{2.1}$$

where $MC^{\rm had}_{\rm mc,i}$ ($MC^{\rm par}_{\rm mc,i}$) are the number of selected dijet events on hadron (parton) level in the respective bin. To obtain the final correction factors, $C^{\rm had}_i$, the correction factors obtained from LEPTO and ARIADNE are averaged. The error on $C^{\rm had}_i$ is defined as half the difference between the correction factors obtained from LEPTO and ARIADNE:

$$C^{\rm had}_i = \frac{C^{\rm had}_{\rm LEPTO,i} + C^{\rm had}_{\rm ARIADNE,i}}{2} \quad \text{and} \quad \delta[C^{\rm had}_i] = \frac{|C^{\rm had}_{\rm LEPTO,i} - C^{\rm had}_{\rm ARIADNE,i}|}{2}. \tag{2.2}$$

To correct the calculated cross sections for hadronisation effects and in this way to obtain NLO cross sections on hadron level ($\sigma^{\rm had}_{\rm NLO}$), for every bin the parton level cross section is multiplied by the respective correction factor according to $\sigma^{\rm had}_{\rm NLO,i} = C^{\rm had}_i\ \sigma^{\rm par}_{\rm NLO,i}$.

The applied correction factors are shown in figure 2.5 and 2.6. They typically differ from unity by less than 10 %.

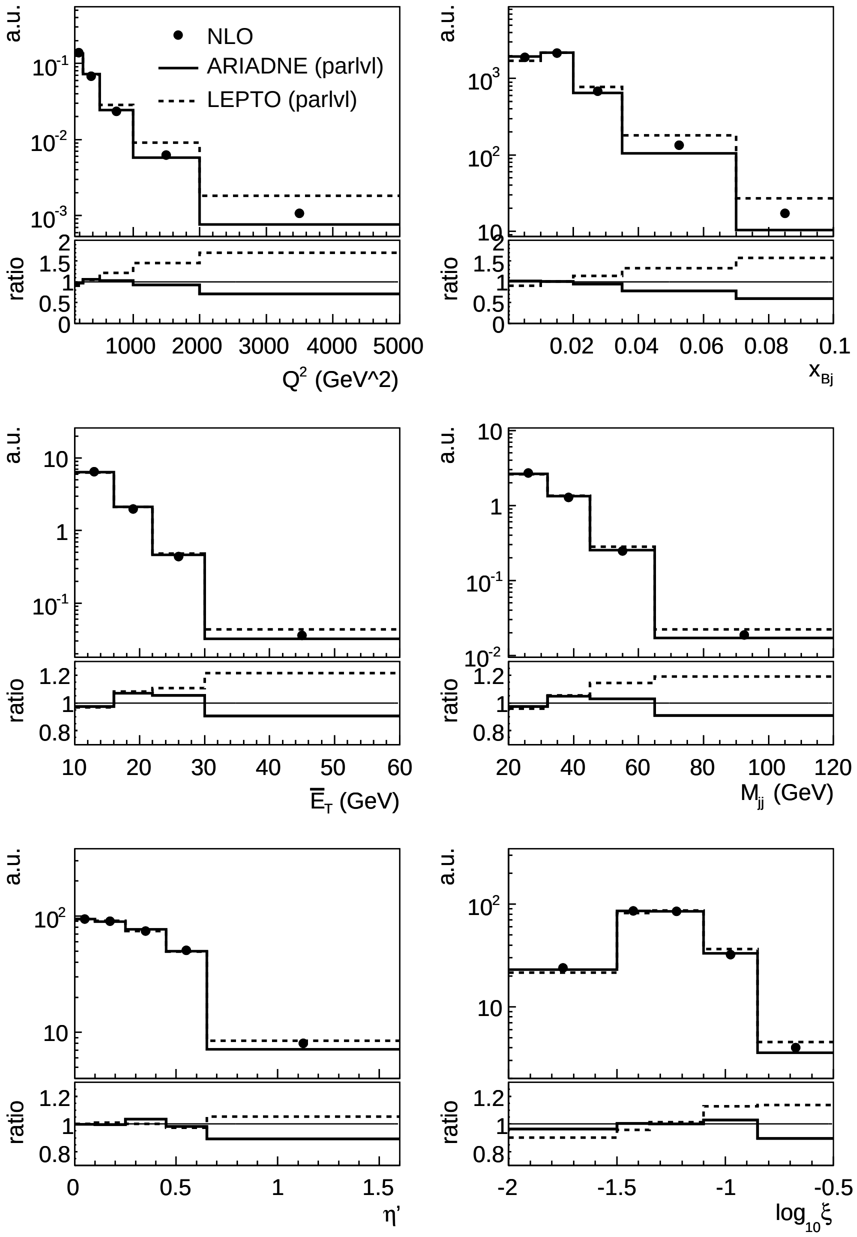

Figure 2.3: Parton level cross sections $d\sigma/dQ^2$, $d\sigma/dx_{Bj}$ $d\sigma/d\bar{E}_T$, $d\sigma/dM_{jj}$, $d\sigma/d\eta'$, and $d\sigma/d\log_{10}\xi$ for dijet production with $E^{jet1(2)}_{T,Breit} > 12\ (8)$ GeV and $-2 < \eta^{jet}_{Breit} < 1.5$, in the kinematic range given by $|cos\gamma_h| < 0.65$ and $125 < Q^2 <\ 5000\ \mathrm{GeV}^2$ as predicted by the DISENT NLO QCD calculation (dots) and the LO Monte Carlo generators ARIADNE (solid line) and LEPTO (dashed line). The MC predictions, that is the number of events in a certain bin divided by the bin width, are scaled such that the integral over the distribution is equal to the total NLO cross section.

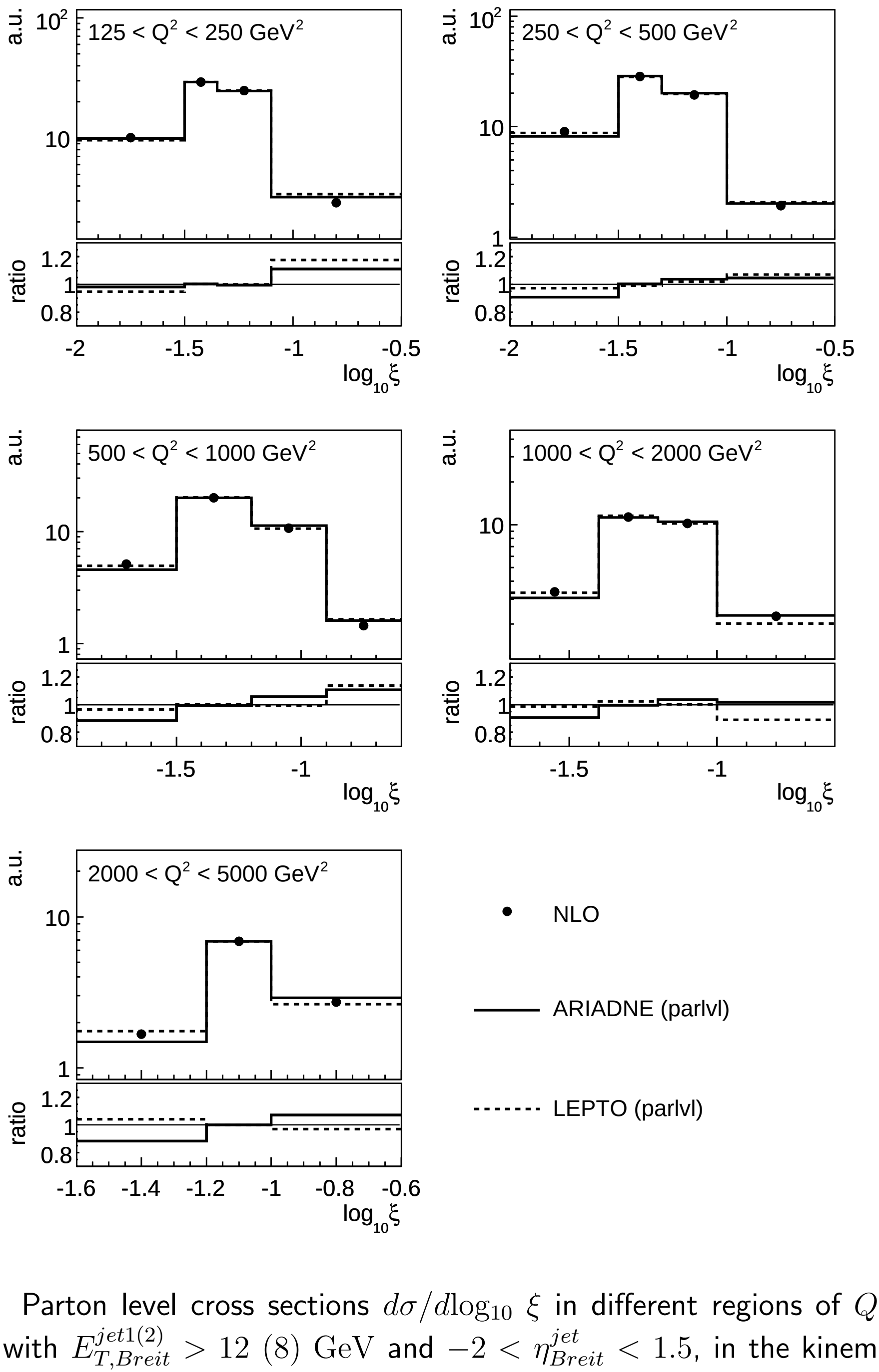

Figure 2.4: Parton level cross sections $d\sigma/d\log_{10}\,\xi$ in different regions of Q^2 for dijet production with $E^{jet1(2)}_{T,Breit} > 12$ (8) GeV and $-2 < \eta^{jet}_{Breit} < 1.5$, in the kinematic range given by $|cos\gamma_h| < 0.65$ as predicted by the DISENT NLO QCD calculation (dots) and the LO Monte Carlo generators ARIADNE (solid line) and LEPTO (dashed line). The MC predictions, that is the number of events in a certain bin divided by the bin width, are scaled such that the integral over the distribution is equal to the total NLO cross section.

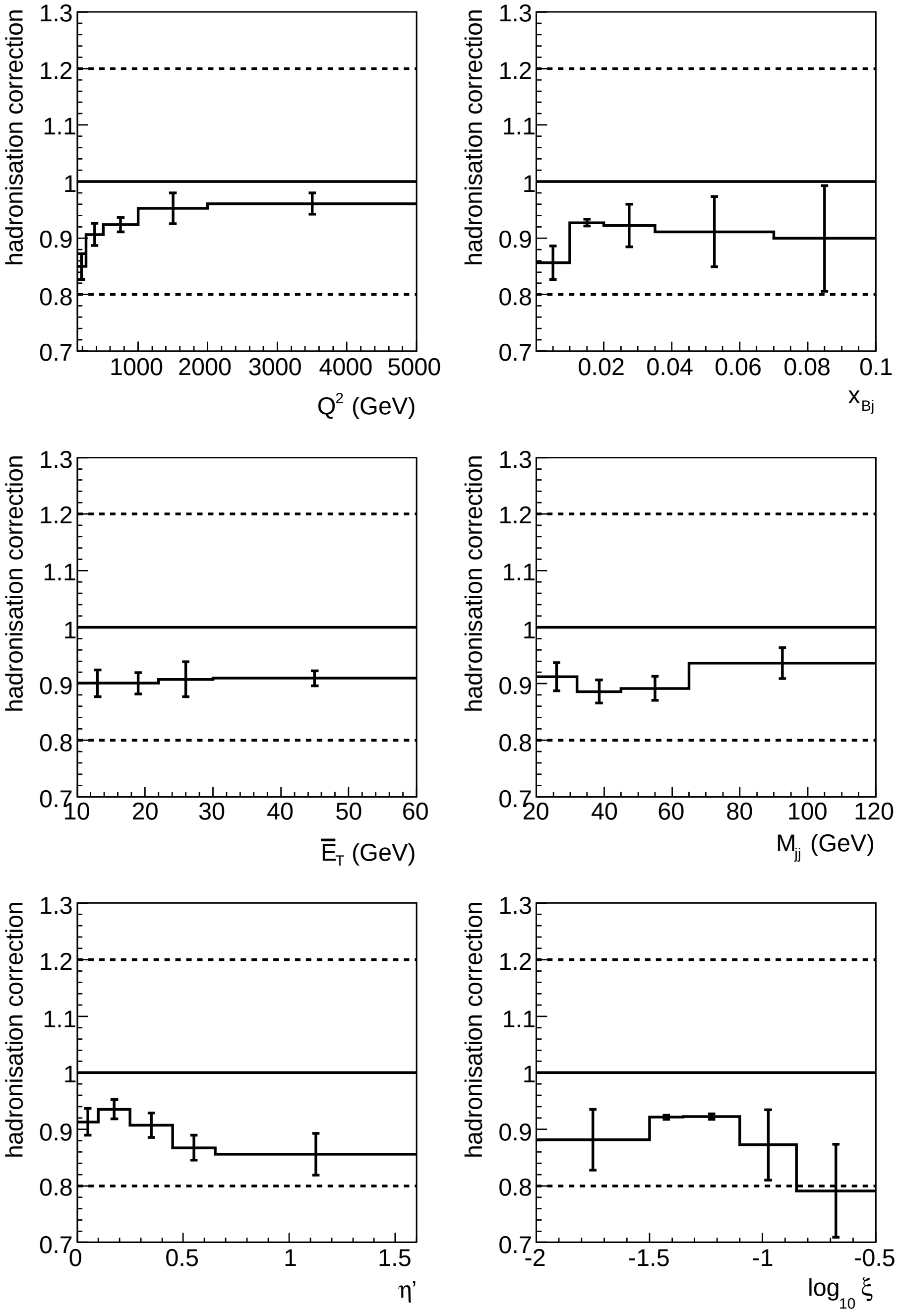

Figure 2.5: Hadronisation correction factors for the NLO cross sections $d\sigma/dQ^2$, $d\sigma/dx_{Bj}$ $d\sigma/d\bar{E}_T$, $d\sigma/dM_{jj}$, $d\sigma/d\eta'$, and $d\sigma/d\log_{10}\xi$. The corrections are obtained by averaging the factors obtained from LEPTO and ARIADNE. The error is defined as half the difference between the correction factors obtained from LEPTO and ARIADNE.

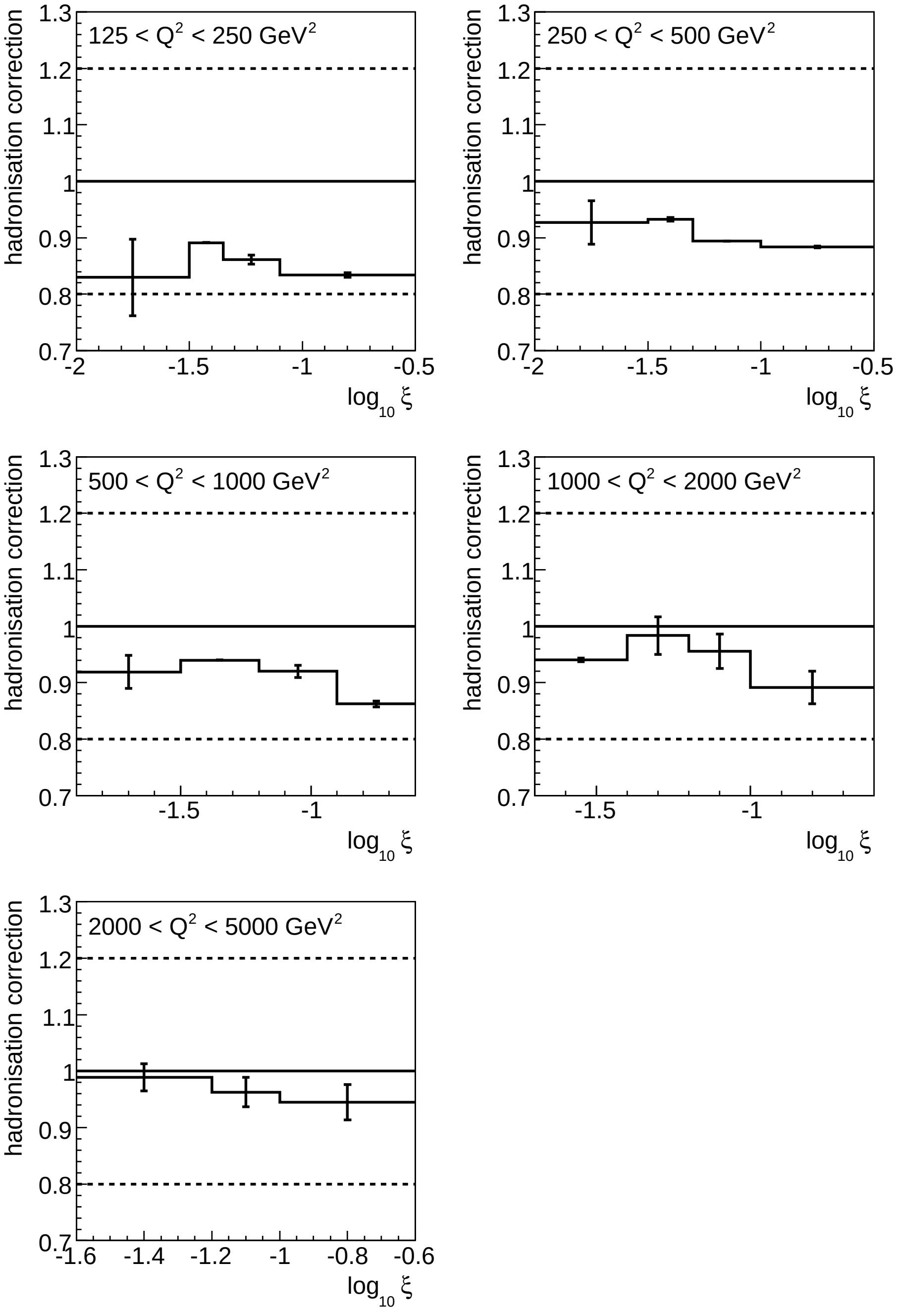

Figure 2.6: Hadronisation correction factors for the NLO cross sections $d\sigma/d\log_{10}\xi$ in different regions of Q^2. The corrections are obtained by averaging the factors obtained from LEPTO and ARIADNE. The error is defined as half the difference between the correction factors obtained from LEPTO and ARIADNE.

2.2.2 Theoretical uncertainties

The results of the NLO calculation depend on parameters of the theory which are only known to a certain precision (like α_s and the proton PDFs) and on the (arbitrary) choice of the renormalisation and factorisation scales, μ_R and μ_f. Due to the hadronisation correction, based on correction factors obtained from MC samples, the results also become dependent on the choice of phenomenological models implemented in the Monte Carlo event generators. To estimate the error on the NLO QCD predictions the calculations are repeated with different settings. The input parameters are varied within their uncertainty range and the calculations are performed using different scales. In this analysis the following sources of uncertainty are considered:

- the uncertainty on the NLO QCD calculations due to terms beyond next-to-leading order is estimated by varying the renormalisation scale by a factor two up and down[2] ($\mu'_R = 0.5\ \mu_R$ and $\mu''_R = 2\ \mu_R$). The related uncertainties on the calculated dijet cross sections are about ±10%, with the largest values approaching ±20% at low values of ξ and Q^2;

- the uncertainty on the NLO QCD calculations due to the uncertainty on the strong coupling constant, α_s, is estimated by repeating the calculations using two additional sets of proton PDFs (CTEQ6A114 and CTEQ6A122 [56]) which were determined assuming $\alpha_s(M_Z) = 0.114$ and $\alpha_s(M_Z) = 0.122$, respectively. The difference between the calculations based on the two PDF sets and the default CTEQ6 PDF [54,55] is scaled by a factor of 0.68 to reflect the current uncertainty on α_s [57]. The resulting uncertainty on the cross sections is typically below ±4%;

- as described in the previous section, the error on the multiplicative hadronisation correction factor is defined as half the difference between the correction factors obtained from LEPTO and ARIADNE, which use the parton shower and the colour-dipole model for the generation of the parton cascades, respectively. The related uncertainty on the corrected NLO cross section is determined by applying error propagation. The resulting uncertainty is typically smaller than 3 %;

- the uncertainty on the NLO calculations due to the uncertainty on the proton PDFs is estimated by repeating the calculations using 40 additional sets from the CTEQ6 analysis, which take into account the statistical and correlated systematic experimental uncertainties of each data set used in the determination of the proton PDFs. The resulting uncertainty on the cross sections is about ±4 % at low Q^2 and decreases to around ±2 % at high Q^2;

---

[2] As described in section 1.3.1 the results of a perturbative QCD calculation, calculated to all orders in α_s, does not (must not!) depend on the choice of the renormalisation scale. However, due to the truncation of higher orders the calculated NLO cross sections become scale-dependent. The strength of the scale dependence can be interpreted as an indicator for the uncertainties related to missing higher orders.

- the uncertainty of the QCD NLO calculations due to the (arbitrary) choice of the factorisation scale, μ_f, is estimated by repeating the calculations with $\mu_f = Q/2$ and $\mu_f = 2\ Q$. The effect on the calculated cross sections is negligible.

The listed uncertainties are added in quadrature to obtain the total theoretical error, δ_{theo}.

Chapter 3

Experimental setup: DESY, HERA, and ZEUS

The 'Deutsches Elektronen-Synchrotron' (DESY) was founded in 1959 as a national research centre for elementary particle physics. Nowadays the main fields of research at DESY are the investigation of the structure of matter with synchrotron radiation, also referred to as photon physics, and elementary particle physics. For the field of photon physics DESY provides the electron ring accelerator DORIS III [58, 59] and the Free-Electron-Laser FLASH [60]. PETRA III [61, 62], which will be the most brilliant storage-ring-based x-ray source worldwide, will start commissioning at DESY in 2009, whereas the commissioning of the European X-ray free electron laser XFEL [63] is planned for 2013. For the field of elementary particle physics DESY provided the only electron[1]-proton ring accelerator worldwide, the 'Hadron-Elektronen-Ring-Anlage' (HERA). HERA, which started operation in 1992, delivered beams to the experiments HERA B[2], HERMES, H1 and ZEUS. In 2001 HERA was upgraded to achieve higher luminosities. The two running periods (before and after the upgrade) are referred to as HERA I and HERA II. The research of HERMES ('HERA Measurement of Spin') is focused on the proton spin and its distribution over the proton constituents (quarks and gluons). The main focus of the experiments H1 and ZEUS is the determination of the proton structure and the investigation of the strong interaction. In addition both experiments gave important contributions to the understanding of the electromagnetic and the weak interaction and their unification at high energies and also contribute to searches for new phenomena. HERA ended operation in June 2007. Though the focus of research has since then slightly shifted towards photon physics, DESY is still very active in the field of particle physics. Besides the ongoing analysis of the full HERA data, the H1 and ZEUS collaborations are also working on combined results. Furthermore DESY

---

[1] HERA could accelerate both, electrons and positrons. In the following the term 'electron' is used for both, electrons and positrons if not stated differently.

[2] The HERA B experiment was designed in order to measure the CP violation in the decays of heavy B-mesons using the proton beam of HERA. It operated from 1999 to 2003.

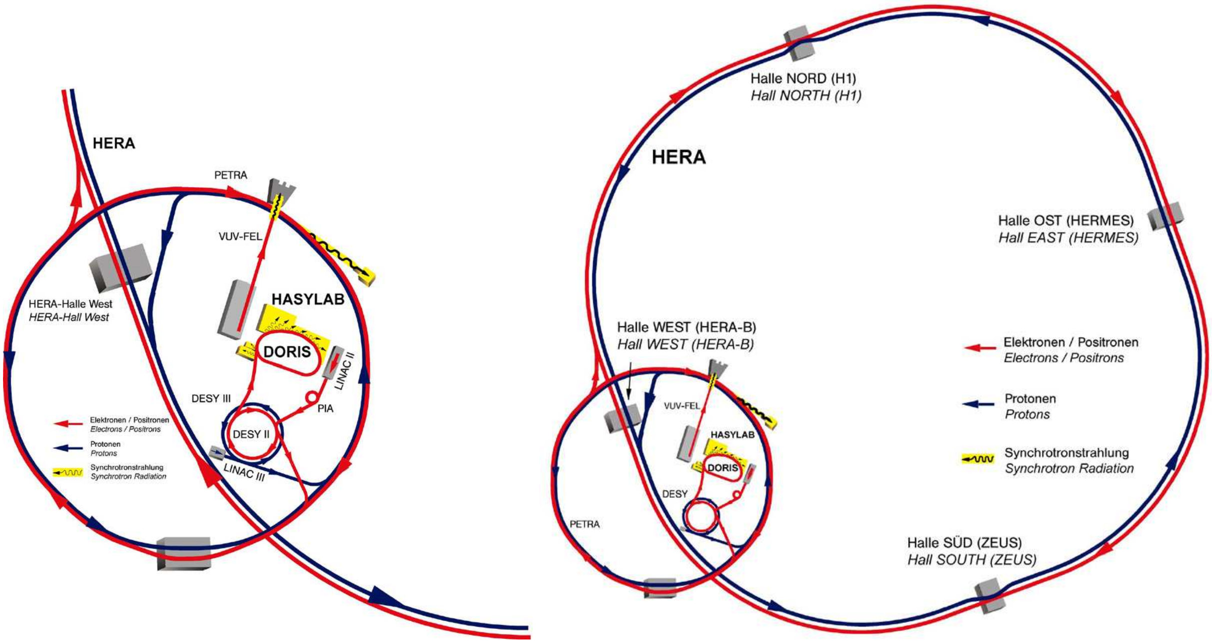

Figure 3.1: Layout of the HERA storage ring and its pre-accelerator system.

groups are involved in the ATLAS [64,65] and CMS [66,67] experiments at the Large Hadron Collider (LHC) [68, 69], the International Linear Collider (ILC) [70], the ALPS [71] experiment (designed to search for axion-like particles) and in the field of astro-particle physics with the neutrino telescopes AMANDA and Ice Cube [72] and the Cherenkov Telescope Array (CTA) [73].

In the following, a short description of the HERA accelerator and the ZEUS detector, which was used to record the analysed data, is given. As the analysis is based on HERA I data the descriptions of the accelerator and the detector are based on the HERA I configuration unless stated otherwise.

3.1 HERA storage ring

At HERA electrons and protons were accelerated up to nominal energies of 27.5 GeV and 920 GeV, resulting in a centre-of-mass energy, $\sqrt{s}$, of about 318 GeV. The HERA tunnel was located 10 to 25 meters below the surface. HERA consisted of four straight segments with a length of 360 meters each and four circular arcs with a radius of 797 meters. Before being injected into the HERA machine the electrons and protons were accelerated by a system of several pre-accelerators (see figure 3.1):

- **electrons/positrons:** Electrons and positrons were produced and initially accelerated in the linear accelerator LINAC II. Here the leptons reached an energy of 450 MeV. After this initial acceleration they were injected into the DESY II ring via the PIA accumulator. In DESY II the leptons were accelerated up to an energy of 7 GeV. Afterwards they were injected into the PETRA II ring. In PETRA II the energy of the leptons was increased to 12 GeV before they were finally transfered into the HERA machine;

- **protons:** To produce protons, H^- ions were accelerated in the LINAC III accelerator. The negative ions were shot through a stripper foil where they lost their electrons. The resulting protons were injected into the DESY III ring where their energy was increased up to 7.5 GeV. After this the protons, just like the electrons, were injected into PETRA II where they were accelerated to an energy of 40 GeV. After this acceleration they were transferred into the HERA ring.

In HERA electrons and protons were stored in separate bunches with a distance of 28.8 m between two successive bunches. This distance lead to a bunch crossing time of 96 ns. The maximum possible number of stored bunches was 210. To estimate the number of background events originating from beam-gas interactions, cosmics, and other 'non-ep' events, unpaired as well as empty bunches were used. To accelerate the electrons up to their final energy, 16 superconducting niobium four-cell cavities supplied an electric field gradient of 5 MV/meter. The electrons were controlled using conventional magnets providing a magnetic field of 0.164 Tesla. The electron's energy loss due to synchrotron radiation (about 127 MeV per circulation) was compensated by 500 MHz copper cavities which were installed inside the straight segments of HERA. To keep the protons on HERA's orbit superconducting magnets providing a bending field of 4.68 Tesla were used.

After the 1994 running period it was decided to accelerate positrons instead of electrons to achieve higher lepton-beam lifetimes, which for electrons suffered from the interaction of the electrons with an almost stationary dust of positively charged particles. The dust was caused by ion getter pumps used for the electron-beam vacuum system. The easiest way to solve this problem was to use positrons instead of electrons. During the shut-down in winter 1997/98 the ion getter pumps were replaced with non-evaporating getter pumps, and HERA started to use electrons again. The proton energy was increased to 920 GeV, leading to a centre-of-mass energy of 318 GeV in the years 1998-2000.[3] The higher momentum of the protons required a magnetic field of 5.3 Tesla. In 1999 HERA started to accelerate positrons again because the lifetime of the lepton-beam was still higher for positrons than for electrons.

Since the number of occurring events is, for a given process, proportional to the cross section of the process and the integrated luminosity, a high luminosity is required to obtain high statistics and thus to be able to observe rare processes. The

---

[3] When HERA started operation in 1992 the proton energy was 820 GeV, resulting in a centre-off-mass energy of about 300 GeV.

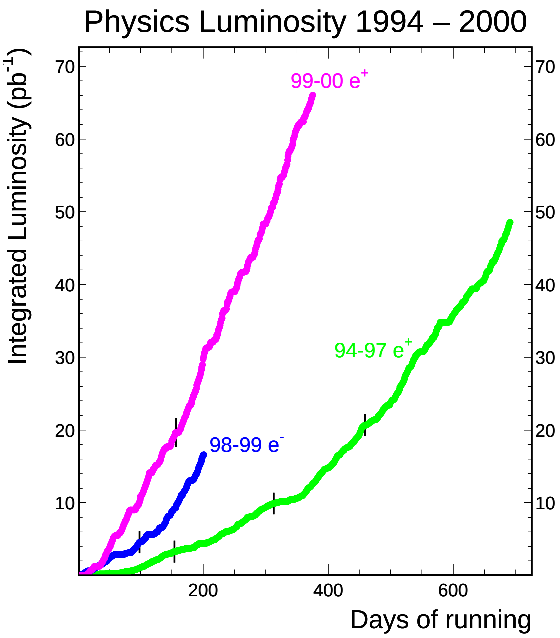

Figure 3.2: Integrated luminosities delivered by HERA in the years 1994 to 2000.

luminosity $\mathcal{L}$ is thus an important parameter which characterises the performance of the storage ring. Its value, given according to

$$\mathcal{L} = f \frac{N_p N_e}{4\pi\sigma_x\sigma_y}, \tag{3.1}$$

can be controlled by adjusting the number of electrons and protons per bunch (N_e and N_p), the spatial extension of the bunches ($\sigma_x \cdot \sigma_y$) and the bunch crossing frequency f. Figure 3.2 shows the integrated luminosities delivered by HERA during the different electron and positron running periods in between the years 1994 to 2000.

3.2 ZEUS detector

ZEUS was one of two multipurpose detectors at the HERA ring accelerator. The detector had a dimension of $12 \times 11 \times 20$ m^3 and a weight of 3600 tons. ZEUS had been designed to study the wide spectrum of HERA physics where particles and jets with energies up to several hundred GeV had to be measured with high precision. A detailed description of the ZEUS detector can be found in [51]. The geometry of ZEUS is described by a right-handed coordinate system with its origin at the nominal interaction point. The z axis is pointing along the direction of the incoming proton, whereas the x axis is pointing horizontally towards the centre of HERA. It is also common to use a polar coordinate system (r, θ, ϕ) where θ is the polar angle

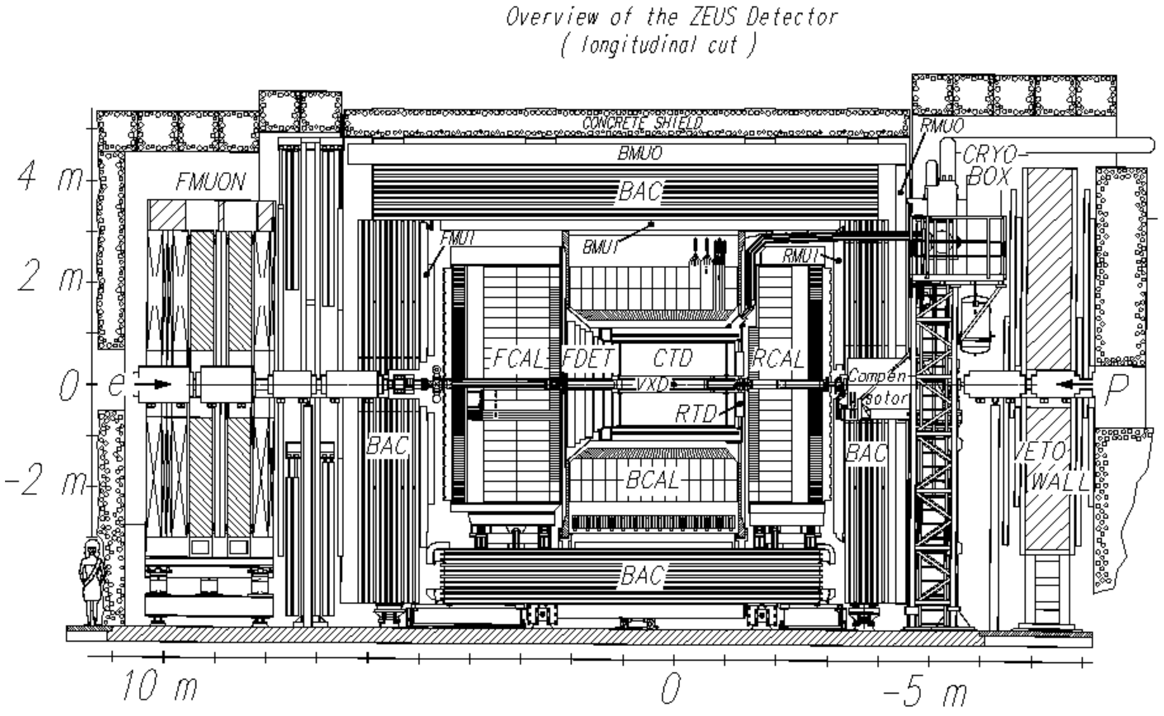

Figure 3.3: Longitudinal cross section of the ZEUS detector.

with respect to the z axis and ϕ is the azimuthal angle with respect to the x axis. Longitudinal and transverse cross sections of the ZEUS detector, showing the main components, are presented in figures 3.3 and 3.4. The asymmetry of the detector reflects the large momentum imbalance between the proton and the electron beam at the HERA machine. In the following a brief description of the main detector components is given.

The innermost part of the ZEUS detector had been a vertex detector which was removed during the shutdown in the years 1995/1996.[4] The central tracking detector (CTD), which was a cylindrical drift chamber, surrounded the beam pipe in the region of the nominal event vertex. The CTD was enclosed by a superconducting magnetic solenoid which provided a bending field of 1.43 Tesla for the determination of charge and momentum in the tracking system. In the backward and forward regions the CTD was supplemented with planar drift chambers, the RTD and FTD. The tracking detector was surrounded by a high-resolution uranium calorimeter (UCAL), which was the main device for energy measurements. The UCAL was enclosed by a low-resolution backing calorimeter (BAC). The BAC was used to measure the energy leakage out of the main uranium calorimeter and also served as a

---

[4] The vertex detector was replaced by a silicon micro vertex detector (MVD) in 2001.

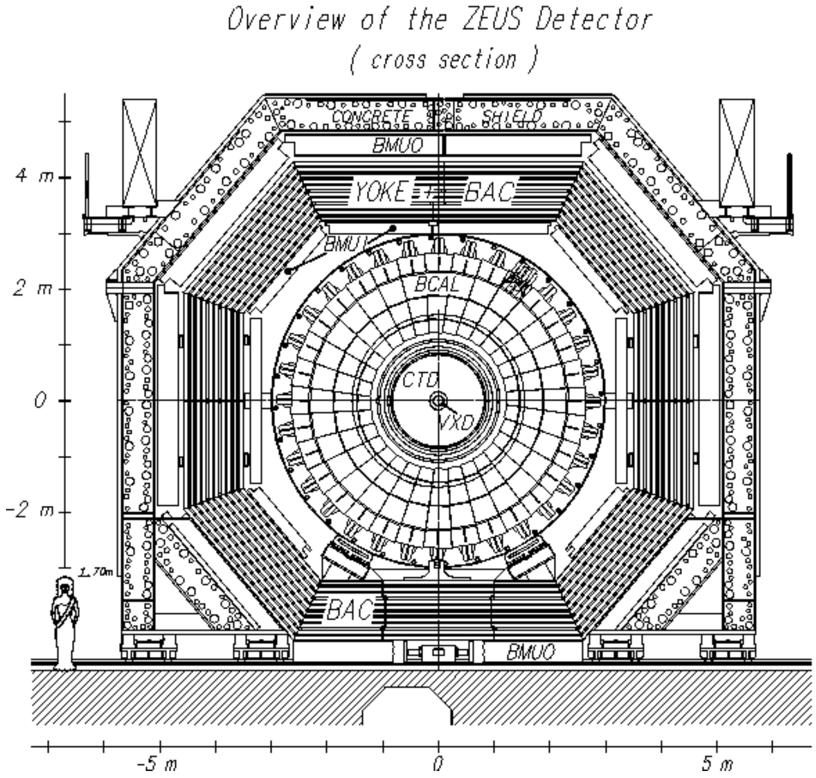

Figure 3.4: Transverse cross section of the ZEUS detector.

return yoke for the magnetic flux of the solenoid. Muon identification chambers were mounted inside and outside the BAC (RMUI, BMUI, FMUI and RMUO, BMUO, FMUO). In the rear region of the detector an iron-scintillator wall (VETOWALL) was installed to reject proton-beam-related background.

In the following a more detailed description of the components most relevant for the presented analysis is given: the central tracking detector, the uranium calorimeter, the luminosity system, and the trigger and data acquisition system.

3.2.1 Central tracking detector (CTD)

The CTD [74–76] was a cylindrical wire chamber oriented parallel to the beam axis. It provided the position and the momentum of charged particles and was used to measure the z position of the event vertex with a resolution of about 4 mm. The longitudinal length of the CTD was 241 cm, covering the polar angle of $15 < \theta < 164^o$. The inner radius of the chamber was 16.2 cm, the outer radius was 85 cm. The chamber was radially organised into nine 'super-layers' of eight sense wire layers each as displayed in figure 3.5. Five of the super-layers (1,3,5,7,9) had wires parallel to the chamber axis and were called 'axial super-layers'. The remaining four layers (2,4,6,8) were so called 'stereo super-layers'. The wires of these stereo super-layers

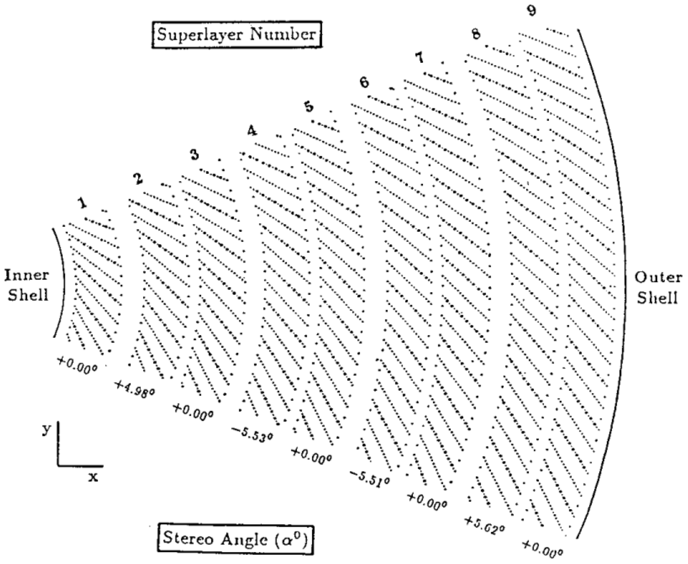

Figure 3.5: Layout of a CTD octant. The wires of the stereo super-layers (even numbers) are slightly tilted with respect to the beam axis. The angle values are displayed below the corresponding super-layer.

were mounted with angles of about $+5^0$ or -5^0 with respect to the beam axis in order to allow track reconstruction of the z coordinate. The obtained resolution was about 2 mm ($\sigma_z = 2$ mm).

The CTD was filled with a gas mixture of argon, carbon dioxide and ethane in the ratio of 83:5:12. In a drift chamber a charged particle ionises the gas and creates electron-ion pairs along its trajectory. Due to the applied electric field the created electrons drift towards the positive sense wires whereas the positively charged ions move towards the negative field wires. In the CTD of ZEUS the (approximately constant) drift velocity of the electrons was about 50 μm/ns. Due to the increase of the electric field in the immediate vicinity of a drift chamber's sense wire the electrons near the wires are strongly accelerated and thus create secondary electron-ion pairs. An avalanche-like multiplication of electrons occurs which in the case of the CTD lead to an amplification factor of about 10^4. The produced electric pulse was read out and digitised by 8-bit flash ADCs. For trigger purposes, the three inner axial layers were additionally equipped with a z-by-timing system. In these layers the electric pulses were read out at both ends of the wires. The z position was then determined from the difference in the arrival time. The obtained resolution was about 4 cm.

The resolution of the CTD was about 230 μm in rϕ, resulting in a transverse momentum resolution of $\sigma_{p_T}/p_T = 0.0058 p_T \oplus 0.0065 \oplus 0.0014/p_T$ [51] for particles traversing all nine super-layers (p_T is the transverse momentum in GeV and $\oplus$ means summation in quadrature). The first term corresponds to the resolution of the hit positions, the second term to the effect of multiple scattering inside the CTD and the last term to multiple scattering before the particle enters the CTD.

3.2.2 High-resolution uranium calorimeter (UCAL)

The high-resolution uranium calorimeter (UCAL) [77–80], which covered about 98% of the full solid angle, was realised as a sampling calorimeter consisting of alternating layers of depleted uranium (absorber) and scintillator plates (active material). The thickness of the plates (uranium: 3.3 mm, scintillator: 2.6 mm) had been chosen to provide linear and equal response for electrons and hadrons over a wide range of energies.

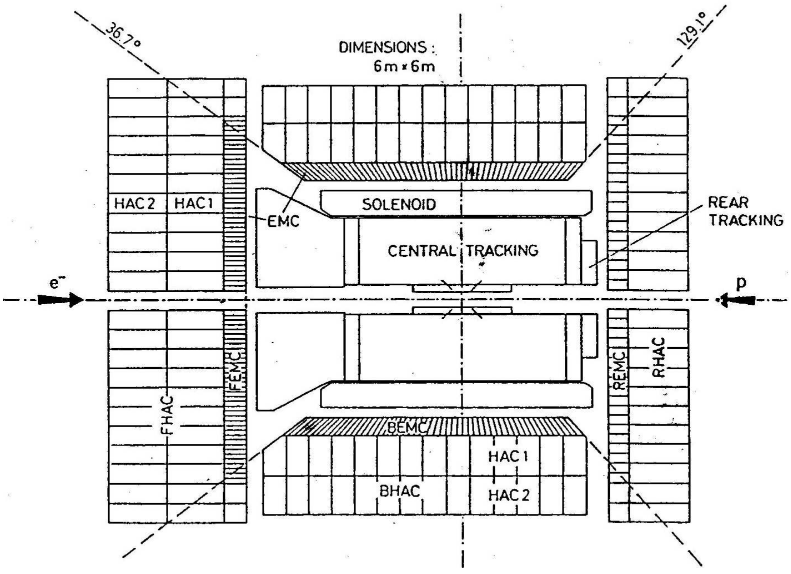

Figure 3.6: Layout of the ZEUS high-resolution uranium calorimeter. The picture shows the three sections of the UCAL and the polar-angle acceptance of each section.

The UCAL was divided into three sections, the forward (FCAL), the barrel (BCAL), and the rear (RCAL) calorimeter (see figure 3.3). The depth of the calorimeter was determined by the maximum energy that had to be absorbed, requiring 99% energy containment [81]. The maximum energy was a function of the polar angle and ranged from about 30 GeV in the RCAL to about 800 GeV in the FCAL. The containment of the highest energetic jets was achieved by the low-resolution backing calorimeter.

The FCAL covered polar angles from 2.2^0 to 36.7^0 (see figure 3.6). It was divided into 23 modules numbered with increasing x. Each module was further

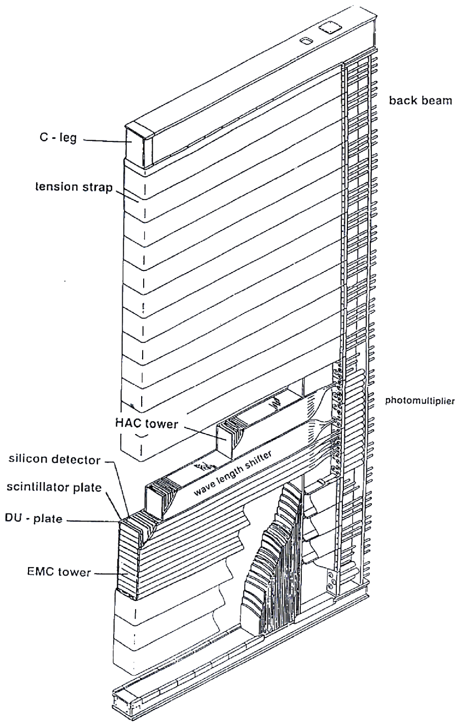

Figure 3.7: Structure of the FCAL modules. The modules were divided into one electromagnetic and two hadronic sections.

segmented into towers with a front surface dimension of 20 × 20 cm^2. The towers, numbered with increasing y, were divided into an electromagnetic (EMC) and two hadronic (HAC) sections. Each hadronic section of a tower was identified as one calorimeter cell whereas the electromagnetic sections were vertically divided into four cells with a front surface dimension of 20 × 5 cm^2. The structure of the FCAL modules is shown in figure 3.7

The RCAL covered polar angles from 129.1^0 to 176.5^0. Its design was very similar to the design of the FCAL. In contrast to the FCAL it contained one hadronic section only and the electromagnetic sections were vertically divided into two cells only. The front surface dimension of the EMC cells were thus 20 × 10 cm^2.

Since the outer regions of the RCAL and the FCAL were shadowed by the BCAL there was no need for a finely segmented EMC section in the corresponding modules. As can be seen in figures 3.6 and 3.8 these modules contained an additional hadronic (HAC0) instead of the electromagnetic section. Figure 3.8 shows the structure of the FCAL and the RCAL in the xy plane as seen from the interaction point.

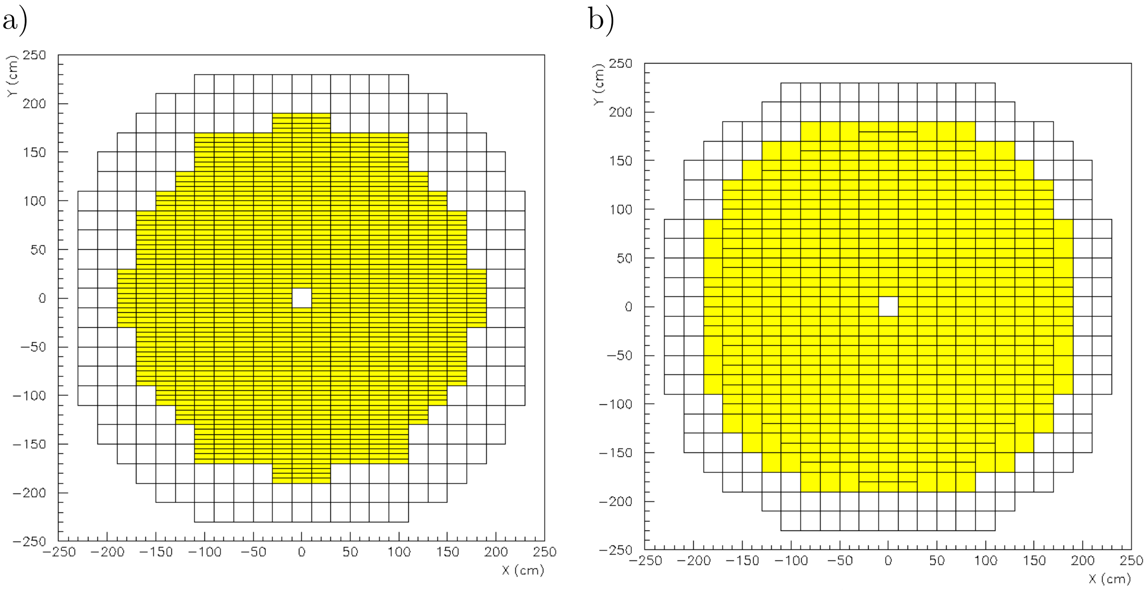

Figure 3.8: Structure of the a) FCAL and the b) RCAL as seen from the interaction point (xy-plane). The electromagnetic section of the FCAL towers is divided into four cells whereas that of the RCAL towers only contains two cells. The outer regions are covered by HAC0 cells.

The BCAL covering polar angles from 36.7^0 to 129.1^0 was divided into 32 wedge-shaped modules (see figure 3.4). It contained one electromagnetic and two hadronic sections. The modules were divided into 14 towers along the z-axis.

Each cell of the calorimeter was read out on opposite sides by two photomultiplier tubes (PMTs). The photomultipliers were coupled to the scintillator plates via wavelength shifters. The impact point of a particle within a cell could be determined from the pulse height difference between the signals of the two related tubes. The UCAL was calibrated [82] on a channel-by-channel basis using the natural radioactivity of the depleted uranium which provided a stable and time independent reference signal. The PMTs were monitored via light emission from LEDs and laser light with well known intensity. The electronic readout system could be calibrated using test pulses simulating the photomultiplier's signal.

The energy resolution of the ZEUS uranium calorimeter measured under test beam conditions was $\sigma/E = 18\%/\sqrt{E} \oplus 1\%$ for electrons and $\sigma/E = 35\%/\sqrt{E} \oplus 1\%$ for hadrons where E is the energy in GeV and $\oplus$ means summation in quadrature. The calorimeter energy response had been calibrated with an accuracy of about 1 %. Angles could be measured within a precision of about 10 mrad. The time resolution of the UCAL was better than 1 ns for energy deposits greater than 4.5 GeV.

3.2.3 Luminosity system

For a given process the event rate, R, is related to the cross section of the process, σ, and the machine luminosity, $\mathcal{L}$, according to

$$R = \mathcal{L}\sigma. \tag{3.2}$$

Any cross section measurement thus relies on an accurate knowledge of the luminosity. As can be seen from equation 3.2 the luminosity can be determined by measuring the event rate of a process with a well known cross section. At ZEUS the luminosity measurement is based on the Bethe-Heitler process $ep \to ep\gamma$. The theoretical cross section of this process, derived from QED calculations, is known with an accuracy of about 0.5 %. In its differential form it is given according to [83]

$$\begin{aligned} \frac{d\sigma^{\rm BH}}{dE_\gamma} &= 4\alpha r_e^2 \frac{E'}{E_\gamma E_e}\left(\frac{E_e}{E'} + \frac{E'}{E_e} - \frac{2}{3}\right)\left(\ln\frac{4E_pE_eE'}{m_pm_eE_\gamma} - \frac{1}{2}\right), & (3.3)\\ \frac{d\sigma^{\rm BH}}{d\theta_e} &\propto \frac{\theta_e}{\left(\left(\frac{m_e}{E_e}\right)^2 + \theta_e^2\right)^2}\quad, & (3.4) \end{aligned}$$

where $d\sigma^{\rm BH}/dE_\gamma$ is the cross section differentially in the photon energy E_γ, $d\sigma^{\rm BH}/d\theta_e$ is the cross section differentially in the angle between the emitted photon and the direction of the incoming electron, θ_γ, α is the electromagnetic coupling constant, r_e is the classical electron radius, E_e and E' are the energies of the electron before and after the emission of the photon (thus $E_e = E' + E_\gamma$), E_p is the energy of the proton and m_e and m_p are the masses of the electron and the proton, respectively.

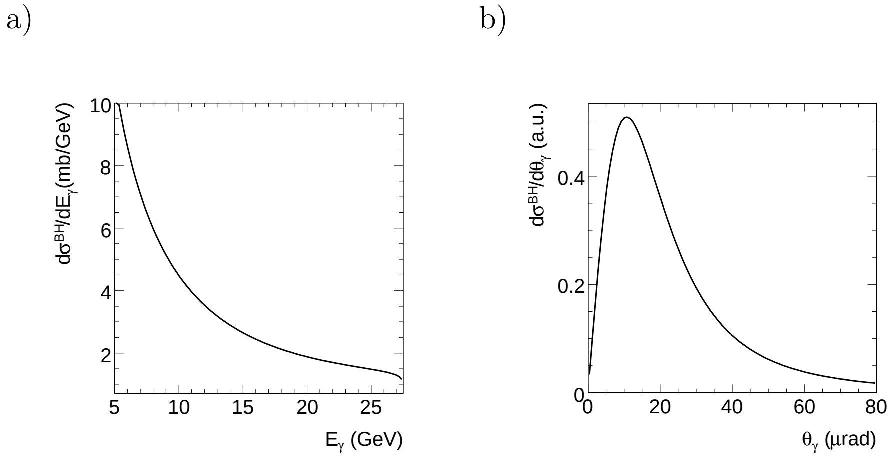

Figure 3.9: Theoretical cross section of the Bethe-Heitler process differentially in a) energy and b) angle of the emitted photon.

Figure 3.9 shows the distributions of the energy E_γ and the angle θ_γ of the photon.

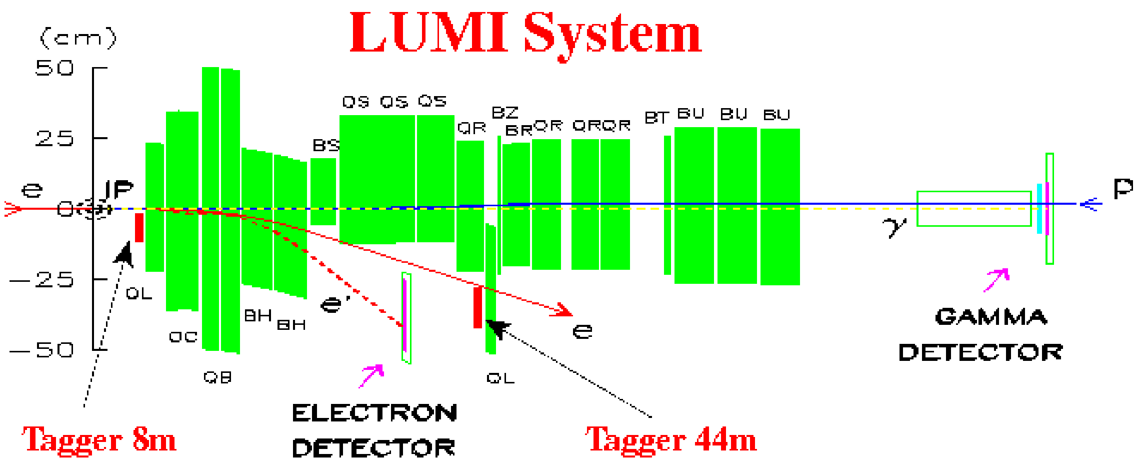

Figure 3.10: Layout of the HERA I luminosity system (LUMI).

As can bee seen from figure 3.9.b most photons are emitted under very small angles. In about 90% of the events the angle is smaller than 60 μrad. It should be noted that for high energetic electrons the same angular distribution approximately holds for the final state electron. The signature of the Bethe-Heitler process thus is the coincidence of a small angle electron and a small angle photon. Since the emission angles were far outside the acceptance of the main detector a dedicated luminosity monitoring system (LUMI) [83–85] consisting of a photon calorimeter (GDET) and an electron calorimeter (EDET) was installed (see figure 3.10).

- **Photon detector (GDET):** The photon detector was a lead/scintillator sandwich calorimeter, with a surface of 180×180 mm^2 and a depth corresponding to 22 radiation lengths, located at about $z = -107$ m distance from the interaction point. A carbon filter, placed in front of the calorimeter, was used to shield it against synchrotron radiation. The energy resolution of the calorimeter, determined under test beam conditions, was $\Delta E/E \approx 18\%/\sqrt{E}$, where the energy, E, is given in GeV. However, the carbon filter reduced the resolution to about $23\%/\sqrt{E}$. The impact position of the incoming photon could be determined with a resolution of about 0.2 cm in x and y using two planes of 1 cm wide horizontally and vertically orientated scintillator fingers located at 7 radiation lengths inside the calorimeter. It should be noted that the photon detector could also be used to measure photons from initial state radiation.

- **Electron detector (EDET):** The electron detector was a lead/scintillator sandwich calorimeter with a surface of 250×250 mm^2 and a depth corresponding to 24 radiation lengths, located at about $z = -35$ m. The energy resolution of the electron calorimeter, determined under test beam conditions, was $\Delta E/E \approx 18\%/\sqrt{E}$ (E in GeV). Electrons which had lost a certain fraction of their energy

> to a Bethe-Heitler photon were deflected by the HERA magnet system in such a way that they could leave the beam pipe through a steel window with a thickness of 0.085 radiation lengths at about $z = -27m$. The acceptance of the electron detector was limited to an energy range of 7-20 GeV.

It turned out that the tagging of the electron was not necessary for a precise measurement of the luminosity. However, the electron detector could also be used to tag photoproduction events. To extend the kinematic region for the tagging of photoproduction electrons additional electron calorimeters (the 8m tagger and the 44m tagger) were installed (see figure 3.10). The main background for the luminosity measurement was the Bremsstrahlung on gas molecules inside the beam pipe. As the signature of Bremsstrahlung events is exactly the same as for Bethe-Heitler events the only way to correct for it is to subtract this background on a statistical basis. To measure the rate of Bremsstrahlung events electron bunches without proton bunch partners were used (empty proton bunches). In this analysis an error of 2 % is estimated for the integrated luminosity.

3.2.4 Trigger and data acquisition system

At HERA one of the technical challenges for the ZEUS data acquisition system was the short bunch crossing time of 96 ns, corresponding to a rate of about 10 MHz. The total interaction rate, which was dominated by background due to beam-gas interaction, was in the order of 10-100 kHz while the rate of ep events in the detector was in the order of a few Hz. To separate these physics events from the dominating background and so to reduce the rate to a few Hz a sophisticated three-level trigger system was connected to the ZEUS detector. A schematic diagram of the ZEUS trigger and data acquisition system is shown in figure 3.11.

The 'first level trigger' (FLT) was a hardware trigger. It had been designed to reduce the input rate to below 1 kHz. Each component had its own first level trigger, which stored the data in a pipeline and made a trigger decision within 2 μs after the bunch crossing. The decisions from the local first level triggers were passed to the 'global first level trigger' (GFLT) which decided whether to accept or reject the event. The decision of the GFLT was returned to the readout systems of the different components within a time of 4.6 μs.

If the event had been accepted by the GFLT the data were transferred to the 'second level trigger' (SLT) which was software-based and ran on a network of transputers. Just as for the FLT every component of the detector had its own SLT. The 'global second level trigger' (GSLT) then received both the decisions of the second level triggers of the individual components and the trigger information of the global first level trigger. The GSLT had been designed to reduce the rate to below 100 Hz and produced a decision within 1-3 ms after the corresponding bunch crossing. If the event had been accepted by the global second level trigger the data

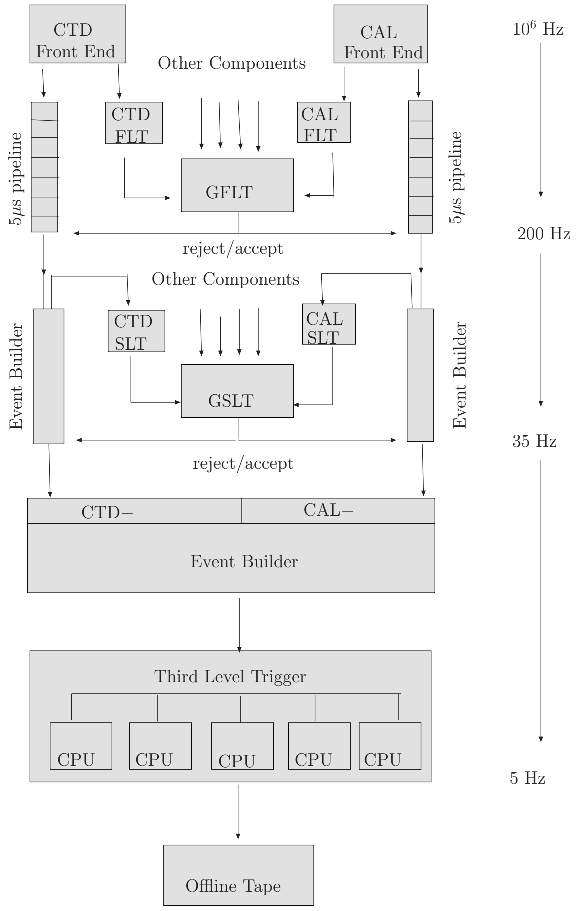

Figure 3.11: Schematic diagram of the ZEUS three-level trigger and data acquisition system

of all components was sent to the 'event builder', which collected the information to reconstruct a complete event.

The event was then passed to the software based 'third level trigger' (TLT). The TLT had been designed to reduce the rate to a few Hz. Events accepted by the third level trigger were written to tape via a fibre-link (FLINK) connection. The size of an event was typically 100 kBytes. The recorded events were available for the full offline reconstruction and data analysis.

Chapter 4

Event reconstruction

This analysis is based on neutral current DIS events where a scattered electron is found in the final state. Thus, to study the hadronic final state of these events a good reconstruction of both, the scattered electron and the hadronic final state, is of vital importance. The reconstruction of the scattered electron and the hadronic final state are described in sections 4.1 and 4.2. The reconstruction of the kinematic variables as defined in section 1.1 is described in section 4.3.

4.1 Reconstruction of the scattered electron

Electrons and hadrons can be discriminated by their different shower topologies. Hadronic showers are typically much broader, both in transverse and longitudinal direction, than showers caused by electrons or photons. Hadrons thus deposit a larger fraction of their energy in the hadronic part of the calorimeter (HAC cells). However, the difference in the shower topology only manifests for sufficiently large energies. For example the fraction of 1 GeV pions entering the calorimeter but depositing no energy in the HAC section is larger than 50% whereas the fraction of 10 GeV pions that deposit less than 2% of their energy in the HAC is less than 1% [86]. In addition to the resulting demand of a minimum electron energy, any discrimination method that is based on the shower topology can be used only, if the showers are well isolated.

At HERA the mayor source for misidentified electrons are neutral pions which decay into two photons[1] ($\pi^0 \rightarrow \gamma\gamma$). If the energy of the pion is sufficiently large the photons are very close and will be detected as one electromagnetic shower that has the same topology as a shower caused by an electron. To reduce this background and to ensure a pure identification of the electron the track information of the CTD can be used by demanding a track assigned to the respective calorimeter cluster.

In this analysis the neural-network based algorithm SINISTRA and the EM

---

[1] Other particles which also decay into photons are due to their higher mass less frequent.

electron finder are used for the reconstruction of the electron[2]. The efficiencies and purities of the two electron finders have been studied in [87]. In the RCAL the efficiency to find the DIS electron is about 95% for both finders.

4.1.1 SINISTRA electron finder

SINISTRA [86] is an algorithm based on a neural network. The neural network was trained using Monte Carlo samples consisting of hadronic and electromagnetic clusters. The number of hidden nodes is four. In a first step, adjacent cells belonging most likely to the shower of a single particle are clustered. In the applied clustering routine, the smallest geometrical unit is a tower. As described in section 3.2.2 the electromagnetic section of towers in the F -and BCAL is divided into four cells whereas in the RCAL it is divided into two cells only. To achieve a common geometry for all clusters, the information from towers of the FCAL and BCAL is reduced to the format of the towers in the RCAL as indicated in figure 4.1. In a next step for each cluster an area of 3×3 towers centred around the cluster tower with the highest energy deposition is defined. This area contains 54 values of energy deposits in the PMTs (36 in the EMC and 18 in the HAC section) (see figure 4.2). These values are then used as input to the neural network. Since the pattern of energy deposits depends on the angle of incidence the angle is used as an additional input parameter. The neural network projects the input parameters to one output parameter, P, that

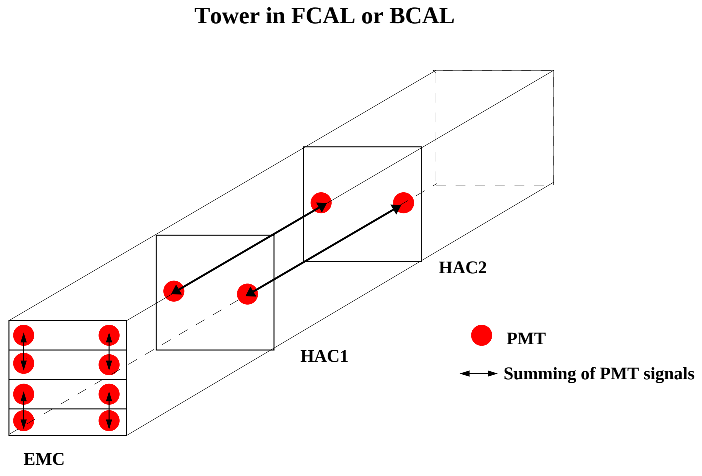

Figure 4.1: To achieve a common geometry for all clusters, the information from the towers of the FCAL and BCAL is reduced to the format of the towers in the RCAL. To achieve this, the signals of the PMTs in the electromagnetic section are summed as indicated by the arrows. The energy deposition in the HAC is determined by summing up the PMTs in HAC1 and HAC2 separately on the left and right side.

---

[2] SINISTRA is used as default whereas the EM electron finder is used for systematic checks.

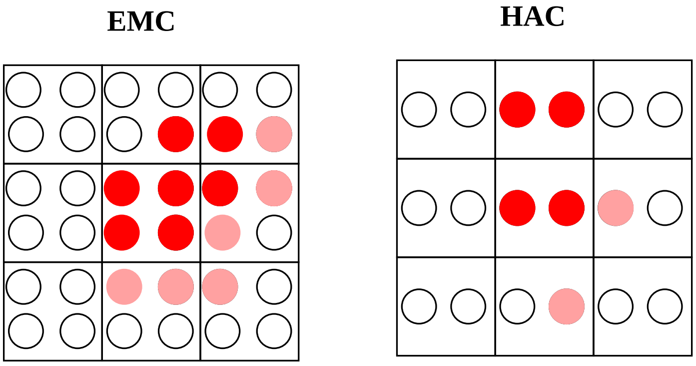

Figure 4.2: Sketch of the area of 3×3 towers centred on the cluster tower with the largest energy deposition. This area contains 54 values of energy deposits in the PMTs (36 in the EMC and 18 in the HAC section). These values are, in addition to the angle of incident, used as an input to the neural network of SINISTRA. Different colours indicate different values of energy deposits.

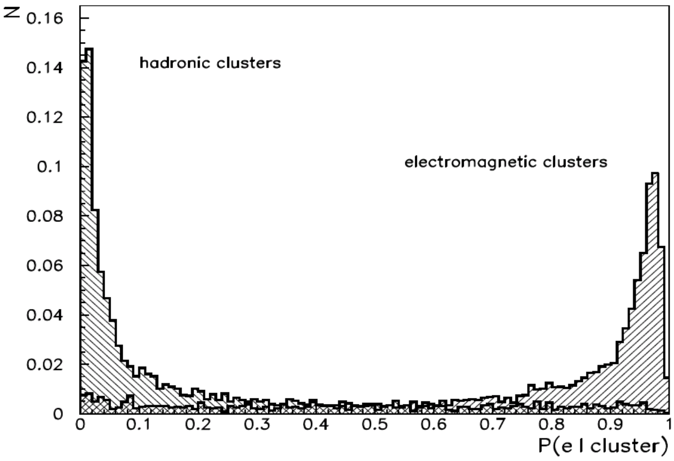

Figure 4.3: Probability distribution of the SINISTRA electron finder. The distributions are obtained from Monte Carlo test samples consisting of electromagnetic and hadronic clusters. Figure taken from [86].

is related to the probability for a cluster to be of hadronic ($P = 0$) or electromagnetic ($P = 1$) origin.

Figure 4.3 shows the SINISTRA probability distribution obtained from Monte Carlo test samples consisting of electromagnetic and hadronic clusters. As can be seen the hadronic and electromagnetic clusters are well separated.

The cluster with the highest probability P is the one assigned to the scattered electron. The energy of the electron is determined from the sum of energy deposits associated to the respective cluster and is corrected for dead material and non-uniformities in the calorimeter response. The impact position of the electron is defined as the logarithmic energy weighted centre of gravity of the cluster. Polar and azimuthal angles are determined from the impact position and the reconstructed event vertex. In the version of SINISTRA used in this analysis, the information of the CTD is used to reject candidates where a photon induced shower fakes an electron.

4.1.2 EM electron finder

The EM electron finder [88] is based on a detailed parametrisation of the ZEUS detector response for electrons. Seven variables (four based on CAL information and three based on tracking information) are used to evaluate whether a calorimeter cluster is an electron. The EM finder is optimised separately for the FCAL, BCAL and RCAL. The variables used are:

- f_{HAC}, the fraction of energy in the hadronic section excluding HAC0 cells;
- $f_{\mathrm{C}}^{\mathrm{Leak}}$, the fraction of energy in the EMC section that is not deposited inside the cell strip pair with the highest energy deposit. A cell strip is a set of EMC cells which have the same tower number and are located in the same calorimeter. $f_{\mathrm{C}}^{\mathrm{Leak}}$ is calculated according to $f_{\mathrm{C}}^{\mathrm{Leak}} = 1 - (f_{\mathrm{C}}(s_{\mathrm{max}}) + \max[f_{\mathrm{C}}(s_{\mathrm{max}} - 1), f_{\mathrm{C}}(s_{\mathrm{max}} + 1)])$, where $f_{\mathrm{C}}(s)$ is the fraction of EMC energy in strip s and s_{max} is the highest energy strip. The strip number s is defined according to $s = 4\ (t-1) + k$ where t is the tower number and k is the cell type (for EMC cells $1 \leq k \leq 4$);
- $f_{\mathrm{M}}^{\mathrm{Leak}}$, the fraction of energy not deposited in the module pair with the highest energy deposit. $f_{\mathrm{M}}^{\mathrm{Leak}}$ is given according to $f_{\mathrm{M}}^{\mathrm{Leak}} = 1 - (f_{\mathrm{M}}(m_{\mathrm{max}}) + \max[f_{\mathrm{M}}(m_{\mathrm{max}} - 1), f_{\mathrm{M}}(m_{\mathrm{max}} + 1)])$, where $f_{\mathrm{M}}(m)$ is the fraction of energy in module m and m_{max} is the module with the highest energy deposit;
- E_{cone}, the energy within a cone of $d_{\eta,\phi} < 0.8$ around the candidate not assigned to the electron candidate;
- $\delta\theta = |\theta_{\mathrm{Trk}} - \theta_{\mathrm{Cal}}|$, the difference between the polar angles, θ_{Trk} and θ_{Cal}, determined from tracking and calorimeter information;
- $\delta\phi = |\phi_{\mathrm{Trk}} - \phi_{\mathrm{Cal}}|$, the difference between the azimuthal angles, ϕ_{Trk} and ϕ_{Cal}, determined from tracking and calorimeter information;
- $\delta\frac{1}{P} = |\frac{1}{E} - \frac{1}{P_{\mathrm{Trk}}}|$, the difference between the inverse of the energy as measured with the CAL and the inverse of the momentum as determined from tracks.

For candidates outside the tracking acceptance or candidates without a matching track only the first four variables are taken into account.
For every candidate a number of seven (four) sub-probabilities, p_i, is determined from the variables described above. The grand probability for a candidate to be of electromagnetic origin is then calculated according to $Q = P \sum_{k=0}^{N-1} \frac{(-\log P)^k}{k!}$, where $P = \prod_{i=1}^{N} p_i$ is the product of the N sub-probabilities.

4.2 Reconstruction of the hadronic final state

The hadronic final state contains charged and neutral particles. The energy of both is measured in the calorimeter. However, a large fraction of the charged particles is also measured by the tracking detector. At low energies and in situations where a charged particle looses part of its energy in dead material before reaching the calorimeter the accuracy of the energy measurement can be improved by using tracking information in addition to the information of the calorimeter [89]. In this analysis the reconstruction of the hadronic final state is therefore based on so called *energy flow objects* (EFOs) [90] which combine calorimeter and tracking information. Before EFOs are reconstructed from the cell and tracking information (see section 4.2.2), the cell energy is corrected for losses in dead detector material and noisy cells are rejected as described in the following section.

4.2.1 Cell energy correction and noise reduction

To compensate for energy losses in dead detector material and other effects that lead to systematic shifts in the energy scale, the energies measured by the calorimeter cells are scaled using a standard set of scale factors. These factors are only applied to the data:

- for the FCAL a factor of 1.024 (0.941) is applied to the EMC (HAC) cells;
- for the BCAL a factor of $1.003 \cdot 1.05$ ($1.044 \cdot 1.05$) is applied to the EMC (HAC) cells;
- for the RCAL a factor of 1.022 is applied to both the EMC and the HAC cells.

The natural radioactivity of the uranium in the UCAL and electronic noise cause a steady background signal in the calorimeter. To suppress this background only cells with an energy deposition in the EMC (HAC) greater than 60 (110) MeV are considered for this analysis. Furthermore a cut of 100 (150) MeV is applied to isolated EMC (HAC) cells. Since the background of the UCAL is included in the detector simulation these cuts are applied to both simulated events and real data. Calorimeter cells that have a significantly higher mean energy or 'firing frequency' compared to other cells are identified as noisy. A list of noisy cells is made for each year and cells that are identified as noisy are not considered for reconstruction if their energy signal is less than three sigma above the noise level. Cells associated to the scattered electron are not taken into account for the reconstruction of the hadronic final state.

4.2.2 Energy flow objects

To reconstruct energy flow objects (EFOs) from the tracks and cells associated to the hadronic final state, in a first step adjacent cells are clustered into cell islands. This is done separately for cells in the EMC, HAC1 and HAC2 sections. In a second step the resulting cell islands are joined to 3-dimensional cone islands (in the following simply denoted as islands). The transverse position of the islands is determined through the logarithmic energy weighted positions of the combined cells, taking into account the exponential fall-off of the shower energy distribution. In a next step, charged tracks have to be matched to the reconstructed islands. Tracks are only taken into account for the matching procedure if they are fitted to the primary event vertex and traverse at least 4 superlayers of the CTD, having a transverse momentum of $0.1 < p_T < 20$ GeV. For tracks that pass more than 7 superlayers the maximum p_T is increased to 25 GeV.

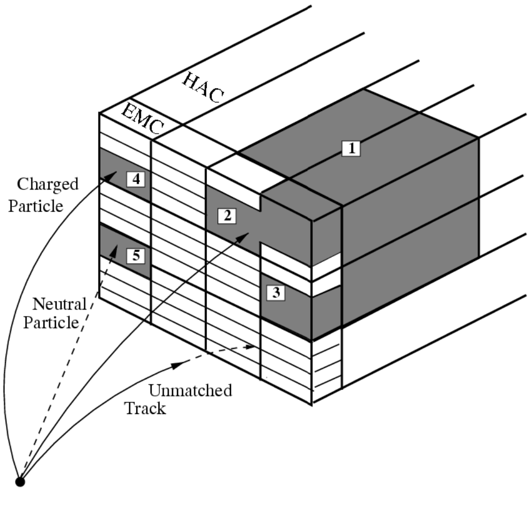

Figure 4.4: Schematic picture of cell and cone clusters in the calorimeter. In the picture four EMC cell islands and one HAC cell island are shown. The EMC cell islands 2 and 3 are clustered with HAC cell island 1 to form a cone island.

A track is matched to an island if the distance of closest approach between the extrapolated track and the position of the island is less than 20 cm, or if the distance of closest approach is less than the maximum radius of the island projected on a plane perpendicular to a ray from the vertex to the island's position. For each energy flow object that can be a single track, a single island, or a group of matched tracks and islands, the decision has to be made whether to take the information of the calorimeter or the tracking detector.

The calorimeter information is used for:

- islands not assigned to any track;
- islands associated with more than three tracks.

The tracking information is used for:

- tracks that are not assigned to any island. To determine the energy the track is assumed to be caused by a pion;
- groups of assigned tracks and islands (in case of a 1-to-1 track-island match) if they fulfil the two following requirements:
  - $\frac{E_{\rm Cal}}{p} < 1.0 + 1.2\,\sigma\left(\frac{E_{\rm Cal}}{p}\right)$: This requirement ensures that the energy deposit in the calorimeter is due to the associated track alone. The uncertainty is determined according to $\sigma\left(\frac{E_{\rm Cal}}{p}\right) = \frac{E_{\rm Cal}}{p^2}\sigma(p) \oplus \frac{1}{p}\sigma(E_{\rm Cal})$, where $\sigma(p)$ and $\sigma(E_{\rm Cal})$ are the resolution of the track momentum and the island energy, respectively, and $\oplus$ means summation in quadrature;
  - $\frac{\sigma(p)}{p} < \frac{\sigma(E_{\rm Cal})}{E_{\rm Cal}}$: The momentum resolution of the track has to be better than the energy resolution of the associated island. As the calorimeter resolution is poor in the supercrack regions between BCAL and FCAL and between BCAL and RCAL, in these regions the requirement is loosened by 20% ($\frac{\sigma(p)}{p} < 1.2\frac{\sigma(E_{\rm Cal})}{E_{\rm Cal}}$).

In cases where two or three tracks are assigned to an island or where more than one island is assigned to a track the energies, momenta and their resolutions have to be replaced by the respective sums according to:

$$\begin{aligned} E_{\rm Cal} \rightarrow \sum_i E^i_{\rm Cal} \quad &, \quad \sigma(E_{\rm Cal}) \rightarrow \sqrt{\sum_i \sigma^2(E^i_{\rm Cal})}, \\ p \rightarrow \sum_j p_j \quad &, \quad \sigma(p) \rightarrow \sqrt{\sum_j \sigma^2(p_j)}. \end{aligned}$$

If a single track is assigned to one or two islands and the energy of the calorimeter is favoured the energy information of the calorimeter and the angular information of the track are used for the EFO.

4.3 Reconstruction of the kinematic variables

At a given centre of mass energy, $\sqrt{s}$, inclusive processes in deep inelastic ep scattering are completely described by two of the three kinematic variables Q^2, x_{Bj}, and y (see chapter 1.1). The ZEUS detector measures energy and scattering angle of both the scattered electron and the hadronic final state particles. The kinematics are therefore over-determined and there a (six) different methods to reconstruct the kinematic variables. Since the input quantities are measured with different precision, the resolution of the reconstructed variables is different for the different methods and depends on the kinematic range. Furthermore, the methods are in different ways sensitive to initial and final state radiation. In this analysis the *electron method* (subscript el), the *double angle method* (subscript da), and the *Jacquet-Blondel method* (subscript jb) are used for the event reconstruction. These methods and the achieved resolutions are discussed in the following section.

4.3.1 Electron method

The electron method [91] uses the energy, E', and the polar angle, θ, of the scattered electron. The kinematic variables are determined according to

$$Q^2_{el} = 4E_eE'\cos^2(\theta/2), \tag{4.1}$$

$$x_{el} = \frac{E_e}{E_p}\frac{E'\cos^2(\theta/2)}{E_e - E'\sin^2(\theta/2)}, \tag{4.2}$$

$$y_{el} = 1 - \frac{E'}{2E_e}(1-\cos\theta), \tag{4.3}$$

where E_e and E_p are the energies of the incoming electron and proton, respectively. The resolutions of Q^2 and x_{Bj} in terms of the energy and the polar angle of the scattered electron are given according to

$$\frac{dx_{el}}{x_{el}} = \frac{1}{y}\frac{dE'}{E'} \oplus \tan(\theta/2)\left(x_{el}\frac{E_p}{E_e} - 1\right)d\theta, \tag{4.4}$$

$$\frac{dQ^2_{el}}{Q^2_{el}} = \frac{dE'}{E'} \ominus \tan(\theta/2)d\theta, \tag{4.5}$$

where $\oplus$ and $\ominus$ both refer to quadratic addition, but $\oplus$ indicates a positive and $\ominus$ a negative correlation. Due to the 1/y term the resolution of x_{el} decreases for small values of y. In this region the resolution strongly depends on the accuracy of the measured electron energy. The resolution of Q^2_{el} is good over the whole kinematic range, except for small scattering angles. Since the electron method uses information of the scattered electron, it is sensitive to initial state radiation where it tends to overestimate the energy of the incoming electron, causing a systematic shift in the reconstructed variables. The effect of final state radiation can be neglected since the emitted photon is in most cases combined into the electromagnetic cluster of the electron candidate.

4.3.2 Jacquet-Blondel method

The Jacquet-Blondel method [92] has been proposed to reconstruct the kinematic variables in charged current events where the scattered neutrino can not be detected. It relies solely on the energy and angle measurement of the hadronic final state particles. The kinematic variables are given according to

$$\begin{aligned} Q^2_{jb} &= \frac{(\Sigma_i p_{xi})^2 + (\Sigma_i p_{yi})^2}{1 - y_{jb}}, && (4.6) \\ y_{jb} &= \frac{\Sigma_i (E_i - p_{zi})}{2E_e}, && (4.7) \\ x_{jb} &= \frac{Q^2_{bj}}{s y_{jb}}, && (4.8) \end{aligned}$$

where the sum runs over all observed final state hadrons and $\sqrt{s}$ is the electron-proton centre-of-mass energy. If we define $p_{T,h} := \sqrt{(\Sigma_i p_{xi})^2 + (\Sigma_i p_{yi})^2}$ and $\Sigma := \Sigma_i (E_i - p_{zi})$ the resolution of Q^2_{jb} is given according to

$$\frac{dQ^2_{jb}}{Q^2_{jb}} = \frac{2 \cdot dp_{T,h}}{p_{T,h}} \oplus \frac{1}{2E_e} \frac{d\Sigma}{1 - y}. \qquad (4.9)$$

Due to the 1/(1-y) term the resolution in Q^2_{jb} decreases as y approaches unity. Since $Q^2 \propto x_{Bj}$ this also affects the resolution of x_{jb}. The Jacquet-Blondel method is not affected by initial state radiation since it uses only information of the hadronic final state.

4.3.3 Double angle method

The double angle method [91] uses only the angles of the final state particles. The kinematic variables are then given according to

$$\begin{aligned} Q^2_{da} &= 4E_e^2 \frac{\sin\gamma_h (1 + \cos\theta)}{\sin\gamma_h + \sin\theta - \sin(\theta + \gamma_h)}, && (4.10) \\ x_{da} &= \frac{E_e}{E_p} \frac{\sin\gamma_h + \sin\theta + \sin(\theta + \gamma_h)}{\sin\gamma_h + \sin\theta - \sin(\theta + \gamma_h)}, && (4.11) \\ y_{da} &= \frac{\sin\theta (1 - \cos\gamma_h)}{\sin\gamma_h + \sin\theta - \sin(\theta + \gamma_h)}, && (4.12) \end{aligned}$$

where θ is the polar angle of the scattered electron and γ_h is the polar angle of the hadronic final state defined according to

$$\cos\gamma_h = \frac{p^2_{T,h} - \Sigma^2}{p^2_{T,h} + \Sigma^2}. \qquad (4.13)$$

The sum runs over all hadrons observed in the final state. In the QPM process γ_h corresponds to the polar angle of the scattered parton. Combining equations (4.1) and (4.10) the energy of the scattered electron can be determined according to

$$E'_{da} = \frac{2E_e \sin\gamma_h}{\sin\gamma_h + \sin\theta - \sin(\gamma_h + \theta)}. \tag{4.14}$$

Since the double angle method only uses angle information it does, in first order, not depend on the energy calibration and resolution of the detector. The energy of the electron reconstructed with the double angle method, E'_{da}, can thus be used to calibrate the calorimeter.

4.3.4 Resolution of the kinematic variables

The resolution of the kinematic variables reconstructed with the electron, double angle and Jacquet-Blondel methods has been studied in a phase space similar to the phase space of this analysis [93]. The best resolution of Q^2 and x_{Bj} is achieved using the double angle method where the resolutions are better than 8% and 16%, respectively, over the whole range observed. The highest resolution of the energy of the scattered electron for small values of E' ($E' < 20$ GeV) is achieved by the electron method. At higher energies the resolution achieved with the double angle method (smaller than 4%) is superior to the resolution achieved with the electron method. Therefore in this analysis Q_{da} is used to cut on the photon virtuality, E' is used to cut on the electron energy, and E_{da} is used for the boost from the laboratory to the Breit reference frame.

Chapter 5

Selection of the inclusive DIS sample

5.1 Data sample

The data used for this analysis were recorded with the ZEUS detector in the years 1998, 1999 and 2000. In this period HERA provided electrons and positrons with an energy of 27.5 GeV and protons with an energy of 920 GeV, resulting in a centre-of-mass energy of 318 GeV. At ZEUS the data recorded during a period of time under constant physical conditions are collected into so called runs. For every run the status of all detector components is recorded. This information is used to reject runs where components essential for the analyses did not work properly. In the year 2000 some runs (run numbers 37588-37639) were recorded with shifted vertex positions. These runs are not taken into account for this analysis. After the rejection of the respective runs the used data correspond to an integrated luminosity of 81.74 pb^{-1}. An overview of the different data taking periods between the years 1998 and 2000 is given in table 5.1. As the phase space for this analysis is restricted by a cut on the virtuality of the exchanged boson according to $Q^2 < 5000$ GeV, the exchange of Z^0 bosons and thus the difference between e^+ and e^- data due to γ/Z^0 interference can be neglected[1]. Therefore the electron and positron data sets are combined.

5.2 Event selection

To reject events that are not well reconstructed and those not being relevant for the analysis a set of cuts is applied to the data. A list of all cuts applied to select the inclusive DIS sample is given in the following. The cuts are listed in the same order in which they are applied to data and detector-level Monte Carlo events.

---

[1] A dijet analysis based on HERA II data [94] showed that for $Q^2 < 5000$ GeV^2 corrections due to γ/Z^0 interference are typically smaller than one percent.

year	lepton	run range	# of accepted runs	luminosity of accepted runs
1998	e^-	30758 - 31752	417	4.60 pb^{-1}
1999	e^-	31784 - 32906	462	12.08 pb^{-1}
1999	e^+	33125 - 34485	516	19.66 pb^{-1}
2000	e^+	35031 - 37715	1009	45.41 pb^{-1}
			Σ 2404	Σ 81.74 pb^{-1}

Table 5.1: Overview of the different data taking periods between the years 1998 and 2000. The data recorded in this years correspond to an integrated luminosity of 81.74 pb^{-1} .

5.2.1 Trigger requirement and trigger efficiency

Events are only taken into account for the further analysis if they are selected by the DIS03 electron trigger which consists of DST bit 12 and TLT DIS bit 03. Events are selected by the DIS03 trigger if both trigger bits have been activated. The trigger requires a well isolated electron candidate corresponding to a photon virtuality of at least 80 GeV^2. The efficiency of the electron trigger has been studied [95] using an event sample that passes the full dijet selection but is selected by an alternative jet trigger. The jet trigger asks for at least one of TLT HPP bits 1, 2, 3, 4, 9, 11, 14, 15, 21, 22, 23, 25, 26, and 27. Each of the bits requires at least one, two or three jets. The basic assumption is that all events selected by the alternative jet trigger are relevant for the analysis and thus must not be rejected by the applied electron trigger DIS03 under test. However any real trigger has inefficiencies. The efficiency of the electron trigger is defined as the fraction of events that pass the full dijet selection including the jet trigger that also activate the electron trigger:

$$\epsilon_{\text{electron trigger}} = \frac{\mathcal{N}^{\text{jet trigger \&\& electron trigger}}}{\mathcal{N}^{\text{jet trigger}}}. \tag{5.1}$$

In figure 5.1 the measured efficiency is shown as a function of the photon virtuality Q^2_{da}. The efficiency is almost 100% over the whole Q^2 range observed and the data are well described by the LEPTO Monte Carlo predictions. However the trigger efficiency has to be taken with care as on FLT level there is a small overlap between both triggers. The required independence between electron and jet trigger is thus not completely given.

5.2.2 Cuts on the electron candidate

In order to guarantee a pure and efficient reconstruction of the scattered electron and to reject photoproduction events the following cuts are applied to the SINISTRA electron candidate:

- **electron probability:** Events are rejected if no electron candidate with an electron probability of at least 90 % is found by SINISTRA. This requirement

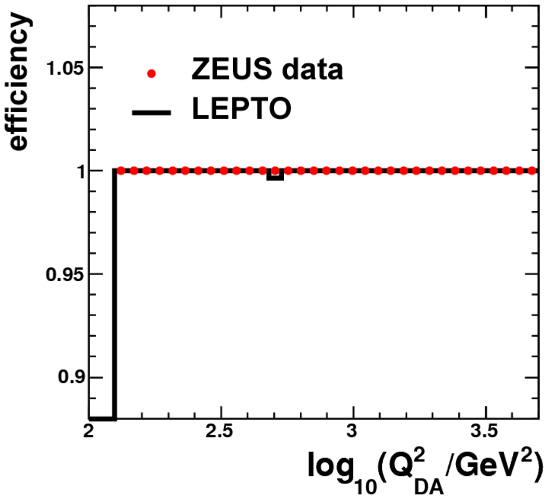

Figure 5.1: Efficiency of the electron trigger as a function of the photon virtuality Q^2 for data (dots) and Monte Carlo (solid line). The efficiency is almost 100 % over the whole Q^2 range observed. The efficiency of the real trigger is well simulated by the LEPTO Monte Carlo.

suppresses background from photoproduction events, in which the scattered electron escapes undetected down the rear beampipe;

- **electron energy:** The energy of the most probable electron candidate has to be greater than 10 GeV. This requirement ensures a high and well understood electron-finding efficiency. Motivated by its good resolution in the respective energy range, the cut is applied to the electron energy reconstructed with the electron method E'_{el} (see chapter 4.3.4);

- **isolation of the electron:** If the total energy not associated to the electron candidate in a cone of 0.7 in the $\eta\phi$ plane around the candidate's direction is larger than 10 % of the candidate's energy, the candidate is rejected and the event is discarded. This condition removes photoproduction and DIS events in which part of a jet is falsely identified as the scattered electron.

5.2.3 Cleaning cuts

After the cuts on the electron candidate the event sample still contains background events such as non-ep events, photoproduction and charged current events where a jet was misidentified as the scattered electron, and events induced by cosmic rays. In order to remove these kind of events the following cleaning cuts are applied to the data and detector-level MC events:

- $\mathbf{z}_{\mathrm{vtx}}$: The event vertex is reconstructed using track information of the CTD. Due to the finite extension of the proton bunches the reconstructed vertex can be shifted with respect to the nominal vertex. For ep events this shift is in the order of some centimetres in z direction. In contrast to this, the z components of beam-gas and beam-wall event vertices are distributed along all the detector's z axis. To reject non-ep events a cut on the z component of the event vertex is applied to the data. An event is rejected if the distance between the measured event vertex and the nominal vertex is larger than 34 cm. This cut also rejects events that are caused by protons inside so called satellites, small packages of protons before or after the nominal proton bunches;

- $\mathbf{E - p_z}$: Due to conservation of energy and momentum the linear combination $E - p_z$ is a conserved quantity. For the initial electron-proton state its value is two times the lepton's energy. As it is a conserved quantity, the measured $E - p_z$ of the final state should be close to 55 GeV as well. This is true for DIS events where the scattered electron is detected in the calorimeter. For non-ep events $E - p_z$ may be higher or lower. For photoproduction events where the electron escapes undetected into the beam pipe the measured value is typically smaller. In this analysis $E - p_z$ is calculated according to

  $$E - p_z = E'(1 - \cos\theta) + \sum_i E_i^{\mathrm{EFO}}(1 - \cos\theta_i^{\mathrm{EFO}}), \tag{5.2}$$

  where i runs over all energy flow objects that are not associated to the electron and E' and θ_e are the energy and the polar angle of the electron candidate. To reject photoproduction, non-ep, and poorly reconstructed events, a cut on $E - p_z$ is applied to the data and to detector-level Monte Carlo events according to 45 GeV $< E - p_z <$ 65 GeV;

- $\mathbf{P_T}$: In the ZEUS reference frame, where the incoming electrons and protons move along the z direction, the transverse momentum of the initial state equals zero. As the momentum is a conserved quantity, the transverse momentum of the final state thus has to be equal to zero for electron-proton induced events. This is not true for beam-related background and events induced by cosmic rays where the transverse momentum of the initial and thus also of the final state is normally not equal to zero. To reject this kind of events a cut on the vector sum over the transverse momenta P_T as measured with the CAL is applied according to $P_T/\mathrm{GeV} < 2.5\sqrt{E_T/\mathrm{GeV}}$, where E_T is the scalar sum over the transverse energies in the CAL. The factor $\sqrt{E_T}$ takes into account the absolute energy resolution of the calorimeter. This cut also rejects charged current events in which a neutrino exists in the final state and thus some missing transverse momentum $P_{T,\mathrm{miss}}$ occurs which leads to a net transverse momentum[2].

---

[2] In this case the net transverse momentum P_T is equal to the missing transverse momentum $P_{T,\mathrm{miss}}$ carried by the neutrino. Both designations are often used simultaneously which might lead

5.2.4 Phase space cuts

The kinematic region of the inclusive NC DIS sample is restricted by two cuts on the photon virtuality, Q^2, and on the scattering angle of the hadronic system, $\cos\gamma_h$. The scattering angle is reconstructed from the hadronic final state according to

$$\cos\gamma_h = \frac{(1-y_{jb})x_{jb}E_p - y_{jb}E_e}{(1-y_{jb})x_{jb}E_p + y_{jb}E_e}, \tag{5.3}$$

where y_{jb} and x_{jb} are the inelasticity and the Bjorken x reconstructed with the Jacquet-Blondel method and E_p, and E_e are the proton and the electron beam energy. Both cuts are applied to the data and to the detector-, hadron-, and parton-level Monte Carlo events. The effect of these cuts on the phase space is shown in figure 5.2.

- **photon virtuality $\mathbf{Q^2}$:** This analysis is performed in the middle and high Q^2 region ($125 < Q^2 < 5000$ GeV^2). In this region, the dependence of the calculated cross sections on the renormalisation scale is supposed to be small, and NLO calculations are expected to be reliable. The upper cut on Q^2 avoids the region where contributions from Z^0 exchange are sizable. Since the resolution of the double angle method is better than the one achieved by the Jacquet-Blondel or the electron method (see section 4.3.4) the cut is applied to Q^2_{da};

- **scattering angle of the hadronic system $\cos\gamma_\mathbf{h}$:** Figure 5.3 shows the distribution of the scattering angle of the hadronic system, $\cos\gamma_h$. The data (dots) are well described by the Monte Carlo detector-level simulation (solid line). However, in the very forward region ($\cos\gamma_h \to 1$) the hadronic system is unlikely to be well reconstructed. In the rear region of the detector ($\cos\gamma_h \to -1$), the agreement between data and Monte Carlo detector level is still good. However there are large differences between Monte Carlo events on detector and on hadron level. In this region, the acceptance is limited by the requirement on the electron energy, leading to large acceptance corrections (see section 7.1.1). To avoid the problematic regions, a cut on the scattering angle of the hadronic system is applied according to $|\cos\gamma_h| < 0.65$. A more detailed motivation for this cut can be found in [96].

After the event selection the inclusive DIS sample contains 141,343 events.

5.3 Comparison between data and Monte Carlo

After all cuts have been applied the data are compared to detector-level Monte Carlo predictions. A good agreement between data and MC is one of two basic requirements for the applicability of the correction procedure used to correct the data for the

---

to confusion. In the following only the notation P_T is used.

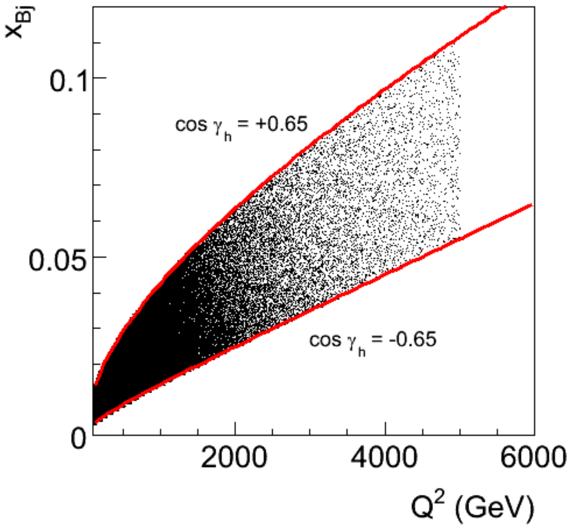

Figure 5.2: Kinematic plane of the DIS sample in the variables x_{Bj} and Q^2. The phase space is restricted by two cuts on the photon virtuality, Q^2, and on the scattering angle of the hadronic system, $\cos\gamma_h$, according to $125 < Q^2 < 5000$ GeV^2 and $|\cos\gamma_h| < 0.65$. The effect of the $\cos\gamma_h$ cut on the phase space is indicated by the solid lines. The point density indicates the relative distribution of selected hadron-level events.

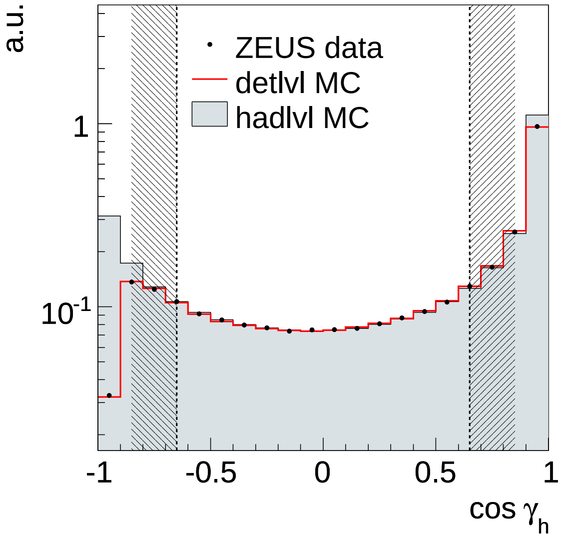

Figure 5.3: Distribution of the scattering angle of the hadronic system $\cos\gamma_h$. The data (dots) are well described by the Monte Carlo detector-level simulation (solid line). However, in the very forward region ($\cos\gamma_h \to 1$) the hadronic system is unlikely to be well reconstructed. In the rear region of the detector ($\cos\gamma_h \to -1$) the acceptance is limited by the cut on the electron energy. In this region the detector-level distribution is far below the hadron-level prediction (filled histogram). To avoid these regions where acceptance corrections are large a cut is applied to γ_h according to $|\cos\gamma_h| < 0.65$. The distributions are normalised such that the area under the distributions in the range $|\cos\gamma_h| < 0.65$ equals one. The cuts are indicated by vertical lines.

limited acceptance of the detector (see section 7.1.1). In this analysis two different sets of neutral current DIS MC event samples, obtained from the ARIADNE and LEPTO event generators, are used. For the MC events all information is available on parton, hadron and detector level. On detector level the reconstruction of the kinematic variables is, just like for the data, based on the detector information about the scattered electron and/or the hadronic final state (see section 4.3). At parton and hadron level all event information, including the four-momentum of the exchanged boson, q, is exactly known. At these levels the kinematic variables and the angle of the hadronic final state, $\cos\gamma_h$, can thus be obtained using the exact theoretical expressions

$$Q^2_{\mathrm{true}} = -q^2 \quad , \quad x_{\mathrm{true}} = \frac{Q^2_{\mathrm{true}}}{2\; p \cdot q} \quad , \quad y_{\mathrm{true}} = \frac{Q^2_{\mathrm{true}}}{s\; x_{\mathrm{true}}}, \tag{5.4}$$

$$(\cos\gamma_h)_{\mathrm{true}} = \frac{(1-y)x_{\mathrm{true}}E_p - y_{\mathrm{true}}E_e}{(1-y)x_{\mathrm{true}}E_p + y_{\mathrm{true}}E_e}, \tag{5.5}$$

where p is the four momentum of the incoming proton, $\sqrt{s}$ is the ep centre of mass energy and E_p and E_e are the proton and electron beam energies. In order to be comparable to the data, MC events are selected in the same kinematic region as the data:

$$125 < Q^2 < 5000 \text{ GeV}^2 \qquad , \qquad |\cos\gamma_h| < 0.65.$$

At parton and hadron level the event selection is restricted to the phase space cuts on the true variables. At detector level the same cuts are applied as for the data.

As described in section 2.1 in ARIADNE the simulation of the QCD cascade is based on the colour dipole model (CDM) while in LEPTO it is based on the parton shower model. However for the inclusive quantities shown in this section the effect of the QCD cascade model should be small and thus no large difference between ARIADNE and LEPTO is expected.

Figure 5.4 shows the distributions of the azimuthal and polar angles of the scattered electron, Θ and Φ, and of the energy of the scattered electron as reconstructed with the electron and the double angle method, E' and $\mathrm{E}'_{\mathrm{da}}$. The data are compared to the detector-level predictions of ARIADNE and LEPTO. The lower part of the plots shows the ratio between data and Monte Carlo prediction. As the energy and the momentum of the scattered electron are later used to boost particles from the laboratory to the Breit reference frame, a good description of the electron quantities is of vital importance. As can be seen in the figure, the electron is well described by the detector-level Monte Carlo predictions. The difference between data and Monte Carlo is typically below 5% and no systematic trend is observed. Only for very small electron energies measured with the electron method and for small azimuthal angles (forward region of the detector) a poor description is found. However, as for the boost from the laboratory to the Breit reference frame the electron energy reconstructed with the double angle method is used, and as for most of the events the electron is found in the rear region of the detector, these deficits can be ignored.

Figure 5.5 shows the distributions of the kinematic variables Q^2_{da}, x_{da}, and y_{da} as reconstructed with the double angle method as well as the distributions of the scattering angle of the hadronic system, $\cos\gamma_h$, the global variable $E - p_z$, and the z component of the reconstructed event vertex, z_{vtx}, after the event selection. As can been seen the data are well described by the detector-level Monte Carlo predictions. The difference between data and Monte Carlo prediction is typically below 5% and no systematic trend is observed. Only for high values of x Bjorken ($x_{da} > 0.09$) and small values of z_{vtx} discrepancies greater than 20% are observed. As only a marginal fraction of the events is found in this regions, these deficits can be ignored. The tails of the $E - p_z$ distribution are also poorly described by the Monte Carlo. Although the reason for this is not yet understood, this effect can be ignored as it again only concerns a marginal fraction of the data set.

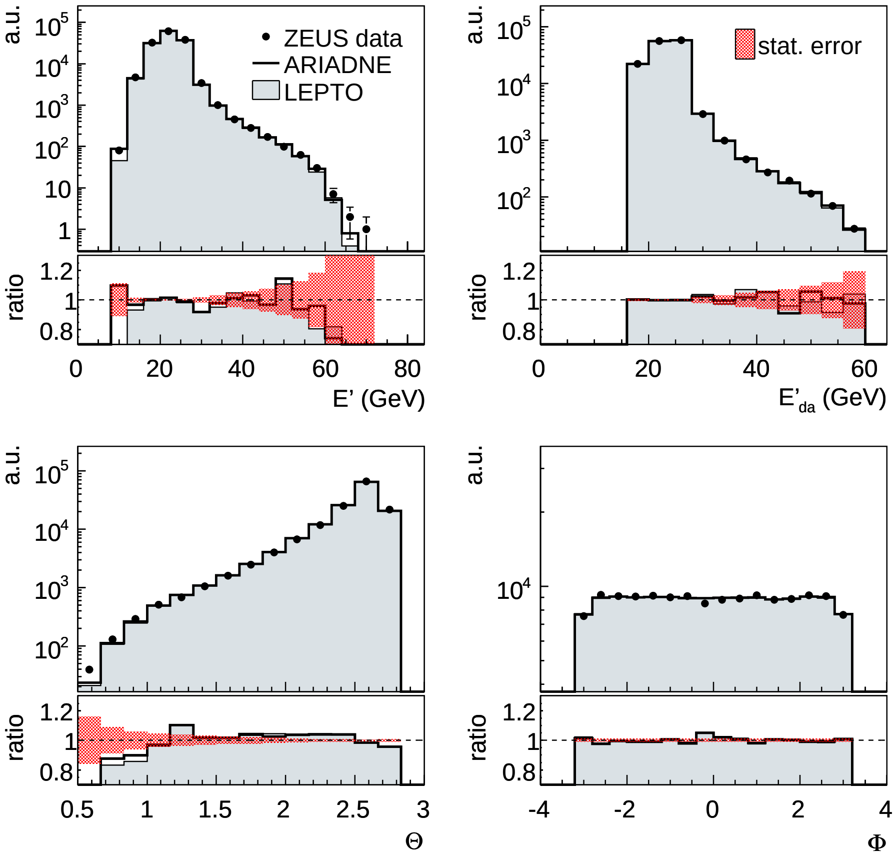

Figure 5.4: Distributions of the electron quantities E', E'_{da}, Θ, and Φ. The data (dots) are compared to the detector-level Monte Carlo predictions as provided by ARIADNE (solid line) and LEPTO (filled histogram). The error bars indicate the statistical error on the data. The distributions are normalised such that the area under the distribution is equal to one (shape-normalised). In the lower part of the plots the ratio between the Monte Carlo predictions and the data is shown. The relative statistical error on the data is indicated by the hatched area. The data are well described by the Monte Carlo predictions. The difference between data and Monte Carlo is typically below 5% and no systematic trend is observed.

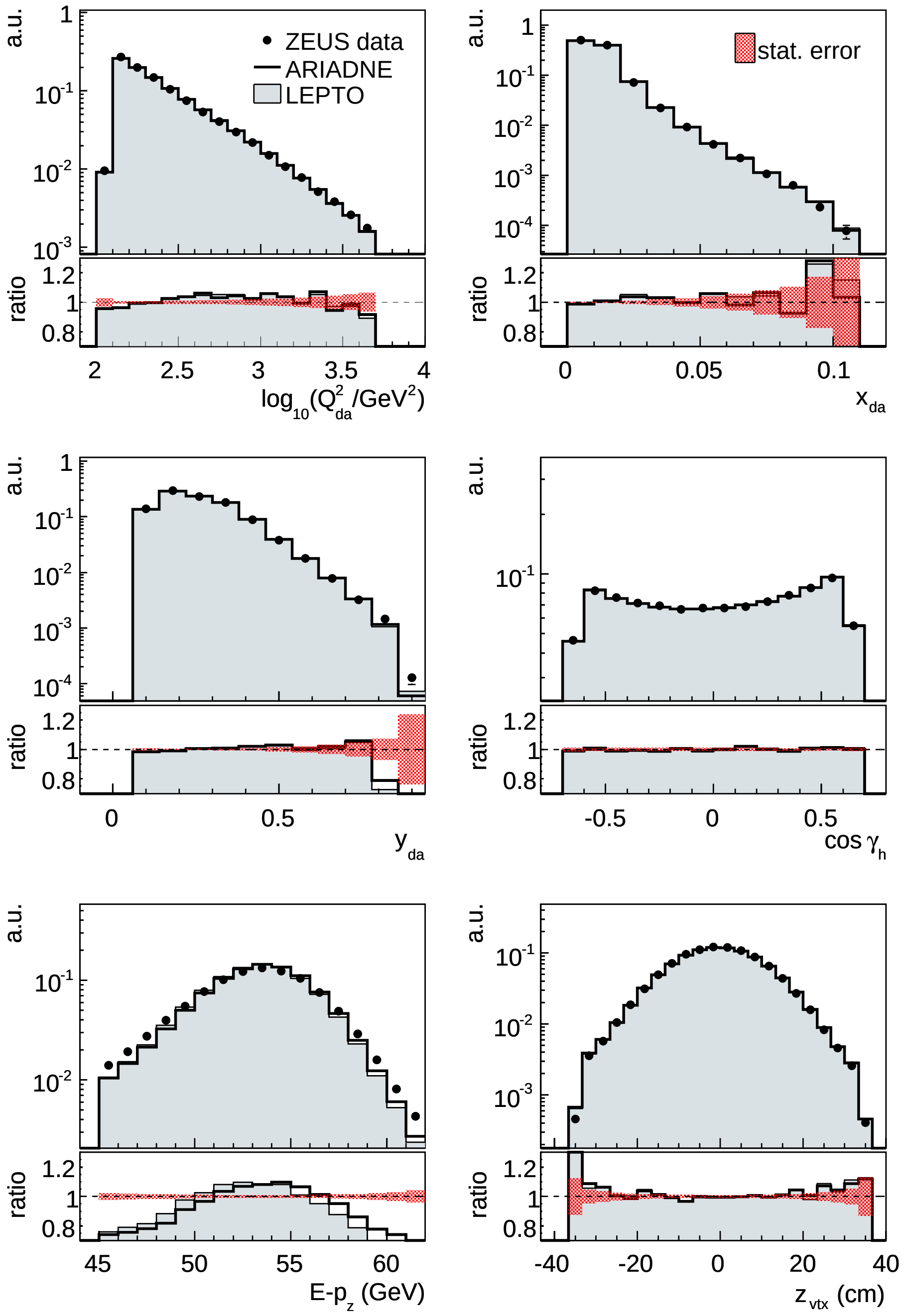

Figure 5.5: Distribution of the variables Q^2_{da}, x_{da}, y_{da}, $\cos\gamma_h$, $E-p_z$, and z_{vtx}. Details as in figure 5.4. For most distributions the data are well described by the detector-level Monte Carlo predictions. The difference between data and Monte Carlo is typically below 5% and no systematic trend is observed. Larger differences are observed for high values of x_{da}, small values of z_{vtx} and at the tails of the $E-p_z$ distribution. As this only effects a marginal fraction of the events, these deficits can be ignored.

Chapter 6

Selection of the dijet sample

6.1 Jet reconstruction

After the selection of the inclusive NC DIS sample (see section 5.2), jets are reconstructed using the k_T cluster algorithm in the longitudinally-invariant inclusive mode (see section 1.4.2). Jets are reconstructed for the selected data sample and for the NC DIS Monte Carlo samples generated with LEPTO and ARIADNE (see chapter 5.3). For the MC samples jets are reconstructed on parton, hadron and detector level. On detector level the jet reconstruction is based on energy flow objects (EFOS) (see section 4.2). All jets are reconstructed in the $\eta - \phi$ plane of the Breit reference frame (see section 1.4.3). The reconstructed jets are boosted back to the laboratory frame. After this, for all jets all information is available in the Breit and in the laboratory reference frame.

6.2 Cuts on jet variables and jet selection

After the jet reconstruction two additional cuts are applied to the inclusive DIS data sample and to the inclusive DIS MC samples on detector level. These cuts reject events where a real photon emitted by the incoming or scattered electron (initial and final state radiation (see section 1.1.2)) fakes a jet [96]:

- **distance between jets and electron candidate:** For every jet with a transverse energy greater than 5 GeV ($E^{\text{jet}}_{T,\text{Breit}} > 5$ GeV) the distance to the most probable electron candidate is calculated according to

  $$d_{\text{jet,e}} = \sqrt{(\eta^{\text{jet}}_{\text{Lab}} - \eta^{\text{e}}_{\text{Lab}})^2 + (\phi^{\text{jet}}_{\text{Lab}} - \phi^{\text{e}}_{\text{Lab}})^2}, \tag{6.1}$$

  where $\eta^{\text{jet}}_{\text{Lab}}$, $\phi^{\text{jet}}_{\text{Lab}}$ and $\eta^{\text{e}}_{\text{Lab}}$, $\phi^{\text{e}}_{\text{Lab}}$ are the pseudorapidities and the azimuthal angles of the jet and the electron, respectively. If the distance is smaller than 1 the event is rejected. This cut ensures a good isolation of the electron. It also suppresses events where a final state radiation photon fakes a jet and removes some photoproduction background;

- **jets in the backward region:** If a jet with an energy greater than 5 GeV ($E_{T,\mathrm{Breit}} > 5$ GeV) is found in the very backward region ($\eta^{\mathrm{jet}}_{\mathrm{Lab}} < -2$) the event is rejected. This cut rejects events where a real photon emitted by the electron is misidentified as a jet in the Breit frame.

For the remaining events jets are only considered for the further analysis if they fulfil the following requirements:

- $E^{\mathrm{jet}}_{T,\mathrm{Lab}} > 3$ GeV: This cut is applied to avoid the presence of low transverse energy jets in the selected sample;
- $\eta^{\mathrm{jet}}_{\mathrm{Lab}} < 2.5$: This cut removes jets in the very forward region of the detector. In this region hadrons that disappear undetected into the beam pipe lead to a bad reconstruction of the jet to which they belong.

These two cleaning cuts are the only ones applied in the laboratory reference frame. They are applied on detector level jets only. The jet phase space is restricted by two cuts on the energy and the pseudorapidity in the Breit reference frame according to:

- $E^{\mathrm{jet}}_{T,\mathrm{Breit}} > 5$ GeV: This cut rejects QPM events where, in the Breit reference frame, no transverse energy occurs in the final state (see 1.4.3);
- $-2 < \eta^{\mathrm{jet}}_{\mathrm{Breit}} < 1.5$.

The phase space cuts are applied to all jets (data and MC) on detector, hadron and parton level.

6.3 Jet energy correction

Due to energy losses into dead detector material measured jet energies are typically underestimated. There are different methods to correct the jet energies. In this analysis a standard procedure based on Monte Carlo samples is utilised. The correction procedure makes use of the detector-level and hadron-level event information. In this analysis the inclusive jet sample (see section 6.2) obtained from the LEPTO inclusive NC DIS sample is used. The jet energy correction is applied to data and detector level MC events and proceeds according to the following steps:

- for each hadron level jet of an event the distance d to every detector level jet of the same event is calculated according to

  $$d = \sqrt{(\eta_{\mathrm{had}} - \eta_{\mathrm{det}})^2 + (\phi_{\mathrm{had}} - \phi_{\mathrm{det}})^2}. \tag{6.2}$$

  The pair with the minimum distance is defined as *matched pair* if the distance is smaller than 0.5;

- for matched pairs the mean transverse detector level jet energy, $E_{T,\mathrm{Breit}}^{\mathrm{jet,det}}$, is plotted as a function of the hadron level jet energy, $E_{T,\mathrm{Breit}}^{\mathrm{jet,had}}$[1]. The resulting distribution shows a linear correlation between $E_{T,\mathrm{Breit}}^{\mathrm{jet,det}}$ and $E_{T,\mathrm{Breit}}^{\mathrm{jet,had}}$ and can thus be fitted by a linear function which is given according to
$$E_{T,\mathrm{Breit}}^{\mathrm{jet,det}} = p_1 \cdot E_{T,\mathrm{Breit}}^{\mathrm{jet,had}} + p_0. \tag{6.3}$$
Since the slope of the distribution is different in different $E_{T,\mathrm{Breit}}^{\mathrm{jet,had}}$-regions, up to three different sets of fit parameters (p_0, p_1) are determined for every distribution;

- after the distribution is fitted and the fit parameters (p_0, p_1) are determined, the corrected jet energy $E_{T,\mathrm{Breit}}^{\mathrm{jet,corr}}$ is obtained by inverting equation 6.3 according to
$$E_{T,\mathrm{Breit}}^{\mathrm{jet,corr}} = \frac{E_{T,\mathrm{Breit}}^{\mathrm{jet,det}} - p_0}{p_1}; \tag{6.4}$$

- the four momenta of the jets are scaled with a correction coefficient which is obtained according to
$$c_{\mathrm{corr}} = \frac{E_{T,\mathrm{Breit}}^{\mathrm{jet,corr}}}{E_{T,\mathrm{Breit}}^{\mathrm{jet,det}}}. \tag{6.5}$$

Since the amount of dead material and thus the amount of energy loss is different in different regions of the detector, the procedure is performed differentially in 18 equidistant bins of η_{Lab}, covering the whole η_{Lab}-range observed ($-2 < \eta_{\mathrm{Lab}} < 2.5$). Matched jets are assigned to an $\eta_{\mathrm{Lab}}^{\mathrm{jet}}$-bin according to the pseudorapidity of the detector level jet. The correction coefficient is determined from jet energies given in the Breit reference frame. Since the results of this analysis depend on a good jet energy reconstruction in the Breit frame this seems to be the natural choice.

Figure 6.1 shows the correlation between the transverse jet energy on hadron and detector level before and after the jet energy correction is applied. Energies are given in the Breit reference frame. The figures display the entire η-range given according to $-2 < \eta_{\mathrm{Lab}}^{\mathrm{jet,det}} < 2.5$.

Figure 6.2 shows the distribution of the mean correction factors $< c_{\mathrm{corr}} >$ as a function of $E_{T,\mathrm{Breit}}^{\mathrm{jet,det}}$ (averaged over all jet pseudorapidity ranges) and as a function of $\eta_{\mathrm{Lab}}^{\mathrm{jet,det}}$ (averaged over all transverse jet energies). The correction is typically below 5 %. The correction is largest in the very forward and backward regions of the detector.

Figure 6.3 shows the distributions of the corrected transverse jet energies and the jet pseudorapidities in the Breit and in the laboratory reference frame. The

---

[1] To be more accurate the mean transverse energy $< E_{T,\mathrm{Breit}}^{\mathrm{jet,det}} >_i$ of all detector level jets, that have a matched hadron level jet in a certain $E_{T,\mathrm{Breit}}^{\mathrm{jet,had}}$-bin, i, is plotted as a function of $E_{T,\mathrm{Breit}}^{\mathrm{jet,had}}$.

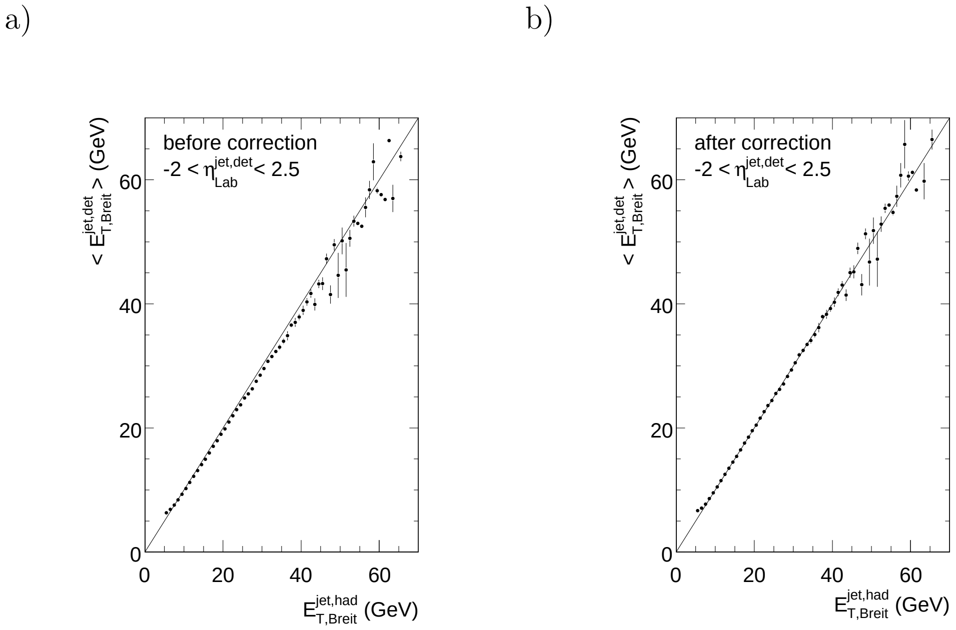

Figure 6.1: Correlation between the transverse jet energy on hadron and detector level a) before and b) after the jet energy correction is applied. Jet energies are given in the Breit reference frame. The correction procedure is performed differentially in 18 different $\eta_{\rm Lab}^{\rm jet,det}$-regions. The figure displays the entire η-range ($-2 < \eta_{\rm Lab}^{\rm jet,det} < 2.5$). The solid line represents the identity ($E_{T,\rm Breit}^{\rm jet,det} = E_{T,\rm Breit}^{\rm jet,had}$).

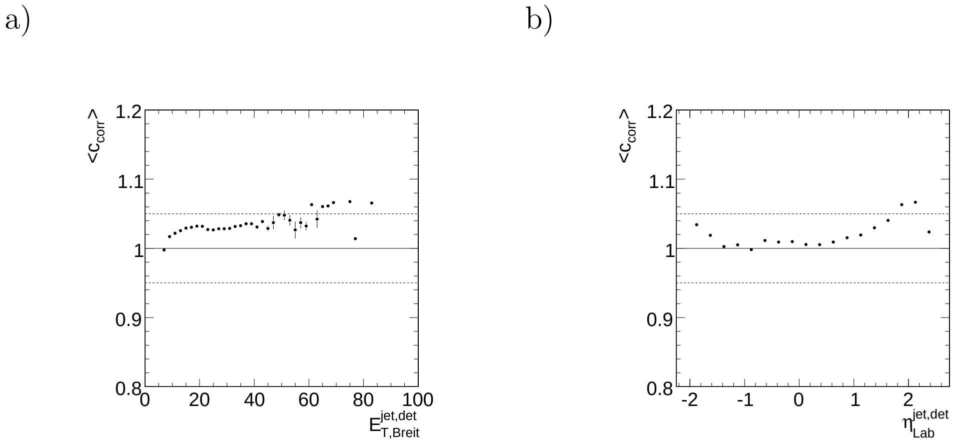

Figure 6.2: Jet energy correction factors, $< c_{\rm corr} >$, as functions of a) $E_{T,\rm Breit}^{\rm jet,det}$ and b) $\eta_{\rm Lab}^{\rm jet,det}$. The correction is typically below $5\ \%$ (indicated by the dashed lines). The correction is largest in the very forward and backward regions of the detector.

c

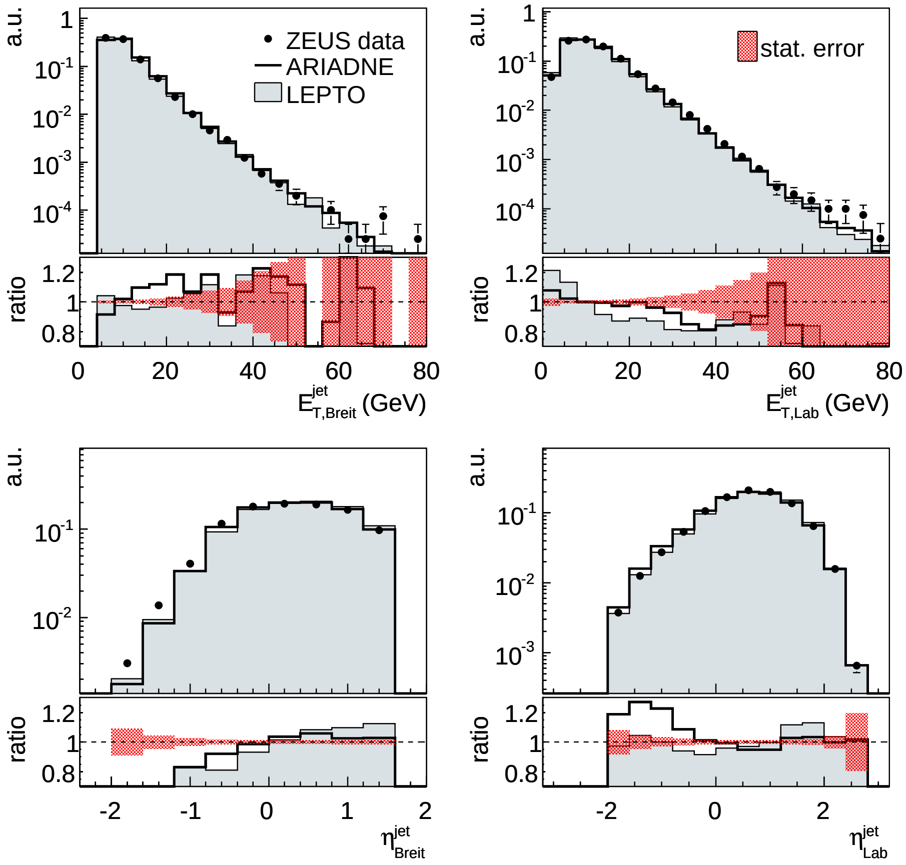

Figure 6.3: Distributions of transverse jet energies (upper row) and jet pseudorapidities (lower row) in the Breit (left column) and laboratory reference frame (right column) after the jet energy correction. The phase space for the jet production is defined according to $125 < Q^2_{da} < 5000$ GeV^2, $|\cos\gamma_h| < 0.65$, $E^{\rm jet}_{T,\rm Breit} > 5$ GeV and $-2 < \eta^{\rm jet}_{\rm Breit} < 1.5$. The data (dots) are compared to the detector-level predictions of the ARIADNE (solid line) and LEPTO (filled histogram) event generators. The error bars indicate the statistical error on the data. The distributions are shape normalised. The lower part of the plots shows the ratio between the MC predictions and the data. The relative statistical error on the data is indicated by the hatched area.

ratio between the MC predictions and the data is shown in the lower part of the figures. As can be seen the data is well described by the predictions of both MC event generators. Exceptions are the highest jet energy regions ($E^{\rm jet}_{T,\rm Lab} > 60$ GeV) and the regions of small $\eta^{\rm jet}_{\rm Breit}$ ($\eta^{\rm jet}_{\rm Breit} < -1$) where the MC underestimates the data. LEPTO gives a slightly better description of the $\eta^{\rm jet}_{\rm Lab}$-distribution than ARIADNE.

6.4 Selection of dijet events

After the jet energy correction is applied, the final dijet event sample is selected from the inclusive NC DIS sample. Events are candidates for the dijet sample if at least two jets with transverse energies greater than 5 GeV ($E_{T,\mathrm{Breit}} > 5$ GeV) are reconstructed in the pseudorapidity range given by $-2 < \eta^{\mathrm{jet}}_{\mathrm{Breit}} < 1.5$. The final selection is based on an asymmetric cut (see section 1.4.4) on the transverse jet energy in the Breit reference frame according to

$$E^{\mathrm{jet1}}_{T,\mathrm{Breit}} > 12 \text{ GeV} \quad \text{and} \quad \mathrm{E}^{\mathrm{jet2}}_{\mathrm{T,Breit}} > 8 \text{ GeV}. \tag{6.6}$$

The cut is applied to data and detector, hadron and parton level Monte Carlo events. After this final selection cut the phase space for the dijet event sample is given according to

The dijet phase space:

$$\begin{array}{rcl} 125 < Q^2 < 5000 \text{ GeV}^2 & , & |\cos\gamma_h| < 0.65, \\ E^{\mathrm{jet1(2)}}_{T,\mathrm{Breit}} > 12(8) \text{ GeV} & , & -2 < \eta^{\mathrm{jet}}_{\mathrm{Breit}} < 1.5. \end{array}$$

After all cuts are applied the dijet sample contains 3,868 events.

6.5 Comparison between data and Monte Carlo

In this section the selected dijet events are compared to the detector level predictions of the LEPTO and ARIADNE event generators.

Figure 6.4 shows the distributions of the transverse energies and pseudorapidities as given in the Breit reference frame for the two highest energetic jets. The jets are ordered in η_{Lab}. The index 1 corresponds to the most forward jet ($\eta^{\mathrm{jet1}}_{\mathrm{Lab}} > \eta^{\mathrm{jet2}}_{\mathrm{Lab}}$). The ratio between the data and the MC predictions is shown in the lower part of the figures. The measured energy and pseudorapidity distributions are well described by the MC predictions. For $\eta^{\mathrm{jet1}}_{\mathrm{Breit}} < -0.5$ LEPTO provides a better description of the pseudorapidity distribution than ARIADNE.

Figures 6.5 and 6.6 show the distributions of Q^2, x_{Bj}, $\overline{E}_T$, M_{jj}, $\eta^{'}$, and ξ and for ξ measured in different regions of Q^2. The ratio between the data and the MC detector-level predictions is shown in the lower part of the plots. The data are well described by the predictions of both event generators. For large values of Q^2 ($Q^2 > 2000$ GeV^2) and for medium and large values of Bjorken x ($x_{Bj} > 0.05$) LEPTO provides a better description of the data than ARIADNE. The LEPTO dijet

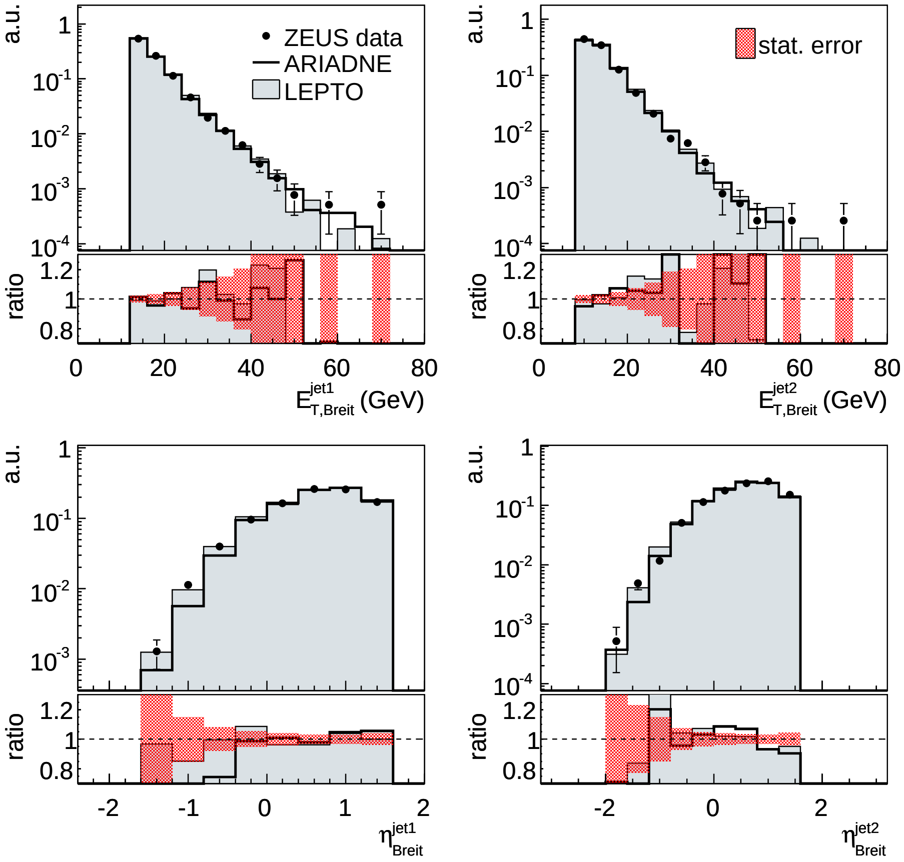

Figure 6.4: Distributions of the transverse jet energies (upper row) and the pseudorapidities (lower row) in the Breit reference frame for the two highest energetic jets in the phase space given by $125 < Q^2 < 5000$ GeV^2, $|\cos\gamma_h| < 0.65$, $E_{T,\mathrm{Breit}}^{\mathrm{jet1(2)}} > 12(8)$ GeV and $-2 < \eta_{\mathrm{Breit}}^{\mathrm{jet}} < 1.5$. The jets are ordered in η_{Lab}. The index 1 corresponds to the most forward jet ($\eta_{\mathrm{Lab}}^{\mathrm{jet1}} > \eta_{\mathrm{Lab}}^{\mathrm{jet2}}$). The data (dots) are compared to the detector-level predictions of the ARIADNE (solid line) and LEPTO (filled histogram) event generators. The statistical error on the data is indicated by the error bars. The distributions are normalised to shape. The lower part of the plots shows the ratio between the MC predictions and the data. The relative statistical error is indicated by the hatched area.

sample is therefore utilised to correct the data for acceptance and QED effects as described in the following chapter.

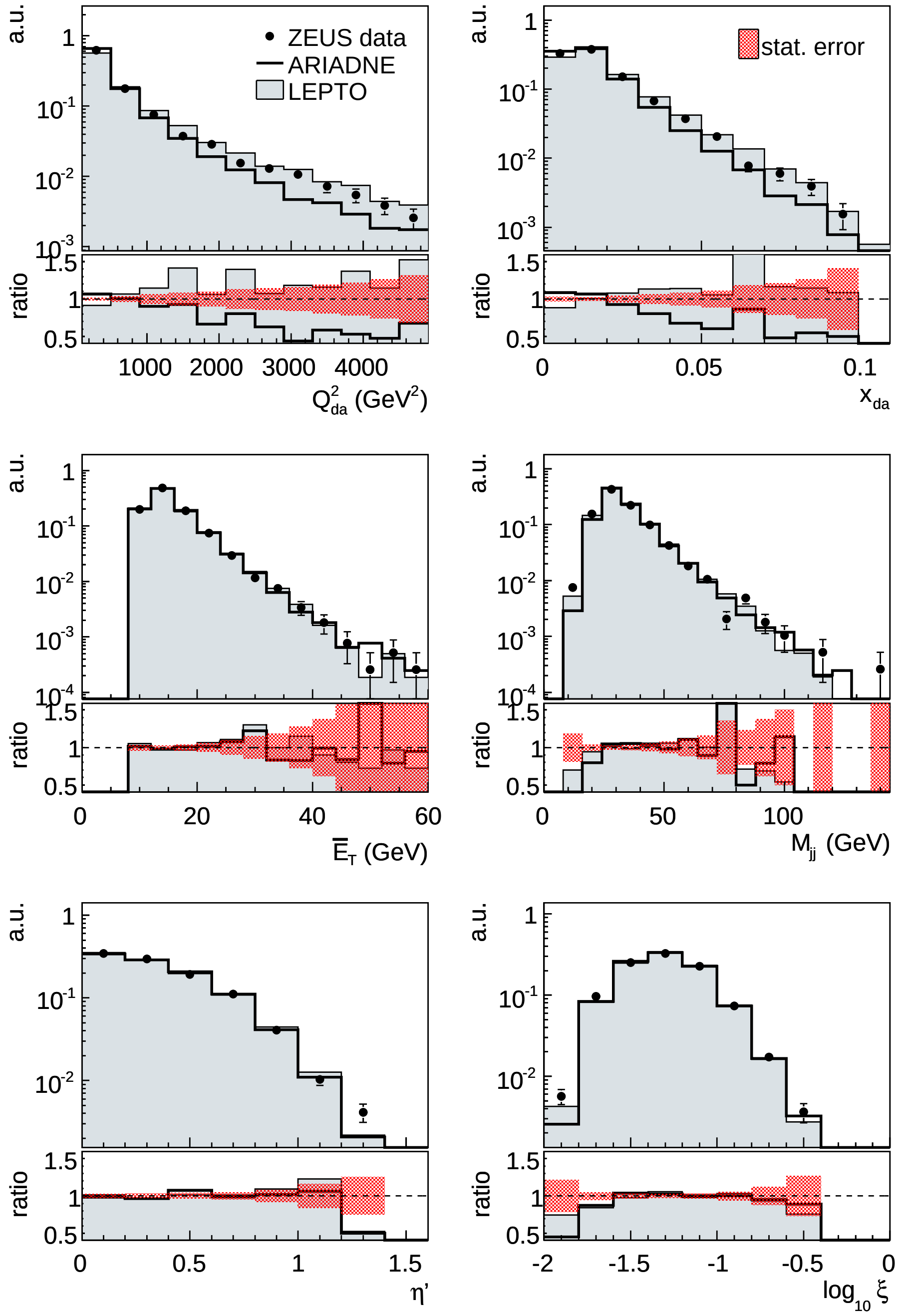

Figure 6.5: Distributions of Q^2, x_{Bj}, $\overline{E}_T$, M_{jj}, η' and ξ for dijet production in the kinematic region defined according to $125 < Q^2 < 5000$ GeV^2, $|\cos\gamma_h| < 0.65$, $E_{T,\mathrm{Breit}}^{\mathrm{jet1(2)}} > 12(8)$ GeV and $-2 < \eta_{\mathrm{Breit}}^{\mathrm{jet}} < 1.5$. The data (dots) are compared to the detector-level predictions of the ARIADNE (solid line) and LEPTO (filled histogram) event generators. The statistical error on the data is indicated by the error bars. The distributions are normalised to shape. The lower part of the plots shows the ratio between the MC predictions and the data. The relative statistical error is indicated by the hatched area.

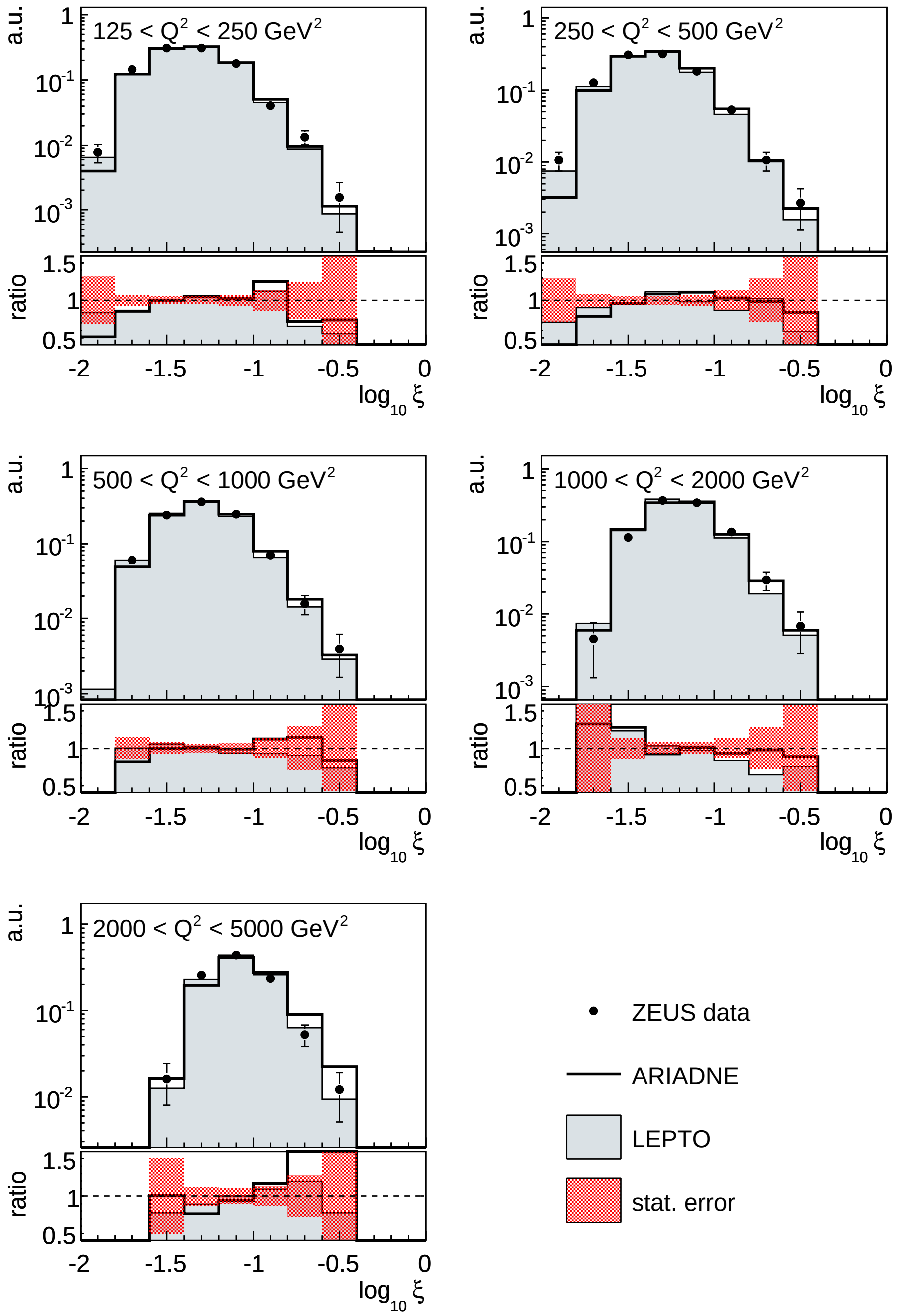

Figure 6.6: Distribution of ξ in different regions of Q^2 for dijet production in the kinematic region defined according to $|\cos\gamma_h| < 0.65$, $E_{T,\mathrm{Breit}}^{\mathrm{jet1(2)}} > 12(8)$ GeV and $-2 < \eta_{\mathrm{Breit}}^{\mathrm{jet}} < 1.5$. Other details as described in the caption to figure 6.5.

Chapter 7

Cross section determination

7.1 Correction of the data

Due to the finite resolution, efficiency and acceptance of the detector, the measured distributions do not reflect the physical truth but the physical truth as 'seen' through the detector. Mathematically the measured distributions can be written as the convolution of the (hadron-level) true distribution with the acceptance-times-resolution distribution of the detector[1]. Thus to determine the distribution on hadron level, the response function of the detector has to be exactly known. It is obtained from MC programs including a full detector simulation. Once the acceptance function of the detector is known, the measured distributions can be corrected to obtain the (hadron level) true information.

In this analysis the bin-by-bin method is utilised to correct the data for the described detector effects. The correction procedure, also referred to as acceptance correction, is described in section 7.1.1. The bin-by-bin method is also used to correct the data for QED effects. The QED correction is necessary to be able to compare the measured distributions, which include QED processes like initial and final state radiation, with the fixed order QCD calculations, not including QED processes. The QED correction is described in section 7.1.2.

7.1.1 Acceptance correction

In this analysis the bin-by-bin method is utilised for the acceptance correction. The method is based on a MC sample containing event and jet information on detector and on hadron level. For every observable and every bin i a multiplicative correction factor, C_i^{acc}, is determined according to

$$C_i^{\mathrm{acc}} = \frac{MC_i^{\mathrm{had}}}{MC_i^{\mathrm{det}}}, \tag{7.1}$$

---

[1] In the following the term 'acceptance' is used as short form for 'acceptance-times-resolution' if not stated differently.

where MC_i^{had} (MC_i^{det}) are the number of hadron (detector) level events in bin i that fulfil the selection criteria. To correct the data, the measured number of events in bin i is multiplied with the respective correction coefficient. This method can be applied only if the following two requirements are fulfilled:

- the data has to be well described by the detector level MC predictions;
- migrations between bins have to be small.

As LEPTO provides a slightly better description of the data than ARIADNE (see section 6.5) in this analysis the LEPTO MC event sample is utilised for the acceptance correction. Before the correction can be applied the binwidths have to be chosen according to the resolutions in the respective intervals. This prevents that migrations and thus correlations between the bins become too large.

Migrations, efficiencies, and purities

As described above, the bin-by-bin correction method can only be applied if migrations and thus correlations between bins on hadron and on detector level are small. Purity $\mathcal{P}$ and efficiency $\mathcal{E}$ of an observable can be used as an indicator for migration effects. They are defined separately for every bin i according to

$$\mathcal{P}_i = \frac{MC_i^{\mathrm{GEN}\wedge\mathrm{REC}}}{MC_i^{\mathrm{REC}}} \quad \text{and} \quad \mathcal{E}_\mathrm{i} = \frac{\mathrm{MC}_\mathrm{i}^{\mathrm{GEN}\wedge\mathrm{REC}}}{\mathrm{MC}_\mathrm{i}^{\mathrm{GEN}}}, \tag{7.2}$$

where MC_i^{GEN} (MC_i^{REC}) is the number of generated (reconstructed) events in bin i and $MC_i^{\mathrm{GEN}\wedge\mathrm{REC}}$ is the number of events that are reconstructed in the same bin they were generated in. In the notation used above the events on hadron (detector) level correspond to generated (reconstructed) events. Every dijet event that is selected either on hadron or on detector level (or on both) is considered for the calculation. The selected events are registered in a two-dimensional migration matrix where the x-axis (y-axis) corresponds to the bins on hadron (detector) level. Every event that is selected on both levels is registered in the respective two-dimensional interval. According to this, the diagonal of the matrix contains those events that are reconstructed in the same bin they were generated in (events that are not migrated). Events that are only selected on hadron (detector) level and can therefore not be assigned to a physical bin on detector (hadron) level are registered in bin 0. To determine the purity (efficiency) the number of entries in a diagonal bin $n_{i,i}$ is divided by the sum of entries in the respective row (column) $N_{\mathrm{row,i}}$ and $N_{\mathrm{col,i}}$

$$\mathcal{P}_i = \frac{n_{i,i}}{N_{\mathrm{row,i}}} \quad \text{and} \quad \mathcal{E}_\mathrm{i} = \frac{\mathrm{n}_\mathrm{i,i}}{\mathrm{N}_\mathrm{col,i}}. \tag{7.3}$$

The errors are given according to

$$\Delta\mathcal{P}_i = \sqrt{\frac{\mathcal{P}_i(1-\mathcal{P}_i)}{N_{\mathrm{row,i}}}} \quad \text{and} \quad \Delta\mathcal{E}_\mathrm{i} = \sqrt{\frac{\mathcal{E}_\mathrm{i}(1-\mathcal{E}_\mathrm{i})}{\mathrm{N}_\mathrm{col,i}}}. \tag{7.4}$$

var.	bin 1	bin 2	bin3	bin 4	bin 5
Q^2(GeV^2)	[125,250[	[250,500[	[500,1000[	[1000,2000[	[2000,5000]
x_{Bj}	[0.0001,0.01[	[0.01,0.02[	[0.02,0.035[	[0.035,0.07[	[0.07,0.1]
$\overline{E}_T$ (GeV)	[10,16[	[16,22[	[22,30[	[30,60]	–
M_{jj} (GeV)	[20,32[	[32,45[	[45,65[	[65,120]	–
η'	[0,0.1[	[0.1,0.25[	[0.25,0.45[	[0.45,0.65[	[0.65,1.6]
$\log_{10}\ \xi$	[-2,-1.5[	[-1.5,-1.35[	[-1.35,-1.1[	[-1.1,-0.85[	[-0.85,-0.5]
$\log_{10}\ \xi$ (Q^2-bin1)	[-2,-1.5[	[-1.5,-1.35[	[-1.35,-1.1[	[-1.1,-0.5]	–
$\log_{10}\ \xi$ (Q^2-bin2)	[-2,-1.5[	[-1.5,-1.3[	[-1.3,-1[	[-1,-0.5]	–
$\log_{10}\ \xi$ (Q^2-bin3)	[-1.9,-1.5[	[-1.5,-1.2[	[-1.2,-0.9[	[-0.9,-0.6]	–
$\log_{10}\ \xi$ (Q^2-bin4)	[-1.7,-1.4[	[-1.4,-1.2[	[-1.2,-1[	[-1,-0.6]	–
$\log_{10}\ \xi$ (Q^2-bin5)	[-1.6,-1.2[	[-1.2,-1[	[-1,-0.6]	–	–

Table 7.1: Definition of the final binning for the observables Q^2, x_{Bj}, $\overline{E}_T$, M_{jj}, η', and ξ and for ξ measured in different regions of Q^2.

The final bin width is chosen in such a way that purities and efficiencies are typically larger than 40 % (see figures 7.3 and 7.4).

Table 7.1 shows the final binning for the observables Q^2, x_{Bj}, $\overline{E}_T$, M_{jj}, η', ξ and for ξ measured in different regions of Q^2. Figures 7.1 and 7.2 show the two-dimensional migration matrices. Purities and efficiencies are shown in figures 7.3 and 7.4.

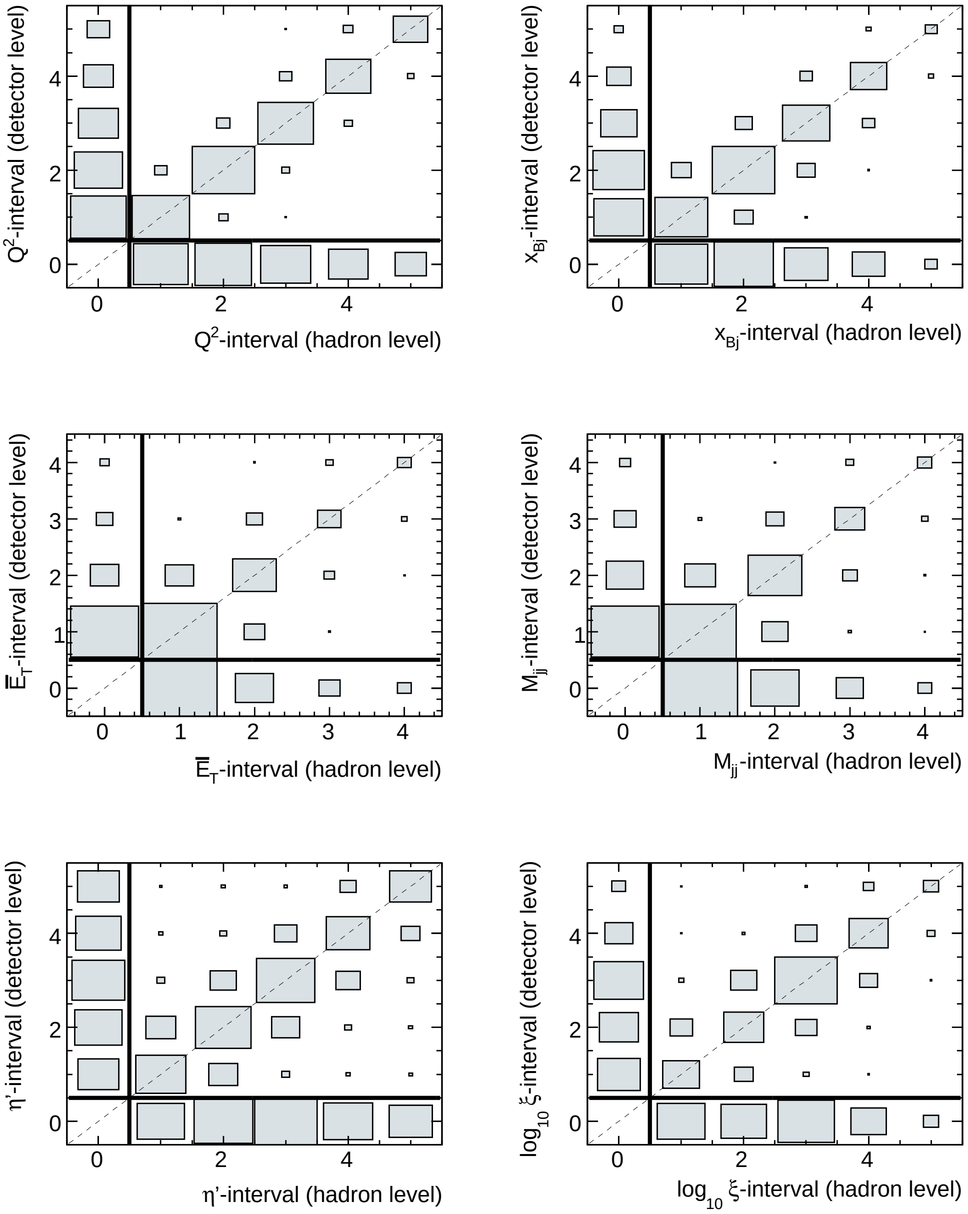

Figure 7.1: Two-dimensional migration matrices for the observables Q^2, x_{Bj}, $\overline{E}_T$, M_{jj}, $\eta^{'}$, and ξ. The numbers on the axes refer to the bins defined in table 7.1. The x-axis (y-axis) indicates intervals given on hadron (detector) level . Events that are reconstructed in the same interval they were generated in (events that did not migrate) are registered in the diagonal (bins along the dashed line). Events that can not be assigned to a physical bin on hadron or detector level are registered in bin zero.

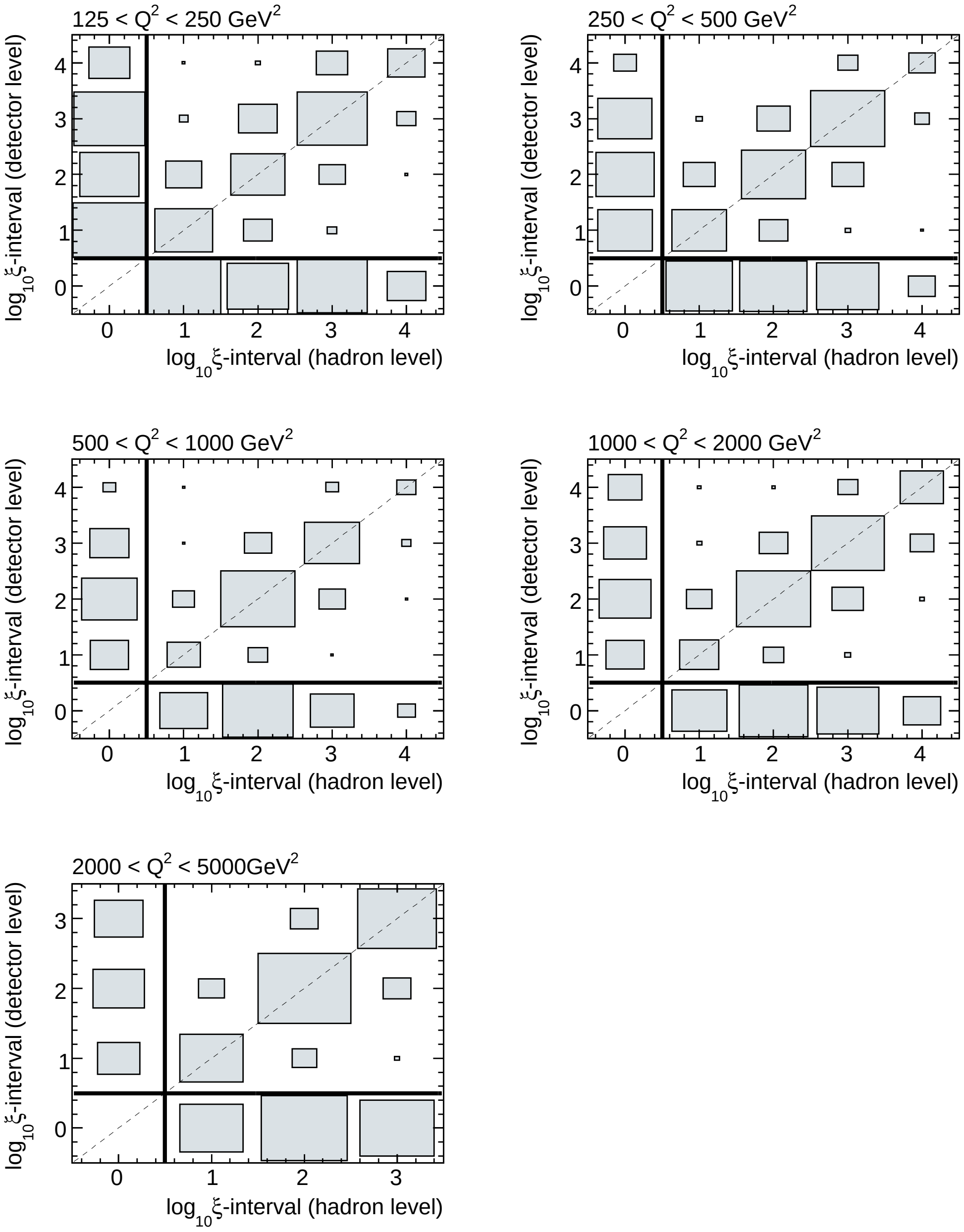

Figure 7.2: Two-dimensional migration matrices for ξ measured in different regions of Q^2. Other details as in the caption to figure 7.1.

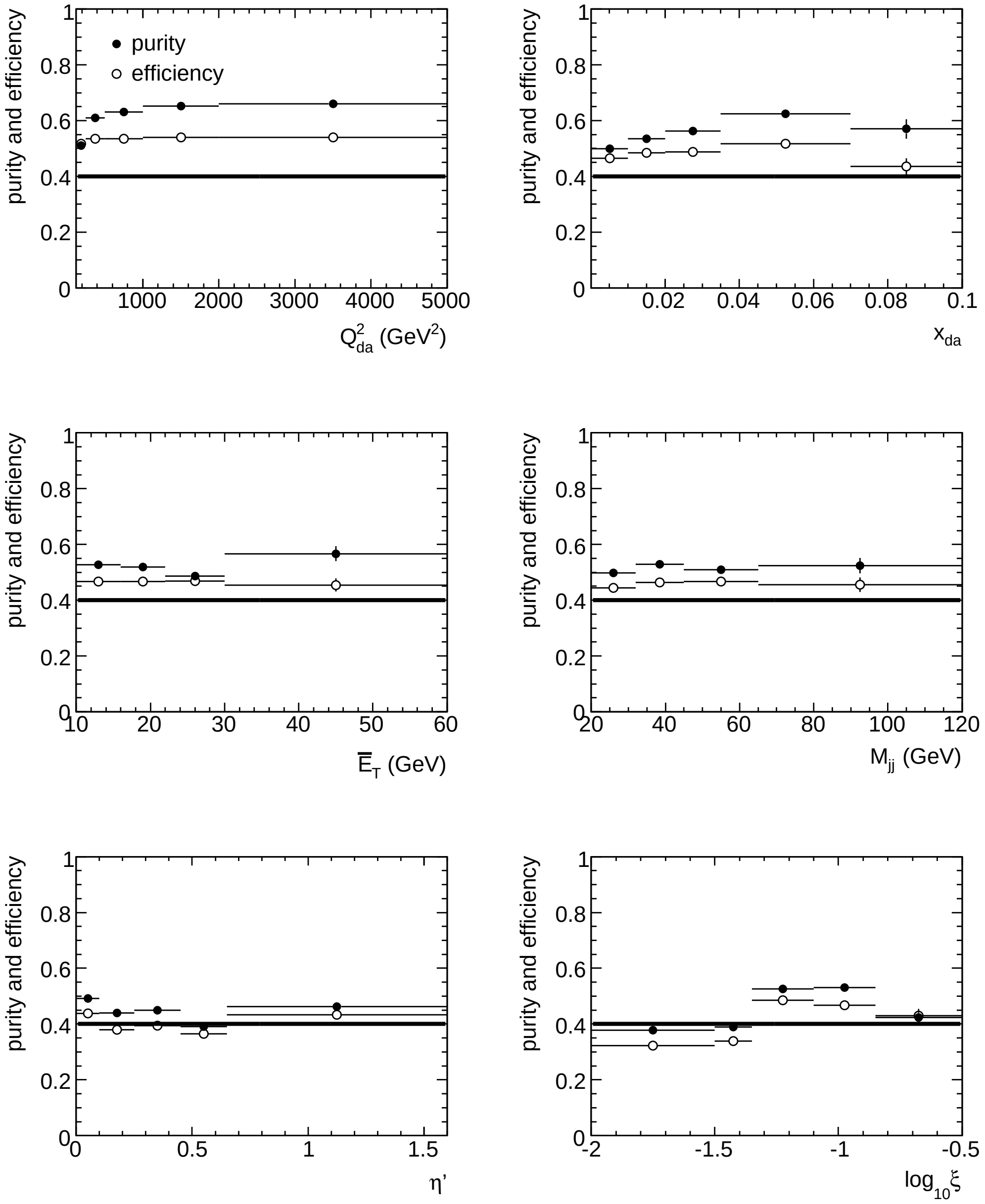

Figure 7.3: Purities (black dots) and efficiencies (open circles) of the observables Q^2, x_{Bj}, $\overline{E}_T$, M_{jj}, η', and ξ. The final bin width is chosen in such a way that purities and efficiencies are typically greater than 40 % (black line).

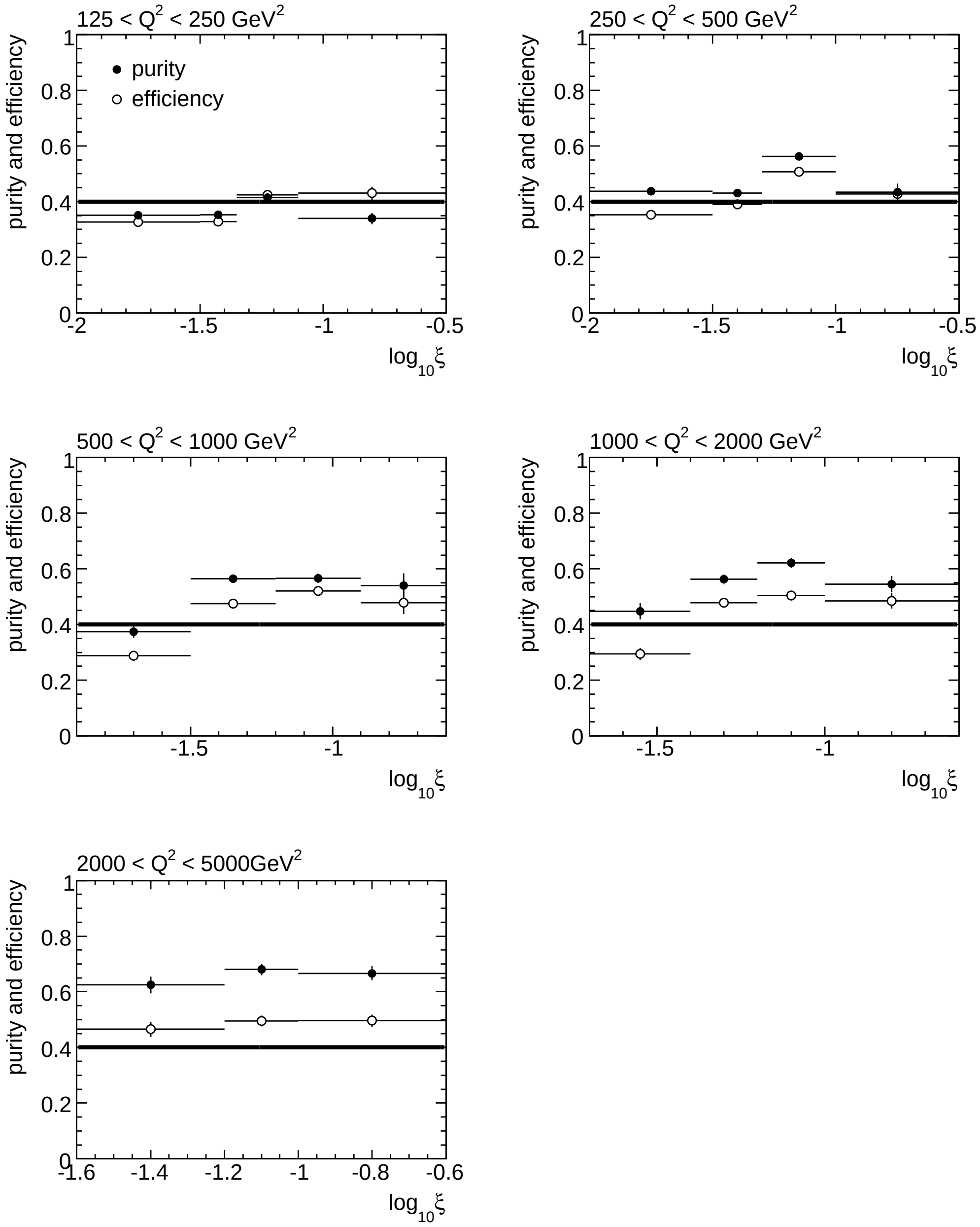

Figure 7.4: Purities (black dots) and efficiencies (open circles) of ξ measured in different regions of Q^2. The final bin width is chosen in such a way that purities and efficiencies are typically greater than 40 % (black line).

Correction coefficients

After the final binwidth is chosen such that migrations between bins are small the correction coefficients can be determined according $C_i^{\mathrm{acc}} = MC_i^{\mathrm{had}}/MC_i^{\mathrm{det}}$ (equation 7.1). Since the number of MC events in a certain bin, i, follows a Poisson distribution the statistical errors of MC_i^{had} and MC_i^{det} are given according to

$$\delta_{\mathrm{stat}}[MC_i^l] = \sqrt{MC_i^l} \quad \text{with} \quad l \in \{\mathrm{had}, \mathrm{det}\}. \tag{7.5}$$

The statistical error of C_i^{acc} arises from error propagation according to

$$\delta_{\mathrm{stat}}\left[C_i^{\mathrm{acc}}\right] = \sqrt{\left(\frac{1}{MC^{\mathrm{det}}} \cdot \delta_{\mathrm{stat}}\left[MC^{\mathrm{had}}\right]\right)^2 + \left(\frac{MC^{\mathrm{had}}}{(MC^{\mathrm{det}})^2} \cdot \delta_{\mathrm{stat}}\left[MC^{\mathrm{det}}\right]\right)^2}. \tag{7.6}$$

As the same MC sample is used on hadron and detector level and thus MC_i^{had} and MC_i^{det} are correlated this corresponds to an upper limit of the true error.

Figure 7.5 and 7.6 show the acceptance corrections obtained from the LEPTO MC sample for the observables Q^2, x_{Bj}, $\overline{E}_T$, M_{jj}, η', and ξ and for ξ in different regions of Q^2. The corrections are typically in the order of $10 - 20$ %. The correction coefficients are typically larger than 1 reflecting the finite acceptance of the detector (typically not all generated particles are detected). Values smaller than 1 mean that more particles are detected than have been generated in the respective bin. The appearance of bins with $C_i^{acc} < 1$ can be explained by migrations (events are detected in a different bin than they were generated in).

7.1.2 QED correction

As written above the measured distributions include QED processes, like initial and final state radiation and virtual corrections, which are not included in the fixed order QCD calculation. In order to be able to compare the measured cross sections to the predictions of the NLO calculation, the data are corrected for QED effects. The correction is based on the bin-by-bin method (described in the previous section) and utilises two different Monte Carlo samples including and not including QED corrections. For every observable and every bin i the multiplicative QED correction coefficient C_i^{QED} is determined according to

$$C_i^{\mathrm{QED}} = \frac{MC_i^0}{MC_i^{\mathrm{QED}}} \cdot f_L, \tag{7.7}$$

where MC_i^{QED} (MC_i^0) is the number of events in bin i that have been selected from the MC sample including (not including) the QED-vertex corrections and f_L corresponds to the ratio between the integrated luminosities of the two Monte Carlo samples.

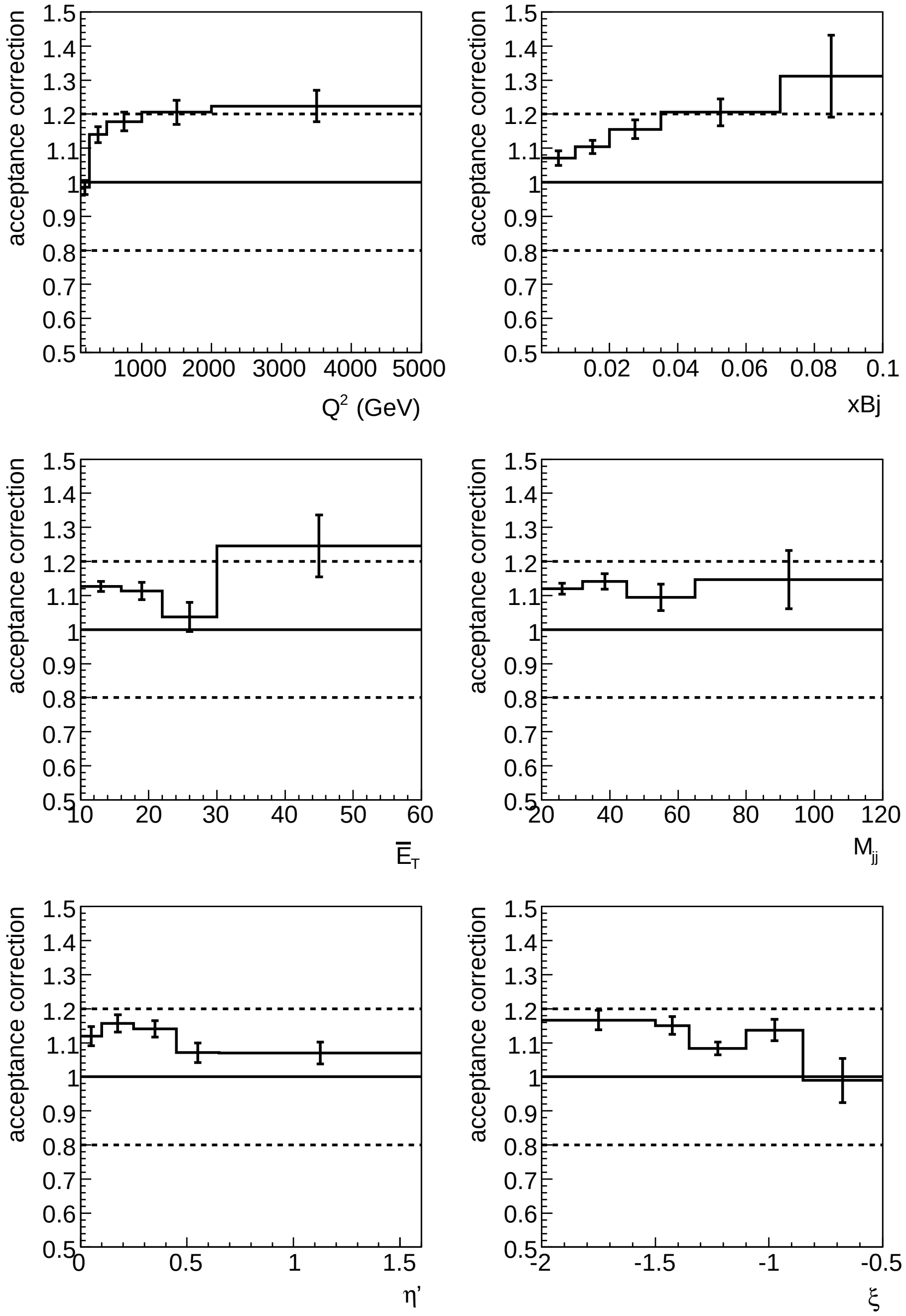

Figure 7.5: Acceptance corrections for the observables Q^2, x_{Bj}, $\overline{E}_T$, M_{jj}, $\eta^{'}$, and ξ. The corrections are typically in the order of $10 - 20$ %. The error bars indicate the statistical errors.

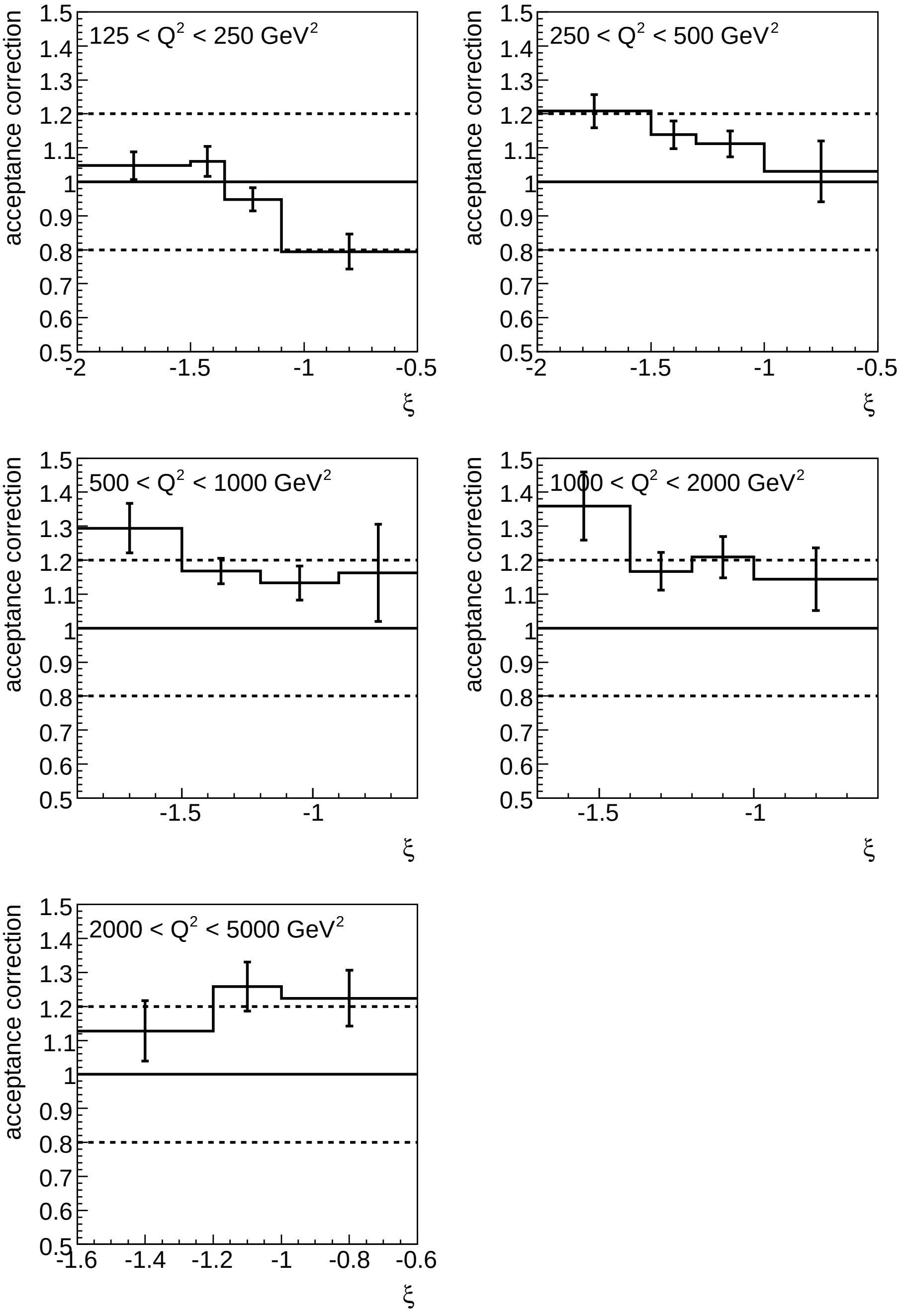

Figure 7.6: Acceptance corrections for ξ in different regions of Q^2. The corrections are typically in the order of $10 - 20$ %. The error bars indicate the statistical errors.

Figures 7.7 and 7.8 show the obtained QED correction factors for the observables Q^2, x_{Bj}, $\overline{E}_T$, M_{jj}, $\eta^{'}$, and ξ and for ξ in different regions of Q^2. The corrections are typically in the order of $5 - 10$ %.

7.2 Cross sections and experimental uncertainties

The cross sections are determined from the measured distributions according to

$$\frac{d\sigma_i}{dx} = \frac{N_i^{data}}{\Delta_i x \cdot \mathcal{L}} \cdot C_i^{acc} \cdot C_i^{QED} \qquad x \in \{Q^2,\ x_{Bj},\ \overline{E}_T,\ M_{jj},\ \eta^{'},\ \xi\} \tag{7.8}$$

where N_i^{data} is the number of measured events in bin i, $\Delta_i x$ is the respective binwidth, $\mathcal{L}$ is the integrated luminosity and C_i^{acc} and C_i^{QED} are the acceptance and QED correction coefficients described in sections 7.1.1 and 7.1.2. Due to the limited statistics available and due to uncertainties related to the experimental environment the measured cross sections contain statistical and systematic errors. A discussion of uncertainties taken into account in this analysis is given in sections 7.2.1 and 7.2.2.

7.2.1 Statistical uncertainties

Due to the limited statistics available, both in data and MC, the measured cross sections contain statistical errors. There are three sources of statistical uncertainties propagating into the final results: the statistical error on the data ($\delta_{stat}[N^{data}]$) and the statistical errors on the acceptance and QED correction coefficients ($\delta_{stat}[C_i^{acc}]$ and $\delta_{stat}[C_i^{QED}]$). Since the number of events in a certain bin follows a Poisson distribution the statistical error of N^{data} is given according to $\delta_{stat}[N^{data}] = \sqrt{N^{data}}$. The statistical error of C_i^{acc} is given according to equation 7.6 (see section 7.1.1). Due to the large number of MC events used to determine the QED corrections the statistical error on C_i^{QED} can be neglected. The statistical error on the cross section arises from error propagation according to

$$\delta_{stat}[\sigma] = \sqrt{\left(\frac{\partial\sigma}{\partial N^{data}}\delta_{stat}[N^{data}]\right)^2 + \left(\frac{\partial\sigma}{\partial C^{acc}}\delta_{stat}[C^{acc}]\right)^2}, \tag{7.9}$$

where $\sigma := d\sigma_i/dx$ has been used and the errors on the luminosity and on the binwidth are neglected.

7.2.2 Systematic uncertainties

As described in section 7.1.1 the data are corrected for detector effects using a method based on MC models that are utilised to obtain (simulate) the response function of the detector. However, some of the detector characteristics (like the absolute energy scale

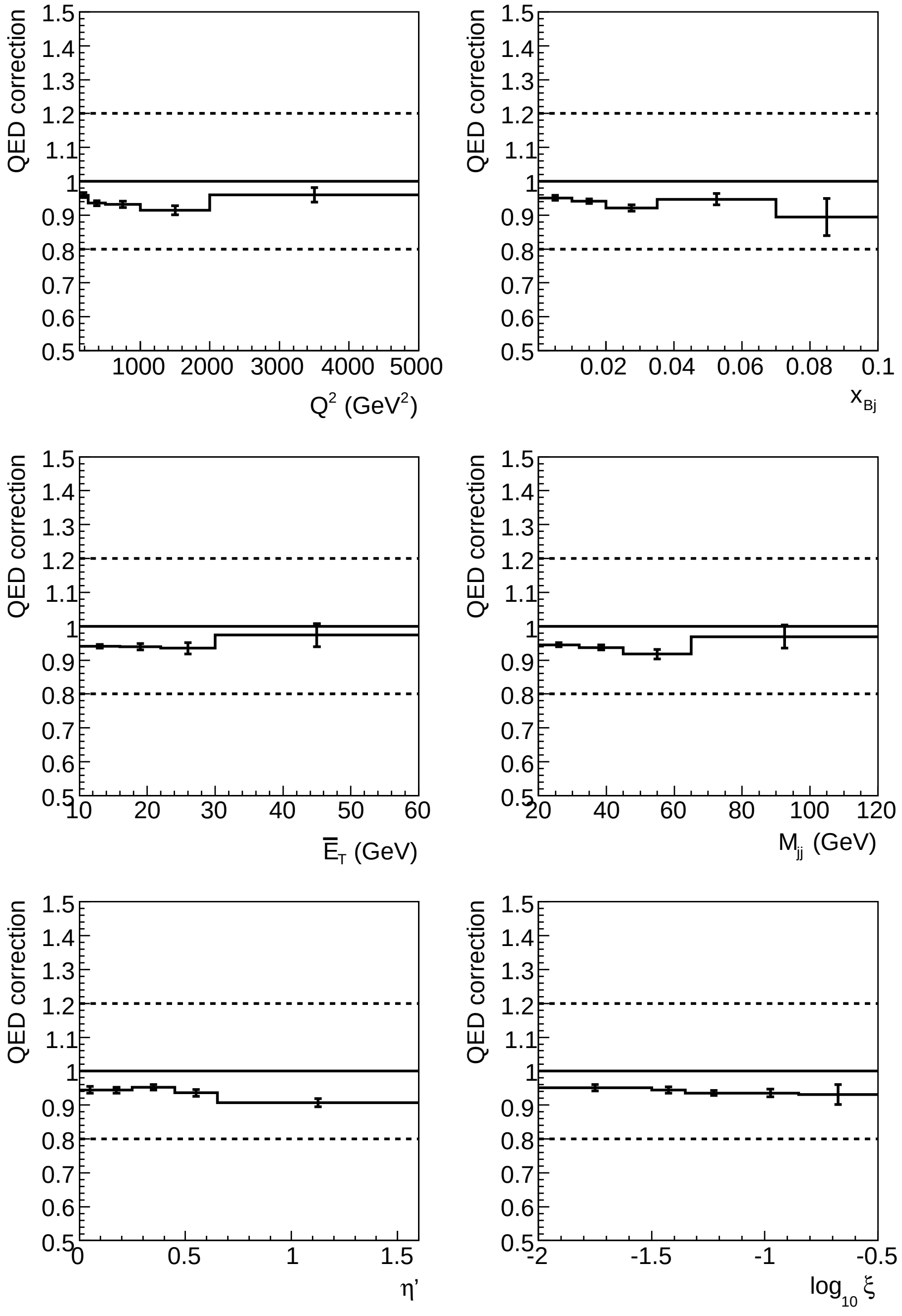

Figure 7.7: QED correction factors for the observables Q^2, x_{Bj}, $\overline{E}_T$, M_{jj}, $\eta^{'}$, and ξ. The corrections are typically in the order of $5-10$ %. Due to the large statistics of the MC samples used to obtain the correction coefficients, statistical errors cen be neglected.

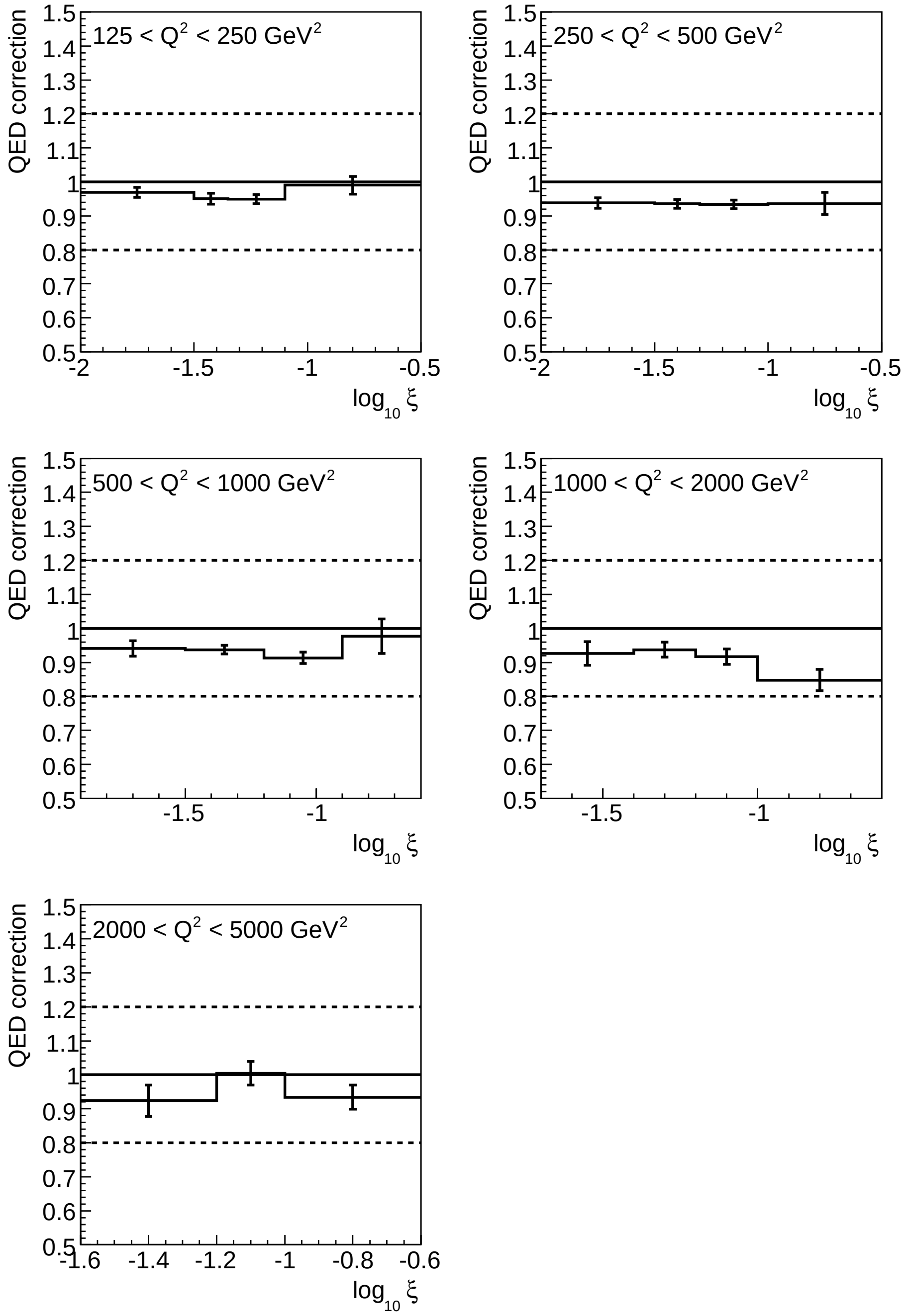

Figure 7.8: QED correction factors for ξ in different regions of Q^2. The corrections are typically in the order of $5 - 10$ %. Due to the large statistics of the MC samples used to obtain the correction coefficients, statistical errors cen be neglected.

for electrons and jets) are only known and modelled within a certain precision. One way to estimate the related uncertainties on the measured cross sections is to vary the respective variables within their uncertainty ranges. The variation is typically only applied to the MC detector-level events.

Due to the MC-based acceptance correction the measured cross sections depend on the models which are used to simulate the parton cascades and the hadronisation processes. The uncertainty due to the model dependency is usually taken to be the difference in the cross sections when correcting the data using a different MC sample (including different models).

The uncertainty related to the choice of the applied electron reconstruction procedure is estimated in a similar way by repeating the analysis using an alternative electron reconstruction algorithm.

Another source of uncertainty is related to the selection cuts applied on detector level. These cuts are applied in order to suppress background processes and to avoid regions in which a reasonable particle reconstruction is not guaranteed or regions in which the MC does not provide a reasonable description of the data. The choice of the exact cut value is, however, a little arbitrary and the final result should not depend on the exact value. This demand is fulfilled as long as physical correlations are well simulated by the MC event generators . In this case a change in the value of a detector level cut will change the number of measured events, but this change will be compensated by a contrary change in the applied acceptance correction. A way to check the independence of the final results from the exact cut values is to vary the cuts (typically within their uncertainty range) and to study the effect on the measured cross sections.

In the following a list of all sources of systematic uncertainties taken into account in this analysis is given:

- the uncertainty on the measured cross sections related to that on the absolute jet energy scale is estimate by varying the jet energy within the jet energy scale uncertainty range. For energies larger than 10 GeV ($E_{T,Lab}^{jet} > 10$ GeV) the jet energy is varied by ±1 %, for smaller energies ($E_{T,Lab}^{jet} < 10$ GeV) by ±3 % (uncertainties are taken from [97–99]). In order to simulate a possible shift in the absolute jet energy scale between data and MC, the variation is only applied to the MC detector-level jets. The resulting uncertainty on the cross section is typically in the order of ±5 %. It increases to about ±10 % for certain regions of the dijet phase space;

- the uncertainty on the measurement due to that on the absolute energy scale of the electron candidate is estimated by varying the electron energy within the uncertainty range of the absolute electron energy scale (±1% [100]). In order to simulate a possible shift in the absolute energy scale between data and MC, the variation is only applied to the MC detector-level events. The resulting uncertainty on the dijet cross sections is typically below ±1 %;

- the uncertainty on the measurement due to that on the longitudinal component of the absolute energy scale for both hadrons and electrons is estimated by raising and lowering $E - p_z$ (see Eq. 5.2) by ±3%. The variation is applied only to the MC detector-level events in order to simulate a possible shift between data and MC. The resulting uncertainty on the dijet cross sections is typically below ±1 %;

- to estimate the uncertainty related to the MC-based acceptance correction and the resulting dependence on the choice of the phenomenological model used to simulate the parton cascade, the analysis is repeated using correction coefficients obtained from ARIADNE instead the (default) ones obtained from LEPTO. The difference in the cross sections is typically below ±8 %;

- to estimate the uncertainty on the cross sections related to the choice of the applied electron reconstruction algorithm the analysis is repeated using the EM electron finder instead of the default SINISTRA algorithm (see section 4.1). The resulting uncertainty on the measured cross sections is typically below ±3 %;

- the η_{Lab}^{jet} cut used to suppress the contamination due to photons falsely misidentified as jets in the Breit frame is lowered (raised), both for data and detector-level MC-events, from -2 to -3 (-1.5). The resulting uncertainty on the measured cross sections is typically below ±1 %;

- the $E_{T,Lab}^{jet}$ cut is raised from 3 to 4.5 GeV. The change is applied to data and detector-level MC-events. The resulting uncertainty is typically smaller than ±1 %;

- the $\mathbf{z_{vtx}}$ cut is changed from 34 cm to 30 cm, both for data and detector-level MC-events. The effect on the measured cross sections is typically smaller than ±2 %;

The systematic uncertainties not associated with the absolute energy scale of the jets were added in quadrature to the statistical error in order to determine the total experimental uncertainty, δ_{exp}. In addition there is an overal normalisation uncertainty of 2.2 % from the luminosity determination.

Chapter 8

Results

In this chapter the measured dijet cross sections are presented. Single-differential dijet cross sections have been measured as functions of Q^2, x_{Bj}, $\overline{E}_T$, M_{jj}, $\eta^{'}$ and ξ. The cross sections as function of ξ have also been measured double-differentially in different regions of Q^2. The cross sections have been measured in the phase-space region defined according to $125 < Q^2 < 5000\ \mathrm{GeV}^2$ and $|\cos\gamma_h| < 0.65$. Jets have been reconstructed with the k_T cluster algorithm in the Breit reference frame. Events have been taken into account for the measurement if at least two hadronic jets with $E^{\mathrm{jet1(2)}}_{T,\mathrm{Breit}} > 12(8)$ GeV have been reconstructed for the respective event in the pseudorapidity range given according to $-2 < \eta^{\mathrm{jet}}_{\mathrm{Breit}} < 1.5$. The data have been corrected for detector and QED effects as described in section 7.1.1 and 7.1.2. The obtained cross sections are compared to the predictions of a fixed order QCD calculation of the order of $\mathcal{O}(\alpha_s^2)$, which for the observed dijet processes is the next to leading order. The QCD calculations have been performed with DISENT. In order to be comparable to the measured cross sections the calculated parton level cross sections have been corrected to hadron level as described in section 2.2.1.

The single-differential cross sections measured as functions of Q^2 and x_{Bj} and as functions of $\overline{E}_T$, M_{jj}, $\eta^{'}$ and ξ are shown in figures 8.1 and 8.2. The double-differential cross sections as functions of ξ measured in different regions of Q^2 are shown in figure 8.3. The cross sections are also given in tables 8.1 to 8.7. They are compared to the predictions of the NLO calculation performed with $\mu_R^2 = Q^2 + \overline{E}_T^2$. NLO cross sections calculated with $\mu_R^2 = Q^2$ and $\mu_R^2 = \overline{E}_T^2$ are also shown[1]. The relative differences to the NLO cross sections calculated with $\mu_R^2 = Q^2 + \overline{E}_T^2$ are shown in the lower part of figures 8.1 and 8.2 and in figure 8.4. The displayed differences are determined according to

$$\Delta \;=\; \frac{\sigma - \sigma_{\mathrm{NLO}}}{\sigma_{\mathrm{NLO}}} \quad \text{with} \quad \sigma \in \{\sigma_{\mathrm{data}}, \sigma_{\mathrm{NLO}}^{\mu_{\mathrm{R}}^2=\mathrm{Q}^2}, \sigma_{\mathrm{NLO}}^{\mu_{\mathrm{R}}^2=\overline{\mathrm{E}}_{\mathrm{T}}^2}\}, \tag{8.1}$$

---

[1] If not stated differently here and in the following the term 'NLO calculation' is used for the calculation performed with $\mu_R^2 = Q^2 + \overline{E}_T^2$.

where σ_{data} are the measured cross sections and σ_{NLO}, $\sigma_{\text{NLO}}^{\mu_R^2=Q^2}$, $\sigma_{\text{NLO}}^{\mu_R^2=\overline{E}_T^2}$ are the theoretical predictions obtained with $\mu_R^2 = Q^2 + \overline{E}_T^2$, $\mu_R^2 = Q^2$ and $\mu_R^2 = \overline{E}_T^2$. In all the figures each data point is plotted at the abscissa at which the differential cross section is equal to its bin-averaged value[2].

For a quantitative comparison the deviation between measured and calculated cross section is also calculated in multiples of the total error, δ_{tot},

$$\chi = \frac{\sigma_{\text{data}} - \sigma_{\text{NLO}}}{\delta_{\text{tot}}} \quad \text{with} \quad \delta_{\text{tot}} = \delta_{\text{exp}} + \delta_{\text{theo}} \tag{8.2}$$

where δ_{exp} and δ_{theo} are the experimental and the theoretical uncertainties as defined in sections 7.2.2 and 2.2.2. The deviation between data and NLO is called significant if $\chi > 1$ or in other words $(\sigma_{\text{data}} - \sigma_{\text{NLO}}) > (\delta_{\text{exp}} + \delta_{\text{theo}})$. A detailed description of the single- and double-differential cross sections is given in the following sections.

8.1 Single-differential cross sections

8.1.1 Dijet cross section as function of Q^2

The differential dijet cross section as a function of Q^2 exhibits a fall-off of more than two orders of magnitude within the range studied ($125 < Q^2 < 5000$ GeV^2). The data is well described by the NLO calculation over the whole range observed. The deviation in multiples of the total error, χ, varies between -0.35 and 0.88 and is largest in the highest Q^2 bin where the NLO calculation underestimates the data. For $125 < Q^2 < 2000$ GeV the theoretical error, δ_{theo}, is larger than the experimental error by a factor $3.1 < \delta_{\text{theo}}/\delta_{\text{exp}} < 1.6$. For larger values of Q^2 and thus higher values of the renormalisation scale the theoretical uncertainty decreases and the experimental error becomes the dominant source of uncertainty. In this region the statistical error is of the same order as the systematic uncertainty. Since the mean dijet energy $\overline{E}_T$ is typically below ≈ 60 GeV, the default renormalisation scale $\mu_R^2 = Q^2 + \overline{E}_T^2$ is, in most regions, dominated by the Q^2 contribution. According to this no larger difference is observed between the NLO calculations performed with $\mu_R^2 = Q^2 + \overline{E}_T^2$ and $\mu_R^2 = Q^2$. In contrast to this the calculation performed with $\mu_R^2 = \overline{E}_T^2$ systematically lies above the default NLO predictions and, in all but the highest Q^2 bins, overshoots the data.

8.1.2 Dijet cross section as function of x_{Bj}

The differential dijet cross section as function of Bjorken x exhibits a fall-off of about two orders of magnitudes within the range studied ($0.0001 < x_{Bj} < 0.1$). The decrease

---

[2] In order to be able to determine the intersection between the bin-averaged value and the continuous differential cross section the NLO calculation is repeated with a fine binning to approximate the continuous distribution.

of $d\sigma/dx_{Bj}$ with increasing x_{Bj} reflects the decrease in the parton density functions of the proton towards large values of Bjorken x. The measured cross sections are well described by the NLO calculation. The only exception is the largest x_{Bj} bin where the NLO calculation underestimates the data by almost 40 %. Due to the large systematic and statistical uncertainties in this region ($\delta_{\rm stat} \approx \delta_{\rm syst} \approx 20$ %) the deviation between data and NLO is still smaller than the total uncertainty. Over the whole range observed the deviation between data and NLO in multiples of the total uncertainty varies inbetween $-0.49 < \chi < 0.9$. Within the range $0.0001 < x_{Bj} < 0.07$ the theoretical error exceeds the experimental uncertainty by a factor of $1.5 < \delta_{\rm theo}/\delta_{\rm exp} < 3.7$. For larger values of x_{Bj} the experimental error becomes the dominant source of uncertainty ($\delta_{\rm theo}/\delta_{\rm exp} = 0.42$). Both the relative statistical and the sysytematic uncertainty increase from about 3 % in the low x_{Bj} region to more than 20 % in the highest x_{Bj} bin.

8.1.3 Dijet cross section as function of $\overline{E}_T$

The differential cross section as a function of the mean transverse jet energy $\overline{E}_T$ shows a fall-off of more than two orders of magnitude. Jets are accessible within the energy range $10 < \overline{E}_T < 60$ GeV. The data are well described by the NLO calculation over the whole range observed. The deviation between data and NLO is always smaller than the sum of the experimental and theoretical errors ($-0.67 < \chi < 0.72$). For the smallest mean jet energies ($10 < \overline{E}_T < 16$ GeV) the error is dominated by the theoretical uncertainty ($\delta_{\rm theo}/\delta_{\rm exp} = 5.31$). For larger energies ($16 < \overline{E}_T < 30$ GeV) all uncertainties are of the same order. In the highest $\overline{E}_T$ bin the uncertainty is dominated by the experimental error ($\delta_{\rm theo}/\delta_{\rm exp} = 0.19$). The relative uncertainty related to that on the jet energy scale is about 5 % over the whole range studied. For $\overline{E}_T \gtrsim 20$ GeV the differences between the NLO calculations, calculated with the different scales, can be neglected. For smaller energies the cross section calculated with $\mu_R^2 = \overline{E}_T^2$ is larger than the other NLO cross sections and overshoots the data.

8.1.4 Dijet cross section as function of M_{jj}

The differential dijet cross section as function of the the invariant dijet mass, M_{jj}, is in many aspects similar to the cross section measured as function of $\overline{E}_T$. Just like $d\sigma/d\overline{E}_T$, $d\sigma/dM_{jj}$ shows a fall-off of more than two orders of magnitudes within the range studied. The accessible dijet mass lies within $20 - 120$ GeV. The NLO calculation provides a very good description of the data over the whole range observed. The deviation in multiples of the total uncertainty is always smaller than 0.2 ($-0.18 < \chi < 0.12$). In the lowest M_{jj} region the total error is dominated by the theoretical uncertainty ($\delta_{\rm theo}/\delta_{\rm exp} = 5.6$) , whereas for the highest M_{jj} region the experimental error is the largest source of uncertainty ($\delta_{\rm theo}/\delta_{\rm exp} = 0.37$). The relative uncertainty related to that on the jet energy scale is about 5 % over the whole range observed. For $M_{jj} \gtrsim 50$ GeV almost no difference occurs between the NLO calculations performed with different renormalisation scales. For smaller dijet masses the cross sections calculated with $\mu_R^2 = \overline{E}_T^2$ are larger than the cross sections calculated with $\mu_R^2 = Q^2$ and $\mu_R^2 = Q^2 + \overline{E}_T^2$ and overshoot the data.

8.1.5 Dijet cross section as function of η'

The differential dijet cross section as function of η' exhibits a plateau in the low-η' region ($0 < \eta < 0.25$) followed by an increasing fall-off of more than one order of magnitude in the medium -and high-η' region ($0.25 < \eta' < 1.6$). The data is very well described by the NLO calculation over the whole range observed. The deviation between data and NLO in multiples of the total unvertainty is always smaller than 0.6 ($-0.53 < \chi < 0.19$). The theoretical error is the dominant source of uncertainty over the whole η' range and exceeds the experimental uncertainty by a factor of up to 3 ($1.4 < \delta_{\text{theo}}/\delta_{rmexp} < 3$). The relative uncertainty related to that on the jet energy scale is typically ≈ 5 %. The NLO cross sections calculated with $\mu_R^2 = \overline{E}_T^2$ exceed those calculated with $\mu_R^2 = Q^2 + \overline{E}_T^2$ by about 10 % and overshoot the data over the whole range observed.

8.1.6 Dijet cross section as function of ξ

The differential dijet cross section as a function of ξ shows an increase in the low-ξ region followed by a plateau and a fall-off of more than one order of magnitude in the high-ξ region. The suppression of the measured cross section in the low-ξ region is related to the requirement of two high-energetic jets in the final state. The decrease of the cross section at high values of ξ reflects the decrease of the quark and gluon densities at high ξ. The restriction of the Q^2 range implicitly limits the accessible ξ range to $0.09 \lesssim \xi \lesssim 0.37$. The data is very well described by the NLO calculation over the whole range observed. The deviation in multiples of the total uncertainty varies between $-0.32 \leq \chi \leq 0.79$. In the low-$\xi$ region ($-2 < \log_{10} \xi < 1.1$) the theoretical error is the dominant source of uncertainty and exceeds the experimental error by a factor of $2.6 < \delta_{\text{theo}}/\delta_{\text{exp}} < 4.3$. In the highest ξ bin the experimental error becomes the dominant source of uncertainty and exceeds the theoretical error ($\delta_{\text{theo}}/\delta_{\text{exp}} = 0.6$).

8.2 Double-differential cross sections

8.2.1 $d\sigma/d\xi$ in different regions of Q^2

The cross sections as a function of ξ have also been measured double-differentially in five different regions of Q^2 (see figure 8.3). In all Q^2 regions the shape of the cross section distribution is similar to that of the single-differential cross section $d\sigma/d\xi$ described in the previous section. All curves exhibit an increase in the low-ξ region followed by a plateau and a fall-off towards the high-ξ region. As described in the

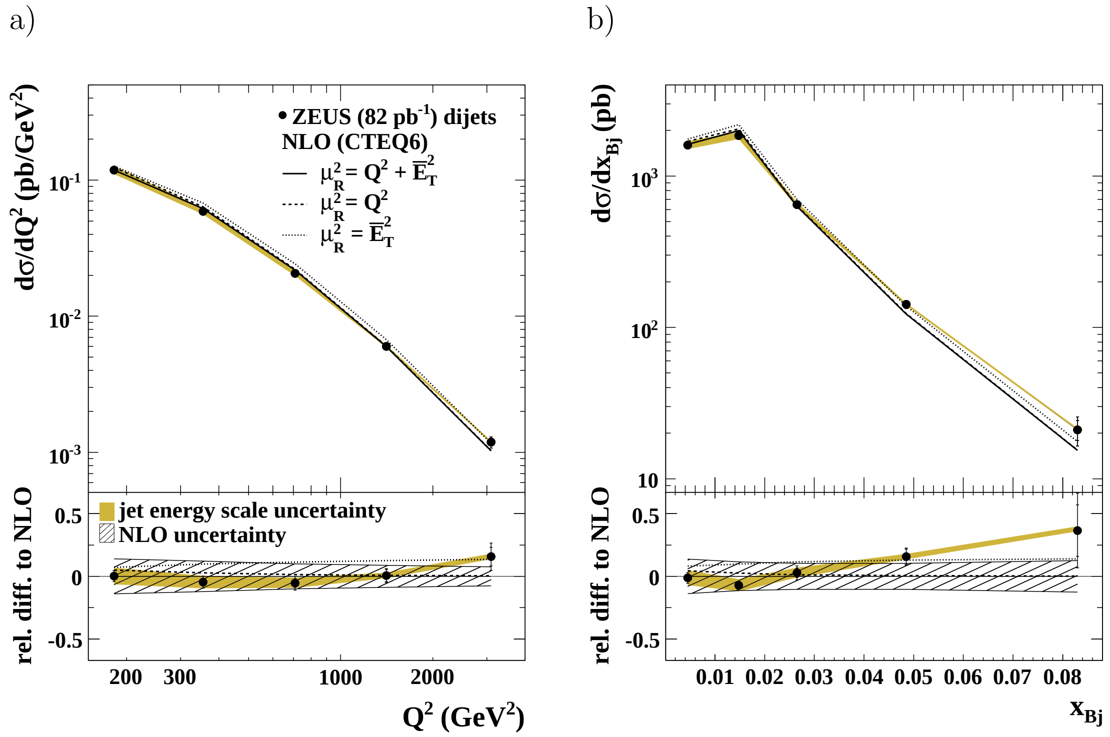

Figure 8.1: Measured (dots) differential cross sections $d\sigma/dQ^2$ and $d\sigma/dx_{Bj}$ for dijet production with $E_{T,\mathrm{Breit}}^{\mathrm{jet1(2)}} > 12\ (8)\ \mathrm{GeV}$ and $-2 < \eta_{\mathrm{Breit}}^{\mathrm{jet}} < 1.5$, in the kinematic range given by $|\cos\gamma_h| < 0.65$ and $125 < Q^2 < 5000\ \mathrm{GeV}^2$. The inner error bars represent the statistical uncertainty. The outer error bars show the statistical and systematic uncertainties, not associated with the uncertainty in the absolute energy scale of the jets, added in quadrature. The shaded bands display the uncertainties due to the absolute energy scale of the jets. The NLO QCD calculations with $\mu_R^2 = Q^2 + \overline{E}_T^2$ (solid lines), $\mu_R^2 = Q^2$ (dashed lines), and $\mu_R^2 = \overline{E}_T^2$ (dotted lines), corrected for hadronisation effects and using the CTEQ6.1 parametrisation of the proton PDFs, are also shown. The lower parts of the figures show the relative differences with respect to the NLO QCD calculation with $\mu_R^2 = Q^2 + \overline{E}_T^2$: measurements (dots), NLO QCD calculations with $\mu_R^2 = Q^2$ (dashed lines) and with $\mu_R^2 = \overline{E}_T^2$ (dotted lines); the hatched bands display the total theoretical uncertainty.

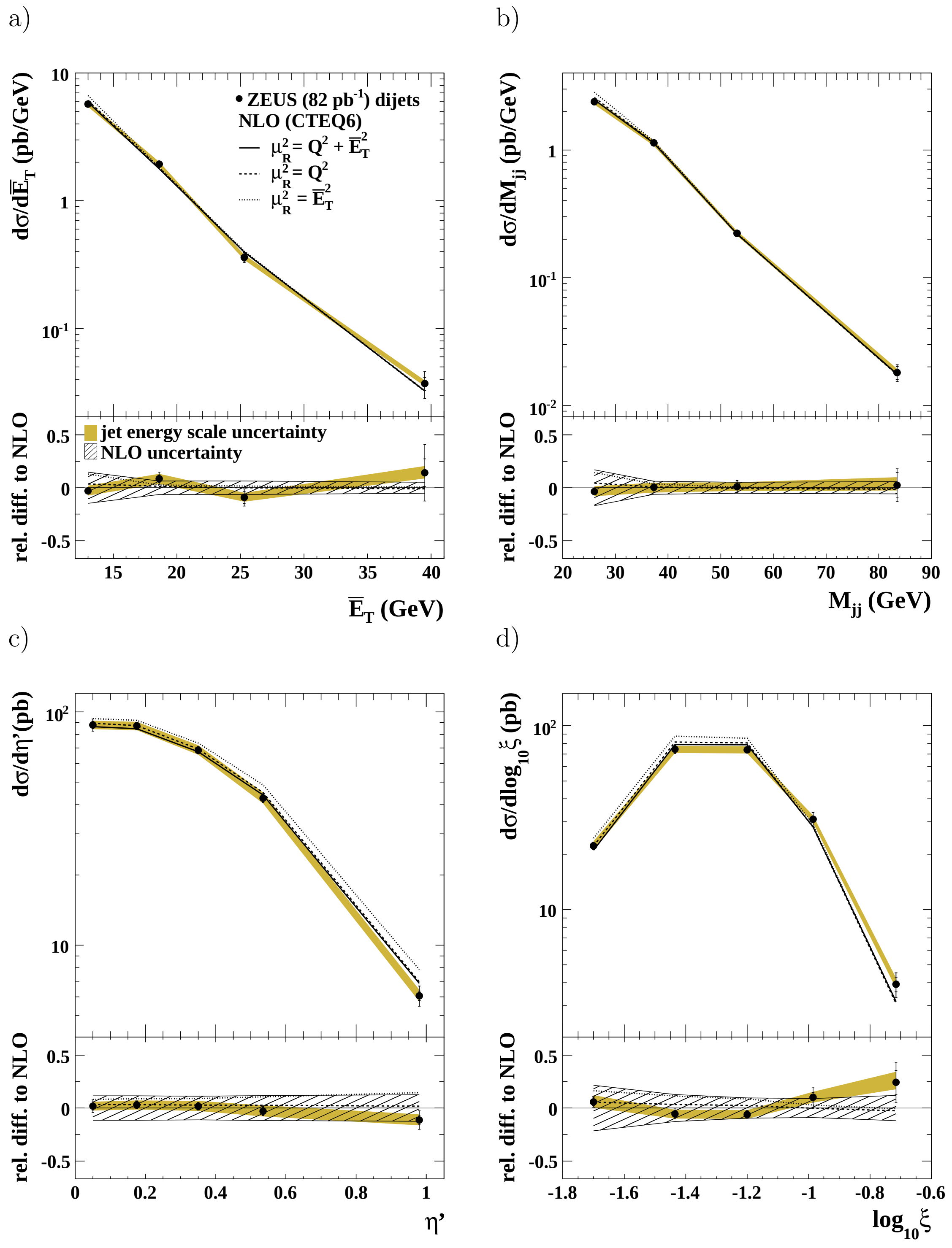

Figure 8.2: Measured differential cross sections $d\sigma/d\overline{E}_T$, $d\sigma/dM_{jj}$, $d\sigma/d\eta'$, and $d\sigma/d\log_{10}\xi$ for dijet production with $E_{T,\text{Breit}}^{\text{jet1(2)}} > 12\ (8)\ \text{GeV}$ and $-2 < \eta_{\text{Breit}}^{\text{jet}} < 1.5$ (dots), in the kinematic range given by $|\cos\gamma_h| < 0.65$ and $125 < Q^2 < \ 5000\ \text{GeV}^2$. Other details as in caption to figure 8.1.

previous section, the suppression of the measured cross sections in the low-ξ region is related to the requirement of two high-energetic jets in the final state whereas the decrease towards higher values of ξ reflects the decrease of the parton density functions in the high-ξ region.

The predictions of the NLO calculation give a good description of the data in all five Q^2 regions. The deviation between data and NLO is typically much smaller than the sum of experimental and theoretical errors ($-0.62 < \chi < 0.68$). The only exceptions are the two lowest ξ bins in the highest Q^2 region ($2000 < Q^2 < 5000$ GeV^2), where the deviation is in the order of or even exceeds the total error ($\chi = 0.98$ and $\chi = 1.10$).

In the low- and medium-Q^2 region ($125 < Q^2 < 1000$ GeV^2) the theoretical uncertainty typically exceeds the experimental uncertainty ($1.4 < \delta_{\text{theo}}/\delta_{\text{exp}} < 3.0$). Exceptions are the highest ξ regions where, due to the decreasing statistics, the experimental error becomes the dominant source of uncertainty. For higher values of the photon virtuality ($1000 < Q^2 < 5000$ GeV^2) the experimental error becomes the dominant source of uncertainty. In this region, where the statistics is small, the statistical error ranges between $8 - 16$ %. The relative uncertainty related to that on the jet energy scale is in the order of 10 % in the lowest Q^2 region and is reduced to about 3 % in the highest Q^2 region.

As can be seen in figure 8.4 the theoretical uncertainty is in all Q^2 regions largest at small values of ξ and decreases towards the high-ξ region. The figure also shows that the theoretical uncertainty decreases with increasing values of Q^2.

Figure 8.5 shows the contributions to the relative theoretical uncertainty induced by the variation of the renormalisation scale, μ_R, and by the uncertainties on the proton PDFs. As can be seen the theoretical uncertainties are in most regions dominated by the contributions from the variation of the renormalisation scale. This scale uncertainty exhibits a strong dependence on ξ and Q^2. The uncertainty decreases as ξ and Q^2 increase. In contrast to this the contributions from the PDF uncertainties are approximately constant and show almost no dependence on ξ or Q^2. At high values of ξ the decreasing contributions related to the scale dependency and the constant contributions related to the PDF uncertainties are of the same size. In some regions the PDF contribution becomes even dominant. As can bee seen in figure 8.6 in these regions the fraction of gluon-induced events to the dijet cross section is still in the order of $40 - 60$ %. The double-differential dijet cross sections might thus have the potential to further constrain the gluon PDF in the high-ξ regions.

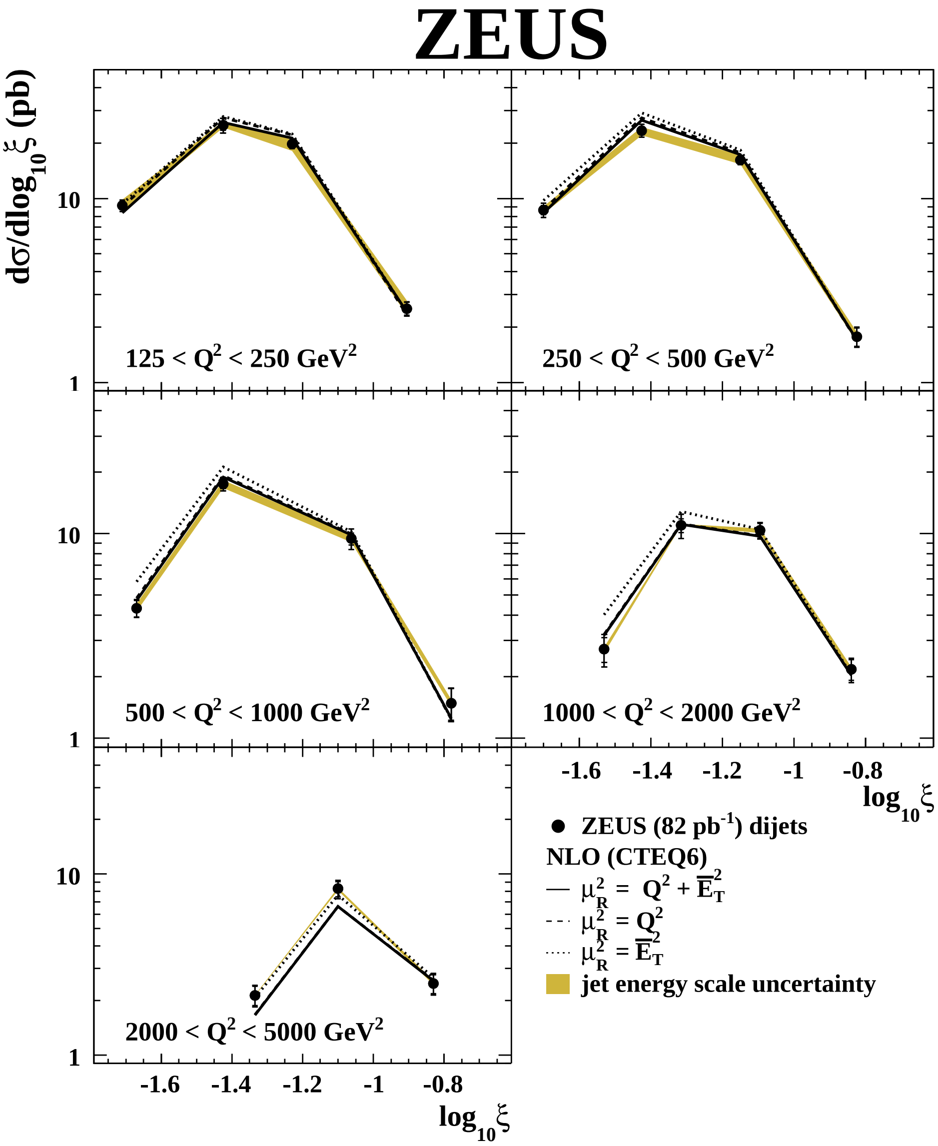

Figure 8.3: Differential cross section $d\sigma/d\log_{10}\xi$ for dijet production with $|\cos\gamma_h| < 0.65$, $E_{T,\mathrm{Breit}}^{\mathrm{jet1(2)}} > 12$ (8) GeV and $-2 < \eta_{\mathrm{Breit}}^{\mathrm{jet}} < 1.5$ in different regions of Q^2. Other details as in caption to figure 8.1.

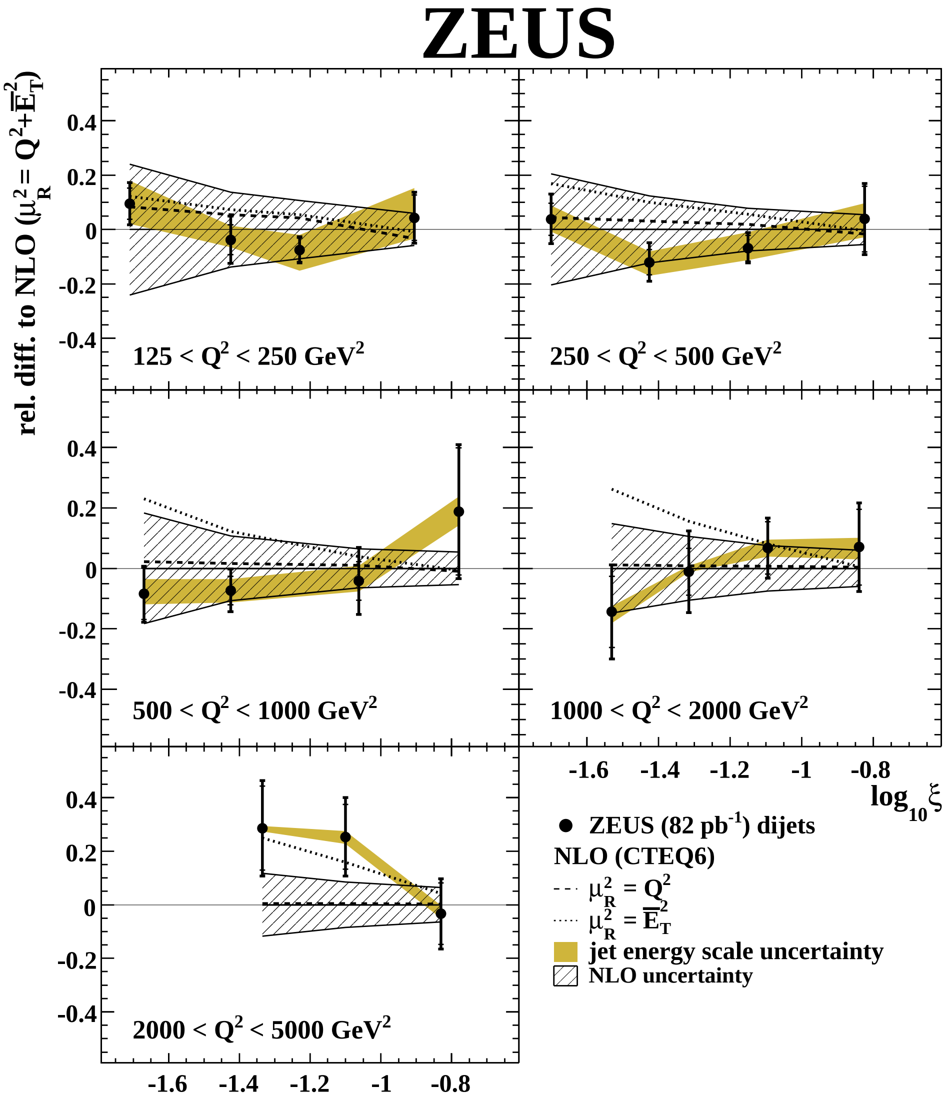

Figure 8.4: Relative differences between the measured differential cross sections $d\sigma/d\log_{10}\xi$ presented in figure 8.3 and the NLO QCD calculations with $\mu_R^2 = Q^2 + \overline{E}_T^2$ (dots). Relative differences between the NLO QCD calculations with $\mu_R^2 = Q^2$ and $\mu_R^2 = \overline{E}_T^2$ to those with $\mu_R^2 = Q^2 + \overline{E}_T^2$ are also shown as dashed and dotted lines. Other details as in the caption to figure 8.1.

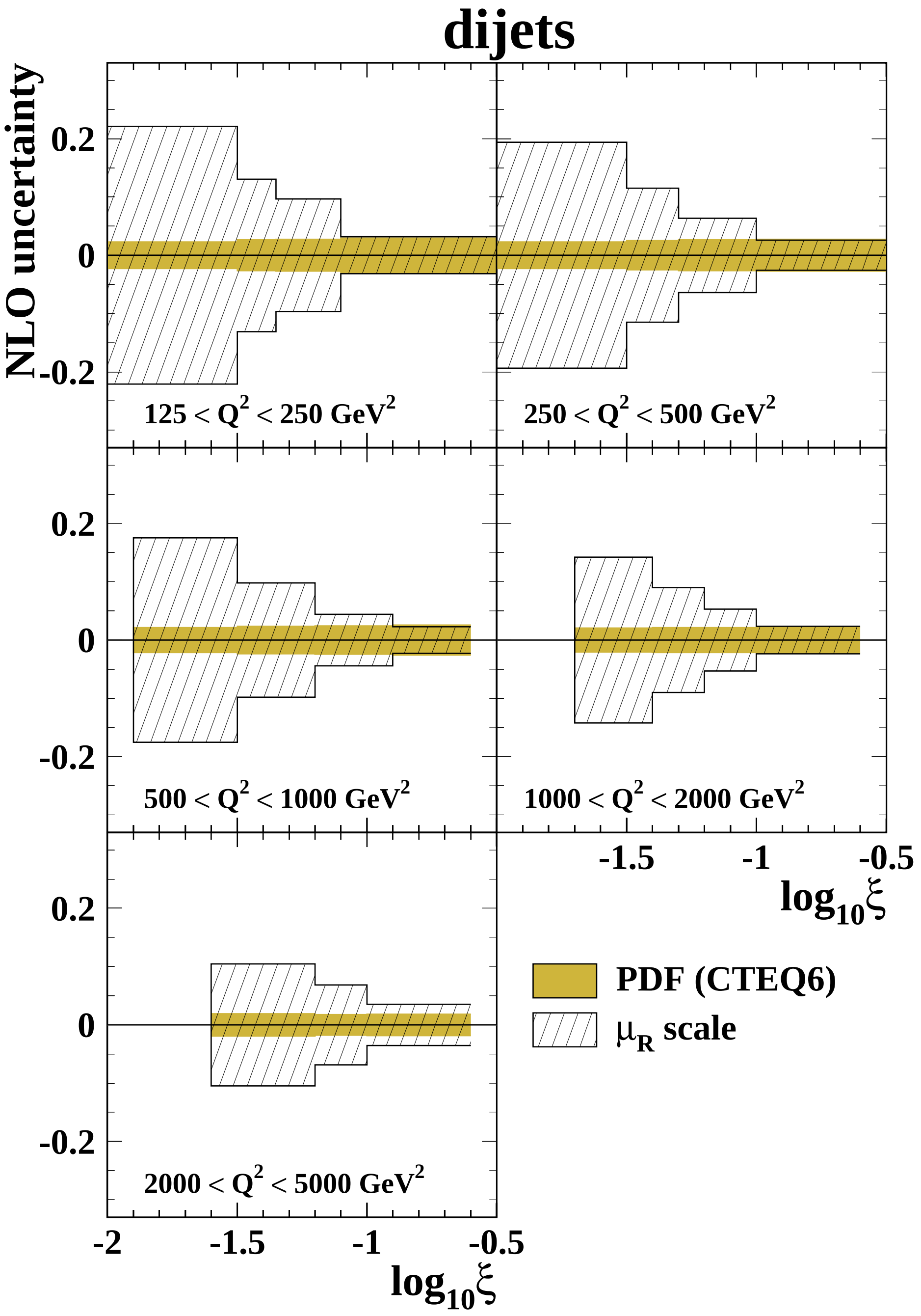

Figure 8.5: Contributions to the theoretical uncertainty as functions of $\log_{10}\xi$ in bins of Q^2 for $|\cos\gamma_h| < 0.65$, $E_{T,\mathrm{Breit}}^{\mathrm{jet1(2)}} > 12\ (8)$ GeV, and $-2 < \eta_{\mathrm{Breit}}^{\mathrm{jet}} < 1.5$. Shown are the relative uncertainties induced by the variation of the renormalisation scale μ_R (hatched area) and by the uncertainties on the proton PDFs (shaded area).

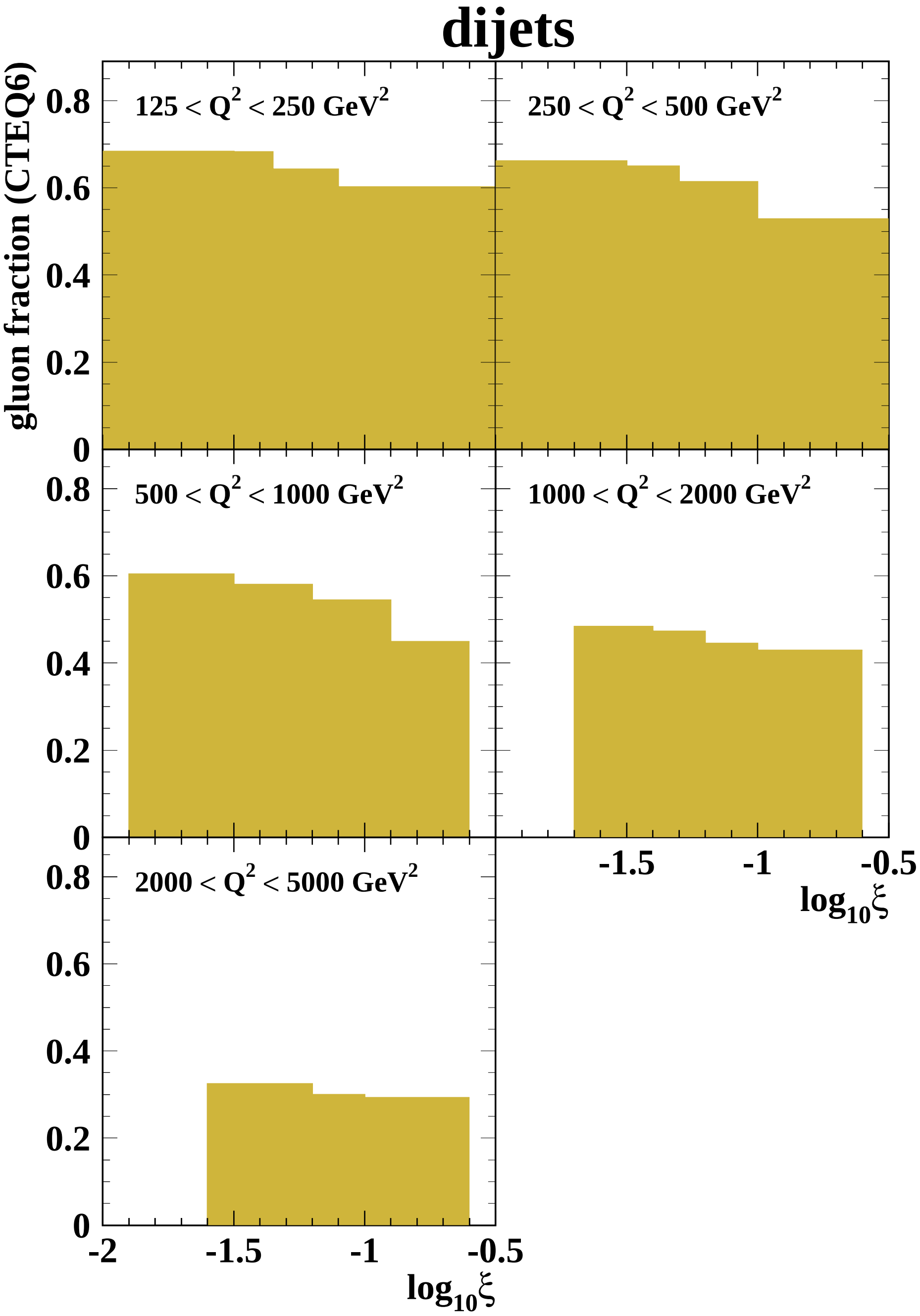

Figure 8.6: NLO QCD predictions of the gluon-induced fraction of the cross section $d\sigma/d\log_{10}\,\xi$ as function of log $\log_{10}\,\xi$ in different regions of Q^2 for $|\cos\gamma_h| < 0.65$, $E_{T,\mathrm{Breit}}^{\mathrm{jet1(2)}} > 12\ (8)\ \mathrm{GeV}$, and $-2 < \eta_{\mathrm{Breit}}^{\mathrm{jet}} < 1.5$ (shaded histograms) using the CTEQ6.1 parametrisations of the proton PDFs.

Q^2 bin (GeV^2)	$d\sigma/dQ^2$ (pb/GeV^2)	δ_{stat}	δ_{syst}	δ_{ES}	C_{QED}	C_{had}
125-250	0.1183	± 0.0033	$^{+0.0041}_{-0.0040}$	$^{+0.0081}_{-0.0077}$	0.96	0.85
250-500	0.0589	± 0.0018	$^{+0.0025}_{-0.0023}$	$^{+0.0032}_{-0.0030}$	0.94	0.91
500-1000	0.02061	± 0.00074	$^{+0.00094}_{-0.00094}$	$^{+0.00096}_{-0.00083}$	0.93	0.92
1000-2000	0.00602	± 0.00028	$^{+0.00018}_{-0.00018}$	$^{+0.00014}_{-0.00013}$	0.91	0.95
2000-5000	0.001189	± 0.000075	$^{+0.000083}_{-0.000083}$	$^{+0.000025}_{-0.000020}$	0.96	0.96

Table 8.1: Dijet cross section $d\sigma/dQ^2$ for jets of hadrons in the Breit frame selected with the longitudinally invariant k_T cluster algorithm. The statistical, uncorrelated systematic and jet-energy-scale (ES) uncertainties are shown separately. The multiplicative corrections applied to correct for QED radiative effects, C_{QED}, and for hadronisation effects, C_{had}, are shown in the last two columns.

x_{Bj} bin	$d\sigma/dx_{\text{Bj}}$ (pb)	δ_{stat}	δ_{syst}	δ_{ES}	C_{QED}	C_{had}
0.0001-0.01	1599	± 45	$^{+54}_{-52}$	$^{+101}_{-92}$	0.95	0.86
0.01-0.02	1849	± 48	$^{+37}_{-37}$	$^{+98}_{-95}$	0.94	0.93
0.02-0.035	647	± 24	$^{+26}_{-25}$	$^{+26}_{-23}$	0.92	0.92
0.035-0.07	141.7	± 7.5	$^{+4.0}_{-4.0}$	$^{+2.9}_{-2.6}$	0.95	0.91
0.07-0.1	21.1	± 3.2	$^{+3.3}_{-3.3}$	$^{+0.5}_{-0.1}$	0.89	0.90

Table 8.2: Dijet cross section $d\sigma/dx_{\text{Bj}}$ for jets of hadrons in the Breit frame selected with the longitudinally invariant k_T cluster algorithm. Other details as in the caption to Table 8.1.

$\overline{E}_T$ bin (GeV)	$d\sigma/d\overline{E}_T$ (pb/GeV)	δ_{stat}	δ_{syst}	δ_{ES}	C_{QED}	C_{had}
10-16	5.71	± 0.11	$^{+0.12}_{-0.12}$	$^{+0.30}_{-0.26}$	0.94	0.90
16-22	1.935	± 0.064	$^{+0.086}_{-0.084}$	$^{+0.081}_{-0.091}$	0.94	0.90
22-30	0.361	± 0.023	$^{+0.023}_{-0.023}$	$^{+0.017}_{-0.016}$	0.94	0.91
30-60	0.0371	± 0.0043	$^{+0.0076}_{-0.0076}$	$^{+0.0021}_{-0.0018}$	0.97	0.91

Table 8.3: Dijet cross section $d\sigma/d\overline{E}_T$ for jets of hadrons in the Breit frame selected with the longitudinally invariant k_T cluster algorithm. Other details as in the caption to Table 8.1.

$M_{\rm jj}$ bin (GeV)	$d\sigma/dM_{\rm jj}$ (pb/GeV)	$\delta_{\rm stat}$	$\delta_{\rm syst}$	$\delta_{\rm ES}$	$C_{\rm QED}$	$C_{\rm had}$
20-32	2.382	± 0.051	$^{+0.055}_{-0.054}$	$^{+0.123}_{-0.109}$	0.95	0.91
32-45	1.134	± 0.034	$^{+0.047}_{-0.047}$	$^{+0.049}_{-0.055}$	0.94	0.89
45-65	0.222	± 0.012	$^{+0.006}_{-0.006}$	$^{+0.009}_{-0.009}$	0.92	0.89
65-120	0.0180	± 0.0021	$^{+0.0017}_{-0.0017}$	$^{+0.0013}_{-0.0009}$	0.97	0.94

Table 8.4: Dijet cross section $d\sigma/dM_{\rm jj}$ for jets of hadrons in the Breit frame selected with the longitudinally invariant k_T cluster algorithm. Other details as in the caption to Table 8.1.

η' bin	$d\sigma/d\eta'$ (pb)	$\delta_{\rm stat}$	$\delta_{\rm syst}$	$\delta_{\rm ES}$	$C_{\rm QED}$	$C_{\rm had}$
0-0.1	87.9	± 3.4	$^{+4.0}_{-3.9}$	$^{+3.7}_{-3.7}$	0.95	0.91
0.1-0.25	87.0	± 2.8	$^{+1.6}_{-1.6}$	$^{+3.6}_{-3.7}$	0.94	0.94
0.25-0.45	68.5	± 2.1	$^{+1.3}_{-1.1}$	$^{+3.5}_{-3.0}$	0.95	0.91
0.45-0.65	42.7	± 1.6	$^{+1.0}_{-1.0}$	$^{+2.5}_{-2.2}$	0.94	0.87
0.65-1.60	6.07	± 0.28	$^{+0.54}_{-0.52}$	$^{+0.37}_{-0.34}$	0.91	0.86

Table 8.5: Dijet cross section $d\sigma/d\eta'$ for jets of hadrons in the Breit frame selected with the longitudinally invariant k_T cluster algorithm. Other details as in the caption to Table 8.1.

$\log_{10}\xi$ bin	$d\sigma/d\log_{10}\xi$ (pb)	$\delta_{\rm stat}$	$\delta_{\rm syst}$	$\delta_{\rm ES}$	$C_{\rm QED}$	$C_{\rm had}$
-2 - -1.5	22.22	± 0.78	$^{+0.72}_{-0.71}$	$^{+1.34}_{-1.17}$	0.95	0.88
-1.5 - -1.35	74.4	± 2.6	$^{+2.8}_{-2.8}$	$^{+3.2}_{-3.4}$	0.94	0.92
-1.35 - -1.1	73.9	± 1.9	$^{+2.2}_{-2.0}$	$^{+3.4}_{-3.2}$	0.94	0.92
-1.1 - -0.85	31.0	± 1.3	$^{+2.4}_{-2.4}$	$^{+1.5}_{-1.4}$	0.94	0.87
-0.85 - -0.5	3.93	± 0.36	$^{+0.48}_{-0.48}$	$^{+0.32}_{-0.21}$	0.93	0.79

Table 8.6: Dijet cross section $d\sigma/d\log_{10}\xi$ for jets of hadrons in the Breit frame selected with the longitudinally invariant k_T cluster algorithm. Other details as in the caption to Table 8.1.

$\log_{10}\xi$ bin	$d\sigma/d\log_{10}\xi$ (pb)	δ_{stat}	δ_{syst}	δ_{ES}	C_{QED}	C_{had}
$125 < Q^2 < 250$ GeV^2						
–2.00 - –1.50	9.17	± 0.48	$^{+0.44}_{-0.44}$	$^{+0.70}_{-0.62}$	0.97	0.83
–1.50 - –1.35	25.0	± 1.4	$^{+1.8}_{-1.8}$	$^{+1.4}_{-0.7}$	0.95	0.89
–1.35 - –1.10	19.74	± 0.93	$^{+0.43}_{-0.41}$	$^{+1.17}_{-1.65}$	0.95	0.86
–1.10 - –0.50	2.52	± 0.20	$^{+0.10}_{-0.10}$	$^{+0.26}_{-0.19}$	0.99	0.83
$250 < Q^2 < 500$ GeV^2						
–2.00 - –1.50	8.65	± 0.49	$^{+0.59}_{-0.57}$	$^{+0.42}_{-0.38}$	0.94	0.93
–1.50 - –1.30	23.4	± 1.2	$^{+1.5}_{-1.4}$	$^{+1.1}_{-1.3}$	0.94	0.93
–1.30 - –1.00	16.18	± 0.83	$^{+0.55}_{-0.44}$	$^{+1.02}_{-0.78}$	0.93	0.89
–1.00 - –0.50	1.77	± 0.21	$^{+0.09}_{-0.09}$	$^{+0.10}_{-0.11}$	0.94	0.88
$500 < Q^2 < 1000$ GeV^2						
–1.90 - –1.50	4.32	± 0.40	$^{+0.15}_{-0.18}$	$^{+0.23}_{-0.17}$	0.94	0.92
–1.50 - –1.20	17.50	± 0.88	$^{+1.00}_{-1.00}$	$^{+0.72}_{-0.75}$	0.94	0.94
–1.20 - –0.90	9.45	± 0.63	$^{+0.90}_{-0.90}$	$^{+0.50}_{-0.35}$	0.91	0.92
–0.90 - –0.60	1.48	± 0.26	$^{+0.09}_{-0.09}$	$^{+0.06}_{-0.06}$	0.98	0.86
$1000 < Q^2 < 2000$ GeV^2						
–1.70 - –1.40	2.72	± 0.37	$^{+0.33}_{-0.33}$	$^{+0.06}_{-0.12}$	0.93	0.94
–1.40 - –1.20	10.98	± 0.86	$^{+1.23}_{-1.23}$	$^{+0.22}_{-0.01}$	0.94	0.98
–1.20 - –1.00	10.37	± 0.84	$^{+0.48}_{-0.48}$	$^{+0.26}_{-0.28}$	0.92	0.96
–1.00 - –0.60	2.17	± 0.25	$^{+0.15}_{-0.15}$	$^{+0.06}_{-0.08}$	0.85	0.89
$2000 < Q^2 < 5000$ GeV^2						
–1.60 - –1.20	2.14	± 0.26	$^{+0.14}_{-0.14}$	$^{+0.01}_{-0.02}$	0.92	0.99
–1.20 - –1.00	8.28	± 0.80	$^{+0.54}_{-0.54}$	$^{+0.14}_{-0.18}$	1.00	0.96
–1.00 - –0.60	2.48	± 0.30	$^{+0.16}_{-0.16}$	$^{+0.08}_{-0.04}$	0.93	0.94

Table 8.7: Dijet cross sections $d\sigma/d\log_{10}\xi$ for jets of hadrons in the Breit frame selected with the longitudinally invariant k_T cluster algorithm in different regions of Q^2. Other details as in the caption to Table 8.1.

Chapter 9

Summary and outlook

Summary

Single- and double-differential dijet cross sections have been measured in neutral current deep inelastic electron-proton scattering at HERA. The data used for the presented analysis were recorded with the ZEUS detector in the years 1998, 1999 and 2000 and correspond to an integrated luminosity of 81.74 pb^{-1}. In this period HERA delivered protons and leptons (electrons and positrons) with energies of 920 and 27.52 GeV, respectively, resulting in a centre-of-mass energy of 318 GeV. The measurement is restricted to DIS events with a photon virtuality, Q^2, between 125 and 5000 GeV^2. Due to the upper limit on the virtuality the exchange of Z^0 bosons is negligible. The phase space is defined by an additional cut on the polar angle of the hadronic final state, γ_h, according to $|\cos\gamma_\text{h}| < 0.65$.

After the selection of the inclusive DIS sample the reconstructed kinematics of the electron and the hadronic final state have been compared to the predictions of the leading order Monte Carlo generators LEPTO and ARIADNE, which utilise a parton-shower algorithm and an implementation of the colour-dipole model for the simulation of higher orders via the generation of parton cascades. The shape of the kinematic variables is well described by both MC generators. Deviations are typically smaller than 5 %.

For the selected DIS events jets have been reconstructed with the inclusive k_T cluster algorithm in the Breit reference frame. The transverse jet energies have been corrected for losses in dead detector material using a standard routine based on MC events for which jets have been reconstructed on hadron and detector level. Events have been selected for the final dijet sample if at least two jets with energies greater than 12 and 8 GeV have been reconstructed in the pseudorapidity range $-2 < \eta_{Breit} < 1.5$.

For the selected dijet events, differential cross sections have been measured as functions of the photon virtuality, Q^2, the scaling variable, Bjorken x, the mean transverse jet energy, $\overline{E}_T$, the invariant dijet mass, M_{jj}, the difference in jet pseudorapidity, $\eta' = |\eta^\text{jet1} - \eta^\text{jet2}|$ and the momentum fraction, ξ. The cross sections as function of ξ have also been measured in different regions of the photon virtuality.

The measured cross sections have been corrected for detector effects and QED-vertex corrections using the bin-by-bin method. The corrected cross sections have been compared to the predictions of a fixed-order QCD calculation performed with DISENT. The QCD calculation is of order $\mathcal{O}(\alpha_s^2)$, which for the observed processes is the next-to-leading order (NLO). Before being compared to the data, the NLO cross sections have been corrected for non-perturbative hadronisation effects. For both the acceptance and the hadronisation correction, samples of DIS MC events with reconstructed jets on parton, hadron and detector level have been used. For the QED corrections, two MC samples with and without QED-vertex corrections have been used. As for the dijet events the description of the data has shown to be better for LEPTO than for ARIADNE, the acceptance and the QED corrections are based on the predictions as obtained from the LEPTO event generator. For the hadronisation correction the correction factors obtained from ARIADNE and LEPTO have been combined.

The presented dijet analysis represents a very detailed test of perturbative QCD and QCD dynamics. The comparison of the data to the NLO QCD predictions, calculated for a default renormalisation scale of $\mu_R^2 = Q^2 + \overline{E}_T^2$, shows a good agreement in the order of 5 % for the single-differential cross sections and 5 − 10 % for the double-differential cross sections. As the renormalisation scale is in most regions dominated by the Q^2 contribution[1], the predictions obtained for $\mu_R^2 = Q^2$ also provide a good description of the data. In contrast to the good agreement achieved for $\mu_R^2 = Q^2 + \overline{E}_T^2$ and $\mu_R^2 = Q^2$, the predictions obtained for (the typically smaller renormalisation scale) $\mu_R^2 = \overline{E}_T^2$ systematically overshoot the data by typically 10 %.

The uncertainties on the dijet cross sections are in most regions by far dominated by the theoretical uncertainties which are (in case of the double-differential cross sections) for all but the highest Q^2 and ξ regions dominated by the contributions from missing higher orders as estimated by varying the renormalisation scale. This clearly demonstrates the need for fixed order QCD calculations of order $\mathcal{O}(\alpha_s^3)$ (or higher) which for the observed dijet processes would be the next-to-next-to-leading order (NNLO). The systematic experimental uncertainty is in most regions dominated by the jet-energy scale uncertainty which is assumed to be 1(3) % for high (low) E_T jets. The resulting uncertainty on the measured cross sections is typically in the order of 5 % and increases to about 10 % for some regions of the dijet phase space (double-differential cross sections)[2].

---

[1] Q^2 covers the range from $125 < Q^2 < 5000$ GeV^2 whereas $\overline{E}_T$ is restricted to values smaller than 60 GeV.

[2] The uncertainty related to the MC-based acceptance correction is another major source of systematic uncertainty. Within a ZEUS dijet analysis based on HERA II data it has been shown that the respective uncertainty can be by reduced by re-weighting the MC samples. The re-weighting yields a better description of the data and significantly reduces the difference between the MC predictions as obtained from ARIADNE and LEPTO [101].

It has been shown that the cross sections measured in different regions of Q^2 are sensitive to the gluon density of the proton. The gluon-induced fraction of the respective cross sections is in the order of 60 % for low and medium values of the photon virtuality and still about $30 - 40$ % in the high-Q^2 region ($Q^2 > 1000$ GeV^2). The precise measurements obtained here are therefore of particular relevance for improving the determination of the gluon density in future (NNLO) QCD fits.

A first significant measurement of double-differential dijet cross sections based on a data set of about 33 pb^{-1} was published by the H1 collaboration in 2001 [102]. It should be noted that the results of the presented dijet analysis, published in 2006 [3], are based on a much larger data sample. The statistics was increased by a factor of almost 2.5 with respect to the 2001 measurement, resulting in a reduction of the statistical uncertainty. Moreover the presented analysis provided the basis for the latest results on dijet cross sections from the ZEUS collaboration [94] which combined the presented HERA I cross sections with cross sections as obtained from additional 128 pb^{-1} of HERA II data[3]. The single- and double-differential dijet cross sections, measured in this combined analysis, are in good agreement with the NLO predictions. They are (over a wide kinematic range) also dominated by the theoretical uncertainties which get as large as 25 %. Due to the large statistics used for this analysis ($\mathcal{L}_{\text{int}} \approx 210$ pb^{-1}) the statistical error of the data could be reduced to about $2 - 10$ %. A similar measurement by H1 (albeit for dijet distributions normalised to the inclusive NC cross section) is using the full HERA I+II statistics of about 395 pb^{-1} [103].

Outlook

Since the end of the HERA running in 2007, the experiments H1 and ZEUS have prepared for the final analysis of all HERA (HERA I and HERA II) data. There are also ongoing efforts to combine (dijet) cross sections as obtained from the H1 and ZEUS collaborations and in this way to make use of the maximum available HERA statistics ($\mathcal{L}^{\text{H1+ZEUS}}_{\text{int,HERA}} \approx 1$ fb^{-1}). The combination would not only yield a further reduction of the statistical uncertainty but would, due to cross-calibration effects, also result in a significant reduction of systematic uncertainties like those related to the absolute jet-energy scale.

Due to the good understanding of the detectors, including calibration and energy scales, and due to the high statistics available, the uncertainties of recent HERA jet measurements are in most regions by far dominated by the theoretical uncertainties. Here, in most regions the contributions from missing higher orders are dominating and exceed the contributions from the uncertainties on the proton PDFs. In order to make full use of the obtained experimental precision by including the

---

[3] The author of this thesis contributed to the analysis by cross-checking the obtained HERA II results.

data in QCD fits and thus to be able to reduce the uncertainty on the PDFs, it is mandatory to provide (dijet) predictions in next-to-next-to-leading order (NNLO).

As stated before the correction of the predictions from the NLO QCD calculation with factors obtained from LO Monte Carlo models is somehow inconsistent and unsatisfactory. In the last few years NLO Monte Carlo generators such as *MC@NLO* have been developed. Unfortunately at present no such NLO Monte Carlo generator exists for deep inelastic electron-proton scattering. Particularly with regard to the need for NNLO calculations the development of such NLO or even NNLO generators is mandatory.

Part II

Towards a measurement in HERA II

Chapter 10

HERA luminosity upgrade

In the years 2000 and 2001 HERA was upgraded from HERA I to HERA II. The aim of the upgrade was to increase the luminosity by a factor of 4-5 in order to be able to collect about 1 fb^{-1} of data until the end of the HERA operation in 2007. The luminosity upgrade was motivated by the expected increase in statistical precision that would allow more stringent tests of the electroweak and the strong interaction and by the enhanced sensitivity to rare processes like heavy quark production, NC and CC events in the very high-Q^2 region, and new phenomena beyond the Standard Model.

As can be seen from equation 3.1, one way to increase the luminosity is to decrease the spatial extension σ of the bunches which are related to the beam emittance, ϵ, and the amplitude function, β, according to $\sigma = \sqrt{\epsilon\,\beta}$. It was concluded that the most promising way to increase the luminosity was to reduce the β-functions [104]. The reduction was achieved by a new design of the interaction regions which allowed to place the lepton and proton low-β quadrupoles closer to the interaction point.

The shutdown of HERA also allowed an upgrade of the ZEUS detector in order to adapt it to the high-luminosity environment and to the HERA II physics programme. In order to enhance the tagging capabilities for short-lived particles a vertex detector based on silicon strip sensors, also referred to as silicon microvertex detector (MVD), was installed inside the CTD. In the forward region, the ZEUS detector was supplemented by a straw tube tracker (STT) which replaced the transition radiation detector (TRD). Additionally a new luminosity (monitoring) system consisting of three components (a photon calorimeter, a photon spectrometer and an electron tagger) was installed. The new luminosity system had been designed to cope with the higher rate of synchrotron radiation and Bethe-Heitler events in the HERA II environment.

A brief description of the upgraded ZEUS interaction region, the MVD, the STT and the upgraded luminosity system is given in the following.

10.1 Upgraded interaction region

The upgraded interaction region [105] was designed to facilitate an early separation of the electron and proton beams, close to the interaction point (IP), by using combined (focussing + bending) function magnets that were installed inside the detector. This allowed to move the proton final focus magnets from 26m (at HERA I) to 11m from the interaction point, resulting in a reduced spot size of 120×30 μm. The spot size of the electrons was matched to the same values by reducing both, the IP β-functions as well as the beam emittance. The schematic layout of the upgraded interaction region is shown in figure 10.1. The focussing scheme was different for the two beams. The electrons (or positrons) were focused by a triplet structure that consisted of three single quadrupoles. On the left side the first quadrupole was the superconducting GO, followed by the two normal conducting magnets GI and GJ. On the right side the quadrupole component of the superconducting GG quadrupole was set to zero and the triplet structure consisted of two GIs and one GG.

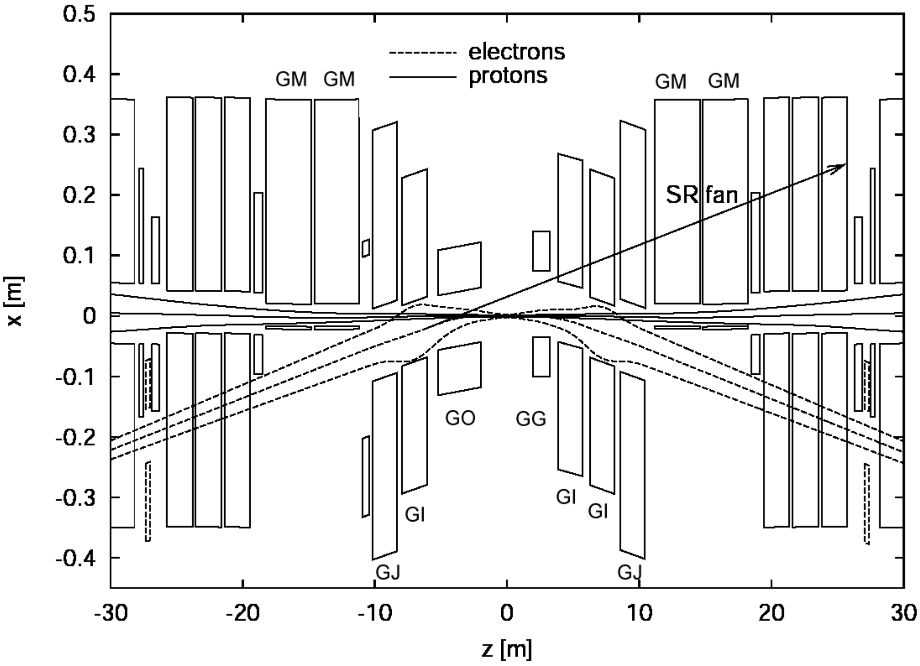

Figure 10.1: Top view schematic layout of the upgraded interaction region. 20 σ_x and 12 σ_x beam envelopes are shown for electrons (dashed lines) and protons (solid lines), respectively. Figure taken from [106].

The protons were focused by a double doublet structure, i.e. four lenses. Because of the high beam energy each lens had to be made of several quadrupoles. In total the double doublet consisted of 13 magnets, most of them more than 3 m long. The first exclusive proton quadrupoles were two GMs, which were designed as half quadrupoles with mirror plates in order to allow a close passage of the electron beam.

10.2 Microvertex detector (MVD)

The ZEUS microvertex detector was designed in order to enhance the tracking capabilities of the ZEUS experiment. The aim was to provide a detector with the capability of tagging heavy quarks and other short-lived particles by identifying secondary vertices and to improve the efficiency, acceptance and resolution of the ZEUS tracking system. The MVD was subdivided into the barrel and the forward MVD (BMVD and FMVD). The barrel part of the detector was a 63 cm long cylinder placed inside the CTD, with silicon sensors arranged around the elliptical beam pipe. The forward part consisted of four circular shaped disks, each consisting of two sensor layers. For both the BMVD and the FMVD, single-sided silicon strip detectors with a readout pitch of 120 μm were used. In total the MVD contained over 200,000 channels and 2.9 m^2 of silicon. The single-hit resolution of the BMVD was 25 μm and the impact-parameter resolution of the BMVD+CTD system for high momentum tracks was 100 μm.

Figure 10.2a shows the layout of the silicon sensors in the barrel MVD (xy-view). The sensors were arranged like roof tiles along three concentric cylindric layers around the beam pipe. The innermost layer provided a coverage of only about 75 % in azimuth angle. Figure 10.2b displays the wheel geometry of the forward MVD. The MVD consisted of four wheels arranged perpendicular to the beam axis. The forward section extended the angular coverage of the MVD down to 7° from the beam line.

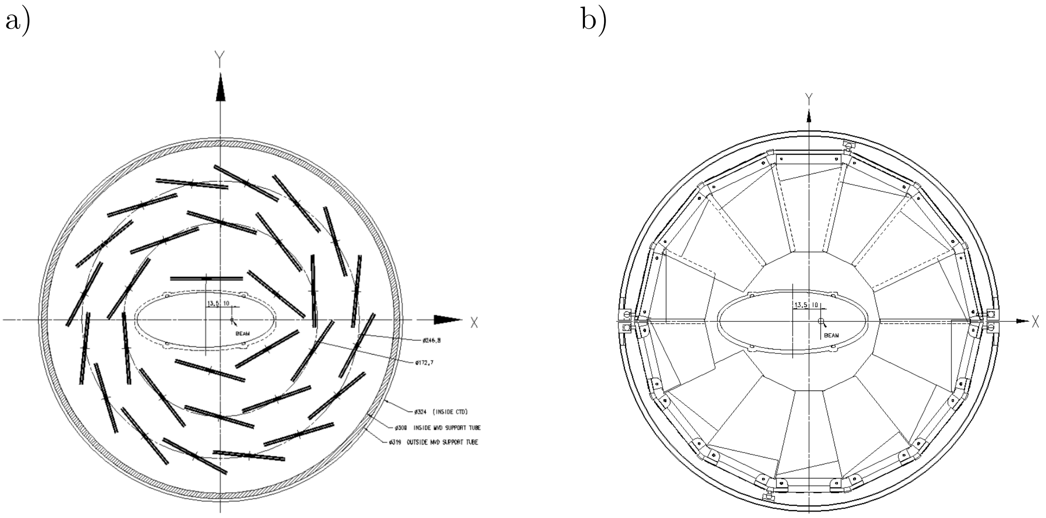

Figure 10.2: a) Cross section of the barrel MVD. The silicon strip sensors are arranged like roof tiles along three concentric cylindric layers around the beam pipe. b) Wheel geometry of the forward MVD.

10.3 Straw tube tracker (STT)

During the HERA I running period the forward tracking detector (FDET) of ZEUS comprised three planar tracking chambers (FTD) and four transition radiation chambers (TRD). The four TRD modules, used for the electron identification, were accommodated inside the two gaps between the FTD chambers (see figure 3.3). Within the upgrade of ZEUS, the forward tracker was supplemented with a straw tube tracker (STT) which replaced the TRD, covering the pseudorapidity range from $1.5 < \eta < 3$ ($5.5^\circ < \theta < 25^\circ$). The STT had been designed in order to improve the track finding and reconstruction capabilities in the forward region of the ZEUS detector.

The STT consisted of straw drift tube layers grouped into sectors of trapezoidal shape (wedges). In z-direction the sectors were grouped into four super-layers. The super-layers were located inside the two gaps between the FTD chambers. Two layers were placed inside each of the gaps, respectively. The four super layers were rotated by 15° with respect to each other. Each super-layer contained two planes rotated by 30° with respect to each other, each plane comprising six sectors covering the full azimuthal angle. Each sector consisted of three layers of straw tubes along the z-direction. Depending on the z-position the wedges contained 196-280 straw tubes with an outer diameter of 8 mm. In total the STT comprised 11616 straw tubes grouped into 48 wedges.

Figure 10.3 displays the design of the super-layers and the complete straw tube tracker. In figure 10.4 the cell design of the STT is compared to that of the FTD. In contrast to the FTD, the cell size of the STT decreased with decreasing radius. The STT design thus avoided the draw-back of large cell sizes in a region with high track multiplicity, which leads to high cell occupancies. The gained improvement in the tracking efficiency at small radii was of vital importance for the analysis of high-Q^2 events, where the track multiplicity was typically high in the very forward region.

10.4 Upgraded luminosity system

Due to the strong focusing required to increase the luminosity and due to the early separation of the two beams, the rate of synchrotron radiation at HERA II increased by a factor of almost 7 compared to that at HERA I. Furthermore, as a direct consequence of the increasing luminosity, the rate of Bethe-Heitler (BH) events, used for the luminosity measurement, increased by a factor of 4-5. Insufficient shielding of both synchrotron radiation and photons from BH events would lead to significant radiation damage in most scintillator-based calorimeters. The high rate of BH events also leads to a higher number of-pile up events. The upgraded luminosity system had been designed to cope with these difficulties. It comprised three sub-components:

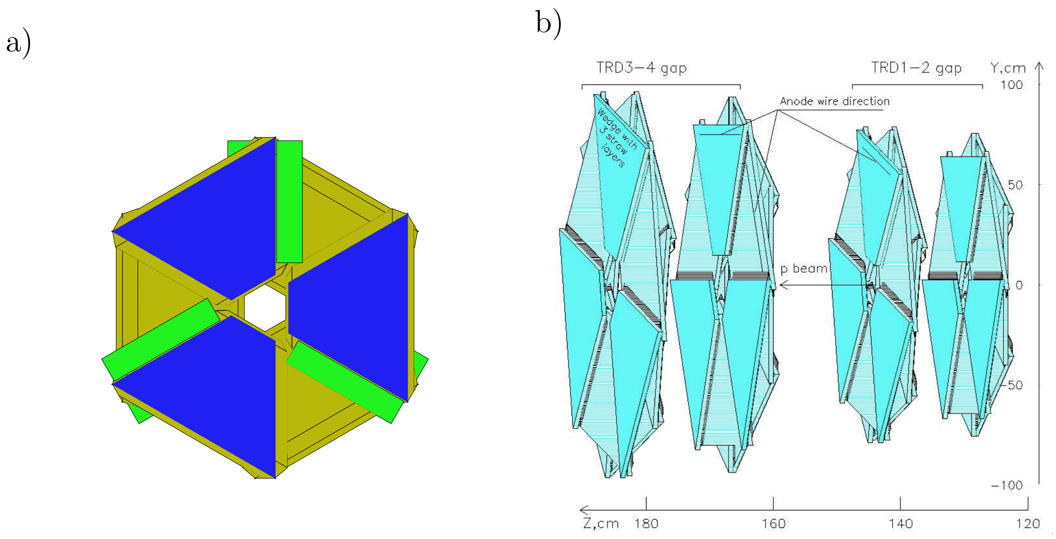

Figure 10.3: a) Layout of an STT super-layer (xy view). Each super-layer comprised six sectors covering the full azimuthal angle. b) Sketch of the complete straw tube tracker. The STT consisted of four super-layers. Always two super-layers were placed together in one of the gaps between the FTD chambers. Each super-layer contained two planes rotated by 30° with respect to each other. The super-layers were rotated by 15° with respect to each other.

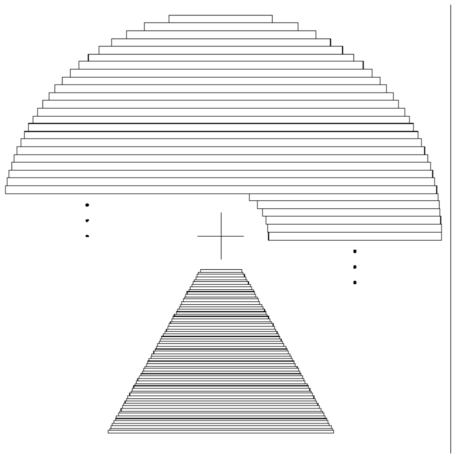

Figure 10.4: Comparison between the FTD and the STT design. In contrast to the FTD the cell size of the STT decreased with decreasing radius. This design avoids the drawback of large cell sizes in a region with high track multiplicity, which leads to high cell occupancies.

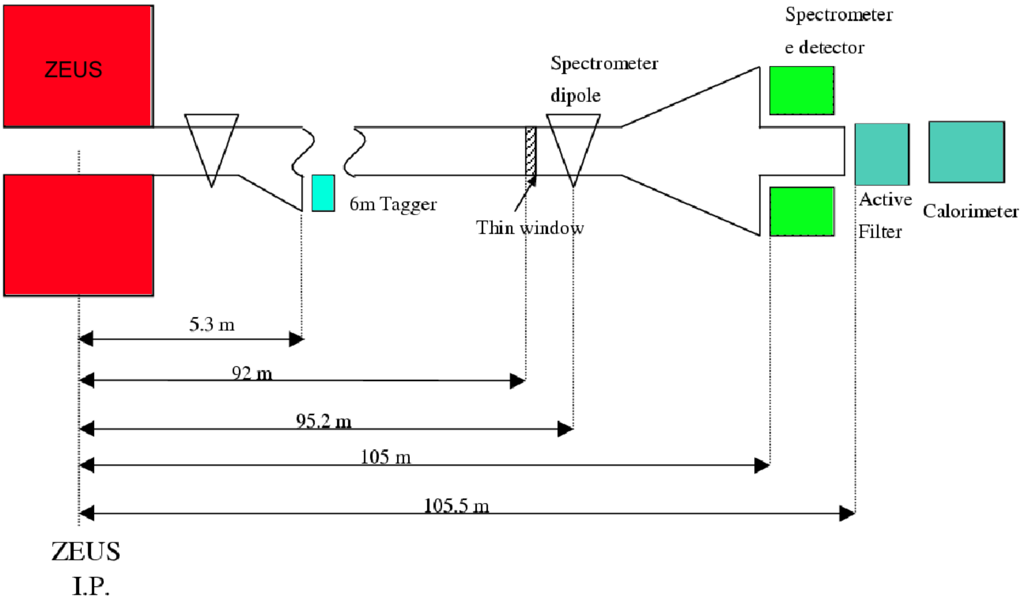

Figure 10.5: Design of the upgraded ZEUS luminosity system. The system comprised three sub-components: The 6m (electron) tagger (blue), the photon spectrometer (green) and the photon calorimeter (bluish green).

the photon calorimeter, the photon spectrometer and the 6m tagger. While the photon calorimeter and the photon spectrometer were both utilised for the luminosity measurement, the 6m tagger was primarily used for the energy calibration and the acceptance determination of the other two components. With the upgraded system, the luminosity at HERA II could be measured with an accuracy of 2.5 %. The luminosities determined with the photon calorimeter and the photon spectrometer agreed with each other typically within 1 % [107].

The positions of the photon calorimeter, the photon spectrometer and the 6m tagger are indicated in figure 10.5. A brief description of the three components is given in the following. A more detailed description can be found in [108].

Photon calorimeter: The photon calorimeter was a lead/scintillator sandwich calorimeter with a depth of 24 X_0 and a surface of 20×20 cm^2. A position detector , consisting of 16 vertical and 14 horizontal scintillator fingers of dimension $15.0 \times 1.0 \times 0.3$ cm^3 and $18.0 \times 1.0 \times 0.3$ cm^3, was inserted at 4 X_0. In order to screen the detector from the high flux of synchrotron radiation, the calorimeter was preceded by an active filter. The filter consisted of two 2 X_0 blocks of carbon absorber each followed by a slab of aerogel acting as Cerenkov counter that measured a signal proportional to the energy deposits in the filters. The energy can be reconstructed from the energy deposit in the calorimeter, E_{cal}, and the number of photo-electrons measured by the two Cerenkov counters, N_1 and N_2, according to

$$E_{\text{cal}}^{\text{corr}} = c_0 E_{\text{cal}} + c_1 N_1 + c_2 N_2, \tag{10.1}$$

where c_1 and c_2 are constants determined from MC simulations. A MC study showed that using the reconstruction method described above, the energy resolution can be improved from $\approx 90\ \%/\sqrt{E}$ (photon calorimeter + carbon absorber) to $\approx 25\ \%/\sqrt{E}$ (photon calorimeter + active filter), which should be compared to the intrinsic resolution of the calorimeter of $\approx 15\ \%/\sqrt{E}$ [108]. To determine the luminosity with the photon calorimeter the rate of BH events (photons) was measured by counting the hits with an energy deposit above a certain threshold [1].

Photon spectrometer: The photon spectrometer [109, 110] had been designed in order to measure the approximately 10 % of Bremsstrahlungs photons which converted to e^+e^- pairs when traversing the beam pipe window at about 92 m from the interaction point. According to the design of the measurement the problems of pile-up events and radiation damage due to Bremsstrahlung became almost negligible. The spectrometer comprised a 60 cm long dipole magnet with a typical field strength of $B_x \approx 0.5$ T (used to seperate the e^+e^- pairs) and two tungsten/scintillator sandwich calorimeters that were used to measure the energies and positions of the separated leptons with resolutions of about $17\ \%/\sqrt{E}$ and < 1 mm, respectively. The passive layers of the calorimeters contained 26 plates of 3.5 mm thick tungsten alloy corresponding to 24 electromagnetic radiation lengths (24 X_0). The active elements consisted of scintillating fingers, alternating after each plate in the x and y direction, each finger 7.9 mm wide and 2.6 mm thick. The calorimeters had dimensions of $128 \times 120 \times 158.6$ mm^3 (lower calorimeter) and $128 \times 88 \times 158.6$ mm^3 (upper calorimeter) and were placed 9.8 m downstream of the exit window. In order to diminish the exposition to synchrotron radiation, they were positioned off the xz-plane. The luminosity was determined by measuring coincident energy deposits of similar size (in energy) in the two calorimeters.

6m (electron) tagger: The 6m tagger was a small tungsten/scintillator spaghetti calorimeter located at about 6m from the interaction point in the rear region of the ZEUS detector. The tagger had been designed in order to measure the electrons from Bethe-Heitler processes. It was primarily used to cross-calibrate the two other luminosity components and to determine their acceptance. Within the measurement of the longitudinal structure function, F_L, the tagger was also used to determine the photoproduction background to that measurement. A detailed description of the tagger including the design of the dedicated 6m tagger-trigger, the position and energy reconstruction, the calibration procedure and the monitoring of the radiation damage is given in the next chapter.

---

[1] For the luminosity measurement the uncorrected energy deposit in the cal, E_{cal}, was used.

Chapter 11

ZEUS 6m tagger

11.1 Design

The 6m tagger was a sampling calorimeter with 'spaghetti-like' structure with tungsten alloy (DENSIMET with a nominal composition of 90.5 % W, 7 % Ni, 2.5 % Cu [111]) as absorber and organic scintillator (fibres of type SCSF-38M) as active material. The tagger had a dimension of $x \times y \times z = 84 \times 23.4 \times 100$ mm^3. It consisted of 84 absorber plates (stacked in x), each with a dimension of $1 \times 23.4 \times 100$ mm^3. In order to accommodate the scintillating fibres, half-cylindrical grooves with a diameter of 0.56 mm were milled into the plates (22 on one and 23 on the other side). In total the tagger contained 1890 fibres. The fibres had a length of 1.5 m and a diameter of 0.5 mm. The part of the fibres not contained inside the tungsten body of the tagger was used to guide the produced light to one of the 70 photomultipliers (PMTs) of type Hamamatsu R7400U-03, which each read out the signals of 27 fibres. In this way the tagger was divided into a matrix-like structure of 5×14 cells, each with a dimension of 6×4.68 mm^2 (see figure 11.1).

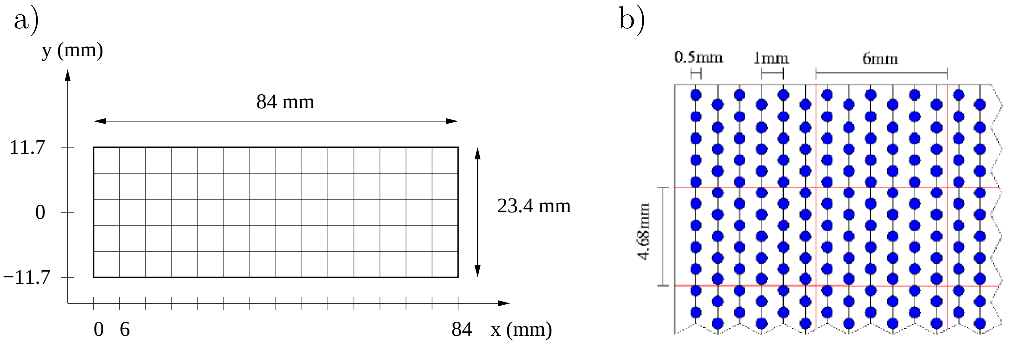

Figure 11.1: Sketch of the 6m tagger (xy view) and definition of the 6m tagger coordinate system. The tagger was divided into a matrix-like structure of 5×14 cells, each with a dimension of 6×4.68 mm^2. Each cell contained 27 scintillating fibres.

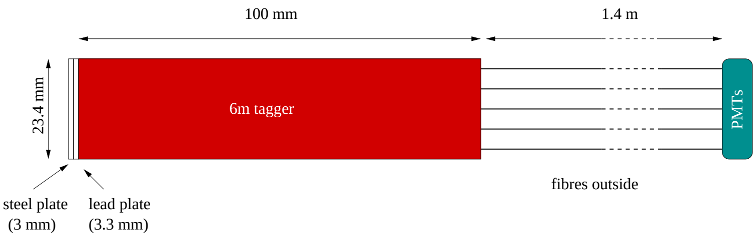

Figure 11.2: Sketch of the 6m tagger (yz view). The tagger had a dimension of $84 \times 23.4 \times 100$ mm^3. It contained 1890 scintillating fibres with a diameter of 0.5 mm. The fibres had a total length of 1.5 m. The part of the fibres not contained inside the tagger was used to guide the produced light to the 70 photomultipliers which each read out the signals of 27 fibres. The front surface of the tagger was covered by a lead and a steel plate with thicknesses of 3.3 mm and 3 mm, respectively.

In order to protect the tagger from scattered synchrotron radiation, its front surface was covered by a lead and a steel plate with thicknesses of 3.3 mm and 3 mm, respectively. The design of the tagger is shown in figures 11.1 (xy view) and 11.2 (yz view). The 6m tagger coordinate system is defined in figure 11.1.

The 6m tagger was located inside the HERA quadrupole magnet GIR5 (see figure 11.3). Its front surface was situated at $z = -5.512$ m (given in the ZEUS coordinate system). The distance from the left side of the tagger to the nominal electron (positron) beam orbit was 64.5 mm (68.8 mm). Vertically the tagger was approximately centred with respect to the beam. In this way it covered the y range from -11.7 to 11.7 mm.

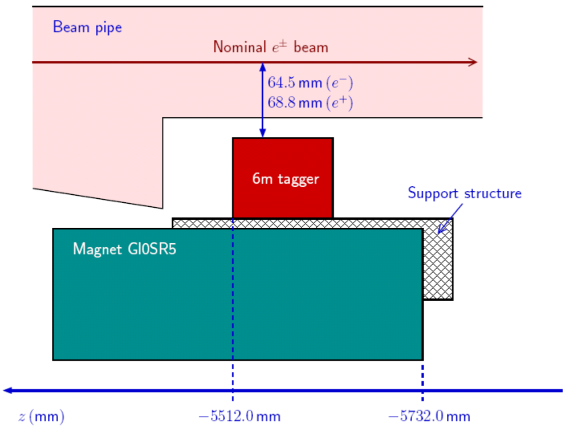

Figure 11.3: Position of the 6m tagger inside the quadrupole magnet GIR5 in the ZEUS reference frame. Figure taken from [112].

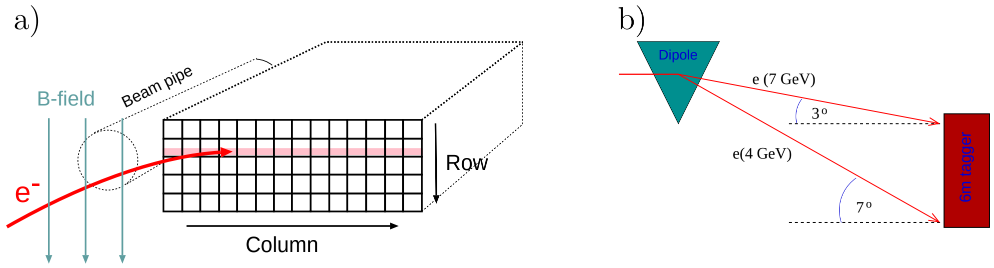

Figure 11.4: a) The bending power of the magnetic dipole field in front of the tagger was such that electrons with energies of about $4-7$ GeV hit the tagger. The impact position on the tagger was correlated to the energy of the incident electron. b) Depending on their energy the electrons hit the tagger with incident angles of about $3-7\,\text{deg}$ w.r.t. the normal in the xz plane. Figures taken from [112].

The bending power of the magnetic dipole field in front of the tagger was such that electrons with energies of about $4-7$ GeV [112], which were produced with small opening angles at the ZEUS interaction point, were deflected out of the nominal beam orbit and hit the tagger (see figure 11.4). The impact position on the tagger was correlated to the energy of the incident electron. With decreasing energy the electrons were bent more strongly and thus hit the tagger at the right side corresponding to larger x values (in the coordinate system of the tagger). Depending on their energy the electrons hit the tagger with incident angles of about $3-7^\circ$ w.r.t. the normal in the xz plane (see figure 11.4b).

The main properties of the 6m tagger are given in table 11.1. The radiation length of the tagger (mixture of absorber and fibres), X_0^{tag}, has been calculated according to [113]

$$X_0^{\text{tag}} = \left(\frac{\omega^{\text{abs}}}{X_0^{\text{abs}}} + \frac{\omega^{\text{act}}}{X_0^{\text{act}}} \right)^{-1}, \tag{11.1}$$

where $\omega^{\text{abs(act)}}$ and $X_0^{\text{abs(act)}}$ are the weight fractions and the radiation lengths of the tungsten absorber (the active scintillator material). The weight fractions have been determined according to the geometry of the tagger. The Molière radius of the tagger R_M^{tag} has been calculated according to [113]

$$R_M^{\text{tag}} = E_s \left(\frac{\omega^{\text{abs}} E_c^{\text{abs}}}{X_0^{abs}} + \frac{\omega^{\text{act}} E_c^{\text{act}}}{X_0^{\text{act}}} \right)^{-1} \quad \text{with} \quad E_c = \frac{800\ \text{MeV}}{Z+1.2}, \tag{11.2}$$

where $E_s = 21.21$ MeV and E_c are the scaling energy and the critical energy, respectively. The atomic numbers of the absorber and the scintillator have been approximated by the atomic number of tungsten ($Z_W = 74$) and carbon ($Z_C = 6$), respectively.

Dimension of the tagger (tungsten body)	$84 \times 23.4 \times 100$ mm^3 $(x \times y \times z)$
Width of the front lead plate	$d_{\text{lead}} = 3.3$ mm
Width of the front steel plate	$d_{\text{steel}} = 3.0$ mm
Absorber	84 plates of tungsten alloy (DENSIMET)
Dimension of the plates	$1 \times 23.4 \times 100$ mm^3 $(x \times y \times z)$
Number and diameter of the grooves	$N_{\text{groove}} = 22/23$, $d = 0.56$ mm
Density, absorption length, Molière radius	$\rho = 17.0\ \frac{\text{g}}{\text{cm}^3}$, $X_0 = 3.5$ mm, $R_M = 6.977$ mm
Active material	1890 fibres of organic scintillator (type SCSF-38M)
Diameter, length	$d = 0.5$ mm, $l \approx 1.5$ m
Emission peak, decay time, att. length	$\lambda_{emiss}^{max} = 428$ nm, $t_d = 2.3$ ns, $\lambda > 3$ m
Density, absorption length, Molière radius	$\rho = 1.032\ \frac{\text{g}}{\text{cm}^3}$, $X_0 = 424$ mm, $R_M = 80.919$ mm
Mixture	(absorber + scintillator)
Density, absorption length, Molière radius	$\rho = 13.169\ \frac{\text{g}}{\text{cm}^3}$, $X_0 = 3.569$ mm, $R_M = 7.104$ mm
Photomultiplier	Hamamatsu, type R7400U-03

Table 11.1: Main properties of the 6m tagger, the absorber, the active material and the photomultipliers. The radiation length of tungsten ($X_0 = 3.5$ mm) is used as a approximation for the radiation length of the densimet absorber.

11.2 6m-tagger trigger

The 6m tagger was used to determine the photoproduction background to the measurement of the longitudinal structure function of the proton, F_L [114]. For this measurement a dedicated 6m tagger first-level trigger was developed. The aim of the trigger was to select with high efficiency and purity those events, where an electron candidate was found in the tagger.

Trigger design

A fiducial volume was defined such that it contained all cells excluding those located within the first and last column and row of the 6m tagger. For the cells contained within the fiducial volume, the mean values and the widths of the pedestals, $\overline{\text{Ped}}_i$ and σ_i^{Ped}, were determined by fitting Gauss functions to the signal distributions (given in ADC counts) recorded during empty bunch crossings. Figure 11.5 shows as an example the pedestal distributions for different channels as obtained from run 57050. As can be seen the distributions are well described by the Gaussian fits. For every channel an individual threshold was then defined according to

$$T_i(n) = \overline{\text{Ped}}_i + n\ \sigma_i^{\text{Ped}} \quad n \in 0, 1, 2, 3, \dots \quad , \tag{11.3}$$

where n is a parameter that was tuned in order to optimise the efficiency-to-noise ratio. For the final trigger design it was set to n=8. An event was selected by the trigger if at least one cell within the fiducial volume had a signal above its threshold. In order to guarantee a stable performance of the trigger the pedestals were carefully monitored and the thresholds were adjusted if necessary. A new set of thresholds was implemented whenever the pedestals had changed such, that for at least one channel

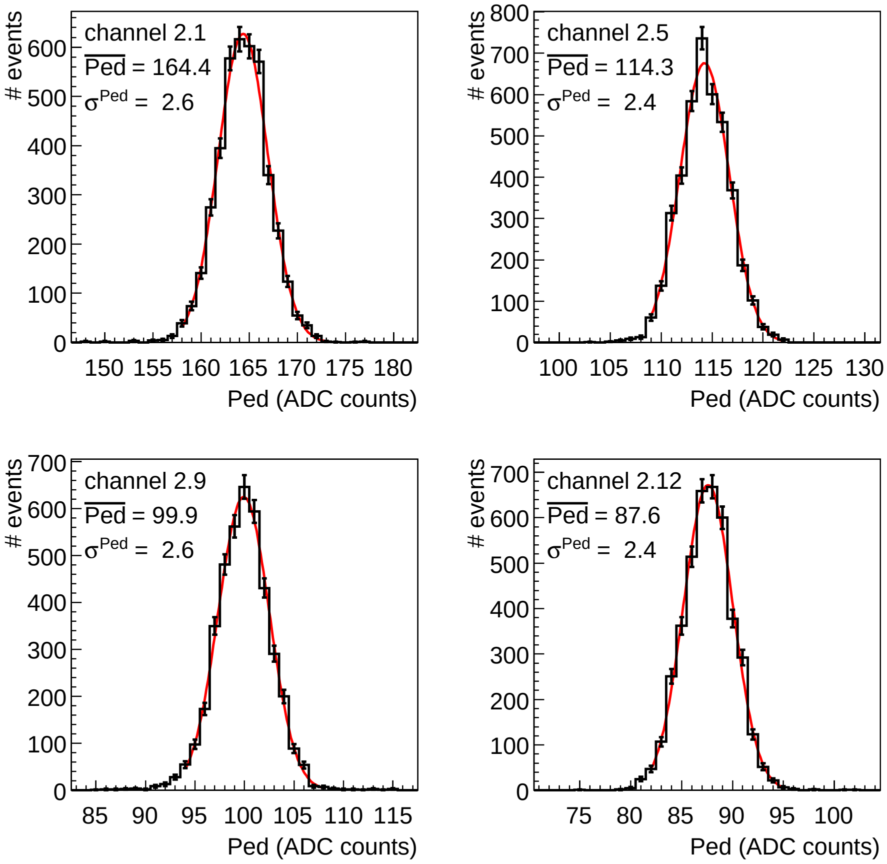

Figure 11.5: Pedestal distributions for different channels of the 6m tagger recorded during empty bunch crossings. The distributions are obtained from run 57050. In order to determine the mean values and the widths of the pedestals, $\overline{\text{Ped}}_i$ and σ_i^{Ped}, the distributions are fitted with Gauss functions.

within the fiducial volume the threshold calculated from equation 11.3 differed by more than 4 ADC counts from the one used.

Trigger efficiency

The efficiency of the trigger is determined using data from run 57040. The event sample contains all kinds of physics events and background and thus events with and without an electron in the tagger. In order to select those events where an electron hits the tagger the following selection cuts are applied:

- **electron energy:** The reconstructed energy of the electron candidate (see sections 11.3 and 11.4) has to be within the range of 4 to 11 GeV ($4 < E_{\text{tag6}} < 11$ GeV);

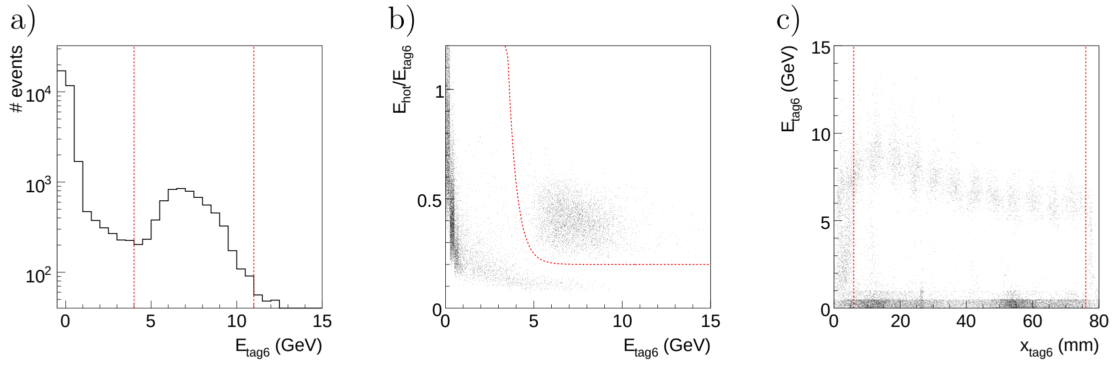

Figure 11.6: a) Distribution of the reconstructed energy E_{tag6}, b) fraction of the reconstructed energy contained within the hottest cell as a function of E_{tag6}, reconstructed energy as a function of the reconstructed position, x_{tag6}. The applied cuts are indicated by the dashed lines.

- **shower shape:** The fraction of the measured energy deposited in the hottest cell has to exceed a certain energy-dependent value ($E_{\text{hot}}/E_{\text{tag6}} > 0.2 + \exp(-7 - \frac{2 \cdot E_{\text{tag6}}}{\text{GeV}})$). This empirically derived cut is used to separate events with well-confined electromagnetic showers from events with a smeared-out shower profile. The ratio $E_{\text{hot}}/E_{\text{tag6}}$ is determined using calibrated energies;
- **x position:** The reconstructed x position (see section 11.3) has to be within the range of $6 < x_{\text{tag6}} < 76$ mm. This cut removes events where the electron hits the tagger at the edges and where the shower is not completely contained within the tagger, thus leading to a bad reconstruction of the electron energy.

Figure 11.6 shows the distributions of the reconstructed energy, E_{tag6}, the fraction $E_{\text{hot}}/E_{\text{tag6}}$ as a function of E_{tag6}, and the energy E_{tag6} as a function of the reconstructed x position, x_{tag6}. The applied cuts are indicated by the dashed lines.

According to the selection criteria the data sample is divided into events with and without an electron candidate in the tagger, that is events that should and should not be selected by the 6m-tagger trigger. The efficiency of the trigger is defined as the fraction of selected events (events with an electron candidate in the tagger) that pass the (simulated) trigger:

$$\text{eff} = \frac{N^{\text{trigger \&\& selection}}}{N^{\text{selection}}}. \tag{11.4}$$

The noise is defined as the fraction of events without an electron candidate in the tagger (rejected events) that pass the trigger:

$$\text{noise} = \frac{N^{\text{trigger \&\& }\overline{\text{selection}}}}{N^{\overline{\text{selection}}}}. \tag{11.5}$$

Figure 11.7 shows the efficiencies versus noise values for different values of the parameter n, that is different sets of thresholds, $T_i(n)$ (see equation 11.3). For the final

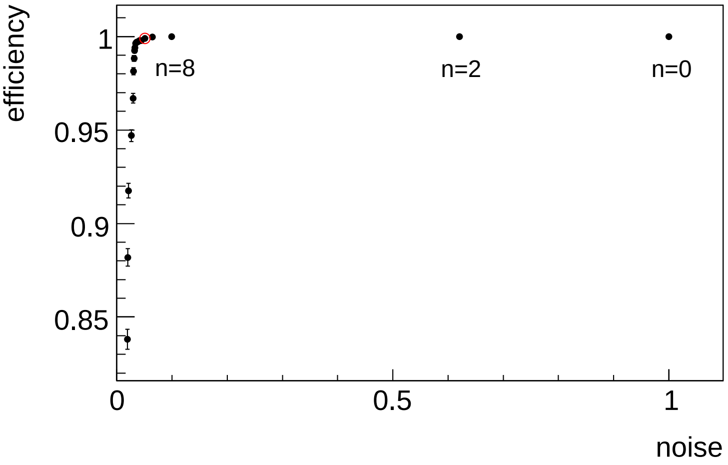

Figure 11.7: Efficiency and noise of the 6m-tagger trigger for different values of the parameter n corresponding to different sets of thresholds $T_i(n)$. For the final trigger design the thresholds were set to $T_i(n) = \overline{\mathrm{Ped}}_i + 8\ \sigma_i^{\mathrm{Ped}}$. The corresponding value is indicated by the circle.

trigger design n was set to $n = 8$. The corresponding (noise,eff) value is indicated by the circle. The efficiency for the final trigger design is 99.9 %, while the noise is reduced to 5.1 %. Figure 11.8 shows the efficiency as a function of the reconstructed horizontal position, x_{tag6}.

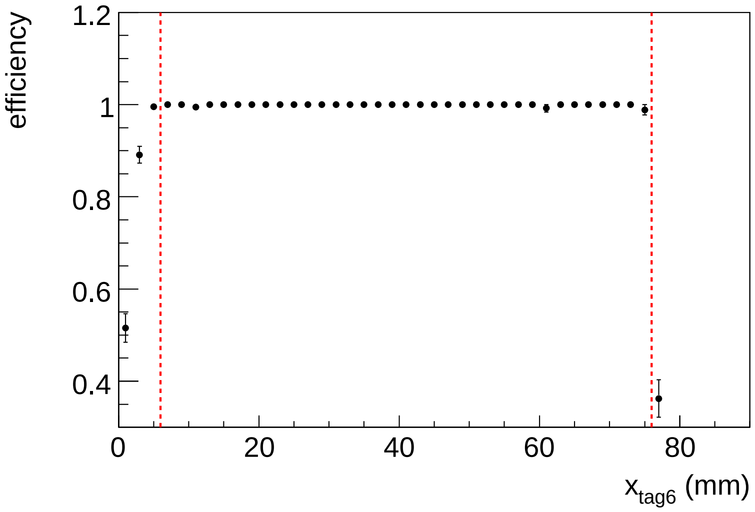

Figure 11.8: Efficiency of the 6m-tagger trigger as a function of the reconstructed horizontal position, x_{tag6}. Within the fiducial volume the efficiency is almost 100 %.

11.3 Position and energy reconstruction

An electron that hit the 6m tagger produced an electromagnetic shower. Since the Molière radius of the tagger ($R_M \approx 7$ mm) was in the order of the cell size ($6 \times 4.68\,\mathrm{mm}^2$), most energy was deposited in just a few cells around the shower maximum. Most of the cells thus only contain noise. In order to optimise the signal-to-noise ratio it is thus convenient to define a reconstruction volume, V_{rec}, which contains (almost) all the energy of the electromagnetic shower and is at the same time as small as possible. For the reconstruction of both the energy and the position of the electromagnetic shower the reconstruction volume is defined such that it contains those 3×3 cells centred around the hottest cell, that is the cell with the largest (calibrated) energy deposit. A simulation showed that about 90 % of the shower energy are contained within this 3×3 volume [115]. If the hottest cell is located at the edges of the tagger and the reconstruction volume thus exceeds the tagger, the reconstruction volume is reduced to those cells contained within the tagger [112] (see figure 11.9).

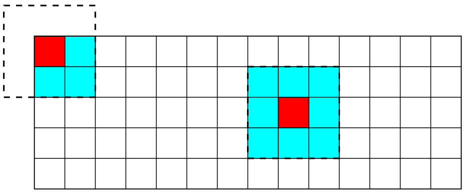

Figure 11.9: Reconstruction volume of the 6m tagger. The volume contains those 3×3 cells centred around the hottest cell. If the reconstruction volume exceeds the volume of the 6m tagger, it is reduced to those cells contained within the tagger.

The energy of the electromagnetic shower is reconstructed from the cells within the reconstruction volume by summing up their calibrated signals (energies) according to

$$E_{\mathrm{tag6}} = \sum_{V_{\mathrm{rec}}} E_i. \tag{11.6}$$

The position of the electromagnetic shower is reconstructed from the energy-weighted cell positions according to

$$x_{\mathrm{tag6}} = \frac{\sum_{V_{\mathrm{rec}}} x_i E_i}{\sum_{V_{\mathrm{rec}}} E_i} \quad \text{and} \quad y_{\mathrm{tag6}} = \frac{\sum_{V_{\mathrm{rec}}} y_i E_i}{\sum_{V_{\mathrm{rec}}} E_i}, \tag{11.7}$$

where x_i and y_i are the coordinates of the centre of cell i given in the coordinate system of the tagger and E_i is its calibrated signal (energy). The sum takes into account all cells within the reconstruction volume. The obtained position is corrected for non-linearities by applying a polynomial correction [115].

11.4 Calibration

As described before, the signals of the 27 scintillating fibres contained within one cell were read out by one of the 70 photomultipliers. The signals of the PMTs were converted into ADC counts, A_i, by analogue-to-digital converters. The ADC counts are converted into energies, E_i, by subtracting the mean pedestal, $\overline{\mathrm{Ped}}_i$ (given in ADC counts), and multiplying a conversion factor, $c^{\mathrm{base}} = 0.0157875 \, \frac{\mathrm{GeV}}{\mathrm{ADC\ count}}$:

$$E_i \;=\; c^{\mathrm{base}}(A_i - \overline{\mathrm{Ped}}_i). \tag{11.8}$$

The mean pedestal values are determined from Gauss functions fitted to the signal distributions recorded during empty bunch crossings. Pedestals are determined for all runs with more than 15,000 Third-Level-Trigger events. For smaller runs the pedestals obtained from the closest run with more than 15,000 Third-Level-Trigger events are used.

In order to obtain calibrated cell energies, four different sets of multiplicative calibration constants are applied: A first set of calibration constants is obtained from test beam measurements [116]. The set consists of 70 different calibration constants, one for each cell.

A second set of calibration constants [117] is obtained using Bethe-Heitler events in which both the photon and the electron are detected by the spectrometer and the 6m tagger, respectively (coincidence between spectrometer and 6m tagger). The basic assumption is that the sum of the electron energy measured with the 6m tagger, E_{tag6}, and the photon energy measured with the spectrometer, E_{spec}, has to be equal to the lepton beam energy , E_e,

$$E_e \;=\; E_{\mathrm{tag6}} + E_{\mathrm{spec}}. \tag{11.9}$$

This assumption is used to determine a set of 14 calibration constants, one for every column of the tagger. Calibration constants are obtained for each run with more than 15,000 Third-Level-Trigger events. For smaller runs the calibration constants of the closest run for which constants have been determined are used. This calibration is optimised for a reconstruction volume of 5 × 5 cells.

The final calibration procedure [112] is again based on Bethe-Heitler events. The procedure is separated into a vertical and a horizontal calibration. The vertical calibration procedure utilises the expected transverse shower profile of the electromagnetic showers in the tagger to obtain a consistent relative calibration of the cells within one column. The procedure introduces one calibration constant per cell. The final horizontal calibration procedure is again based on the assumption given by equation 11.9. The calibration is used to optimise the calibration for a reduced reconstruction volume of 3 × 3 cells. The horizontal calibration procedure introduces one calibration constant per column.

11.5 Radiation damage and Cobalt scans

As the 6m tagger was located very close to the beam pipe (see figure 11.3), it was exposed to a high rate of scattered synchrotron radiation.[1] In addition, due to the high HERA II luminosity, it was exposed to a high rate of Bethe-Heitler electrons. In irradiated scintillators absorption centres are created that cause a reduction of the attenuation length, resulting in a reduction of the response signal. A simple model used to simulate the described effects is presented in section 11.5.1. In order to monitor the radiation damage a series of 12 Cobalt scans was performed from December 2003 to July 2007. At each scan the response of the tagger to a Cobalt-60 (^{60}Co) source of known activity was recorded. A fraction of the recorded data has been presented in [118] and [117]. This is, however, the first time that the complete data set is presented (section 11.5.2).

11.5.1 Simulation of the radiation damage

A high-energy electron hitting an absorber produces an electromagnetic shower. The longitudinal shower profile can be parametrised according to [113]

$$\frac{dE}{dt}(t) \;=\; E_0 b\,\frac{(bt)^{a-1}e^{-bt}}{\Gamma(a)}, \tag{11.10}$$

where dE/dt is the energy loss per length in units of the radiation length ($t = x/x_0$), E_0 is the energy of the incoming electron and a and b are parameters that depend on the material of the absorber. The two parameters are related to each other according to

$$a \;=\; 1 + b\left(\ln\frac{E}{E_c} - 0.5\right), \tag{11.11}$$

where E_c is the critical energy that is defined as the energy at which the energy loss due to Bremsstrahlung is equal to the energy loss due to ionisation.
Due to the radiation, absorption centres are created inside the scintillating fibres resulting in a decrease of the attenuation length, λ. The number of absorption centres created within an interval $[t, t+dt]$, $N_{\text{abs}}(t)dt$, is proportional to the total flux of incoming electrons, Φ, and to the energy deposition within this interval, dE:

$$N_{\text{abs}}(t,\Phi)dt \;=\; \alpha\Phi dE. \tag{11.12}$$

α is a parameter that depends on the material of the scintillating fibre. The attenuation length, λ, is related to the number of absorption centres created within the interval $[t, t+dt]$ according to [118]

$$\lambda(t,\Phi) \;=\; \frac{\lambda_0}{1+\frac{N_{\text{abs}}(t,\Phi)}{N_0}} = \frac{\lambda_0}{1+\alpha'\Phi\frac{dE}{dt}}, \tag{11.13}$$

---

[1] Since the 6m tagger was located at the inside of the HERA ring it was not exposed to direct synchrotron radiation.

where N_0 and λ_0 are the intrinsic number of absorption centres and the intrinsic attenuation length of the fibres before irradiation. Due to the finite attenuation length the signal strength of light traversing a scintillating fibre is reduced. The reduction of the signal strength per interval dL/dt is given according to

$$\frac{dL}{dt} = -\frac{LX_0}{\lambda(t,\Phi)}. \tag{11.14}$$

Equations 11.10-11.14 have been used to simulate the response of the 6m tagger to the radiation of the Cobalt source as a function of the longitudinal position of the source. For the simulation the parameter b has been set to 0.5 and the critical energy, E_c, has been calculated for the tungsten absorber (Z=74) according to E_c = 800 MeV/(Z + 1.2). The radiation length has been set to X_0 = 3.5 mm and the intrinsic attenuation length of the fibres has been set to λ_0 = 3.5 m. Simulations have been performed for electron fluxes of $\alpha'\Phi = 100, 200, 500, 1000, 2000, 5000, 10000, 20000$ and $50000\ \frac{1}{\mathrm{GeV}}$.

Figure 11.10a shows the longitudinal profile, dE/dt, of an electromagnetic shower in tungsten induced by a 5 GeV electron. Figure 11.10b shows, for different values of the electron flux Φ, the resulting attenuation lengths of the scintillating fibres as functions of the longitudinal position within the tagger. The attenuation length decreases with increasing values of the electron flux. Figure 11.11 shows the simulated signal strengths as functions of the longitudinal position of the ^{60}Co source. At $z = 100$ mm the signal strengths are set to one. This boundary condition corresponds to a readout directly at the rear end of the tagger. Losses within the fibres outside the tagger are not incorporated in the simulation.

Time dependence of the signal
At a given position, t', the attenuation length only depends on the electron flux ($\lambda = \lambda(\Phi)$) and the solution of equation 11.14 is given according to

$$L = L_0 \exp\left(-\frac{X_0}{\lambda}t'\right) = L_0 \exp\left(-\frac{X_0}{\lambda_0}\left(1 + \alpha'\Phi\frac{dE}{dt}\right)t'\right). \tag{11.15}$$

Assuming a constant mean rate of electrons hitting the tagger, R_e, the total electron flux is related to the time, τ, according to $\Phi = R_e\,\tau$ and the time dependence of the signal strength at a given position can be parametrised by an exponential function,

$$L(\tau) \propto \exp(-C\tau). \tag{11.16}$$

Although the rate of electrons hitting the tagger was, at time scales in the order of hours and days, at HERA strongly fluctuating, at larger scales (within the order of months) the assumption of a constant mean rate seems to be a reasonable approximation.

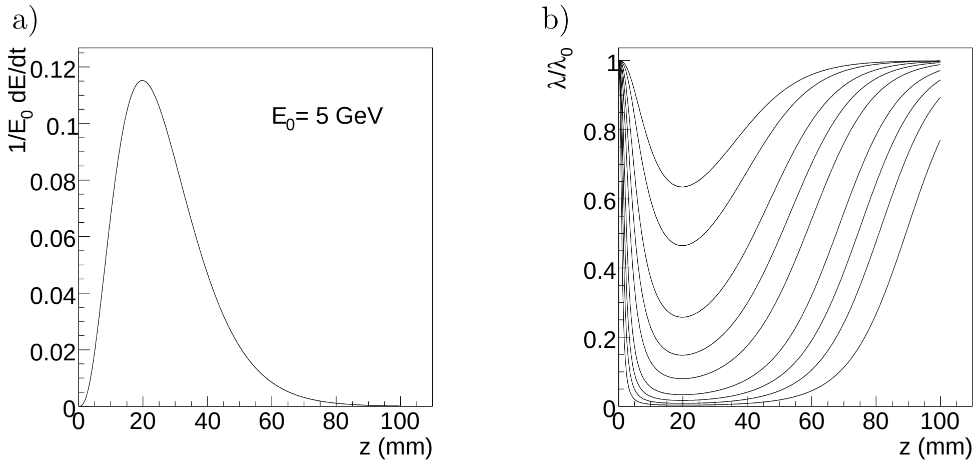

Figure 11.10: a) Longitudinal shower profile dE/dt of an electromagnetic shower in tungsten induced by a 5 GeV electron. b) Resulting attenuation lengths of the scintillating fibres as functions of the longitudinal position within the tagger. The different curves correspond to electron fluxes of $\alpha'\Phi = 100,\ 200,\ 500,\ 1000,\ 2000,\ 5000,\ 10000,\ 20000 \text{ and } 50000\ \frac{1}{\text{GeV}}$. The attenuation length decreases with increasing values of the electron flux.

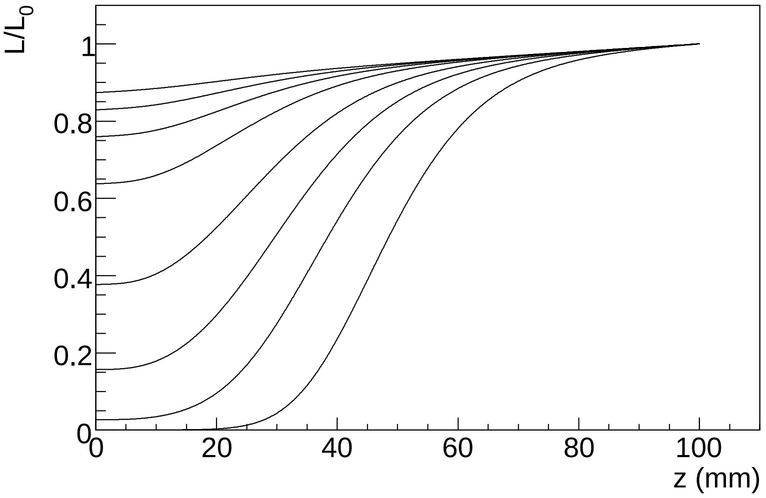

Figure 11.11: Simulated signal strengths as functions of longitudinal position of the ^{60}Co source. At $z = 100$ mm the signal strengths are set to one. This boundary condition corresponds to a readout directly at the rear end of the tagger. Losses within the fibres outside the tagger are not incorporated in the simulation. The different lines correspond to electron fluxes of $\alpha'\Phi = 100,\ 200,\ 500,\ 1000,\ 2000,\ 5000,\ 10000,\ 20000 \text{ and } 50000\ \frac{1}{\text{GeV}}$.

11.5.2 Cobalt scans

In order to monitor the radiation damage, 12 Cobalt scans were performed from December 2003 to July 2007. During each scan the response of each channel to the irradiation with a ^{60}Co source was recorded as a function of the longitudinal (z) position of the source. ^{60}Co decays via beta decay into the stable isotope ^{60}Ni emitting one electron of 316 keV and two photons of 1.17 and 1.33 MeV, respectively. The half life time of ^{60}Co is 5.271 years. The dates of the scans as well as the corresponding activity of the utilised Cobalt source are given in table 11.2.

scan number	date (dd.mm.yyyy)	Δt (days)	^{60}Co activity (MBq)
0	04.12.2003	(-63)	47.91
1	05.02.2004	0	46.83
2	06.05.2004	91	45.32
3	03.06.2004	119	44.87
4	16.08.2004	193	43.69
5	05.01.2005	335	41.51
6	13.04.2005	433	40.07
7	07.12.2005	671	36.78
8	02.05.2006	817	34.89
9	06.09.2006	944	33.33
10	06.12.2006	1035	32.26
11	02.07.2007	1243	29.93

Table 11.2: Number of the scan, date of the scan, time difference to scan number 1, and activity of the ^{60}Co source at the date of the scan.

In order to be able to locate the source at a well defined and reproducible position, 10 guiding tubes were permanently mounted on the surface of the tagger along the z direction (parallel to the fibres). The positions of the guiding tubes named top1-top5 and bot1-bot5 are indicated in figure 11.12. The figure also shows the cell-tube assignment which defines which tube was used to monitor which cell. An alternative cell-tube assignment used to estimate the related systematic uncertainty is also shown. During the scans the source, which was mounted on the tip of a small wire, was moved inside the guiding tubes using a stepping motor. In this way the response of the channels to the ^{60}Co source could be recorded as a function of the longitudinal z position of the source. For the scans the outputs of the photomultipliers were connected to the ADC cards of a portable computer which was used to record the response signals. For every scan pedestal values were taken without cobalt irradiation in order to be subtracted from the signals recorded during the scan.

Figure 11.13 shows the signals recorded for channels 2.0 (located close to the beam pipe) and 2.6 (located in the middle of the tagger). The position of the cells is indicated in figure 11.12. The 11 curves correspond to the 11 scans taken into account

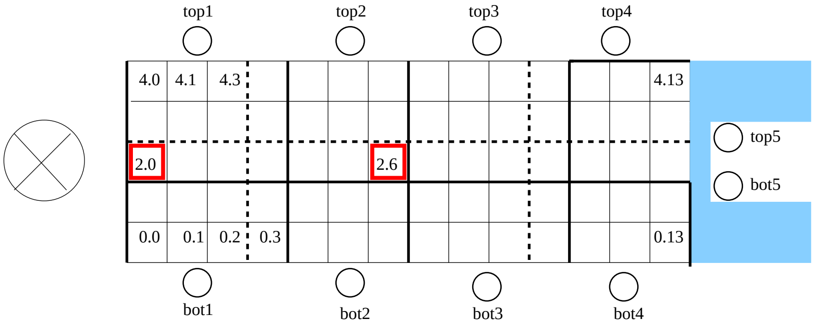

Figure 11.12: Sketch of the 6m tagger surface (xy view), numbering scheme of the cells and position of the guiding tubes. The cell-tube assignment is indicated by the black bold line. An alternative assignment used to determine the related systematic uncertainty is indicated by the dashed lines. The beam pipe is indicated by the crossed circle on the left side of the tagger.

for this analysis.[2] The signal, corrected for the decreasing activity of the ^{60}Co source and for the pedestal, monotonously decreases from the first to the last scan. The individual curves show a characteristic behaviour: A strong rise in the range from 0 to 20 mm followed by a smooth, almost linear increase between 20 and 90 mm. For positions larger than 90 mm the slope starts to rise again. The observed behaviour is not only related to the position-dependent attenuation length, but also depends on purely geometrical effects: If the source is placed at the front edge of the tagger ($z = 0$ mm), the tagger only covers a quarter of the solid angle of the (isotropically) emitted radiation. As the source is moved towards larger z values, more and more radiation hits the tagger leading to a strong increase of the signal. For positions inside the tagger (20 to 90 mm) half of the solid angle of the emitted radiation is covered by the tagger. The slow increase of the signal in this range is related to the decreasing distance the produced light has to cover inside the fibres. The slope of the curve within this range depends on the (position-dependent) attenuation length. At the rear end of the tagger ($z \gtrsim 90$ mm), some fraction of the radiation hits the unprotected fibres outside the tungsten body of the tagger, leading to a strong increase of the signal.

In order to correct the data for the purely geometrical effects described above, the signals of the scans are normalised to the first scan. Figure 11.14 shows the normalised signals for channels 2.0 and 2.6. The curves again exhibit a characteristic behaviour: An almost flat tail in the z range from 0 to 20 mm followed by an almost linear increase towards larger z values. This characteristic behaviour is well reproduced by the simulation as described in section 11.5.1 (see figure 11.11). The main difference between the simulated and the recorded signal is the signal strength

---

[2] The analysis of the data from the first scan (scan number 0) revealed a number of dead channels that were repaired after the scan [117]. For the presented analysis, the data of the first scan are not taken into account.

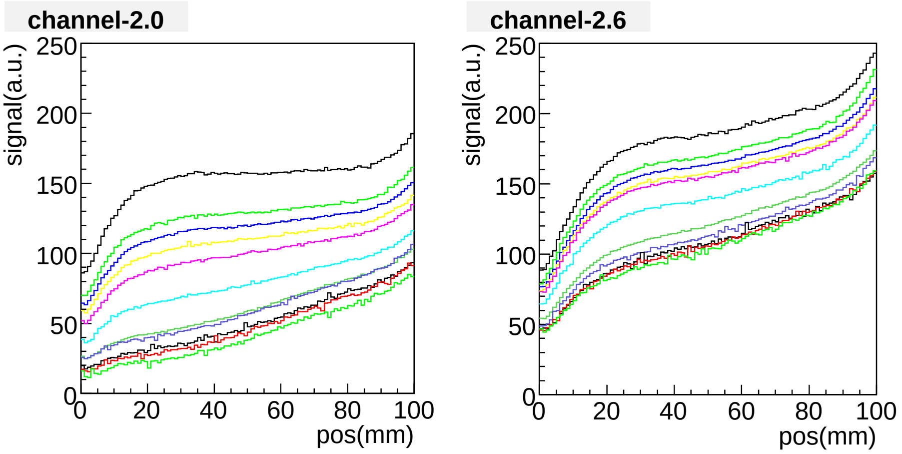

Figure 11.13: Signal strength as a function of the longitudinal position of the Cobalt source for channels 2.0 (located near the beam pipe) and 2.6 (located in the centre of the tagger). The signals are corrected for the decrease of the activity of the ^{60}Co source. The lines correspond to the 11 scans taken into account for this analysis. The signal decreases from the first to the eleventh scan.

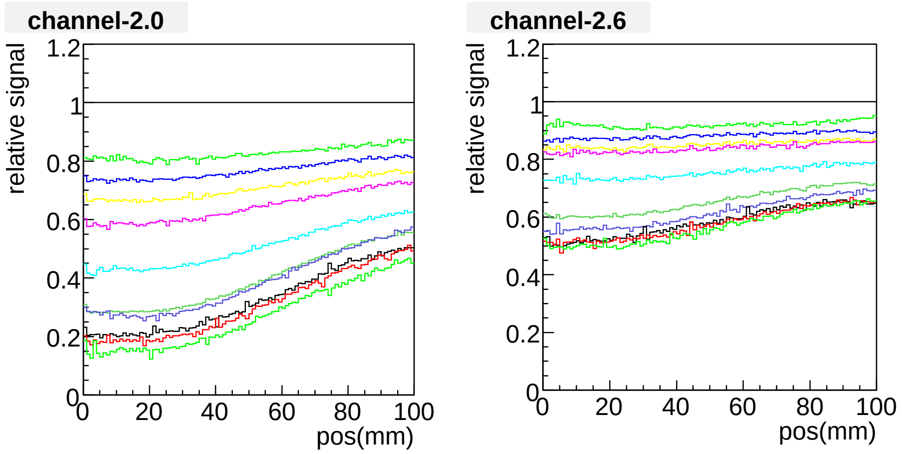

Figure 11.14: Relative signal strength as a function of the longitudinal position of the Cobalt source for channels 2.0 (located near the beam pipe) and 2.6 (located in the centre of the tagger). The signals are corrected for the decrease of the activity of the ^{60}Co source and are normalised to the signal of the first scan. The lines correspond to the 11 scans taken into account for this analysis. The signal decreases from the first to the eleventh scan. The decrease of the signal is more pronounced for channel 2.0, located near the beam pipe.

at the rear end of the tagger ($z = 100$ mm). While it is set to one within the simulation, the signals recorded at $z = 100$ mm exhibit a decrease which is related to

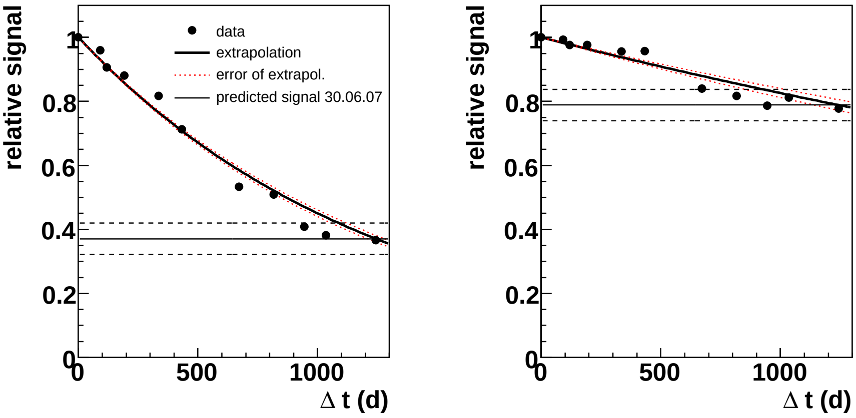

Figure 11.15: Relative signal (R_i^{in}) versus time for fibres inside the tagger for channels 2.0 (left plot) and 2.6 (right plot). Measured values are indicated by black dots. The data of the first seven scans were fitted by exponential functions (solid line) to extrapolate to the last day of the HERA operation in June 2007. The error on the fit is indicated by the dashed lines. The value predicted for June 31^{st} 2007 is indicated by the horizontal solid line. The systematic uncertainty related to the cell-tube assignment is indicated by the horizontal dashed lines.

the radiation damage of the fibres outside the 6m tagger, which has not been taken into account in the simulation.

In order to disentangle the reduction of the signal due to the radiation damage of the fibres inside the tagger from that due to the damage of the fibres outside the tagger, for each scan ,i, two quantities, R_i^{in} and R_i^{out}, are defined according to

$$R_i^{\mathrm{in}} = \frac{\left(\frac{S_{10\mathrm{mm}}}{S_{90\mathrm{mm}}}\right)_i}{\left(\frac{S_{10\mathrm{mm}}}{S_{90\mathrm{mm}}}\right)_1} \quad \text{and} \quad \mathrm{R_i^{out}} = \frac{(\mathrm{S_{100mm}})_\mathrm{i}}{(\mathrm{S_{100mm}})_1}, \tag{11.17}$$

where S_z is the signal at $z = 10, 90$ or 100 mm and the relative signal strength, R^{in} (R^{out}), is a measure for the radiation damage of the fibres inside (outside) the tagger.

Figures 11.15 and 11.16 show the R^{in} and R^{out} values obtained for channels 2.0 and 2.6 as a function of time. The values obtained from the first seven scans were fitted by exponential functions in order to get an estimate for the relative signal strengths at the end of the HERA life time. The values predicted for the last day of the HERA operation at June 30^{st} 2007 are indicated by the solid horizontal line.

In order to estimate the systematic uncertainty on the predicted values the analysis was repeated using an alternative cell-tube assignment. The related

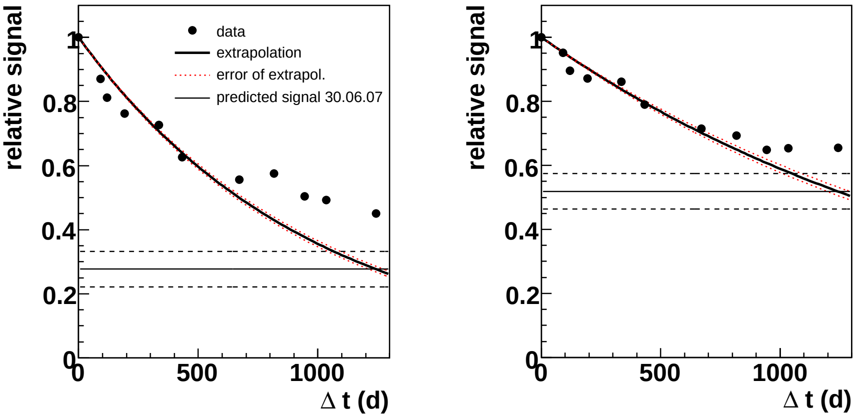

Figure 11.16: Relative signal (R_i^{out}) versus time for fibres outside the tagger for channels 2.0 (left plot) and 2.6 (right plot). Other details as in caption to figure 11.15.

uncertainty is determined according to

$$\sigma_{\text{sys}} = \frac{1}{N}\sum_{i=1}^{N} |R^1_{\text{pred}} - R^2_{\text{pred}}|, \tag{11.18}$$

where R^1_{pred} and R^2_{pred} are the predicted values obtained from the two different cell-tube assignments. The sum runs over all cells for which two different assignments are available (see figure 11.12). The obtained systematic errors on R^{in} and R^{out} are $\sigma^{\text{in}}_{\text{sys}} = 0.049$ and $\sigma^{\text{out}}_{\text{sys}} = 0.055$ [118].

The statistic uncertainty on R^{in} and R^{out} is estimated from cells that show no systematic reduction of the (relative) signal strength R^{in}.[3] For those cells the deviation of R^{in}_i from one is caused by statistical fluctuations only. The related uncertainty is determined according to

$$\sigma^2_{stat} = \frac{1}{N}\sum_{i=1}^{N}(1 - R_i^{\text{in}})^2, \tag{11.19}$$

where the sum runs over all scans and the respective cells. The obtained statistical uncertainty is $\sigma_{\text{stat}} = 0.019$ [118]. The total uncertainty is thus dominated by the systematic uncertainty related to the cell-tube assignment.

Results

Radiation damage inside the tagger

Figure 11.17 shows the relative signal strength (R^{in}_{11}) for each channel recorded at the last scan at July 2^{nd} 2007, two days after the shutdown of HERA. The box size

---

[3] For R^{out} no such channels are available.

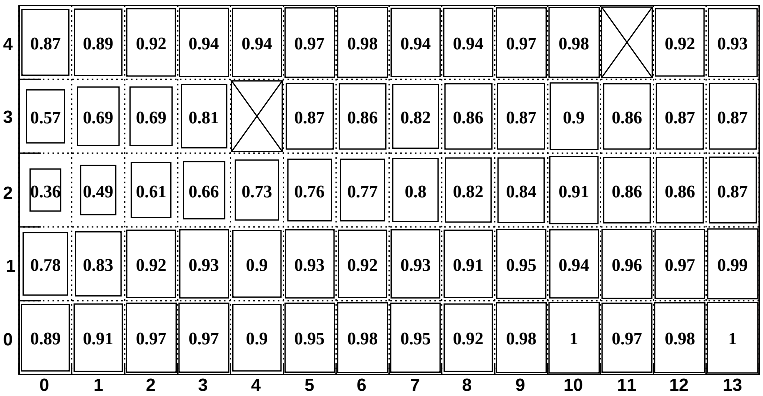

	0	1	2	3	4	5	6	7	8	9	10	11	12	13
4	0.87	0.89	0.92	0.94	0.94	0.97	0.98	0.94	0.94	0.97	0.98	☒	0.92	0.93
3	0.57	0.69	0.69	0.81	☒	0.87	0.86	0.82	0.86	0.87	0.9	0.86	0.87	0.87
2	0.36	0.49	0.61	0.66	0.73	0.76	0.77	0.8	0.82	0.84	0.91	0.86	0.86	0.87
1	0.78	0.83	0.92	0.93	0.9	0.93	0.92	0.93	0.91	0.95	0.94	0.96	0.97	0.99
0	0.89	0.91	0.97	0.97	0.9	0.95	0.98	0.95	0.92	0.98	1	0.97	0.98	1

Figure 11.17: Relative signals (R_{11}^{in}) for fibres inside the tagger measured at the last scan in July 2007, two days after the shutdown of HERA. The relative signal strength is indicated by the box size. Numbers are given for every channel. The distribution of the signals shows that the radiation damage for fibres inside the tagger is largest for cells at the left side of row 2 and 3 where the high-energy electrons hit the tagger.

is proportional to the relative signal. Numbers are given inside the boxes. As can be seen the radiation damage of the fibres inside the tagger is not uniformly distributed but is different for different regions of the tagger. The radiation damage and thus the decrease of the signal is largest for cells located in row 2 and row 3. Here the relative signal is in the order of 90 % for cells at the right edge of the tagger and decreases to about 60 % in row 3 and 36 % in row 2 for cells at the left edge of the tagger, close to the beam pipe. The radiation damage is less pronounced in rows 0, 1, and 4. Here the relative signals fluctuate between about 80 and 100 % in row 1 and between about 90 and 100 % in rows 0 and 4. The results clearly show that the radiation damage of fibres inside the tagger is mainly caused by the incident electrons, which due to the beam geometry hit the tagger most often in row 2 and 3.

Radiation damage outside the tagger

Figure 11.18 shows the relative signal strength (R_{11}^{out}) for each channel recorded at the last scan in July 2007. As can bee seen the radiation damage of the fibres outside the tagger is almost uniformly distributed in y. Horizontally, a trend can be observed between the left and the right edge of the tagger. The cells at the left edge show a slightly higher reduction of the relative signal with respect to cells on the right side. The relative signals vary between 44 and 76 %. The results confirm the assumption that the radiation damage for fibres outside the tagger is mainly caused by scattered synchrotron radiation. Fibres located closer to the beam pipe show a slightly higher radiation damage.

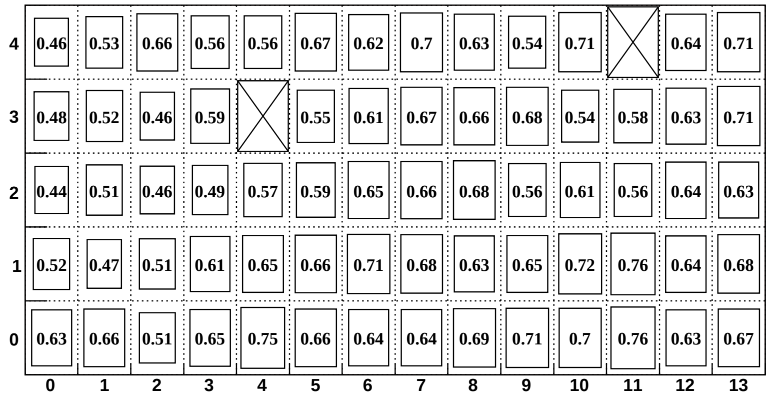

	0	1	2	3	4	5	6	7	8	9	10	11	12	13
4	0.46	0.53	0.66	0.56	0.56	0.67	0.62	0.7	0.63	0.54	0.71		0.64	0.71
3	0.48	0.52	0.46	0.59		0.55	0.61	0.67	0.66	0.68	0.54	0.58	0.63	0.71
2	0.44	0.51	0.46	0.49	0.57	0.59	0.65	0.66	0.68	0.56	0.61	0.56	0.64	0.63
1	0.52	0.47	0.51	0.61	0.65	0.66	0.71	0.68	0.63	0.65	0.72	0.76	0.64	0.68
0	0.63	0.66	0.51	0.65	0.75	0.66	0.64	0.64	0.69	0.71	0.7	0.76	0.63	0.67

Figure 11.18: Relative signals (R_{11}^{out}) for fibres outside the tagger measured at the last scan in July 2007. The relative signal strength is indicated by the box size. Numbers are given for every channel. The distribution of the signals shows that the radiation damage for fibres outside the tagger is almost uniformly distributed. A small trend can be observed between the left (lower signals) and the right edge (higher signals) of the tagger.

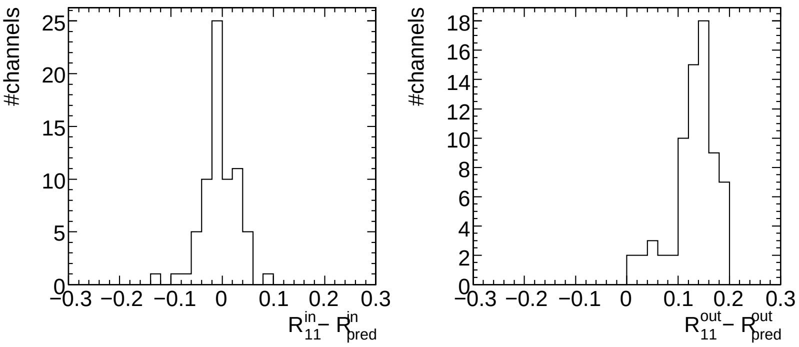

Figure 11.19: Distribution of the difference between the relative signals measured in July 2007 and the predicted values for fibres inside (left figure) and outside the tagger (right figure). For fibres inside the tagger the relative signals measured at July 2007 are in good agreement with the predictions. For fibres outside the tagger the measured values are typically 15 % higher than the prediction, clearly showing the effect of the lead shielding, which was placed between the fibres and the beam pipe after the sevenths scan.

Comparison with the prediction

Figure 11.19 shows the distributions of the differences between the relative signals measured in July 2007 (R_{11}^{in} and R_{11}^{out}) and the respective predicted values ($R_{\text{pred}}^{\text{in}}$ and $R_{\text{pred}}^{\text{out}}$) for fibres inside (left figure) and outside the tagger (right figure). For fibres inside the tagger the relative signals measured at July 2007 are in good agreement with the predictions. For fibres outside the tagger the measured values are typically 15 % higher than the prediction. The observed discrepancy clearly shows the effect of the lead shielding, that was placed between the fibres and the beam pipe after the seventh scan. The shielding reduced the amount of scattered synchrotron radiation the fibres outside the tagger were exposed to.

Chapter 12

HERA II Monte Carlo: The single pion study

In 2007 a detailed study of multiplicities and energy flows based on NC low-Q^2 DIS jet data [119] showed that the energy flow in the upgraded ZEUS detector is not correctly described by the HERA II Monte Carlo predictions. The study revealed that the HERA II Monte Carlo is indeed able to describe the mean energy per detector object, which can either be a cell, an island or an energy flow object (EFO), but fails to describe the number of islands and EFOs. The excess of islands and EFOs in the MC predictions thus leads to an excess in energy flow.

Figure 12.1 shows the ratio between the reconstructed (detector level) and the generated (hadron level) transverse energy as a function of the pseudorapidity. The event reconstruction is based on energy flow objects. As can be seen, in the HERA II MC energy is artificially created within the reconstruction process. The effect is most dominant in the forward super-crack region (the region between the BCAL and FCAL) and in the forward region of the detector. Here the ratio reaches values in the order of 1.8 and 1.4, respectively. It should be noted that in the super-crack region this effect is, though much less pronounced, also present in the HERA I MC. The conclusion of the 2007 study was, that though the upgrade to HERA II only causes small changes in the hadronic final state, the energy flow in the HERA II MC increases by more than 20 %, resulting in a much worse description of the data.

The results of the 2007 study triggered the so called *single pion study.* The basic idea of this study is to generate MC events where single pions are shot into different regions of the detector and look for abnormalities in the detector response. The aim is to identify mechanisms that can cause the observed discrepancies between the MC predictions and the HERA II data, particularly the observed excess in energy flow in the HERA II MC. Since the description of the energy flow dramatically worsened from HERA I to HERA II these mechanisms have to be related to the HERA and ZEUS upgrades.

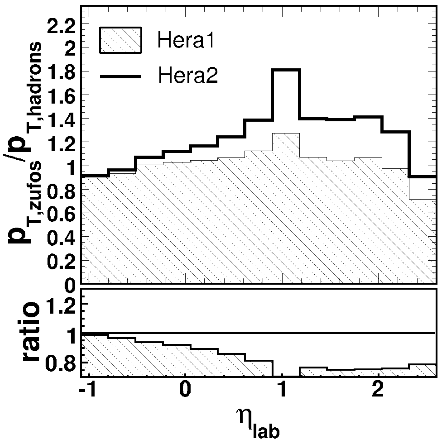

Figure 12.1: Ratio between the reconstructed (detector level) and the generated (hadron level) transverse energy as a function of the pseudorapidity for HERA I (hatched area) and HERA II (solid line). The event reconstruction is based on energy flow objects (EFOs). Figure taken from [119].

12.1 Event generation

For the single pion study, the response of the ZEUS detector to single pions with energies of $E_\pi = 2,\ 5,\ 10,\ 20,\ 50$ and 70 GeV is simulated using the GEANT based MOZART program, which provides a full simulation of the ZEUS detector (see section 2.1.4). The pions generated at $x_{\rm vtx} = y_{\rm vtx} = z_{\rm vtx} = 0$ are shot into

- the very forward region of the detector ($\theta_\pi = 1,\ 2,\ 3,\ 4$ and $6°$);
- the forward super-crack region, that is the region between the FCAL and the BCAL ($\theta_\pi = 27,\ 30,\ 33,\ 36$ and $39°$);
- the barrel region of the detector ($\theta_\pi = 90°$);
- the rear super-crack region, that is the region between the BCAL and the RCAL ($\theta_\pi = 130°$);
- and the rear region of the detector ($\theta_\pi = 160,\ 174$ and $180°$).

The respective regions are indicated in figure 12.2. For each energy and each polar angle a sample of $n_\pi = 10,000$ pions is generated. The pions are generated such that they are uniformly distributed in ϕ (azimuthal angle). In order to investigate possible differences between HERA I and HERA II, two sets of single pion samples are obtained by using the HERA I and the HERA II geometry of the ZEUS detector. For a full event reconstruction, including the reconstruction of energy flow objects, the output of MOZART, that is the detector response to the incident pions, is transfered into the ZEPHYR and ORANGE reconstruction programs.

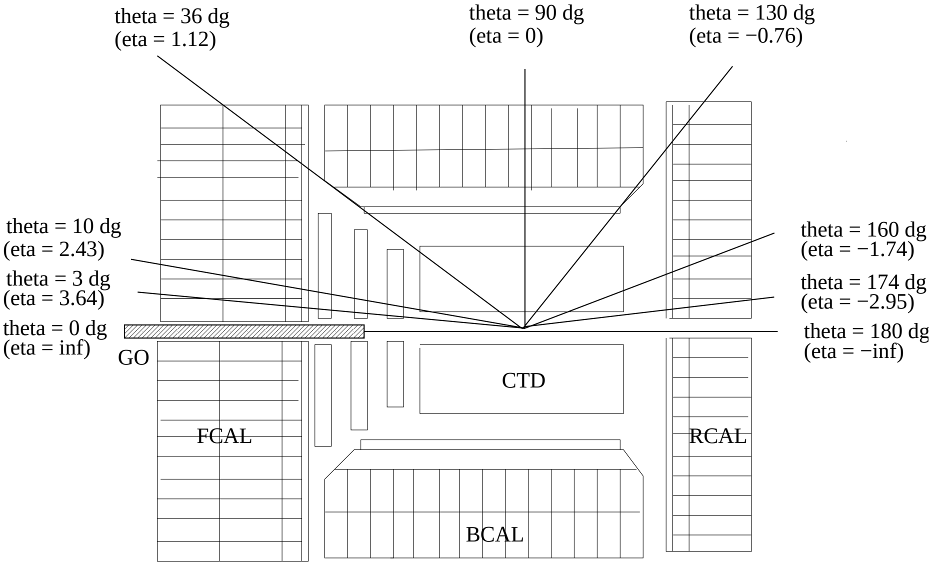

Figure 12.2: Sketch of the ZEUS detector. The angular regions most relevant to the single pion study are indicated by solid lines: $\theta \leq 3^\circ$ (very forward region), $\theta \approx 36^\circ$ (forward super-crack region), $\theta = 90^\circ$ (barrel region), $\theta \approx 130^\circ$ (rear super-crack region), $\theta = 160^\circ$ (rear region) and $\theta \leq 174^\circ$ (very rear region). The figure also indicates the position of the GO magnet, located at a distance of about 1.75 m from the IP, in the forward region of the detector. Particles emitted with polar angles of $\approx 2^\circ$ hit the front surface of the GO magnet.

12.2 Dead material distribution

Within the HERA upgrade a lot of new material was inserted into the ZEUS detector. As described in chapter 10, the changes were most dominant in the forward region. If the modifications are not reasonably transfered in the detector simulation this can result in a deterioration of the description of the data with respect to HERA I. In order to study the distribution of (dead) material within the simulated ZEUS detector and to reveal possible discrepancies between the real detector and its simulation, the distributions of the reconstructed interaction points (IPs) of the single pion events are used. The basic concept is illustrated in figure 12.3 which shows the ZEUS event display for a 50 GeV pion shot into the detector with a polar angle of $\theta = 4^\circ$. As can be seen the pion interacts with one of the wheels of the forward MVD, resulting into a spray of secondary particles. The interaction point, which is reconstructed from the resulting tracks, is close to that point where the pion hits the MVD. In this way the distribution of reconstructed IPs reflects the distribution of dead material in the detector.

Figure 12.4 shows the IP distribution in z direction for 70 GeV pions with a polar angle of $\theta_\pi = 6^\circ$. For pions not interacting with the detector the IP is

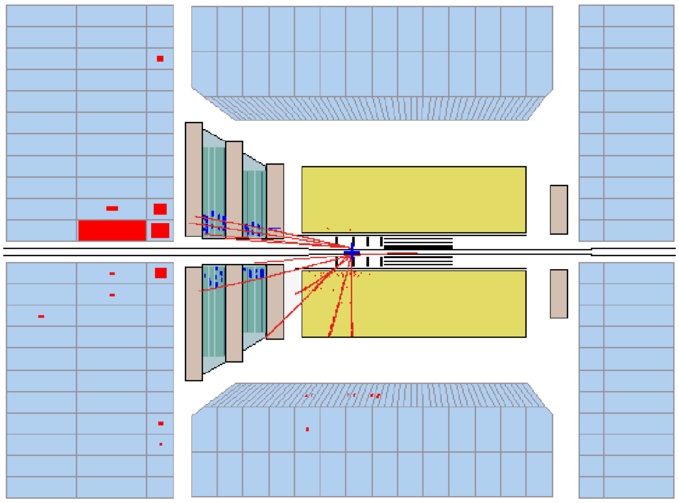

Figure 12.3: ZEUS event display for a 50 GeV pion shot into the detector with a polar angle of $\theta_\pi = 4°$. The pion interacts with one of the wheels of the forward MVD, resulting into a spray of secondary particles. Shown are the MC tracks, the hits in the STT and the energy deposits in the calorimeter. The interaction point, which is reconstructed from the resulting tracks, is indicated by the cross. It is reconstructed close to that point, where the pion hits the MVD. In this way the distribution of reconstructed interaction points reflects the distribution of dead material in the detector.

reconstructed at $z_{\rm vtx} = 0$ cm. It should be noted that, in order to fit within the displayed y range, the peak at $z_{\rm vtx} = 0$ cm is scaled by a factor of 1/50. The second largest accumulation of vertices, starting with a steep rise at $z_{\rm vtx} \approx 20$ cm, is presumably caused by pions interacting with the (elliptical) beam pipe. For smaller values of the incident polar angle, θ_π, this peak is shifted towards higher values of $z_{\rm vtx}$, which is in agreement with this assumption. The observed spectrum, as obtained from the standard HERA II MC version (solid line), shows two additional peaks at about 30 and 45 cm. A detailed comparison of the geometry of the simulated detector with technical drawings of the respective region finally lead to the discovery of an error in the simulation of an MVD flange. In the detector simulation the flange, located at $z \approx 30$ cm, penetrated the beam pipe. The bug was fixed by correcting the position of the MVD flange in the detector simulation. The vertex distribution as obtained from the corrected MC is also shown in figure 12.4 (filled histogram). As can bee seen, the two peaks at about 30 and 45 cm vanish when applying the corrected geometry. It should be noted that for all studies described in the following the corrected MC version is used.

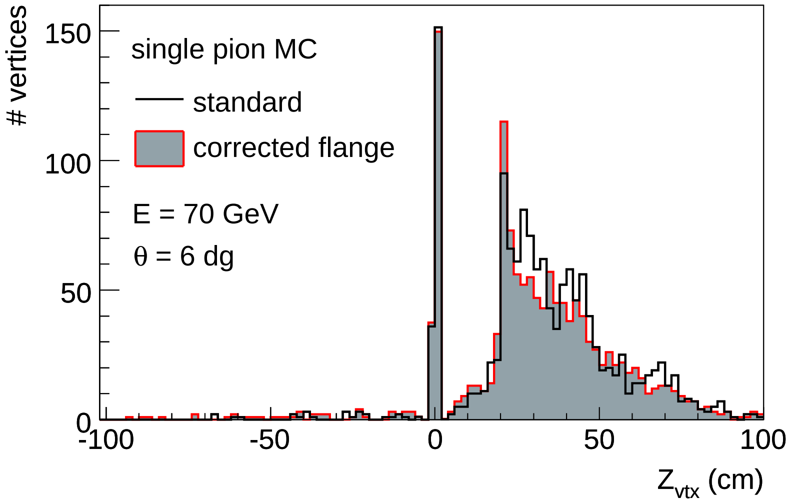

Figure 12.4: z_{vtx} distribution for 70 GeV pions shot into the detector with a polar angle of 6°. Shown are the vertex distributions as obtained from the standard HERA II MC (solid line) and from the corrected MC version (filled histogram). The corrected version includes the correct position of the MVD flange, which in the standard version penetrated the beam pipe at about 30 cm. The peak at ≈ 30 cm vanishes when using the corrected MC version. In order to fit within the displayed y range the peak at $z_{\mathrm{vtx}} = 0$ is scaled by a factor of 1/50.

12.3 Backscattering

During the HERA upgrade the superconducting magnet GO was placed into the forward region of the ZEUS detector. The magnet located at $z = 1.75$ m had an outer diameter of ≈ 19 cm and an aperture of ≈ 8.0 cm in diameter. According to this geometry, a fraction of the particles emitted with small polar angles ($\theta \lesssim 2.5°$), that is particles assigned to the proton remnant, which in HERA I escaped undetected into the beam pipe, hit the magnet and can be (back)scattered into the acceptance region of the detector. In this way the presence of additional material in the HERA II ZEUS detector can result into additional energy flow into the forward region. As the described scattering process occurs in both, data and MC, its presence can not a priori explain the observed discrepancies in the energy flow between data and HERA II Monte Carlo. However, if either the scattering process or the proton remnant are not reasonably modelled within the Monte Carlo simulation the additional amount of backscattering in HERA II can result in a worse description of the data.

Figure 12.5 [101] shows the energy distribution of pions hitting the GO magnet. The figure is based on two NC DIS HERA II MC samples generated with ARIADNE and LEPTO. For the figure only pions with polar angles of $0.5 < \theta_\pi < 3°$, coming from the primary vertex, are taken into account. The events are generated

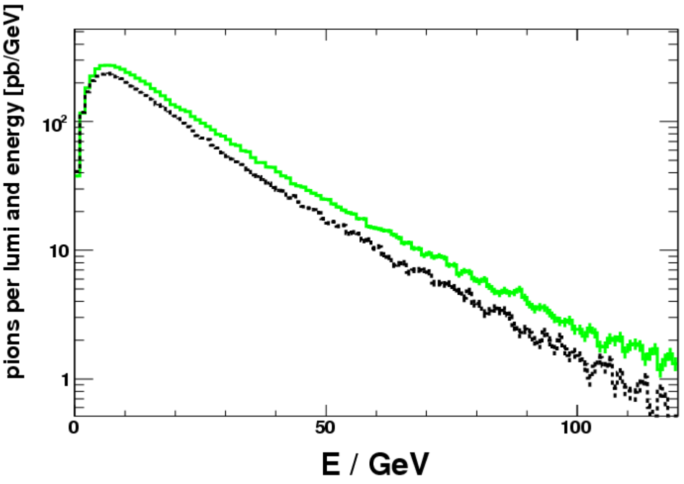

Figure 12.5: Energy distribution of pions hitting the GO magnet. The figure is based on two NC DIS HERA II MC samples generated with ARIADNE (green solid line) and LEPTO (black dashed line). For the figure only pions with polar angles of $0.5 < \theta < 3°$, coming from the primary vertex, are taken into account. The events are generated in a phase space similar to the phase space of the presented HERA I analysis. Figure taken from [101].

in a phase space similar to the phase space of the presented HERA I analysis ($125 < Q^2 < 5000$ GeV^2 and $|\cos\ \gamma_h| < 0.65$). The distribution exhibits a maximum at about 5 GeV and an exponential fall-off towards higher energies. The number of pions per luminosity drops from about 300 pions per pb^{-1} at 5 GeV to about 25 pions per pb^{-1} at 50 GeV and about 10 pions per pb^{-1} at 70 GeV. It should be noted that for pion energies above ≈ 2 GeV the number of pions per luminosity is always higher for ARIADNE than for LEPTO. The observed differences between the two MC samples already indicates an uncertainty in the modelling of the proton remnant. In order to study whether particles from the proton remnant hitting the GO magnet can be scattered into the acceptance region of the detector and in this way have an effect on jet analyses, jets are reconstructed from the single pion samples generated with polar angles of $\theta_\pi = 2°$. Jets are reconstructed with the k_T cluster algorithm. Two sets of jets are obtained by applying the jet algorithm on calorimeter cells (cell jets) and energy flow objects (EFO jets).

Figure 12.6 shows the polar angle distribution of the reconstructed jets for four different energies of the incoming pion ($E_\pi = 10,\ 20,\ 50$ and 70 GeV). For the shown distributions only jets with transverse energies above 3 GeV are taken into account. As can be seen for sufficiently high energies of the incoming pions, jets with $E_T^{jet} > 3$ GeV are reconstructed within the acceptance region of the detector ($\theta > 10°$). In figure 12.7 the number of reconstructed EFO and cell jets is shown

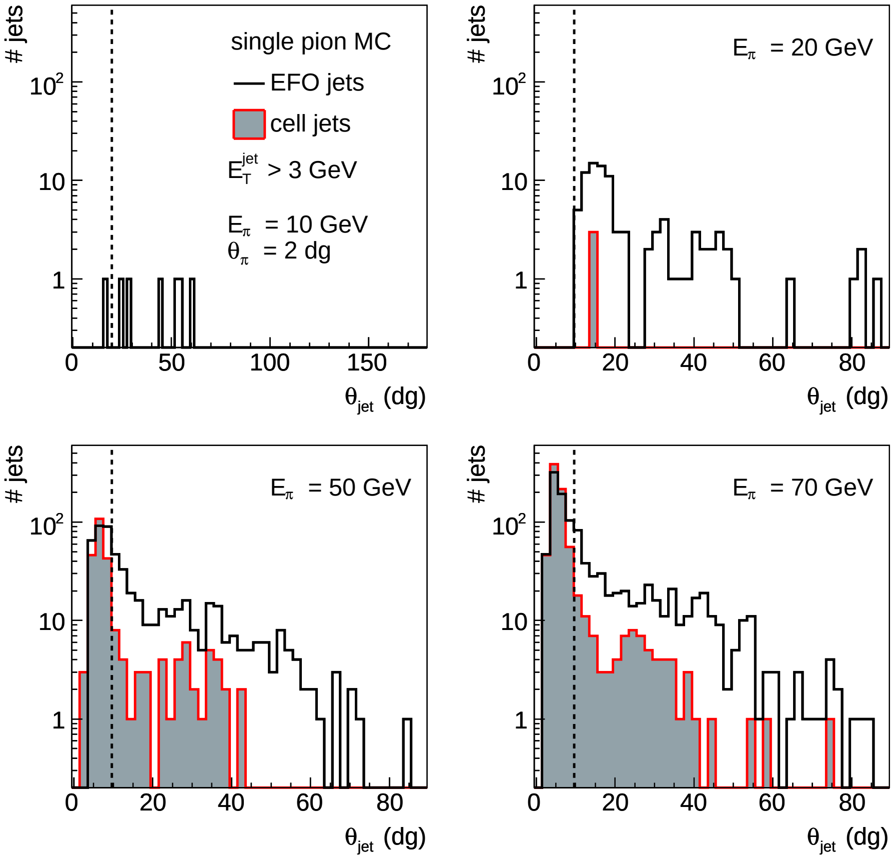

Figure 12.6: Polar angle distribution of jets reconstructed from pions of different energies ($E_\pi = 10, 20, 50$ and 70 GeV) being shot into the GO magnet ($\theta_\pi = 2°$). Jets are reconstructed from energy flow objects (solid line) and calorimeter cells (filled histogram), using the k_T cluster algorithm. For the distribution only jets with transverse energies above 3 GeV are taken into account. As can bee seen for sufficient high energies of the incoming pion jets are reconstructed within the acceptance region of the detector ($\theta_{jet} > 10°$). The number of jets reconstructed from EFOs is for all pion energies significantly higher than the number of jets reconstructed from cells.

as a function of the pion energy. The numbers are obtained from the distributions shown in figure 12.6. The number of jets increases linearly with increasing pion energy. For pion energies of 10, 20, 50 and 70 GeV the number of jets reconstructed with $E_T^{jet} > 3$ GeV and $\theta_{jet} > 10°$ is 7, 93, 296 and 464 (EFO jets) and 0, 3, 50 and 94 (cell jets). The number of jets reconstructed from EFOs is for all pion energies significantly higher than the number of jets reconstructed from cells.

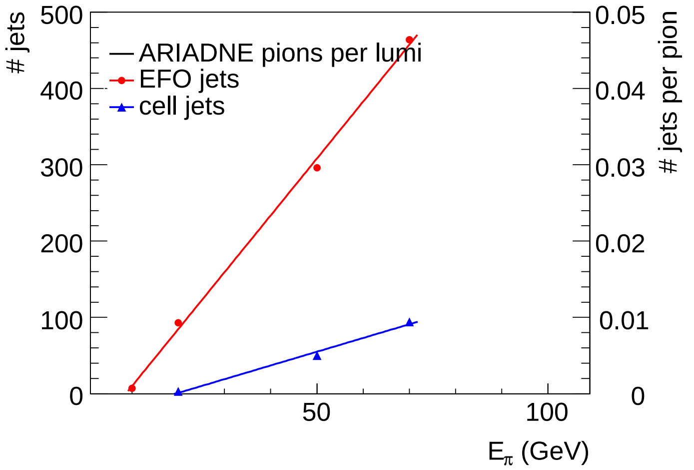

Figure 12.7: Number of reconstructed EFO (dots) and cell (triangles) jets as function of the pion energy. Numbers are obtained from the polar angle distributions shown in figure 12.6. For the figure only jets with $E_T^{jet} > 3$ GeV and $\theta_{jet} > 10°$ are taken into account. The energy dependency can be parametrised by linear functions (solid lines).

The integral,

$$R_{\text{fakejets}} = \int\limits_{E_\pi=0}^{\infty} R_{\text{pions}}(E_\pi) \cdot R_{\text{jets}}(E_\pi)\, dE_\pi, \tag{12.1}$$

where $R_{\text{pion}} = \frac{\text{pions}}{\text{lumi}}(E_\pi)$ is the number of pions per integrated luminosity and per energy interval, ΔE_π, and $R_{\text{jets}} = \frac{\text{jets}}{\text{pion}}(E_\pi)$ is the mean number of jets with $E_T^{jet} > 3$ GeV and $\theta_\pi > 10°$ reconstructed per pion of energy E_π, can be used as an estimate for the rate of fake jets, that is the rate of pions per luminosity hitting the magnet and faking a hard jet within the acceptance region of the detector. R_{jets} is determined by dividing the total number of reconstructed jets by the number of incident pions ($n_{\text{pion}} = 10,000$ for each single pion sample). For the calculation of the integral the energy dependences of R_{pion} and R_{jets} are approximated by exponential and linear functions according to

$$\begin{aligned}
R_{\text{pions}}(E_\pi) &= 530\, \frac{\text{pb}}{\text{GeV}}\, e^{-0.0652\, \frac{E_\pi}{\text{GeV}}} \quad \text{(ARIADNE)}, && (12.2)\\
R_{\text{jets}}^{\text{cell}}(E_\pi) &= \begin{cases} \frac{1}{10000}\left(1.8\, \frac{E_\pi}{\text{GeV}} - 35\right) & \text{for E}_\pi \geq 20 \text{ GeV} \\ 0 & \text{for E}_\pi < 20 \text{ GeV} \end{cases} \quad \text{(cell jets)}, && (12.3)\\
R_{\text{jets}}^{\text{zufo}}(E_\pi) &= \begin{cases} \frac{1}{10000}\left(7.5\, \frac{E_\pi}{\text{GeV}} - 65\right) & \text{for E}_\pi \geq 10 \text{ GeV} \\ 0 & \text{for E}_{\text{pi}} < 10 \text{ GeV} \end{cases} \quad \text{(zufo jets)}, && (12.4)
\end{aligned}$$

which are obtained from fits to the ARIADNE pion energy spectrum and to the number of reconstructed jets as shown in figures 12.5 and 12.7. The resulting rate of fake jets is $\approx 50\frac{\text{jets}}{\text{pb}^{-1}}$ for jets reconstructed from energy flow objects and $\approx 5\frac{\text{jets}}{\text{pb}^{-1}}$ for jets reconstructed from calorimeter cells. It should be noted that the obtained results only provide a very rough estimate of the fake jet rate. The numbers should be compared to the rate of EFO jets with energies above 3 GeV and polar angles larger than 10° in the described dijet analysis which is in the order of $\approx 3000\ \frac{\text{jets}}{\text{pb}^{-1}}$.

In order to study whether the observed (back)scattering of particles from the very forward region into the acceptance region of the detector is a special feature of the HERA II environment the study is repeated using the HERA I geometry of the ZEUS detector. Figure 12.8 shows the polar angle distribution of jets reconstructed from 50 and 70 GeV pions shot into the forward region of the HERA I ZEUS detector ($\theta_\pi = 2°$). Though a very small number of jets is also produced within the HERA I environment, the number of jets with $E_T^{jet} > 3$ GeV reconstructed within the acceptance region of the HERA I detector is significantly lower than for the HERA II geometry. The study thus shows that the amount of (back)scattering of particles from the very forward region into the acceptance region of the detector significantly increases from HERA I to HERA II. In HERA II particles from the proton remnant hitting the GO magnet, can be scattered into the detector and fake hard jets within the acceptance region. If the proton remnant is not correctly modelled within the MC simulation this can result in discrepancies between data and MC within jet analyses.

12.4 Energy flow objects

In order to study the differences between jets reconstructed from energy flow objects and calorimeter cells, jets are reconstructed from the generated 2-70 GeV pions shot into the forward, the super crack, the barrel and the rear region of the detector. Jets are reconstructed using the k_T cluster algorithm. Again two sets of jets are obtained by applying the jet algorithm on cells (cell jets) and EFOs (EFO jets).

Figure 12.9 shows the energy distribution of jets reconstructed from 20 GeV pions shot into the detector with polar angles of $\theta_\pi = 33, 36$ and 39° (forward super-crack region), $\theta_\pi = 90°$ (barrel region), $\theta_\pi = 130°$ (rear super-crack region) and $\theta_\pi = 160°$ (rear region). The most striking feature of the obtained jet energy distributions is the additional energy peak at about two times the energy of the incoming pion for jets reconstructed within the forward and rear super-crack regions ($\theta_\pi = 36$ and 130°). This secondary peak only occurs for jets reconstructed from energy flow objects. A detailed study of the respective events revealed a problem related to the EFO algorithm. As described in section 4.2.2, for particles creating both a track in the tracking system and an energy deposit in the calorimeter, the EFO algorithm has to match the particle's track with the respective calorimeter island. For the events within the secondary energy peak the matching between the track and the calorimeter island seems to fail. Instead of one, two energy flow objects

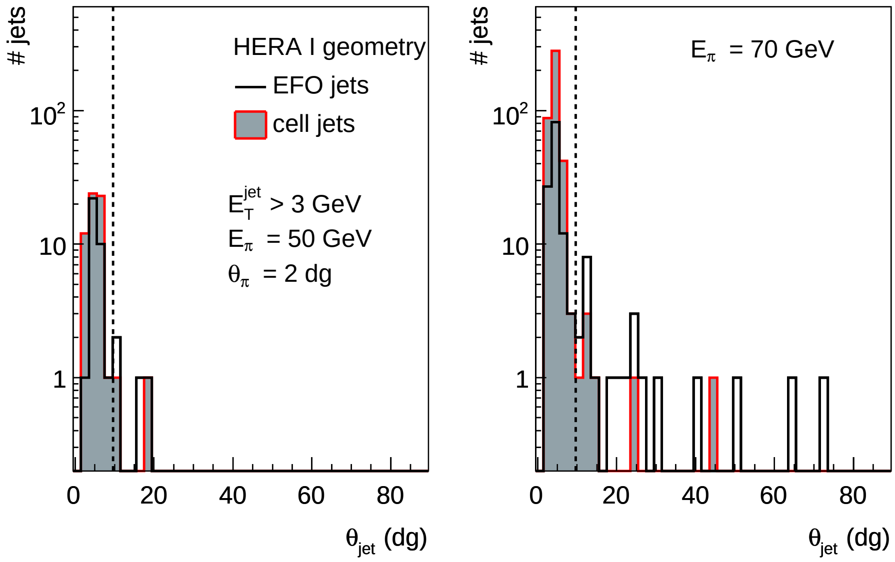

Figure 12.8: Polar angle distribution of jets reconstructed from 50 (left) and 70 GeV (right) pions shot into the very forward region of the HERA I ZEUS detector ($\theta_\pi = 2°$). Jets are reconstructed from energy flow objects (solid line) and cells (filled histogram) using the k_T cluster algorithm. For the distributions only jets with $E_T^{jet} > 3$ GeV are taken into account. As can bee seen almost no jets are reconstructed within the acceptance region of the detector ($\theta > 10°$) .

are reconstructed (one from the track and one from the island), thus leading to a double-counting of particles and energies within the jet reconstruction procedure based on EFOs.

Figure 12.10 shows the energy distribution of jets reconstructed from 5, 10, 20 and 50 GeV pions shot into the forward super crack region ($\theta_\pi = 36°$). As can be seen the additional peak is most pronounced for small energies of the incoming pion and vanishes for $E_\pi \geq 50$ GeV. For pion energies of 5 GeV more than 40 % of the jets are reconstructed within the additional energy peak. This number decreases to 16 and 8 % for 10 and 20 GeV pions. It should be noted that the observed double counting of particles seems to be restricted to the HERA II MC simulation. For jets reconstructed from pions shot into the simulated HERA I detector, no second peak appears in the jet energy spectrum.

The revealed matching problem and the resulting double counting of particles in the super-crack region (one particle creates two EFOs) is in perfect agreement with the results of the 2007 energy flow study. As described in the introduction to this chapter, this study showed that the HERA II MC gives a good description of the mean energy per EFO but overestimates the number of EFOs. Looking at the results

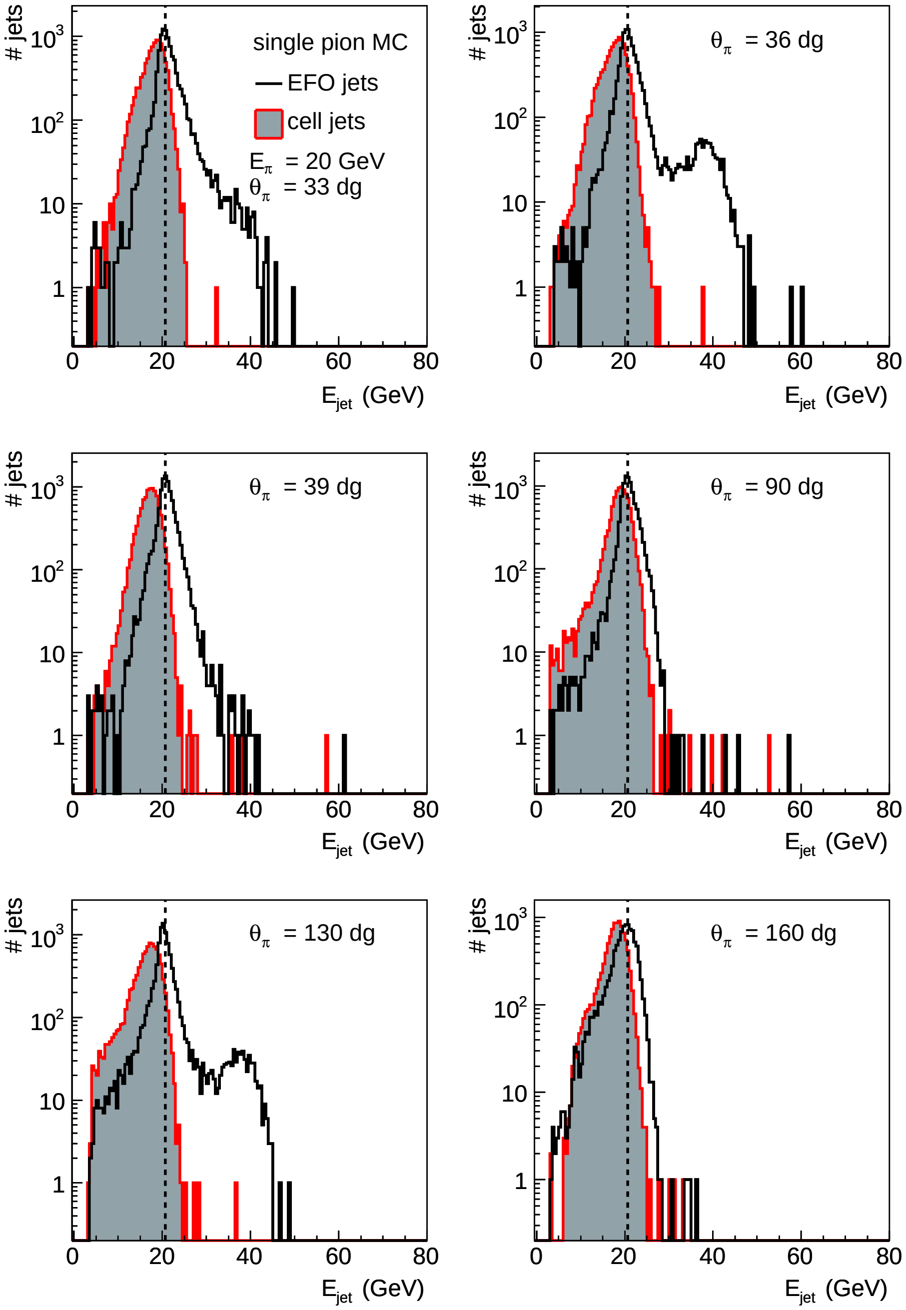

Figure 12.9: Energy distribution of EFO jets (solid lines) and cell jets (filled histograms) reconstructed from 20 GeV pions shot into different regions of the simulated HERA II ZEUS detector. For jets reconstructed within the super-crack regions ($\theta_\pi = 36$ and $130°$) a second peak occurs at about two times the energy of the incoming pion.

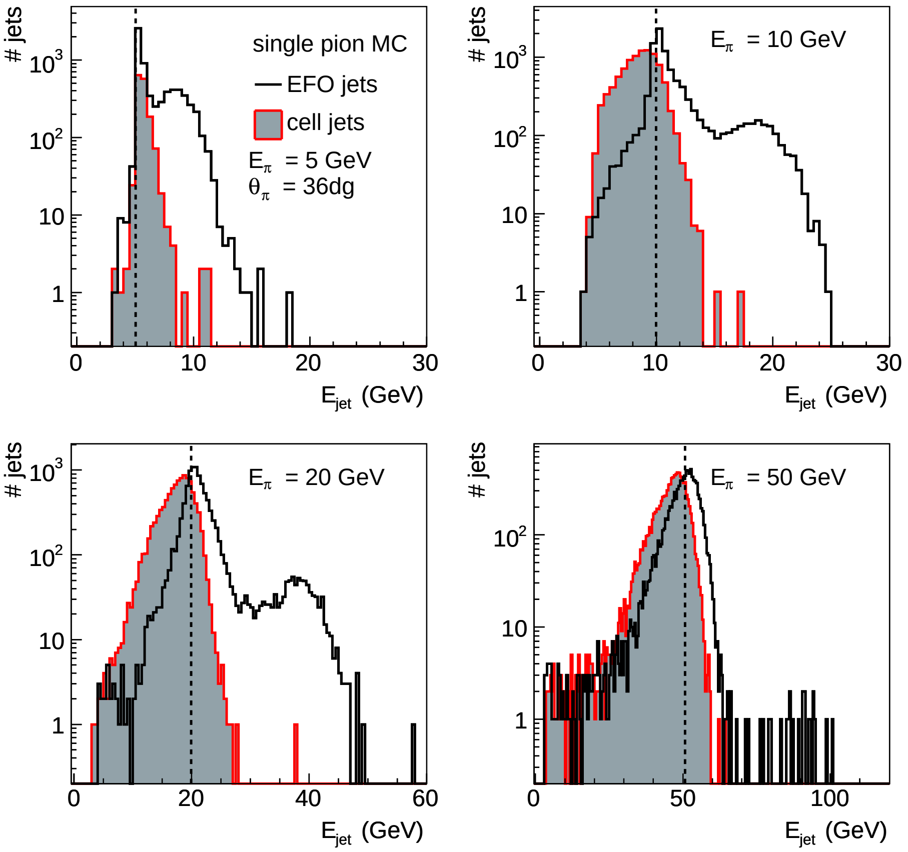

Figure 12.10: Energy distribution of EFO jets (solid lines) and cell jets (filled histograms) reconstructed from 5, 10, 20 and 50 GeV pions shot into the forward super-crack region of the simulated HERA II ZEUS detector. For EFO jets an additional peak occurs at about to times the energy of the incoming pion. For pion energies of $E_\pi = 5$ GeV more than 40 % of the jets are reconstructed within the second energy peak. This number decreases to 16 and 8 % for 10 and 20 GeV pions. The additional peak vanishes for $E_\pi \geq 50$ GeV.

of the 2007 study it seems likely that the observed matching problem is restricted to the MC simulation or at least occurs more often in the MC than in the data.

12.5 Summary and conclusion

Single pions, generated with energies from 2 to 70 GeV, were shot into different regions of the simulated ZEUS detector using the GEANT based program MOZART in order to study the detector response. The MC study helped to reveal differences between the real and the simulated HERA II detector geometry and thus helped to improve the HERA II detector simulation.

Moreover the study showed that at HERA II, particles shot into the very forward region, could be backscattered into the acceptance region of the detector. In this way forward particles, which at HERA I would have escaped undetected into the beam pipe, could cause additional energy flow in the detector. If either the scattering process or the proton remnant are not reasonably modelled this could result in a worse description of the data with respect to HERA I. However, the effect on jet analyses is supposed to be small (< 1 %) and can not explain the discrepancies between data and MC as observed in some HERA II jet analyses.

The single pion study also helped to reveal imperfections of a computer algorithm commonly used for the reconstruction of energy flow objects at ZEUS. In some regions of the detector (namely the super-crack regions between the FCAL/BCAL and BCAL/RCAL), this reconstruction algorithm tended to double-count particles and in this way created additional energy flow in the detector. The observed double-counting (only present at HERA II) is consistent with the results of a study of multiplicities and energy flows performed in 2007 and is able to describe the observed discrepancies between data and MC in HERA II jet analyses, based on energy flow objects.

Bibliography

[1] J. Alcaraz et al. Precision Electroweak Measurements and Constraints on the Standard Model. 2007.

[2] A. M. Cooper-Sarkar. an nlo qcd analysis of inclusive cross-section data and jet production data from the zeus experiment at hera-i. 2004.

[3] S. Chekanov et al. Inclusive-jet and dijet cross sections in deep inelastic scattering at HERA. *Nucl. Phys.*, B765:1–30, 2007.

[4] S. Chekanov et al. Measurement of the Longitudinal Proton Structure Function at HERA. 2009.

[5] Richard P. Feynman. Very high-energy collisions of hadrons. *Phys. Rev. Lett.*, 23:1415–1417, 1969.

[6] Murray Gell-Mann. A Schematic Model of Baryons and Mesons. *Phys. Lett.*, 8:214–215, 1964.

[7] G. Zweig. AN SU(3) MODEL FOR STRONG INTERACTION SYMMETRY AND ITS BREAKING. 2. CERN-TH-412.

[8] J. D. Bjorken. Asymptotic Sum Rules at Infinite Momentum. *Phys. Rev.*, 179:1547–1553, 1969.

[9] Jerome I. Friedman et al. BEHAVIOUR OF THE ELECTROMAGNETIC INELASTIC STRUCTURE FUNCTIONS OF THE PROTON. SLAC-PUB-0907.

[10] F. Halzen and Alan D. Martin. Quarks and Leptons: An Introductory Course in Modern Particle Physics . 1984. New York, Usa: Wiley (1984) 396p.

[11] S. Catani and M. H. Seymour. A general algorithm for calculating jet cross sections in NLO QCD. *Nucl. Phys.*, B485:291–419, 1997.

[12] W.-M. et al.(Particle Data Group) Yao. J. Phys. G 33, 1 (2006) and 2007 partial update for the 2008 edition.

[13] Claudia Glasman. Precision measurements of alphas at HERA. 2007.

[14] Claudia Glasman. Precision measurements of alpha(s) at HERA. *AIP Conf. Proc.*, 792:689–692, 2005.

[15] Stefan Kluth. alpha(s) from LEP. 2007.

[16] Siegfried Bethke. Experimental tests of asymptotic freedom. *Prog. Part. Nucl. Phys.*, 58:351–386, 2007.

[17] R. S. Thorne, A. D. Martin, and W. J. Stirling. MRST parton distributions: Status 2006. 2006.

[18] D. R. Stump. A new generation of CTEQ parton distribution functions with uncertainty analysis. Prepared for 31st International Conference on High Energy Physics (ICHEP 2002), Amsterdam, The Netherlands, 24-31 Jul 2002.

[19] B. Reisert. H1 inclusive cross-section measurements and an extraction of parton distribution functions. *Mod. Phys. Lett.*, A20:1557–1571, 2005.

[20] S. Chekanov et al. A ZEUS next-to-leading-order QCD analysis of data on deep inelastic scattering. *Phys. Rev.*, D67:012007, 2003.

[21] S. Chekanov et al. An NLO QCD analysis of inclusive cross-section and jet- production data from the ZEUS experiment. *Eur. Phys. J.*, C42:1–16, 2005.

[22] Amanda Cooper-Sarkar and Claire Gwenlan. Comparison and combination of ZEUS and H1 PDF analyses. 2005.

[23] R.K. Ellis, W.J. Stirling, and B.R. Webber. QCD and collider Physics. *Cambridge university press, Cambridge*, 1996.

[24] Gerald C. Blazey et al. Run II jet physics. 2000.

[25] William B. Kilgore and W. T. Giele. Next-to-leading order gluonic three jet production at hadron colliders. *Phys. Rev.*, D55:7183–7190, 1997.

[26] Gavin P. Salam and Gregory Soyez. A practical Seedless Infrared-Safe Cone jet algorithm. *JHEP*, 05:086, 2007.

[27] S. Catani, Yuri L. Dokshitzer, and B. R. Webber. The K-perpendicular clustering algorithm for jets in deep inelastic scattering and hadron collisions. *Phys. Lett.*, B285:291–299, 1992.

[28] S. Catani, Yuri L. Dokshitzer, M. H. Seymour, and B. R. Webber. LONGITUDINALLY INVARIANT K(⊥) CLUSTERING ALGORITHMS FOR HADRON HADRON COLLISIONS. *Nucl. Phys.*, B406:187–224, 1993.

[29] Stephen D. Ellis and Davison E. Soper. SUCCESSIVE COMBINATION JET ALGORITHM FOR HADRON COLLISIONS. *Phys. Rev.*, D48:3160–3166, 1993.

[30] John E. Huth et al. TOWARD A STANDARDISATION OF JET DEFINITIONS. Presented at Summer Study on High Energy Physics, Research Directions for the Decade, Snowmass, CO, Jun 25 - Jul 13, 1990.

[31] Stefano Frixione and Bryan R. Webber. MATCHING NLO QCD COMPUTATIONS AND PARTON SHOWER SIMULATIONS. *JHEP*, 06:029, 2002.

[32] G. Ingelman, A. Edin, and J. Rathsman. LEPTO 6.5 - A MONTE CARLO GENERATOR FOR DEEP INELASTIC LEPTON-NUCLEON SCATTERING. *Comput. Phys. Commun.*, 101:108–134, 1997.

[33] Leif Lonnblad. ARIADNE VERSION 4: A PROGRAM FOR SIMULATION OF QCD CASCADES IMPLEMENTING THE COLOUR DIPOLE MODEL. *Comput. Phys. Commun.*, 71:15–31, 1992.

[34] Leif Lonnblad. RAPIDITY GAPS AND OTHER FINAL STATE PROPERTIES IN THE COLOUR DIPOLE MODEL FOR DEEP INELASTIC SCATTERING. *Z. Phys.*, C65:285–292, 1995.

[35] K. Charcula, G. A. Schuler, and H. Spiesberger. *Comput. Phys. Commun.*, 81:381, 1994.

[36] A. Kwiatkowski, H. Spiesberger, and H. J. Mohring. HERACLES: AN EVENT GENERATOR FOR EP INTERACTIONS AT HERA ENERGIES INCLUDING RADIATIVE PROCESSES: VERSION 1.0. *Comp. Phys. Commun.*, 69:155–172, 1992.

[37] H. L. Lai et al. GLOBAL QCD ANALYSIS OF PARTON STRUCTURE OF THE NUCLEON: CTEQ5 PARTON DISTRIBUTIONS. *Eur. Phys. J.*, C12:375–392, 2000.

[38] H. Plothow-Besch. PDFLIB: A LIBRARY OF ALL AVAILABLE PARTON DENSITY FUNCTIONS OF THE NUCLEON, THE PION AND THE PHOTON AND THE CORRESPONDING ALPHA-S CALCULATIONS. *Comput. Phys. Commun.*, 75:396–416, 1993.

[39] Yakov I. Azimov, Yuri L. Dokshitzer, Valery A. Khoze, and S. I. Troian. THE STRING EFFECT AND QCD COHERENCE. *Phys. Lett.*, B165:147–150, 1985.

[40] G. Gustafson. DUAL DESCRIPTION OF A CONFINED COLOUR FIELD. *Phys. Lett.*, B175:453, 1986.

[41] Gosta Gustafson and Ulf Pettersson. DIPOLE FORMULATION OF QCD CASCADES. *Nucl. Phys.*, B306:746, 1988.

[42] Bo Andersson, Gosta Gustafson, Leif Lonnblad, and Ulf Pettersson. COHERENCE EFFECTS IN DEEP INELASTIC SCATTERING. *Z. Phys.*, C43:625, 1989.

[43] E. Butz. DIJET CROSS SECTIONS IN PHOTOPRODUCTION AND AN INVESTIGATION OF DIFFERENCES BETWEEN QUARK-AND GLUON-INITIATED JETS . Diploma Thesis (unpublished), 2005.

[44] O. Gonzalez Lopez. Precise determinations of the strong coupling constant at HERA. DESY-THESIS-2002-020.

[45] Torbjorn Sjostrand. HIGH-ENERGY PHYSICS EVENT GENERATION WITH PYTHIA 5.7 AND JETSET 7.4. *Comput. Phys. Commun.*, 82:74–90, 1994.

[46] Torbjorn Sjostrand. THE LUND MONTE CARLO FOR JET FRAGMENTATION AND E+ E- PHYSICS: JETSET VERSION 6.2. *Comput. Phys. Commun.*, 39:347–407, 1986.

[47] Torbjorn Sjostrand and Mats Bengtsson. THE LUND MONTE CARLO FOR JET FRAGMENTATION AND E+ E- PHYSICS. JETSET VERSION 6.3: AN UPDATE. *Comput. Phys. Commun.*, 43:367, 1987.

[48] Bo Andersson, G. Gustafson, G. Ingelman, and T. Sjostrand. Parton Fragmentation and String Dynamics. *Phys. Rept.*, 97:31–145, 1983.

[49] R. Brun, F. Bruyant, M. Maire, A. C. McPherson, and P. Zanarini. GEANT3. CERN-DD/EE/84-1.

[50] H.C. Fresefeldt. SIMULATION OF HADRONIC SHOWERS. 1985. PITHA 85-02, RWTH Aachen.

[51] ZEUS Collaboration. THE ZEUS DETECTOR, STATUS REPORT 1993 U.HOLM (ED.) DESY (1993) (UNPUBLISHED).
Available on: http://www-zeus.desy.de/bluebook/bluebook.html.

[52] Y. Iga. SIMULATION OF THE ZEUS CALORIMETER. Presented at 5th International Conference on Calorimetry in High Energy Physics, Upton, NY, 25 Sep - 1 Oct 1994.

[53] R. Keith Ellis, D. A. Ross, and A. E. Terrano. THE PERTURBATIVE CALCULATION OF JET STRUCTURE IN E+ E- ANNIHILATION. *Nucl. Phys.*, B178:421, 1981.

[54] J. Pumplin et al. NEW GENERATION OF PARTON DISTRIBUTIONS WITH UNCERTAINTIES FROM GLOBAL QCD ANALYSIS. *JHEP*, 07:012, 2002.

[55] Daniel Stump et al. INCLUSIVE JET PRODUCTION, PARTON DISTRIBUTIONS, AND THE SEARCH FOR NEW PHYSICS. *JHEP*, 10:046, 2003.

[56] J. Pumplin, A. Belyaev, J. Huston, D. Stump, and W. K. Tung. PARTON DISTRIBUTIONS AND THE STRONG COUPLING STRENGTH ALPHA(S). *JHEP*, 02:032, 2006.

[57] S. Bethke. Determination of the QCD coupling α_s. *J. Phys.*, G26:R27, 2000.

[58] H. Nesemann et al. FIRST EXPERIENCE WITH DORIS-III. In *Hamburg 1992, Proceedings, High energy accelerators, vol. 1* 549-551. (Int. J. Mod. Phys. A, Proc. Suppl. 2A (1993) 549-551).

[59] H. Nesemann et al. DORIS III AS A DEDICATED SOURCE FOR SYNCHROTRON RADIATION. Presented at 16th IEEE Particle Accelerator Conference (PAC 95) and International Conference on High Energy Accelerators (IUPAP), Dallas, Texas, 1-5 May 1995.

[60] R. Gehrke and J. Feldhaus. OPERATION OF THE FREE-ELECTRON LASER FLASH AT DESY AND FIRST SCIENTIFIC EXPERIMENTS. *Synchrotron Radiat. News*, 19N6:20–24, 2006.

[61] (ed.) Balewski, K. et al. PETRA III: A LOW EMITTANCE SYNCHROTRON RADIATION SOURCE. TECHNICAL DESIGN REPORT. DESY-04-035.

[62] E. Weckert et al. PETRA III: A NEW HIGH BRILLIANCE SYNCHROTRON RADIATION SOURCE AT DESY. *AIP Conf. Proc.*, 705:73–76, 2004.

[63] (ed.) Altarelli, Massimo et al. XFEL: THE EUROPEAN X-RAY FREE-ELECTRON LASER. TECHNICAL DESIGN REPORT. DESY-06-097.

[64] ATLAS: DETECTOR AND PHYSICS PERFORMANCE TECHNICAL DESIGN REPORT. VOLUME 1. CERN-LHCC-99-14.

[65] ATLAS DETECTOR AND PHYSICS PERFORMANCE. TECHNICAL DESIGN REPORT. VOL. 2. CERN-LHCC-99-15.

[66] G. L. Bayatian et al. CMS PHYSICS: TECHNICAL DESIGN REPORT. CERN-LHCC-2006-001.

[67] G. L. Bayatian et al. CMS TECHNICAL DESIGN REPORT, VOLUME II: PHYSICS PERFORMANCE. *J. Phys.*, G34:995–1579, 2007.

[68] L. R. Evans. LHC: CONSTRUCTION AND COMMISSIONING STATUS. Particle Accelerator Conference PAC07 25-29 Jun 2007, Albuquerque, New Mexico.

[69] (Ed.) Bruning, O. et al. LHC DESIGN REPORT. VOL. I: THE LHC MAIN RING. CERN-2004-003-V-1.

[70] (ed.) Brau, James et al. International Linear Collider reference design report. 1: Executive summary. 2: Physics at the ILC. 3: Accelerator. 4: Detectors. ILC-REPORT-2007-001.

[71] Klaus Ehret et al. Production and detection of axion-like particles in a HERA dipole magnet: Letter-of-intent for the ALPS experiment. 2007.

[72] S. Klein and F. Halzen. The ice cube at the end of the world. *CERN Cour.*, 45N4:17–22, 2005.

[73] G. Hermann, W. Hofmann, T. Schweizer, and Masahiro Teshima. Cherenkov Telescope Array: The next-generation ground- based gamma-ray observatory. 2007.

[74] N. Harnew et al. Vertex Triggering Using Time Difference Measurements in the ZEUS Central Tracking Detector. *Nucl. Instrum. Meth.*, A279:290–296, 1989.

[75] B. Foster et al. The Performance of the Zeus central tracking detector z- by-timing electronics in a transputer based data acquisition system. *Nucl. Phys. Proc. Suppl.*, 32:181–188, 1993.

[76] B. Foster et al. The Design and construction of the ZEUS central tracking detector. *Nucl. Instrum. Meth.*, A338:254–283, 1994.

[77] M. Derrick et al. Design and construction of the ZEUS barrel calorimeter. *Nucl. Instrum. Meth.*, A309:77–100, 1991.

[78] A. Andresen et al. Construction and beam test of the ZEUS forward and rear calorimeter. *Nucl. Instrum. Meth.*, A309:101–142, 1991.

[79] A. Caldwell et al. Design and implementation of a high precision readout system for the ZEUS calorimeter. *Nucl. Instrum. Meth.*, A321:356–364, 1992.

[80] A. Bernstein et al. Beam tests of the ZEUS barrel calorimeter. *Nucl. Instrum. Meth.*, A336:23–52, 1993.

[81] G. Wolf et al. the zeus detector: technical proposal. 1986. DESY-HERA-ZEUS-1.

[82] J. Kruger. calibration of the zeus uranium scintillator calorimeter. *Nucl. Instrum. Meth.*, A315:311–316, 1992.

[83] J. Andruszkow et al. First measurement of HERA luminosity by ZEUS lumi monitor. DESY-92-066.

[84] M. Derrick et al. MEASUREMENT OF TOTAL AND PARTIAL PHOTON PROTON CROSS- SECTIONS AT 180-GEV CENTRE-OF-MASS ENERGY. *Z. Phys.*, C63:391–408, 1994.

[85] J. Andruszkow et al. LUMINOSITY MEASUREMENT IN THE ZEUS EXPERIMENT. *Acta Phys. Polon.*, B32:2025–2058, 2001.

[86] Halina Abramowicz, Allen Caldwell, and Ralph Sinkus. NEURAL NETWORK BASED ELECTRON IDENTIFICATION IN THE ZEUS CALORIMETER. *Nucl. Instrum. Meth.*, A365:508–517, 1995.

[87] A. Viani. ELECTRON FINDER EFFICIENCIES AND IMPURITIES. A COMPARISON BETWEEN SINISTRA95, EM AND EMNET. ZEUS-Note 99-077, 2000.

[88] B. Straub. http://www-zeus.desy.de/straub/ZEUS_ ONLY/doc/em.ps.

[89] Gennady M. Briskin. DIFFRACTIVE DISSOCIATION IN E P DEEP INELASTIC SCATTERING. 1998. DESY-THESIS-1998-036.

[90] N. Tuning. ZUFOS: HADRONIC FINAL STATE RECONSTRUCTION WITH CALORIMETER, TRACKING AND BACK-SPLASH CORRECTION. ZEUS-Note 01-021, 2001.

[91] Stan Bentvelsen, Jos Engelen, and Paul Kooijman. RECONSTRUCTION OF (x, Q^2) AND EXTRACTION OF STRUCTURE FUNCTIONS IN NEUTRAL CURRENT SCATTERING AT HERA. 1991. NIKHEF-H-92-02.

[92] A Blondel and B Jaquet. PROCEEDINGS OF THE STUDY OF AN EP FACILITY FOR EUROPE. 1979. page 391.DESY 79/48.

[93] T. Theedt. MEASUREMENT OF DIJET CROSS SECTIONS IN DEEP INELASTIC EP SCATTERING AT HERA. Diploma Thesis (unpublished), 2005.

[94] ZEUS Collaboration. preliminary result ZEUS-PREL 07-005, 2007.

[95] Private communication Joerg Behr.

[96] O. Gonzales and J. Terron. ANALYSIS IN THE BREIT FRAME AND THE RELATED PROBLEMS . ZEUS-Note 02-006, 2002.

[97] S. Chekanov et al. DIJET PHOTOPRODUCTION AT HERA AND THE STRUCTURE OF THE PHOTON. *Eur. Phys. J.*, C23:615–631, 2002.

[98] S. Chekanov et al. HIGH-MASS DIJET CROSS SECTIONS IN PHOTOPRODUCTION AT HERA. *Phys. Lett.*, B531:9–27, 2002.

[99] M. Wing. SETTING THE JET ENERGY SCALE FOR THE ZEUS CALORIMETER. 2002.

[100] S. Chekanov et al. Measurement of the neutral current cross section and F2 structure function for deep inelastic e+ p scattering at HERA. *Eur. Phys. J.*, C21:443–471, 2001.

[101] Private communication Joerg Behr.

[102] C. Adloff et al. Measurement and QCD analysis of jet cross sections in deep-inelastic positron proton collisions at s of 300-GeV. *Eur. Phys. J.*, C19:289–311, 2001.

[103] H1 Collaboration. preliminary result H1-PREL 08-031, 2008.

[104] U. Schneekloth. The HERA luminosity upgrade. DESY-HERA-98-05.

[105] M. Seidel. The upgraded interaction regions of HERA. DESY-HERA-00-01.

[106] M. Seidel and F. Willeke. Layout of the upgraded HERA interaction regions. Prepared for 7th European Particle Accelerator Conference (EPAC 2000), Vienna, Austria, 26-30 Jun 2000.

[107] Private communication William Schmidke.

[108] ZEUS collaboration. The upgraded luminosity system for the ZEUS experiment. *Proposal submitted to the PRC*, PRC-99-09, 1999.

[109] M. Helbich et al. The spectrometer system for measuring ZEUS luminosity at HERA. *Nucl. Instrum. Meth.*, A565:572–588, 2006.

[110] Stathes D. Paganis. A luminosity spectrometer for the ZEUS experiment at HERA. 2000.

[111] Plansee. http://www.plansee.at/wolfram-densimet.htm.

[112] M. Schroeder. Calibration of the ZEUS 6-m tagger. DESY-THESIS-2008-039.

[113] C. Amsler et al. *s*Review of particle physics. *Phys. Lett.*, B667:1, 2008.

[114] ZEUS collaboration. Measurement of the Longitudinal Proton Structure Function at HERA. 2009. DESY-09-046.

[115] N. Krumnack. Testbeam experiments and Monte Carlo simulation of the ZEUS 6-m tagger. DESY-THESIS-2001-033.

[116] N. Krumnack. Three jet events in deep inelastic scattering. DESY-THESIS-2004-011.

[117] T. Gosau. Measurement of multijet events at low x(Bj) and low Q**2 with the ZEUS detector at HERA. DESY-THESIS-2007-028.

[118] S. Wesch. UNTERSUCHUNG DER STRAHLENSCHAEDIGUNG AM 6M-TAGGER. Studienarbeit der Universitaet Hamburg (unpublished), 2006.

[119] K. Mueller. TOWARD A MEASUREMENT OF INCLUSIVE JET CROSS SECTIONS IN LOW-Q^2 DIS AT HERA II. Diploma Thesis (unpublished), 2007.

Danksagung

Diese Arbeit hätte nicht entstehen können ohne die tatkräftige Unterstützung all jener Menschen, denen ich an dieser Stelle danken möchte. Da nicht alle von ihnen Englisch sprechen, ist dieser Teil auf Deutsch geschrieben:

Mein erster Dank geht an Herrn Prof. Klanner, der trotz seines immervollen Terminkalenders stets ein offenes Ohr für die kleinen und großen Sorgen seiner Mitarbeiter hat und der es neben all seiner administrativen Aufgaben immer noch schafft, sich Zeit für die Physik zu nehmen. Danke Herr Klanner, dass ich so vieles von ihnen lernen durfte!

Mein zweiter Dank geht an Herrn Prof. Schleper für die Aufnahme in seine Arbeitsgruppe und für die Möglichkeit, an so einem spannenden, komplexen und ertragreichen Thema zu arbeiten. Danke Peter!

Ein besonderer Dank gilt meinem Betreuer Dr. Thomas Schörner, der mir jederzeit mit Rat und Tat zur Seite stand und ohne dessen Gespür für das richtige Verhältnis aus 'Zuckerbrot und Peitsche' diese Arbeit und vor allen Dingen die zugrunde liegende Veröffentlichung nie zu Stande gekommen wäre. Danke Thomas, ich habe viel von dir gelernt!

Den Mitarbeitern meiner Arbeitsgruppe danke ich für all die kleinen und großen Tipps rund um die Physik und das Programmieren, für die vielen anregenden oder auch einfach nur amüsanten Gespräche und für die stets angenehme und anregende Atmosphäre in der Gruppe. Danke Alexandra, Antje, Christian, Friederike, Georg, Hanno, Jola, Jörn, Julian, Matthias, Monica, Peter und Uwe.

Danke möchte ich auch dem kleinen Mann mit der großen Tasse, der mir immer dann aus der Patsche geholfen hat, wenn mein Computer mal wieder nicht so wollte wie ich und der mich bei den Cobalt-Scans stets tatkräftig unterstützt hat. Danke Rainer!

Entschuldigen möchte ich mich bei all meinen Freunden, die sich in den letzten Jahren viele komische Geschichten über Monte Carlo Simulationen, NLO-Rechnungen, Energiekorrekturen und Zweijet-Ereignisse anhören mussten, ohne das ihnen irgendwer jemals erklärt hätte, was den überhaupt ein Jet ist. Danke Anke, Barbara, Dennis, Elvan, Inga, Iris, Jette, Katja, Kerstin, Markus, Martin, Nicola, Olaf, Sarah, Sebastian, Sören, Stephan und Thorsten für eure Geduld.

Ein großer Dank geht auch an meine Freundin Munise, die sich stets tapfer meine Ausführungen über die Quanten-Chromodynamik und neuerdings sogar die Halbleiter-Physik anhört und die stets eifrig bemüht ist, meinen kulturellen Horizont zu erweitern. Danke Munise, dass du so ein grosses Herz für verhaltensoriginelle Menschen hast!

Der wohl größte Dank aber geht an meine Eltern, die mich stets unterstützt haben und ohne die dieses Studium nicht möglich gewesen wäre. Ich hoffe ihr könnt erahnen, wie viel mir die Physik bedeutet und wie dankbar ich euch für alles bin.

DANKE!